Part II -

Improving Specifications to Resist Frost Damage in Modern Concrete Mixtures

Pool Fund Study TPF-5-297

Led by Oklahoma DOT

Hope Hall, Justin Becker, Chad Staffileno, Mark Finnell, Lichun Chen, David Welchel,
Jacob Peery, Jake LeFlore, Dan Cook, M. Tyler Ley
Oklahoma State University
Stillwater, Oklahoma

Mehdi Khanzadeh Moradllo, Chunyu Qiao, Rita Maria Ghantous, Mitchell Keys,
Myo Zaw, Steven Reese, W. Jason Weiss
Oregon State University
Corvallis, Oregon

August 31, 2019

Table of Content

I. Determining the Air-Void Distribution in Fresh Concrete with the Sequential Air Method (SAM) 3

II. Field and Laboratory Validation of the SAM 32

III. Tools for mixture design with the Sequential air method 54

IV. Effects of Pumping Concrete Based on The Air Void Paramaters in Fresh and Hardened Concrete 70

V. Establishing a Freeze-Thaw Prediction Model: Electrical Resistivity and Formation Factor of Air-Entrained Concrete 94

VI. Establishing a Freeze-Thaw Prediction Model: Quantifying Fluid Absorption in Air-Entrained Concrete Using Neutron Radiography 120

VII. Establishing a Freeze-Thaw Prediction Model: Quantifying Fluid Filling of the Air Voids in Air Entrained Concrete Using Neutron Radiography 157

VIII. Establishing a Freeze-Thaw Prediction Model: Determining the Freezing and Thawing Performance of Mortar Samples Using Length Change Measurements 185

IX. Time to Reach Critical Saturation (TTRCS) Model 209

X. Using X-ray computed tomography to investigate Mortar Subjected to Freeze-Thaw Cycles 237

DETERMINING THE AIR-VOID DISTRIBUTION IN FRESH CONCRETE WITH THE SEQUENTIAL AIR METHOD (SAM)

1.0 Introduction

Concrete is widely known as the building material of choice when a long-lasting structure is desired. However, concrete can be damaged when it is 1) wet and 2) exposed to freezing temperatures [1, 2]. The damage that occurs due to freezing and thawing can lead to premature deterioration, costly repairs, and the need to replace concrete infrastructure components well before they reach the end of their expected lifetimes. This problem is widely known, and there are many specifications in place designed to minimize these problems.

The most widely adopted approach to producing concrete with frost durability is to add an air-entraining admixture (AEA) while the concrete is being mixed. The AEA creates small, well-dispersed, air-filled bubbles in the fresh concrete. Current theories hypothesize that these bubbles act as pressure-relief reservoirs in the hardened concrete that allow water to move during freezing [2-4]. Because a large number of variables during batching, mixing, and placement impact how AEAs perform in concrete, in practice it can be challenging to provide a consistent air-void system in hardened concrete [5]. The concrete industry would greatly benefit from tools that would help ensure that this process is done correctly and the concrete that is produced will be freeze-thaw durable.

Current specifications for freeze-thaw durability were developed more than half a century ago. These specifications are based on the measurement of total air volume in fresh concrete [6, 7]. This is typically done by comparing the actual density to the theoretical, or by measuring the response of the concrete from an increase in pressure. While this past research looked at concrete with many different characteristics, such as the total volume of air, water-to-cement (w/c) ratio, mixture proportions, and different types of aggregate, the only admixture used in the research was a Vinsol resin AEA, as this was the only admixture available at the time. This work determined the need for 9% +/-1% volume of air in the mortar [6, 7], which has since been simplified to about 6% air by volume of the concrete mixture based on an expected paste volume [8]. If these criteria were met then the mixtures were expected to show satisfactory performance in laboratory freeze-thaw testing. These decades-old recommendations are still widely used to ensure freeze-thaw durability. Because of this, current specifications require the volume of air to be measured in the concrete before it has hardened.

While the specification and measurement of the total volume of air within concrete are useful, more in-depth research has shown that the size and spacing of the air-entrained bubbles are more important. For this paper, the size and spacing of the air bubbles will be combined into a term called the "air void system quality". Historically, the air void system quality is defined by "the Spacing Factor" [4, 9]. The ACI 201 technical committee has recommended that a spacing factor of 200 μm be used to provide concrete with satisfactory freeze-thaw durability [10]. The spacing factor can be determined by a hardened air void analysis or petrographic analysis completed as per ASTM C457 [11]. Unfortunately, the ASTM C457 method requires significant labor, specially trained staff and equipment, and can take between 7 to 14 days to complete. However, the biggest drawback of this testing is that it cannot be used on concrete before it has hardened. This means that several days of construction could proceed before this measurement would indicate that there was an issue. Because of these challenges, most specifications measure the total volume of air in the concrete while it is being placed and assume that the correlation between air volume and air quality suggested in the work from the 1950's is satisfactory. Despite these shortcomings, the ASTM C457 test is helpful, as it can investigate hardened concrete and it provides important insights into the freeze-thaw durability of concrete that the total volume of air cannot [9]. For this reason, it will be an important method to compare to other measurements.

Since the 1950s there have been many changes in the makeup of modern concrete mixtures and so the original recommendations of measuring only the total volume of air within concrete have been questioned [12-17]. For example, modern concrete mixtures commonly use portland cement in combination with other types of supplementary cementitious materials; mixtures often contain between three to five chemical admixtures; cement is made with new types of grinding aids that aim to reduce production energy and provide strength increases; and finally, modern construction practices are much more complex, as machines are used that pump, consolidate, and finish our concrete. There are numerous examples of how these changes have influenced the original relationship between air volume and air quality. Specific examples include different AEAs [12, 13, 15], admixture combinations [14, 15, 17] and pumping [18-21]. There has been little progress made because tools are not readily available to help investigate these issues. Because of these substantial differences in modern mixtures from those investigated in the 1950's, it is not clear if air volume specifications are still appropriate. This highlights the need for a new tool to provide more insight into the quality of the air void system during construction so that near real-time changes can be made to ensure that concrete that is freeze-thaw durable is being used and provide useful insights into how different additives or processes impact the quality of the air void system.

Modern tools are needed to build confidence that concrete construction will be long-lasting in freeze-thaw environments while also minimizing the amount of material that is rejected at the job site. Ideally, these tools could be used during both the development of the concrete mixtures and then again at the job site to evaluate the material. In addition, the measurements should be robust, accurate, and provide answers in a timely manner that correlate to historic measurements of freeze-thaw durability. Previous techniques have tried to address this by measuring the bubbles separated from the concrete through agitation of the mixture in a solution of controlled viscosity. This process liberates bubbles from the mortar and their size distribution is determined by measuring the change in the buoyancy force on an inverted plate over time [22, 23]. This technique has found mixed success but has been suggested by some to be sensitive, variable, and challenging to operate in the field [24].

This paper outlines a procedure that uses sequential pressures to determine the air void quality in fresh concrete. The method is described, and results from both laboratory and field testing are presented along with the variability of the measurement. Finally, a discussion is included over the potential use and impact of the method. The goal of this paper is to introduce and establish the validity of the technique. Other papers over the mechanism and usage over a wider number of materials are in preparation.

2.0 Experimental Methods

2.1 Materials

All the concrete mixtures in this research used a type I cement that met the requirements of ASTM C150 [25]. Both the oxide analysis and Bogue calculations for this cement used is shown in Table 1. The aggregates used were locally available crushed limestone and natural sand used in commercial concrete. The crushed limestone had a maximum nominal aggregate size of 19 mm (3/4”). One mixture contained a blend of the coarse and intermediate aggregate as well. Both the crushed limestone and the sand met ASTM C33 specifications [26] and have proven to be freeze-thaw durable. The absorption of the crushed limestone and sand was 0.60% and 0.55%

respectively. All the admixtures used are described in Table 2 and met the requirements of ASTM C260 and ASTM C494 [27, 28].

Table 1 – Type I cement oxide analysis

	SiO_2 (%)	Al_2O_3 (%)	Fe_2O_3 (%)	CaO (%)	MgO (%)	SO_3 (%)	Na_2O (%)	K_2O (%)	TiO_2 (%)	P_2O_5 (%)	C_3S (%)	C_2S (%)	C_3A (%)	C_4AF (%)	LOI (%)
Cement	21.1	4.7	2.6	62.1	2.4	3.2	0.2	0.3	-	-	56.7	17.8	8.2	7.8	-
Fly Ash	38.7	18.8	5.8	23.1	5.6	1.2	1.8	0.6	1.5	0.4	-	-	-	-	0.6

Table 2 – Admixture references

Short Hand	Description	Application
WROS	Wood Rosin	Air-entraining agent
SYNTH	Synthetic chemical combination	Air-entraining agent
PC	Polycarboxylate	Superplasticizer
WR	Triethanolamine	Water reducer

The wood rosin (WROS) and synthetic (SYNTH) AEA are two popular commercial AEAs. Sixteen different mixture designs were investigated and are shown in Table 3. A subset of mixtures was investigated with either a polycarboxylate (PC) superplasticizer meeting ASTM C1017 or a midrange water reducer (WR) meeting ASTM C494 [27, 29]. A dose of between 60 and 200 mL/100 kg was used to increase the slump of the mixture between 50 mm to 150 mm. Between five and fourteen dosages of AEA were investigated for each mixture to achieve a range of air contents from 2% to 10%. An ASTM C618 Class C fly ash [30] was used in several of the mixtures with a 20% cement replacement by weight.

Testing was also completed with 62 field mixtures from seven different sites in Oklahoma. The majority of these samples were taken from paving projects and more details can be found in other publications [31]. Data is also included in this paper from a study completed by the US Federal Highway Administration (FHWA) Turner Fairbanks Research Lab in McLean, Virgina, USA. This allowed an independent evaluation of the method with other materials but similar methods. This work is summarized in other publications [32].

Table 3–SSD Mixture proportions

w/cm	Cement kg/m^3	Fly-Ash kg/m^3	Paste Volume (%)	Coarse kg/m^3	Fine kg/m^3	Water kg/m^3	Admixture Used
0.45	362	0	29	1098	714	163	WROS
0.45	362	0	29	1098	714	163	SYNTH
0.53	362	0	32	1053	682	192	WROS
0.41	362	0	28	1127	722	148	WROS
0.39	362	0	27	1140	730	141	WROS
0.45	362	0	29	1098	714	163	WROS + PC1
0.45	362	0	29	1098	714	163	SYNTH + PC1
0.45	290	72	30	1089	709	163	WROS
0.45	223	56	23	785/573*	634	126	WROS
0.40	290	72	28	1115	724	145	WROS
0.40	290	72	28	1115	724	145	WROS + PC1
0.35	290	72	28	1127	768	127	WROS + PC1
0.40	290	72	28	1115	724	145	WROS + PC2
0.40	290	72	28	1115	724	145	WROS + PC3
0.40	290	72	28	1115	724	145	WROS + PC4
0.40	290	72	28	1115	724	145	WROS + PC5
0.40	290	72	28	1115	724	145	WROS + WR

* Mixture used a coarse and intermediate aggregate blend.

2.2 Concrete Mixture Procedure and Testing

Aggregates were collected from outside storage piles and brought into a temperature controlled room at 23°C for at least 24 h before mixing. Aggregates were placed in the mixer and spun and a representative sample was taken for a moisture correction. At the time of mixing all aggregate was loaded into the mixer along with approximately two-thirds of the mixing water. This combination was mixed for three min to allow the aggregates to approach the saturated surface dry (SSD) condition and ensure that the aggregates were evenly distributed.

Next, the cement, fly ash (if used), and the remaining water was added and mixed for three min. The resulting mixture rested for two min while the sides of the mixing drum were scraped. After the rest period, the mixer was started and the admixtures were added. If the PC or WR was used then it was added first and allowed to mix for 15 s to 30 s then the AEA was added. After the admixtures were added the concrete was mixed for three min.

Samples were made for hardened air-void analysis (ASTM C457 [11]), and a selection of mixtures was investigated with rapid freeze-thaw testing (ASTM C666 [33]). Two 7 L samples were tested with the Sequential Air Method or SAM. These two samples were investigated simultaneously by different operators to determine the variability of the method.

2.3 Sequential Air Method

The device used to complete the SAM resembles an ASTM C231 [34] Type B pressure meter with some modifications. The meter uses a digital pressure gauge and six restraining clamps instead of the typical four. These additional clamps are required because of the increased pressures during the SAM test. A picture of an initial version of the device is shown in Fig. 1.

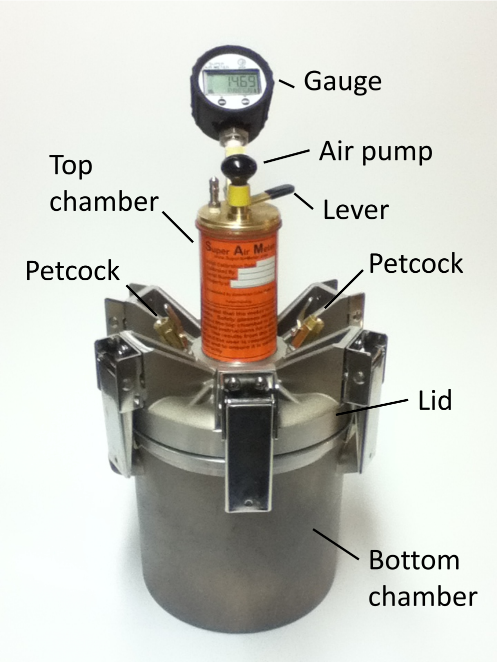

Figure 1 – The device used to complete the SAM.

The different components of the meter are shown in Fig. 1 and are referenced throughout the procedure. The first step in the method is to fill, consolidate, and level fresh concrete in the bottom chamber according to ASTM C231 [34]. A plate is used to level the concrete. Next, the rim and seal between the lid and bottom chamber are cleaned. The lid is then secured to the bottom chamber by the clamps. Water is then added through the petcocks to fill the area between the concrete and the lid. Next, the top chamber is pressurized to 100 kPa ± .7 kPa (14.5 psi ± 0.05 psi) and allowed to stabilize. The petcocks are then closed, and the lever is pressed to bring the two chambers to equilibrium while the bottom chamber is hit on all sides with a rubber mallet. This lever is held for at least 10 s to allow the two chambers to reach equilibrium. The value is recorded and used to calculate the volume of the air in the concrete [35, 36]. Without opening the petcocks, the top chamber is pressurized to 207 kPa ± .7 kPa (30 psi ± 0.05 psi). The lever is then pressed for 10 s to bring the two chambers to equilibrium while the bottom chamber is hit on all sides. The top chamber is then pressurized to 310 kPa ± .7 kPa (45 psi ± 0.05 psi) without opening the petcocks. The lever is then pressed for 10 s and the sides of the bottom chamber are again hit with a rubber mallet. This value should be recorded and will be known as Pc_1. The petcocks are then opened to release the pressure in the bottom chamber. Without removing the lid, water is then added to the bottom chamber to fill the area between the lid and the consolidated concrete and the procedure is repeated. The equilibrium pressure after completing the 310 kPa pressure is recorded as Pc_2. The test takes between eight to ten min by an experienced user to complete. Figure 2 shows a typical data set and a video of the test is available [37].

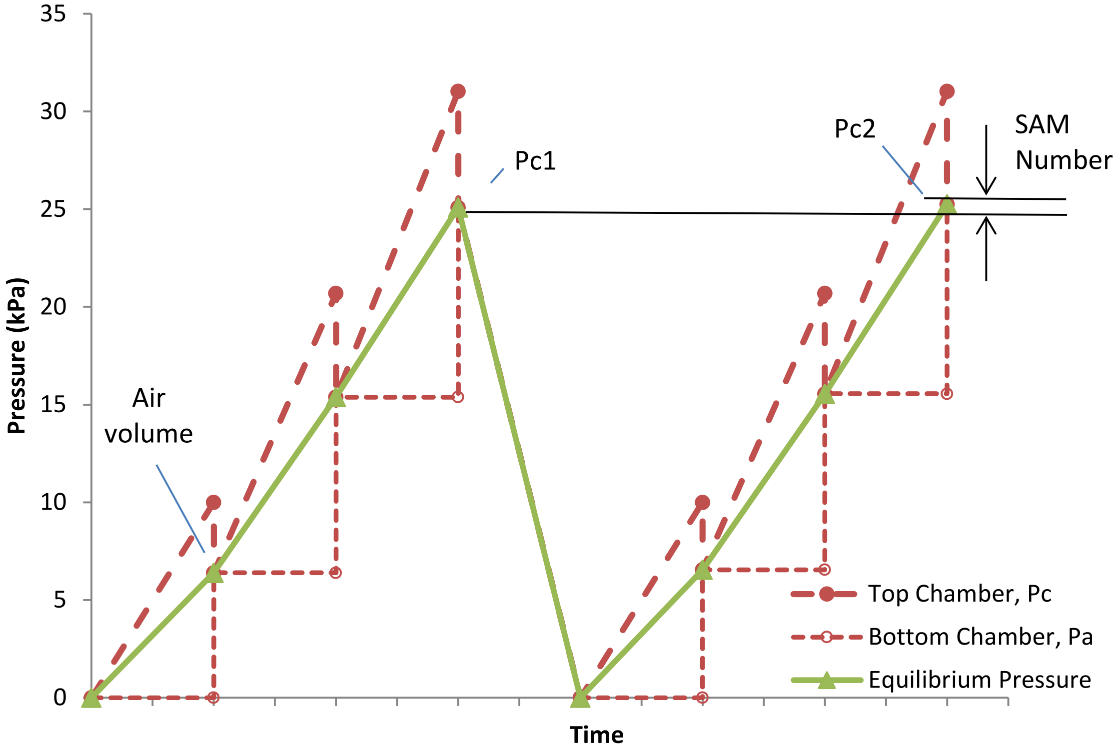

Figure 2 A graphical representation of the pressures in the top and bottom chamber in the SAM.

The device in this paper is an improved version of previous publications [38]. The previous version used five pressure steps with a maximum of 517 kPa (75 psi). This test uses three pressure steps with a maximum pressure of 310 kPa (45 psi) and a more sensitive gauge. These changes increase the speed, accuracy, and create new correlations to air void quality in the test results.

2.3.1 SAM Number calculations

From the results in Fig. 2, it can be seen that the two pressure curves are not exactly the same. To quantify these differences a term called the SAM Number is used. This can be expressed mathematically as:

$$\text{SAM Number} = (Pc_2 - Pc_1)/c$$

Where Pc_2 is the second equilibrium pressure at 310 kPa (45 psi) and Pc1 is the first equilibrium pressure at 310 kPa (45 psi). The value c is a constant that is 1.45 if the units are in kPa and 1.0 if the units are in psi. SAM Numbers in the 303 mixtures investigated ranged from 0.03 to 0.83. The SAM Number is an empirical number that will be correlated to other parameters such as Spacing Factor and Durability Factor. The SAM Number is reported as a unitless value because it does not have a physical meaning and is only used as a correlative number.

2.3.2 Air Content and Aggregate Correction

The volume of air in the concrete can be determined by using Boyle's Law from the first equilibrium pressure at 100 kPa (14.5 psi). This procedure is discussed in other publications [31, 35, 36] and matches the same method and procedure used in the conventional pressure meter (ASTM C231). Past experiments with similar equipment have shown that the air content determined by the SAM closely matched results from the ASTM C231 pressure method [31, 32, 38, 39]. Because the procedures are the same and shown to be equivalent, this is not investigated further in this work.

The calculated air volume with the procedure does not include the aggregate correction factor caused by air contained within the aggregate. The procedure to find the aggregate correction factor is outlined in ASTM C231 [34]. Since the SAM Number compares the difference between two sequential pressures, any impact caused by the aggregate on the response to pressure should be removed by subtracting the two pressure responses from each other. The application of this procedure on aggregates of high porosity, such as lightweight aggregates, is an area of future research.

2.3.3 Variability in measurement

The variability of the SAM Number was evaluated by using two operators to simultaneously investigate the same concrete mixture. To gain more insight, testing was also done by two operators by using water and a calibration vessel that provided a reading of 5% air. By only using water and a calibration vessel then this allowed the variability of the test to be examined without including the variability of the concrete.

2.4 Hardened Air Sample Preparation

Samples were cut into 19 mm thick slabs, the surface was treated with an acetone and lacquer mixture to harden the surface, and then the samples were lapped with sequentially finer grits. The prepared surface was then inspected under a stereo microscope. After a satisfactory surface was obtained the hardener was removed with acetone. The sample was then blackened with black permanent marker, the voids were filled with <1 μm white barium sulfate powder, and the voids within the aggregates were blackened under a stereo microscope. This process left the surface of the concrete sample black and the voids within the paste white. Sample preparation details can be found in other publications [31, 40]. The surface was then investigated with ASTM C457 [11] method C by using the Rapid Air 457 from Concrete Experts, Inc. For a threshold range between

0 and 256, a single value of 185 was used for all samples and the results do not include chords smaller than 30 μm. These settings have been shown to provide satisfactory results with the materials and instrument used and match the practices by others [40-42].

3.0 Results and Discussion

3.1 Establishing the Usefulness of the SAM Number

To highlight how the SAM compares to the air content, Spacing Factor, and the Durability Factor, two concrete mixtures have been compared. These two mixtures are identical except one mixture contains an AEA and the other a water reducer and AEA (see 0.40 WROS and 0.40 WROS + PC1 in Table 3 for more details). Figure 3 shows the relationship between the air content and the Spacing Factor. Lines are shown to highlight the trends in the data. The data shows that the Spacing Factor is quite different between the two mixtures at comparable air contents. For example, the linear trend line for the mixture with just an AEA requires only 4.5% air to have a Spacing Factor of 200 μm and the mixture with the admixture combination requires 7.5% air. This suggests that the two mixtures have a substantially different relationship between air volume and Spacing Factor. This highlights the challenge of only using the air content to determine the quality of the air void system in fresh concrete. This reinforces the findings from previous research that suggests the air void quality and air volume do not have the same relationship in all mixtures.

In Figure 4, these same mixtures are investigated but the SAM Number from these mixtures is compared to the Spacing Factor. The linear trend lines are almost overlapping for both data sets. This shows that for these two mixtures that the SAM Number shows a better correlation to the Spacing Factor or air void quality in the fresh concrete than the volume of air.

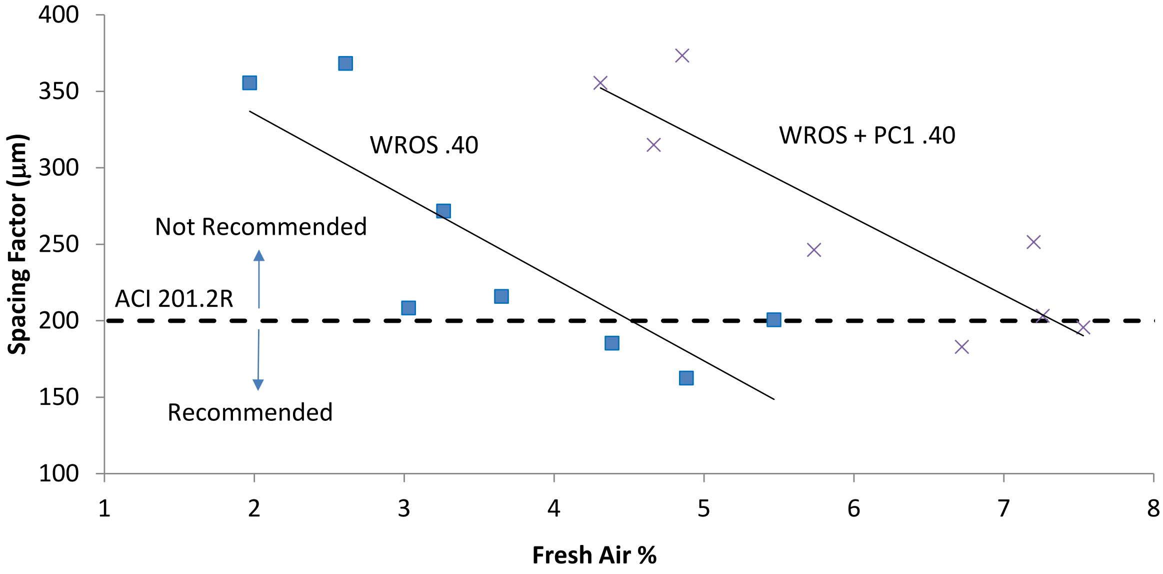

Figure 3 – Air content versus Spacing Factor for two mixtures with very different air void qualities for the same air volume. This highlights how air volume does not necessarily correlate with air void quality.

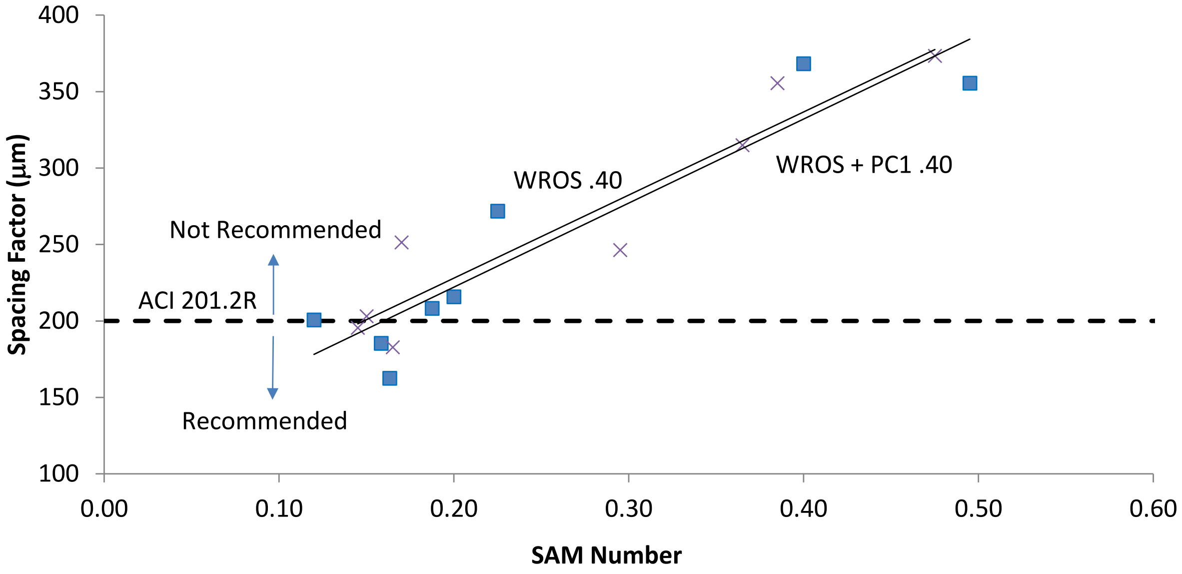

Figure 4 – The SAM Number versus the Spacing Factor for the two mixtures previously shown in Figure 3. These mixtures do not have the same relationship between air content and Spacing Factor but they do have the same SAM Number versus Spacing Factor.

Next, these same mixtures are investigated to determine the relationship between air volume and SAM Number and the Durability Factor. Figure 5 shows that the two mixtures needed drastically different air volumes to produce equivalent Durability Factors. Polynomial trend lines are plotted and show that the mixture with the AEA had a Durability Factor above 70% when the air volume was higher than 2.75% while the mixture with the admixture combination required almost 6% air. This again highlights the inability to use the volume of air to predict the air void quality and in turn the freeze-thaw durability of a concrete mixture.

Figure 6 compares both of these mixtures but now uses the SAM Number and compares it to the Durability Factor. The trend lines are again shown to be almost overlapping for concrete mixtures when the SAM Number is used to investigate their performance. This highlights how the SAM Number does a better job than the volume of air to predict the freeze-thaw durability of the concrete mixtures investigated.

This data is significant as it shows that not all concrete mixtures follow the same variation of air void quality and air content and that the SAM Number is able to provide insights that are not possible by looking at the total volume of air. Next, the SAM Number will be used to investigate a much larger data set. The reader should be reminded that the goal of this paper is to show the validity of the SAM Number and the usefulness of the method to make measurements in fresh concrete that provide important insights into the freeze-thaw durability of concrete mixtures while the mixture can still be manipulated.

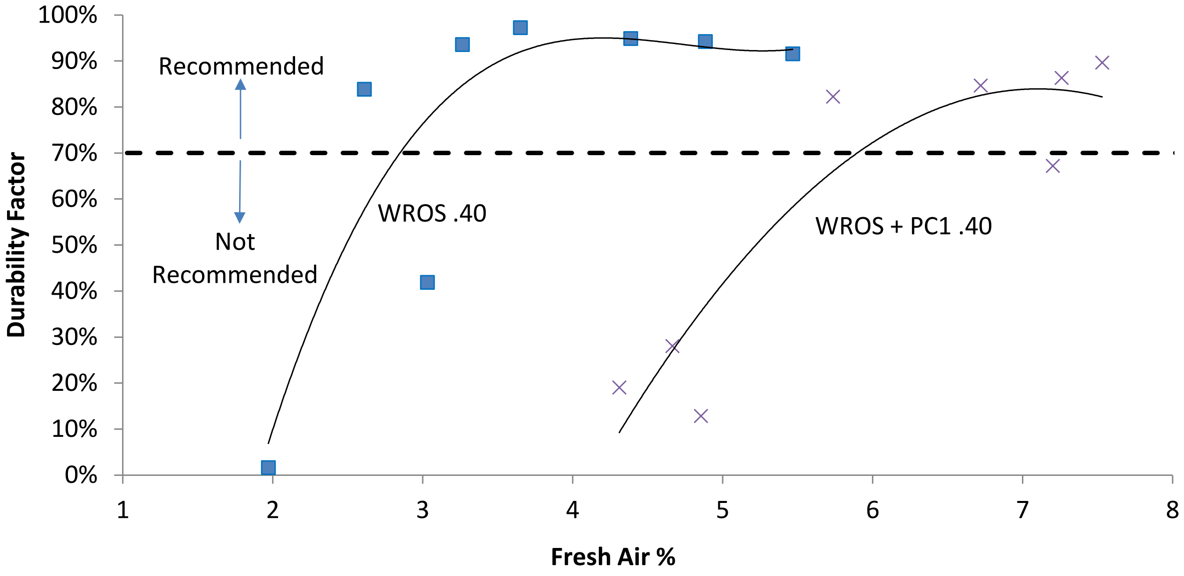

Figure 5 – The air content versus the Durability Factor for the two example mixtures. The two mixtures need significantly different air contents to meet the recommended Durability Factor.

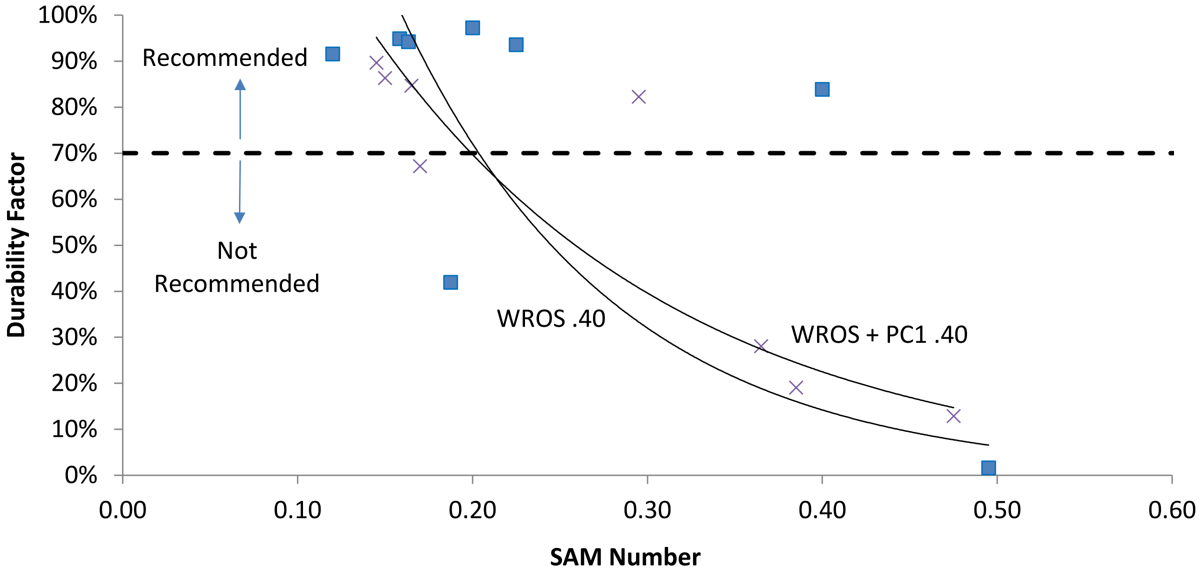

Figure 6 – The SAM Number versus the Durability Factor for the same example mixtures. In this example, both mixtures need approximately the same SAM Number to provide the recommended Durability Factor.

3.2 Evaluation of the SAM Number for Large Data Sets

Figure 7 shows the correlation between the SAM Number and the Spacing Factor for 303 laboratory and field concrete mixtures that were completed by two different labs. These mixtures consisted of 176 laboratory mixtures completed at Oklahoma State University, 65 laboratory mixtures completed at FHWA Turner Fairbanks, and 62 field mixtures from seven different field projects in Oklahoma. All laboratory mixtures completed at Oklahoma State University are contained in the appendix.

While the data in Fig. 7 is scattered, there does seem to be a correlation between the Spacing Factor and SAM Number. This variation could be caused by differences in the measurement procedures, the material, or perhaps another mechanism not yet understood. Despite the variance in the data, the results show that the SAM Number still provides a useful measure that can be completed in fresh concrete that correlates to the Spacing Factor.

While an equation could be fit to the data, the expected variability from the measured and predicted values would make this approach hard to implement. Instead, it was decided to use a single SAM Number as a limiting value much like what is currently done with the Spacing Factor and Durability Factor. For example, Figure 7 shows the suggested Spacing Factor of 200 □m from ACI 201.2R-16 [10] along with a SAM Number of 0.20. By using this single SAM Number as a threshold value it allows the user to determine in a single measurement if a Spacing Factor is above or below a target value. Again, this concept of using a single critical value is commonplace in determining freeze-thaw durability and assists practitioners with implementation.

By using this approach this allowed the Spacing Factor and SAM Number to be separated into four quadrants. In two of these quadrants, the measurements agree. For example, the Spacing Factor and SAM Number are above or below a critical value. In the other two quadrants, the measurements do not agree and one of the measurements indicates a satisfactory value and the other does not. By finding the SAM Number that allowed the most data points to fall within the quadrants that agree this allowed a quantitative method to choose the best SAM Number for the desired Spacing Factor. This was done for spacing factors of 200 µm, 250 µm, and 300 µm and the best correlating SAM Numbers were found. The results of this analysis are shown in Figure 8. It is interesting that when a SAM Number of 0.20 is used that this correlated with a spacing factor of 200 µm for 88% of the comparisons. If the user is interested in determining a Spacing Factor of 250 µm then a SAM Number of 0.25 correctly separates 85% of the comparisons. This almost perfect correlation between the numbers does not continue for a Spacing Factor of 300 µm as a SAM Number of 0.33 shows the best correlation for just over 75% of the data.

This correlation between the two measurements can be quite useful as the SAM Number can be obtained within 10 min in the fresh concrete and allow immediate changes to be made or feedback to the user about the quality of the air void system. Furthermore, the correlation of a single SAM Number and Spacing Factor is quite high and shows a general agreement between the two methods. The use of the SAM to measure the quality of the air void system is much better than waiting the seven to ten days required to cut, polish, and analyze a sample for a Spacing Factor.

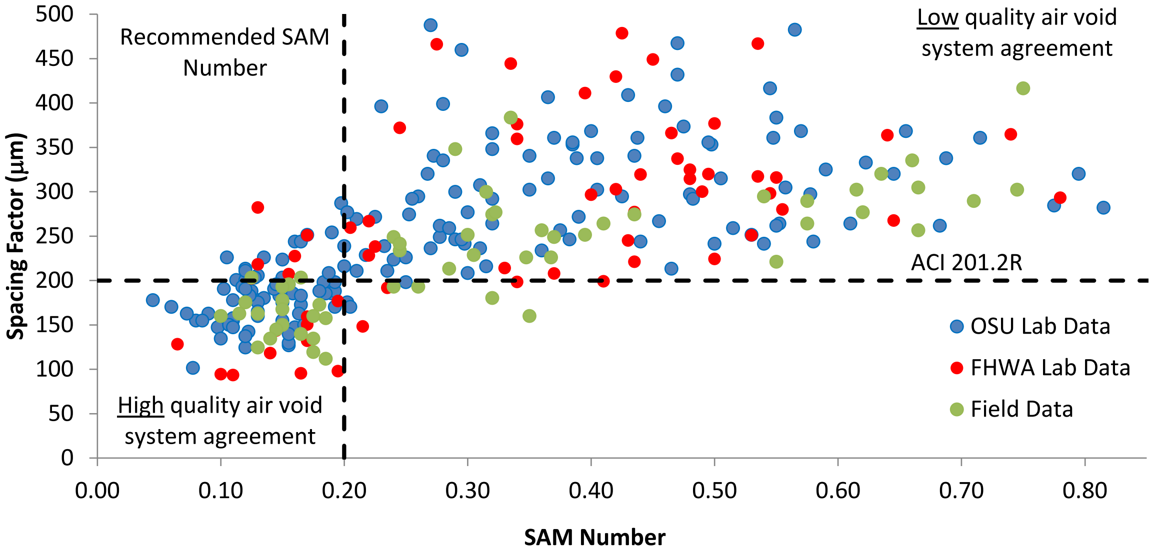

Figure 7 – The SAM Number versus the Spacing Factor for 303 laboratory and field mixtures completed by two different research groups. A SAM Number of 0.20 was able to correctly identify if the Spacing Factor was above or below 200 µm for 88% of the data.

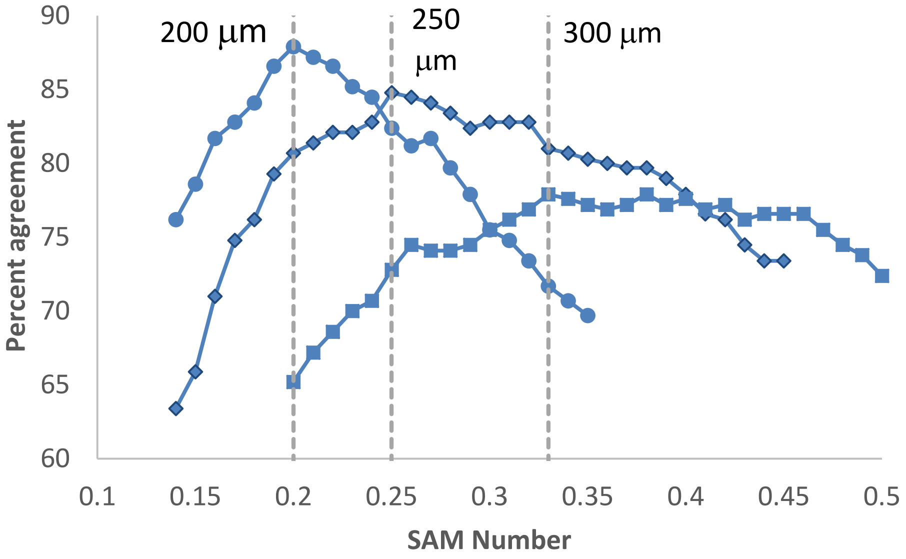

Figure 8 – The percent agreement between the Sam Number and different spacing factors.

3.3 Comparison to Durability Factor

The Spacing Factor has been traditionally used as in lieu of testing for freeze-thaw durability because the test could be completed more rapidly and with less effort than laboratory freeze-thaw testing. Since a good correlation was found between the Spacing Factor and SAM Number one would expect a good correlation between SAM Number and the results from the freeze-thaw testing. However, the best correlation between the SAM Number and Durability Factor may not be the same.

Figure 9 shows the relationship between Durability Factor and SAM Number for 68 different concrete mixtures. Again, a single SAM Number was used to investigate the data. The results of the analysis are shown in Figure 10 for a Durability Factor of 60%, 70%, and 80%. All three of these limit states showed very similar agreement with the SAM Number. The results show that there is no difference between a SAM Number of 0.32 and 0.35. A SAM Number of 0.32 was chosen as the limit as it provides a conservative estimate and it correctly separated nearly 90% of the investigated mixtures. Furthermore, if one was using these results to create a specification then it may be appropriate to use a SAM Number that is even lower in order to provide some safety factor against failure. This will be discussed in more depth later in the paper.

Next, the Spacing Factor and Durability Factor are compared in Figure 11. This was done for the same 68 mixtures that are shown in Figure 9. When a Spacing Factor of 200 mm was compared to a Durability Factor of 70% it was found that this combination of limits correctly separated 69% of the data points. This shows that a SAM Number of 0.32 better correlates to a Durability Factor of 70% for the mixtures investigated. This again is promising data as the SAM Number can be measured in fresh concrete with less effort than either the Durability Factor or Spacing Factor.

More importantly, because the SAM Number can be completed in fresh concrete then it can be used to make immediate changes to the concrete mixture before placement.

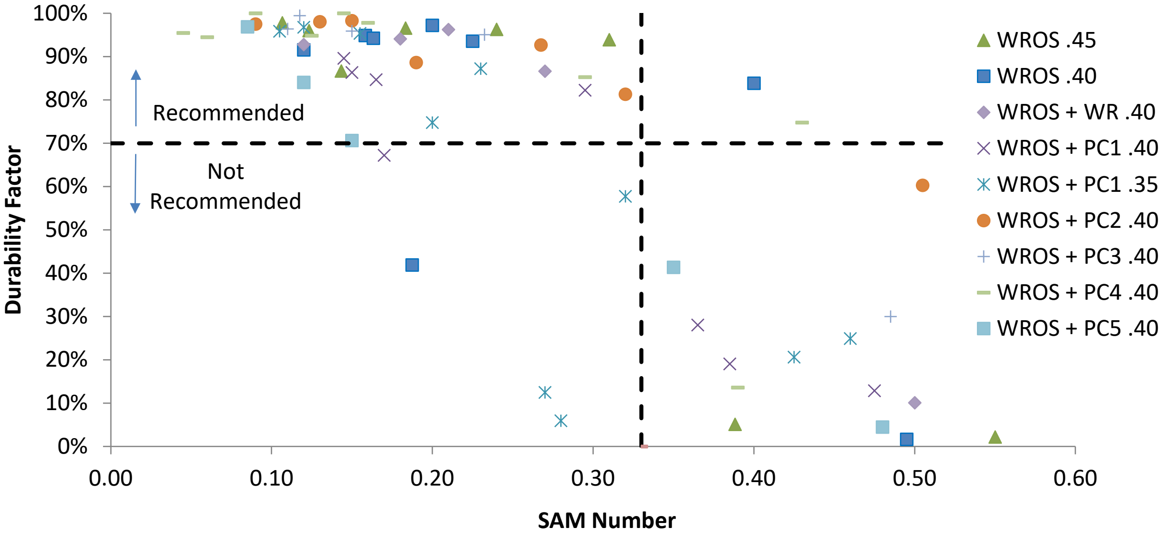

Figure 9 – SAM Number versus Durability Factor for 68 mixtures. A SAM Number of 0.32 identified whether the concrete would have a Durability Factor above 70% for 90% of the mixtures investigated.

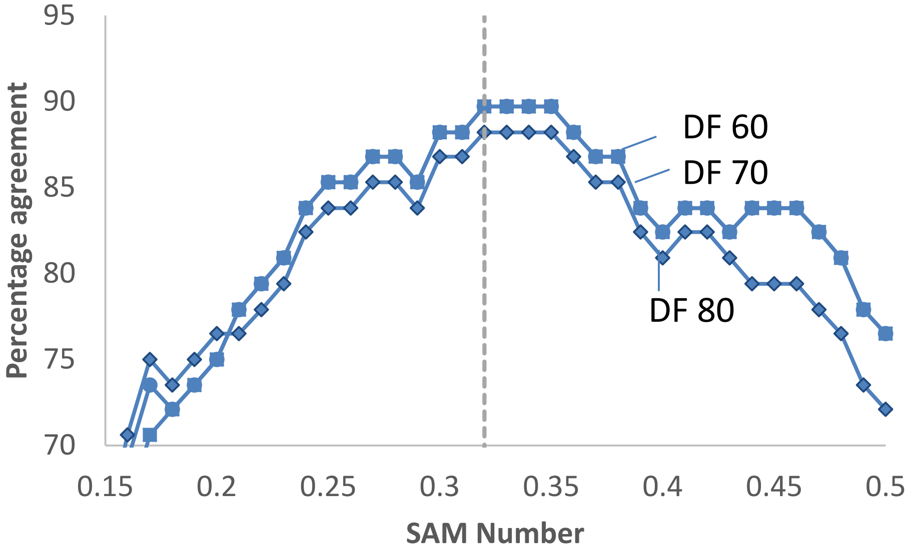

Figure 10 – The percent agreement between the SAM Number and different durability factors.

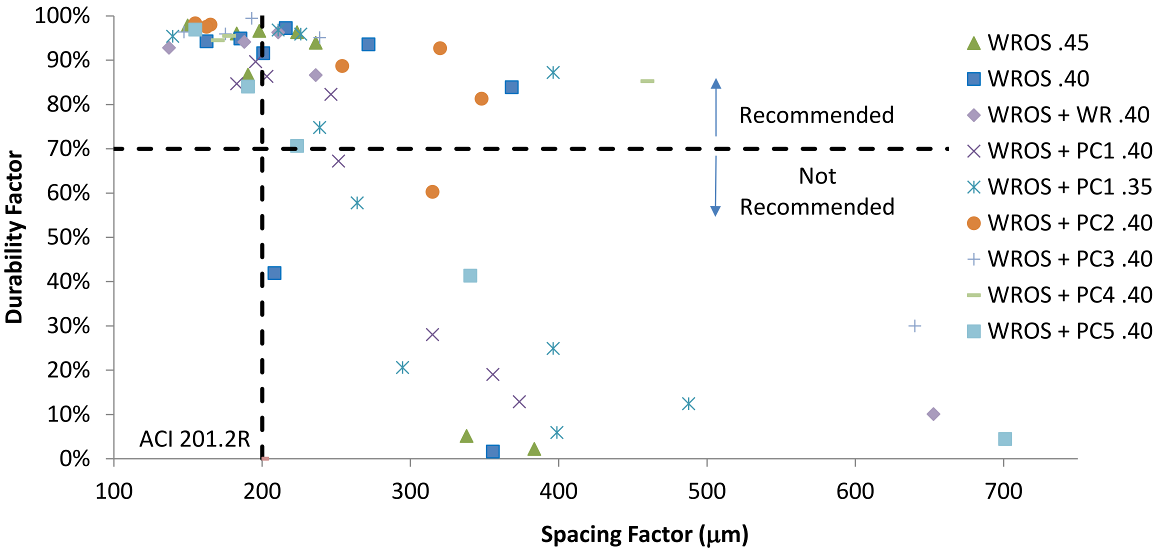

Figure 11 – The Spacing Factor versus the Durability Factor for 68 concrete mixtures. A Spacing Factor of 200 □m identified if the concrete would have a Durability Factor above 70% for 69% of the mixtures investigated.

3.4 Variance of the Measurement

It is important that the variation of a testing method is well understood. To investigate the variability of the test method 170 concrete mixtures were completed with two different SAM meters and two operators simultaneously completing the measurement. The measured SAM Number from each meter is shown in Figure 12. A line of equity has also been added to the graph. Ideally all of the mixtures would fall on the line but as can be seen, there is some variance. This difference in measurements could be caused by variations from operators, materials, or the method itself.

Table 4 shows that the average difference between these two measurements was found to be 0.008 with a standard deviation of 0.049. This means that on average the two measurements between two meters will be off by 0.008 but that the expected difference between two measurements can vary by 0.10 for a 95% confidence interval (two standard deviations). These numbers are important for users to understand when specifying and using the SAM Numbers.

These same operators and equipment were used to examine the SAM Number with the bottom chamber filled with water and a calibration vessel. The results are also shown in Table 4. This was done to simplify the test and remove the complications caused by evaluating concrete. By only using water it removes the variability of sampling, consolidating, finishing, and the inherent variability of the material.

For the water testing, the average difference between the measurements was similar but it reduced from 0.008 to 0.005; however, the standard deviations of the measurement was reduced by 2.3 times. Since the same equipment and operators were used to complete both sets of tests this suggests that the variability of the use of concrete in the test plays a significant role in the variability of the measurement.

To look at this in more detail the variability of hardened air void test (ASTM C457) and the rapid freeze-thaw test (ASTM C666) test was compared to the variance measurements of the SAM Number. This was done because all three of the tests aim to measure the air void quality either directly or indirectly. In order to compare the tests the coefficient of variation (COV) was used. This allows the variation and average value of a test to be compared. This also provides a useful tool to quantitatively compare the variation of different test methods.

Table 5 shows that all three tests have a COV between 15.2% and 22.7% with the SAM Number showing the lowest COV. Because the COVs between these three tests are so similar this could mean that the air void quality in concrete is more variable than other parameters that are more commonly measured such as the compression strength or unit weight. This is also supported by the observation that the variation of the SAM Number was significantly reduced when only investigating water in the test method.

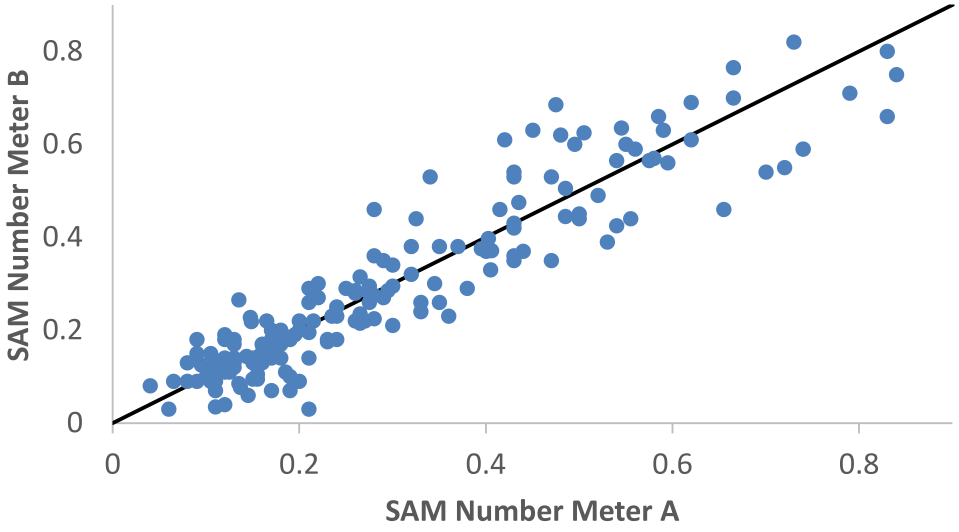

Figure 12 – A comparison of the SAM Number from two different meters measured on the same concrete mixtures. A line of equity is shown for comparison.

Table 4 - A summary of the SAM variance for measurements in concrete and with a calibration vessel in water.

	Concrete	Calibration vessel in water
Average difference for two SAM Numbers	0.008	0.005
Standard deviation between two SAM Numbers	0.049	0.021
Number of observations	170	16

Table 5 – A comparison of the coefficient of variation, agreement with Durability Factor as found in this paper, and the time required to complete the test.

Test Method	Parameter	COV	Agreement with Durability Factor of 70 In ASTM C 666	Time to complete the test
SAM	SAM Number[1]	15.2%	90%	10 min
ASTM C457	Spacing Factor[2]	20.1%	67%	7 days
ASTM C666	Durability Factor[3]	22.7%	-	3.5 months

[1] Assumes a SAM Number of 0.32 and a standard deviation of 0.049 from this paper

[2] From ASTM C457

[3] From ASTM C666 with a durability factor of 75 and Method B

3.5 Different SAM Number Limits and Specifications

ACI 201.2R-16 [10] has suggested that a spacing factor of 200 μm is recommended to obtain freeze-thaw durable concrete. However, for the mixtures investigated a Spacing Factor of 200 μm was found to be a conservative estimate for a Durability Factor between 60% and 80%. Because of this, a higher SAM Number showed a better correlation to a satisfactory Durability Factor then the historically recommended Spacing Factor. It is possible that the historic Spacing Factor limit of 200 mm was chosen with a safety factor to minimize freeze-thaw failures.

In order to use the SAM Number in a specification, a safety factor is needed to ensure the measured values provide a safe estimate of freeze-thaw durability. This means that if a satisfactory Durability Factor is required then the SAM Number should be 0.32 or lower. However, based on the variability in the measurement this means that a target SAM Number of 0.22 (two standard deviations) should be used to obtain a 95% confidence interval. If this number is rounded to 0.20 then this matches the SAM Number correlation to the historic limit of a Spacing Factor of 200 μm. It should be emphasized that this SAM Number of 0.22 or 0.20 if rounded, is not a performance limit for a mixture but a target value for design. As long as a value does not go above 0.32 then the performance in the rapid freeze-thaw test is predicted to be satisfactory. However, a specifier should use a level of confidence that they feel is appropriate for the measurement. These recommendations are currently being investigated with an even wider range of materials and will be reported in future publications.

3.6 Practical Significance

Freeze-thaw specifications currently rely on the measurement of the total volume of air because a technology did not previously exist that could economically and reliably measure the air void quality in fresh concrete. This work presents a technology that shows great promise to address these challenges that could allow new procedures to specify, design, and construct air entrained concrete so that there is a greater understanding of the size and spacing of the bubbles stabilized during mixing. An outstanding feature of this method is that it can be used to investigate concrete **before** it has hardened and determine the quality of the air void system.

This will allow the SAM Number to be used in multiple ways by owners, contractors, and producers. For owners, the device can be used at the point of construction to help ensure that frost durable concrete is being used in their project. This means that once the concrete is delivered to a job site, it can be tested and adjusted to bring it within the specification. These adjustments can be made by adding more AEA to the mixture or mixing the concrete for longer to try and increase the air void quality. The SAM is also a very valuable tool for producers when they are designing a mixture. It can help both contractors and producers better understand how their materials and practices impact the air void quality of the concrete. By making a comparison of systematic measurements the parameter causing the undesirable change in the air void quality can be identified. This can help improve the design of the concrete mixture and identify material-interaction problems before concrete is delivered to the job site. This could reduce the amount of concrete that is rejected for not being freeze-thaw durable. Also, producers will be able to gain new insights into how their materials behave and interact before the concrete is delivered. This will ultimately make it easier to provide longer-lasting concrete and will be of immense benefit to the entire concrete industry.

4.0 Conclusion

This work presents a new method to measure the air void quality in fresh concrete by using sequential pressures. The test can determine both the volume of air and a parameter called the SAM Number that is shown to correlate to hardened air void analysis and rapid freeze-thaw testing. Results from two different testing laboratories and field data from 303 concrete mixtures are included in this paper. In addition, the measurement variance is shown to be lower than hardened air void analysis and rapid freeze-thaw testing. These specific findings have been made:

- A SAM Number of 0.20 and 0.25 shows a correlation to a Spacing Factor of 200 μm and 250 μm with an 88% and 85% agreement respectively.
- A SAM Number of 0.32 correlates with a Durability Factor between 60% and 80% for over 88% of the data investigated, while a Spacing Factor of 200 μm correlated with a Durability Factor of 70% for only 68% of the data.
- The standard deviation of two SAM Numbers from two different operators using different sets of equipment that were run simultaneously was shown to be 0.049 for concrete and 0.021 when

investigating water and a calibration vessel. This lower variability with water suggests that over 50% of the variation in the test is caused by the use of concrete in the test.

- The coefficient of variation of the SAM Number that showed the best correlation to freeze-thaw durability is 15.2%. This value is comparable but lower than similar measurements from hardened air void analysis and rapid freeze-thaw testing.
- A target SAM value of 0.22 or conservatively 0.20 is suggested for design to ensure mixtures have a satisfactory performance in rapid freeze-thaw testing.

Both a large scale field study and investigation into the basic science of the SAM Number are being completed and will be reported in future publications. The construction industry is in dire need of tools that are rapid, and provide critical insights into a material performance that allow almost real-time adjustments to be made to concrete mixtures. These tools help producers meet specifications, contractors to stay on schedule, and owners to obtain the desired performance. The SAM has the potential to fill this need. Furthermore, this method can provide critical insights into how many important variables impact the air void quality of concrete. Some examples include: admixture incompatibility, vibration, pumping, temperature changes, finishing, mixing energy, mixer type, and hauling.

5.0 Acknowledgements

The authors would like to acknowledge funding from the Oklahoma Transportation Center and Pooled Fund TPF-5(297) and the supporting states. Special thanks to Jason Weiss, Larry Sutter, and Peter Taylor for the discussion over this work. We would also like to thank Muwanika Jdiobe, Megan Buchanan, Katie Schrammel, Natalie Schirmer, Hope Hall, David Porter, and Nick Seader for their help with preparing samples.

6.0 References

1. Kosmatka, S.H. and M.L. Wilson, *Design and control of concrete mixtures*. 2016: Portland Cement Assoc.
2. Pigeon, M. and R. Pleau, *Durability of concrete in cold climates*. 1995: CRC Press.
3. Scherer, G.W. and J. Valenza, *Mechanisms of frost damage.* Materials science of concrete, 2005. **7**(60): p. 209-246.
4. Backstrom, J., et al., *Void spacing as a basis for producing air-entrained concrete.* ACI Journ., 1954. **4**: p. 760-761.
5. Whiting, D. and D. Stark, *Control of air content in concrete.* NCHRP report, 1983(258).
6. Kleiger, P., *Studies of the Effect of Entrained Air on the Strength and Durability of Concrete made with Various Maximum Sizes of Aggregate*. 1952: Portland Cement Association.
7. Kleiger, P., *Further Studies on the Effect of Entrained Air on Strength and Durability of Concrete with Various Sizes of Aggregates*. 1956: Portland Cement Association.
8. 211, A.C. *Standard Practice for Selecting Proportions for Normal, Heavyweight and Mass Concrete*. 1991. American Concrete Institute.
9. Powers, T.C. and T. Willis. *The air requirement of frost resistant concrete*. in *Highway Research Board Proceedings*. 1950.
10. 201.2R, A.C. *Guide to Durable Concrete*. 2016. American Concrete Institute.
11. ASTM-C457, *Standard Practice for Microscopical Determination of Air-Void Content and Parameters of the Air-Void System in Hardened Concrete*. 2017, ASTM International: West Conshohocken, PA.
12. Gay, F. *A factor which may affect differences in the determined air content of plastic and hardened air-entrained concrete*. in *Proceedings of the Fourth International Conference on Cement Microscopy, Las Vegas, Int. Cem. Microscopy Assoc*. 1982.
13. Gay, F.T. *The Effect of Mix Temperature on Air Content and Spacing Factors of Hardened Concrete Mixes with Standardized Additions of Air-Entraining Agent*. in *Proceedings, Seventh International Conference on Cement Microscopy, Fort Worth, International Cement Microscopy Assoc., Duncanville, TX*. 1985.
14. Plante, P., M. Pigeon, and C. Foy, *The influence of water-reducers on the production and stability of the air void system in concrete.* Cement and Concrete Research, 1989. **19**(4): p. 621-633.
15. Jana, D., B. Erlin, and M.F. Pistilli, *A closer look at entrained air in concrete.* Concrete international, 2005. **27**(7): p. 61-64.
16. Freeman, J.M., *Stability and quality of air void systems in concretes with superplasticizers*. 2012, Oklahoma State University.
17. Felice, R., J.M. Freeman, and M.T. Ley, *Durable Concrete with Modern Air-Entraining Admixtures.* Concrete international, 2014. **36**(8): p. 37-45.
18. Pleau, R., et al., *Influence of pumping on characteristics of air-void system of high-performance concrete.* Transportation research record, 1995: p. 30-36.
19. Janssen, D., K. Macdonald, and A. Gardiner. *Effects of pumping parameters on the stability of entrained air voids*. in *CONSEC'01: Third International Conference on Concrete Under Severe Conditions*. 2001.
20. Elkey, W.D., D.J. Janssen, and K.C. Hover. *Effects of admixtures on air-void stability of concrete subjected to pressurization*. in *Concrete Under Severe Conditions 2*. 1998.
21. Janssen, D.J., R.M. Dyer, and W.E. Elkey. *Effect of pumping on entrained air voids: role of pressure*. in *CONSEC 95 Concrete Under Severe Conditions*. 1995.

22. Jensen, B.J., *Method of determining the air bubble size distribution in fresh concrete, an analytical assembly and a sample taking device for use herewith*. 1990, Google Patents.
23. Magura, D.D., *Air void analyzer evaluation*. 1996.
24. Desai, D.H., P.J. Tikalsky, and B.E. Scheetz, *Hardened air in concrete roadway pavements in structure*. 2007.
25. ASTM-C150/C150M, *ASTM C150/C150M: Standard Specification for Portland Cement*. 2011, ASTM International: West Conshohocken, PA. p. 9.
26. ASTM-C33, *Standard Specification for Concrete Aggregates*. 2016, ASTM International: West Conshohocken, PA.
27. ASTM-C494, *Standard Specification for Chemical Admixtures for Concrete*. 2005, ASTM International: West Conshohocken, PA.
28. ASTM-C260-10a, *Standard Specification for Air-Entraining Admixtures for Concrete*. 2010, ASTM International: West Conshohocken, PA.
29. ASTM-C1017-13^{e1}, *Standard Specification for Chemical Admixtures for Use in Producing Flowing Concrete*. 2005, ASTM International: West Conshohocken, PA.
30. ASTM-C618, *Standard Specification for Coal Fly Ash and Raw or Calcined Natural Pozzolan for Use in Concrete*. 2008, ASTM International: West Conshohocken, PA. p. 3.
31. Welchel, D., *Determining the Size and Spacing of Air Bubbles in Fresh Concrete*. 2014, Oklahoma State University.
32. Tanesi, J., et al., *Super Air Meter for Assessing Air-Void System of Fresh Concrete.* Advances in Civil Engineering Materials, 2016. **5**(2): p. 22-37.
33. ASTM-C666, *Standard Test Method for Resistance of Concrete to Rapid Freezing and Thawing*. 2015, ASTM International: West Conshohocken, PA.
34. ASTM-C231, *Standard Test Method for Air Content of Freshly Mixed Concrete by the Pressure Method*. 2017, ASTM International: West Conshohocken, PA.
35. Hover, K.C., *Analytical investigation of the influence of air bubble size on the determination of the air content of freshly mixed concrete.* Cement, concrete and aggregates, 1988. **10**(1): p. 29-34.
36. Klein, W. and S. Walker. *A method for direct measurement of entrained air in concrete*. in *Journal Proceedings*. 1946.
37. LeFlore, J. *Super Air Meter Test Video*. 2016; Available from: https://www.youtube.com/watch?v=xAcHqMz_m3I.
38. Ley, M.T. and B. Tabb. *A test method to measure the freeze thaw durability of fresh concrete using overpressure*. in *T&DI Congress 2014: Planes, Trains, and Automobiles*. 2014.
39. ASTM-C156, *Standard Test Method for Water Loss [from a Mortar Specimen] Through Liquid Membrane-Forming Curing Compounds for Concrete*. 2011, ASTM International: West Conshohocken, PA.
40. Ley, M.T., *The effects of fly ash on the ability to entrain and stabilize air in concrete*. 2007: ProQuest.
41. Jakobsen, U., et al., *Automated air void analysis of hardened concrete—a Round Robin study.* Cement and Concrete Research, 2006. **36**(8): p. 1444-1452.
42. Peterson, K., L. Sutter, and M. Radlinski, *The practical application of a flatbed scanner for air-void characterization of hardened concrete*, in *Recent Advancement in Concrete Freezing-Thawing (FT) Durability*. 2010, ASTM International.

FIELD AND LABORATORY VALIDATION OF THE SAM

1.0 Introduction

Throughout the world, concrete is a widely used material for infrastructure construction. The quality of modern concrete mixtures is increasingly more important because of the emphasis on long-term durability and improved constructability. However, the tools used to evaluate these materials during design, production, and construction have not evolved to match these higher expectations or the new materials used in modern concrete.

When concrete becomes critically saturated and experiences a series of freezing and thawing cycles, damage can occur [1, 2]. However, if the concrete mixture contains a well-distributed air void system then this damage can be resisted [3-5]. This is typically done by including an air-entraining admixture (AEA) during mixing. This surfactant creates well-spaced air bubbles within concrete that form voids in the hardened concrete. These voids create pressure-relief regions for water movement during freezing [2, 3, 5, 6]. While most specifications require a certain volume of air within the concrete, it is more important to provide a small and well-distributed bubble system in the fresh concrete that in turn creates a void system with the right size and spacing [7-9]. For this work, a term called the quality of the air void system will be used to describe a satisfactory void size and spacing in the hardened concrete.

The most established method to determine the air void quality is to use a hardened air void analysis and determine a parameter called the Spacing Factor [3, 4]. After the concrete has hardened, it is cut, polished, and the surface is inspected under a microscope to inspect the voids. This process can take weeks and so it cannot be used to provide the immediate feedback needed to modify the fresh concrete. While there are other methods that can measure the volume of air in fresh concrete (ASTM C 231, ASTM C 138, ASTM C 173), the volume of air does not necessarily represent the quality of the air void system [10-12].

The concrete industry needs a test method to determine the size and spacing of the air voids within the fresh concrete that can be completed in either the lab or the field. A new test method that measures the concrete response to sequential pressure steps has been developed to address these needs [5]. This test method gives real time results, allowing for production adjustments before concrete placement and is known as the Sequential Air Method or SAM and is described by AASHTO TP 118 [13]. The SAM results show an 88% agreement with the Spacing Factor of 200μm and a 90% agreement with a Durability Factor of 70% in rapid freeze-thaw testing (ASTM C 666) [5]. The original publications over the SAM used primarily laboratory and only limited field data (241 laboratory and 62 field mixtures) [5]. This work aims to expand that original data set with a special emphasis on gathering field data in a wide array of conditions, with different materials, equipment, and operators. All of the data is combined in this paper to allow stronger conclusions to be gained from a larger dataset.

2.0 Experimental Methods

2.1 Laboratory Materials

Table 1 shows the oxide analysis and Bogue calculations for the Type I cement used in all of the laboratory concrete mixtures in this report. These mixtures met ASTM C150 standards. Crushed limestone and natural sand were the aggregates used from local sources. Some mixtures used a combination of coarse and intermediate sizes. Both aggregates met ASTM C33 standards. The maximum nominal aggregate size of the limestone was 19 mm (3/4”). Table 2 shows the admixtures used that met the ASTM C260 and ASTM C494 standards.

Table 1 – Oxide analysis of materials used in the study. After [5].

Oxide (%)	SiO_2	Al_2O_3	Fe_2O_3	CaO	MgO	SO_3	Na_2O	K_2O	TiO_2	P_2O_5	C_3S	C_2S	C_3A	C_4AF
Cement	21.1	4.7	2.6	62.1	2.4	3.2	0.2	0.3	-	-	56.7	17.8	8.2	7.8
Fly Ash	38.7	18.8	5.8	23.1	5.6	1.2	1.8	0.6	1.5	0.4	-	-	-	-

Table 2 – Admixture References. After [5].

Abbreviation	**Description**	**Generic Chemical Name**
WROS	Wood Rosin	Air-entraining agent
SYNTH	Synthetic chemical combination	Air-entraining agent
PC	Polycarboxylate	Superplasticizer
WR	Triethanolamine	Water reducer

The air-entraining agents (AEAs) in this research are wood rosin (WROS) and synthetic (SYNTH) AEA. These are common commercial AEAs. Table 3 shows the twenty-three different mixture designs studied for the lab testing. A subset of mixtures was examined with either a polycarboxylate (PC) superplasticizer meeting ASTM C1017, a midrange water reducer (WR) meeting ASTM C494, or a shrinkage reducer (SRA) meeting ASTM C494. The PC dosage fell between 60 and 200 mL/100 kg to adjust the slump of the mixture between 50 mm to 200 mm. Some of the mixture designs used a Class C fly ash replacement for 20% of the cement by weight that met ASTM C618 standards. Each mixture design consisted of four to fourteen dosages of AEA to study air contents from 2% to 10%. This allowed 192 mixtures to be investigated. The details are given in the appendix.

Table 3 – SSD Mixture Quantities

w/cm	Cement kg/m^3	Fly-Ash kg/m^3	Paste Volume (%)	Coarse kg/m^3	Fine kg/m^3	Water kg/m^3	Admixture Used
0.45	362	0	29	1098	714	163	WROS
0.45	362	0	29	1098	714	163	SYNTH
0.53	362	0	32	1053	682	192	WROS
0.41	362	0	28	1127	722	148	WROS
0.39	362	0	27	1140	730	141	WROS
0.45	362	0	29	1098	714	163	WROS + PC1
0.45	362	0	29	1098	714	163	SYNTH + PC1
0.45	290	72	30	1089	709	163	WROS
0.45	223	56	23	785/573*	634	126	WROS
0.40	290	72	28	1115	724	145	WROS
0.40	290	72	28	1115	724	145	WROS + PC1
0.35	290	72	28	1127	768	127	WROS + PC1
0.40	290	72	28	1115	724	145	WROS + PC2
0.40	290	72	28	1115	724	145	WROS + PC3
0.40	290	72	28	1115	724	145	WROS + PC4
0.40	290	72	28	1115	724	145	WROS + PC5
0.40	290	72	28	1115	724	145	WROS + WR
0.40	362	0	28	1098	742	145	WROS
0.40	362	0	28	1098	742	145	WROS+PC1
0.45	335	0	27	1142	742	151	WROS
0.45	335	0	27	1142	742	151	WROS+PC1
0.50	335	0	29	1115	724	167	WROS
0.50	335	0	29	1115	724	167	WROS+PC1

* Mixture contained coarse and intermediate aggregates.

he US Federal Highway Administration (FHWA) Turner Fairbanks Highway Research Center laboratory in McLean, Virginia, USA also provided data for this report to show an independent assessment of the test method with different materials. This work is summarized in other publications [14].

2.2 Field Materials

To investigate the field performance of the SAM, testing was completed by either a Department of Transportation or private testing labs from 21 different States and one Canadian Province. Throughout the entire data set, over 15 users completed the SAM test. This data was collected from more than 110 projects. The nine states that provided detailed information used 34 different mix designs. Within those mix designs, there were 62 different aggregates, 19 different cement sources, 20 different fly ash sources and 39 different admixtures. The mixtures investigated consist of approximately 60% pavement mixtures, 20% bridge deck mixtures, and 20% other air-entrained mixtures including self-consolidating, precast, ready mix, and central mix concrete. No light weight aggregate was investigated in this testing. A single sample was used for hardened air void analysis (ASTM C457) and a single measurement from the SAM device was used. Investigating the performance of the SAM on this wide range of materials allows a large number of variables to be investigated that could not be practically completed in a controlled laboratory setting.

2.3 Laboratory Concrete Mixing and Testing Methods

Aggregates from outdoor storage piles were gathered and moved indoors to a controlled temperature of 23°C. After 24 hours, the aggregates were loaded into the mixer and spun. Samples were collected from the mixer for moisture corrections. After moisture corrections were calculated, all of the aggregate and two-thirds of the water was placed in the mixer and spun for three minutes. This time allowed for evenly distributed aggregates and for the aggregates to be closer to saturated surface dry (SSD).

The residual water, cement, and fly ash were added next and mixed for three minutes. While the mixing drum was scraped, the concrete mixture rested for two minutes. Following the rest time, the mixer was spun and the admixtures were added. The AEA was added 15 to 30 seconds after the PC or WR, then the mixture was spun for three minutes.

One hardened air-void analysis (ASTM C457) sample was made from each concrete mixture for testing. Two 7L samples were tested simultaneously with the SAM by different operators. These were used to find the average SAM Number of a mixture.

2.4 Sequential Air Method

The SAM device is similar to the ASTM C231 Type B meter with some modifications. The SAM device uses six restricted clamps to account for increased pressures and a digital pressure gauge for testing. The

SAM can be used to test concrete before it hardens, which provides insight into the air void system to help design and evaluate the air void system of the hardened concrete. The device is shown in Fig. 1.

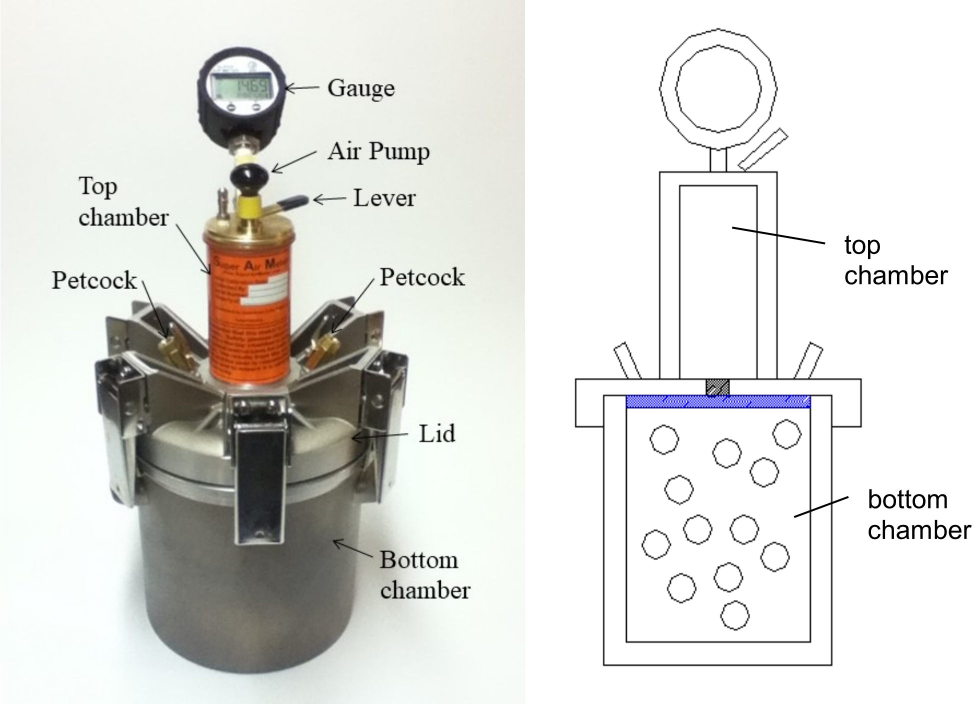

Figure 1 – SAM testing device and section of SAM device showing top and bottom chambers. The detailed image of the device is after [5].

The test takes an experienced user between eight to 10 minutes to complete. Figure 2 shows a typical data set and a video of the test is available [15]. The test applies three sequential pressures to the fresh concrete and the equilibrium pressures are recorded. The pressure is then released and the same steps are applied again to the fresh concrete. The SAM Number is calculated by taking the numerical difference between the final pressure steps. The difference between the pressure responses is an indication of the air void size and spacing in the concrete. Further details can be found in other publications [5].

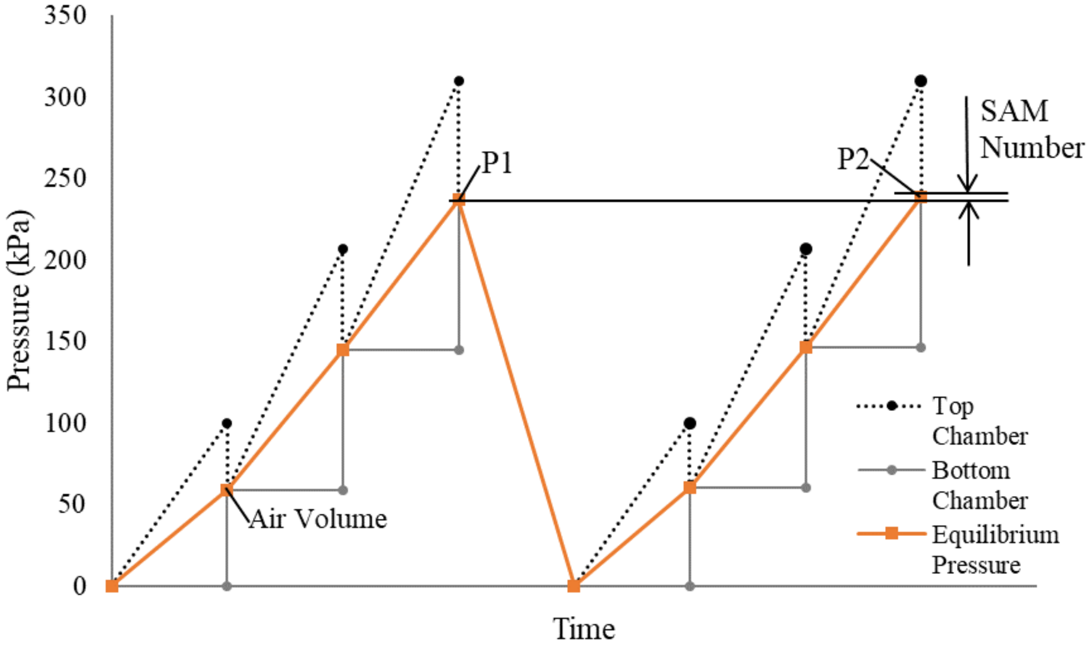

Figure 2 – SAM pressure steps graphically shown for the top and bottom chambers. Image is after [5].

2.4.1 SAM Number Calculations

he SAM Number is can be calculated as: $_{2} - P_1)/c$. Where P_1 is the first equalized pressure at 310 kPa (45 psi) and P_2 is the second equalized pressure at 310 kPa (45 psi). The value c is a constant that is 1.45 if the units are in kPa and 1.0 if the units are in psi. More details can be found in Figure 2. The SAM Numbers ranged from 0.03 to 0.78 for the mixtures represented. The SAM Number is an empirical number that has been correlated to the air void size and spacing from empirical relationships [5].

2.4.2 Air Content and Aggregate Correction

The total volume of air in the mixtures can be found from the first equilibrium pressure at 100 kPa (14.5 psi) by using Boyle’s Law. This procedure is explained in other publications [16-21] and uses the same method and procedure used in the conventional pressure meter (ASTM C231). Previous experiments with similar equipment have shown that the air content found by the SAM agreed with results from the ASTM C231 pressure method [14, 16, 22]. Further, a correction is needed for the air volume measurement if the aggregates are porous. This correction is described in AASHTO TP 118 [13].

2.4.3 Measurement Variability

The variability of the SAM Number is reported to have a standard deviation of 0.049 and a coefficient of variation of 15.2%. The coefficient of variation is lower than the reported values for determining the Spacing Factor and Durability Factor (20.1% and 22.7% respectively) [5].

2.5 Sample Preparation for Hardened Air Void Analysis

oncrete samples were cut into 19 mm thick slabs and polished with sequentially finer grits. The surface of the sample was preserved with an acetone and lacquer mixture to strengthen the surface before it was inspected under a stereo microscope. After an acceptable surface was obtained, the sample is cleaned with acetone. The surface was then colored with a black permanent marker, the air voids were filled with less than 1 μm white barium sulfate powder, and the air voids within the aggregates were blackened under a stereo microscope. This process makes the concrete sample black and the voids in the paste white. Sample preparation details can be found in other publications [16, 23]. The sample analyzed with ASTM C457 method C by using the Rapid Air 457 from Concrete Experts, Inc. A single threshold value of 185 was used for all samples in this research and the results do not include chords smaller than 30 μm. A traverse length of 2286 mm was used for all samples to satisfy the requirements of ASTM C457. These settings and sample processing methods are similar to methods used in other publications [23-25]. All air voids were used for the volume of chords less than 300 μm.

The hardened air-void analysis from Kansas, Iowa, Pennsylvania, and the FHWA Turner Fairbanks Highway Research Center was completed by their staff with methods that may be different from that described above. This accounted for 29% of the lab data and 28% of the field data shown. The hardened air samples that had differences of more than 2% between the fresh and hardened air content were not included in the analysis. This discrepancy could be caused by a fresh air measurement that was not completed correctly, a hardened sample that was not adequately consolidated, or an air-void system that was unstable. An unstable air-void system would cause the fresh concrete to lose air over time. This can cause the fresh air measurements to be higher than the hardened concrete. Regardless of the reason, samples with large differences in the fresh and hardened air content were not used in this study.

3.0 Results and Discussion

3.1 Comparing the Spacing Factor and Air Volume

The air content and Spacing Factor is compared for all of the mixtures in this study. The laboratory concrete is shown in Figure 3 and the field concrete in Figure 4. A horizontal line is shown with a Spacing Factor of 200 μm as this is the value recommended by ACI 201.2R for freeze-thaw durability [26].

It can be seen in both Figure 3 and Figure 4 that the range of air contents needed to provide a Spacing Factor of 200 μm varied from 3.5% to 8% air volume. This wide range shows that it is difficult to develop a specification based on the volume of air to provide freeze-thaw durability. For example, in order to ensure the freeze-thaw durability of some of these mixtures, it would require the air volume in the concrete to be greater than 7.5%. Unfortunately, this would require many mixtures to have much higher air contents than is required. These higher air contents would impact the constructability and the strength of the concrete. This would increase the costs and may reduce the sustainability of a mixture. This reinforces that the air volume and air void quality do not correlate. More insights can be gained by looking at individual mixtures.

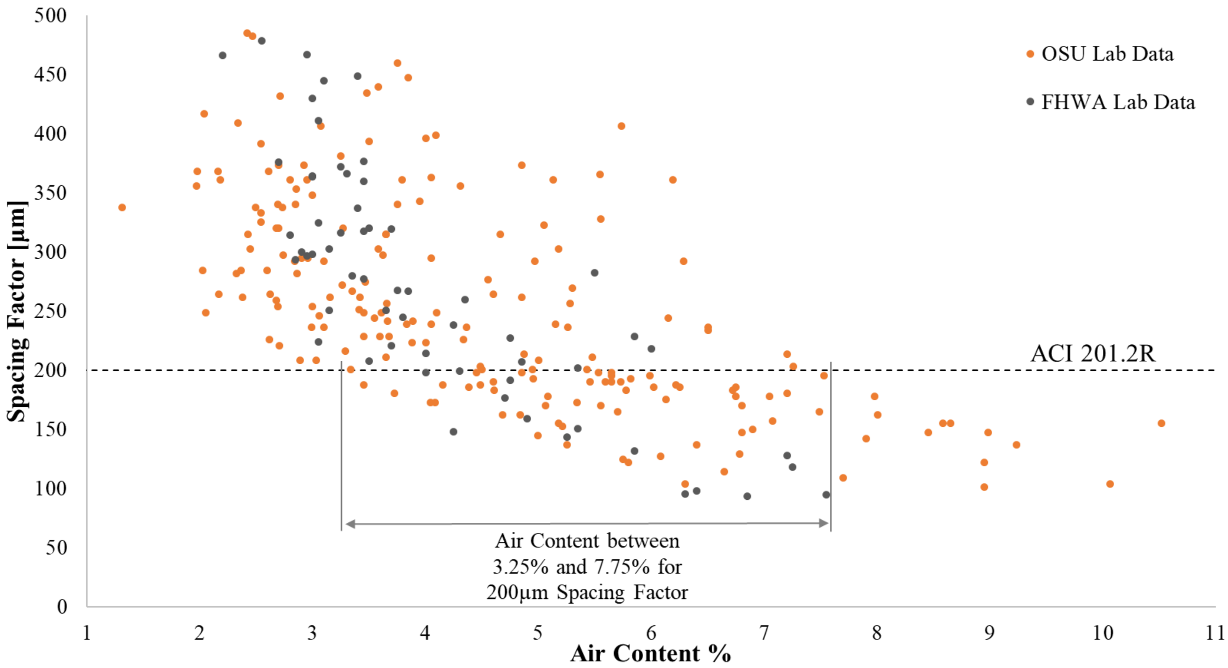

Figure 3 – Air Content versus Spacing Factor for 257 laboratory concrete mixtures completed by two different research groups.

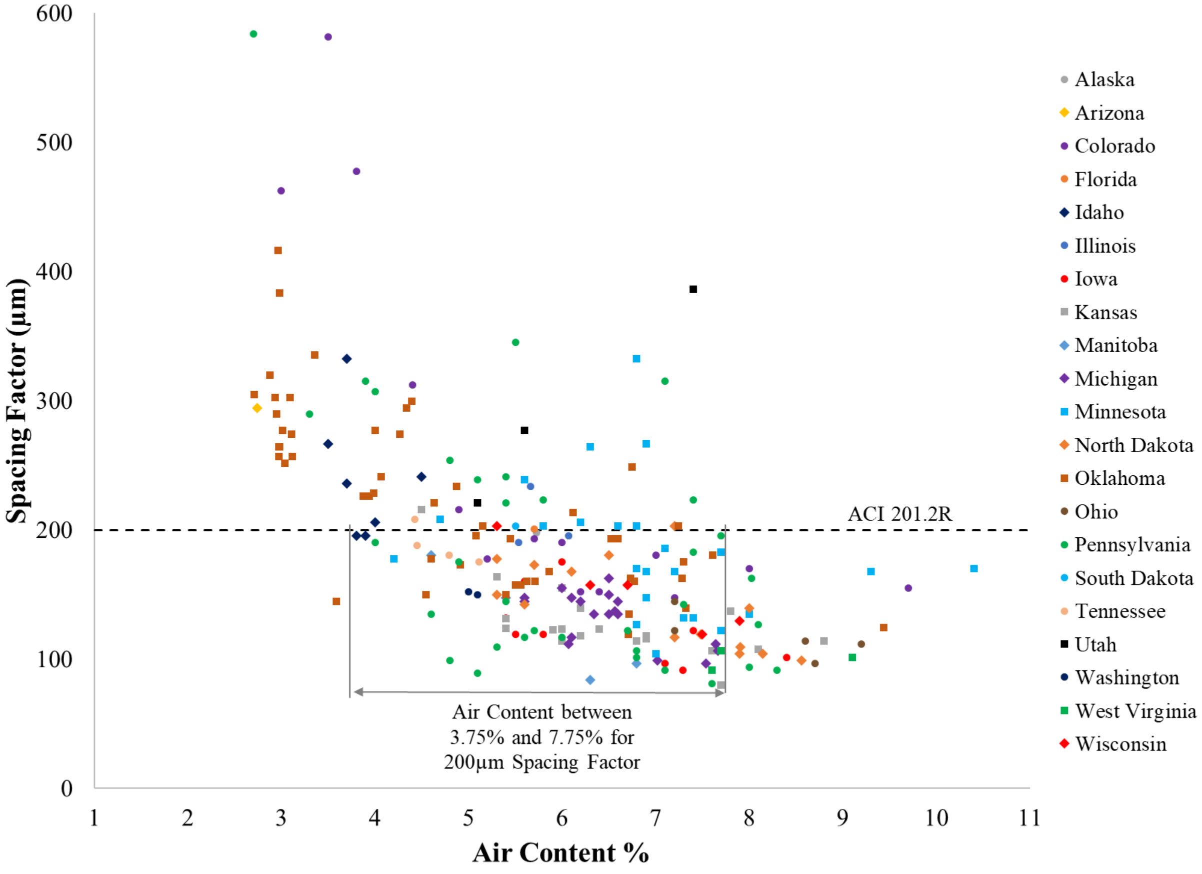

Figure 4 – Air Content versus Spacing Factor for 231 field concrete mixtures completed by 21 different state DOTs with various aggregates and admixtures.

In the following figures, two concrete mixtures are compared to show how the relation between the air content and Spacing Factor and then the Spacing Factor and SAM Number. The only difference between the two mixtures is that one uses a blend of admixtures and the other uses only an AEA. In Figure 5, the comparison between air content and Spacing Factor is presented. Linear trend lines are shown for each mixture. At an air content of 5%, the Spacing Factor is different by almost 200 □m. The mixture with just an AEA needs approximately 4.5% air to reach a Spacing Factor of 200 µm, while the mixture with a blend of admixtures needs approximately 7.5% air to reach 200 µm. This highlights how the volume of air cannot be used to determine the quality of the air within the hardened concrete. This supports previous research stating that air volume and air-void quality do not relate the same to all mixtures [5].

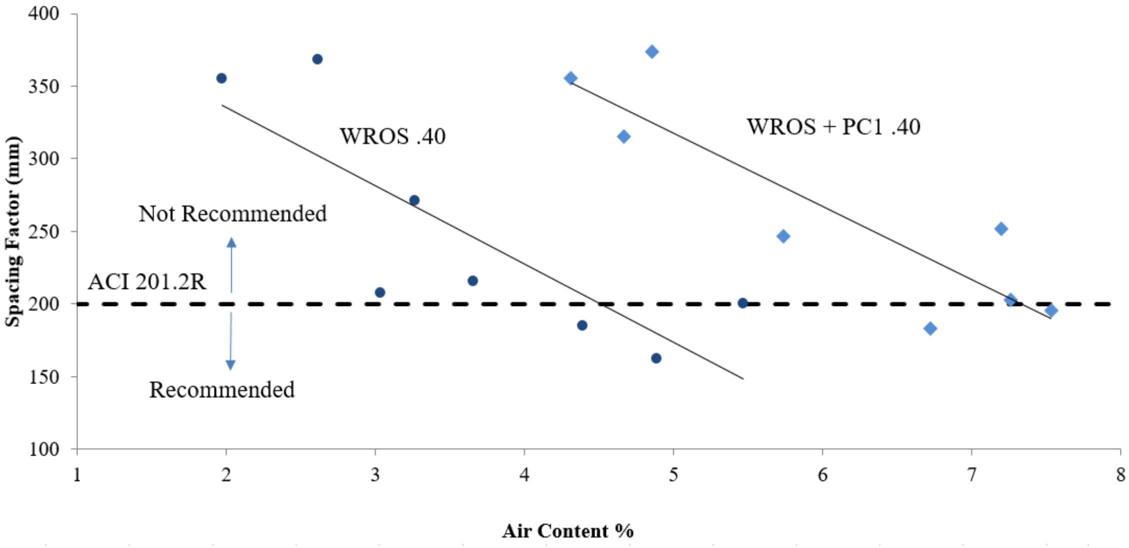

Figure 5 – Air Content versus Spacing Factor for two laboratory mixtures with similar air volume and different air-void qualities. Image after [5].

3.2 Comparing the SAM Number and Spacing Factor

In Figure 6, the comparison between SAM Number and Spacing Factor is presented for the same mixtures shown in Figure 5. In this data, the linear trend lines for each mixture are nearly overlapping. The similarity between the trend lines shows that there is a similar correlation between the SAM Number and Spacing Factor for these two mixtures. This shows that the SAM Number better correlates to the Spacing Factor for these two mixtures than the air volume. This is a large improvement over using the volume of air to specify and evaluate the air void quality of the concrete.

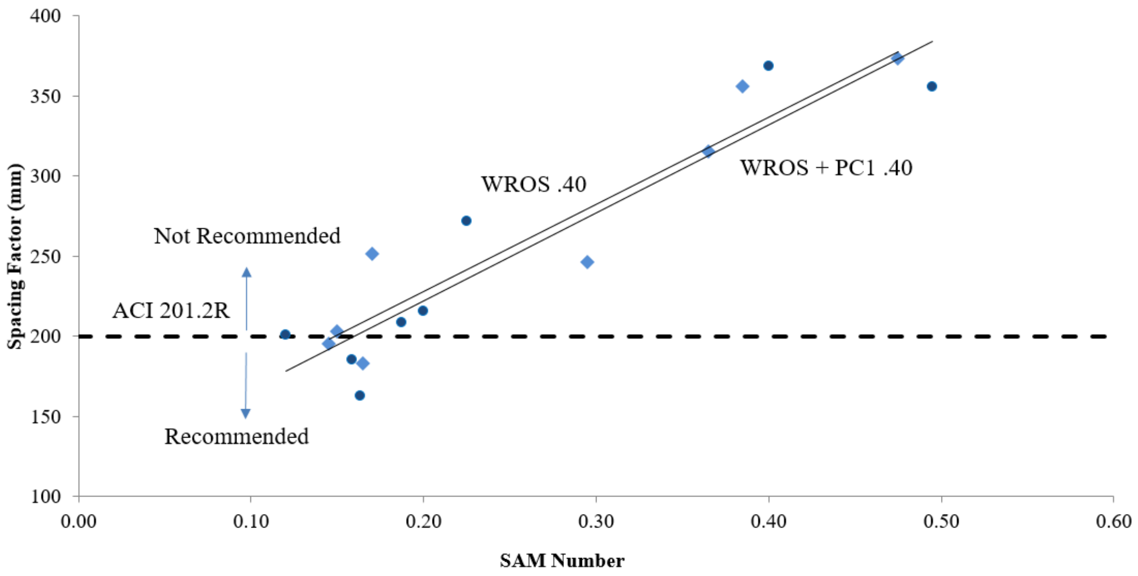

Figure 6 – SAM Number versus Spacing Factor for the two laboratory mixtures previously shown in Figure 5. Image after [5].

Figure 7 shows the relationship between the SAM Number and the air volume of voids less than 300 μm. The results show a cubic and linear relationship between these two parameters. A SAM Number of 0.33 corresponds to a 1.5% volume of voids less than 300 μm. Previous research has shown that a SAM Number of 0.32 best corresponded with performance in the ASTM C666 rapid freeze thaw test [5]. The satisfactory agreement shows that the SAM Number is an indication of the small voids in the concrete and that these voids seem to be important for freeze thaw durability. Care should be taken in only using the volume of small air voids as the measurement does not take into account the paste volume in the mixture as is done by the Spacing Factor [4].

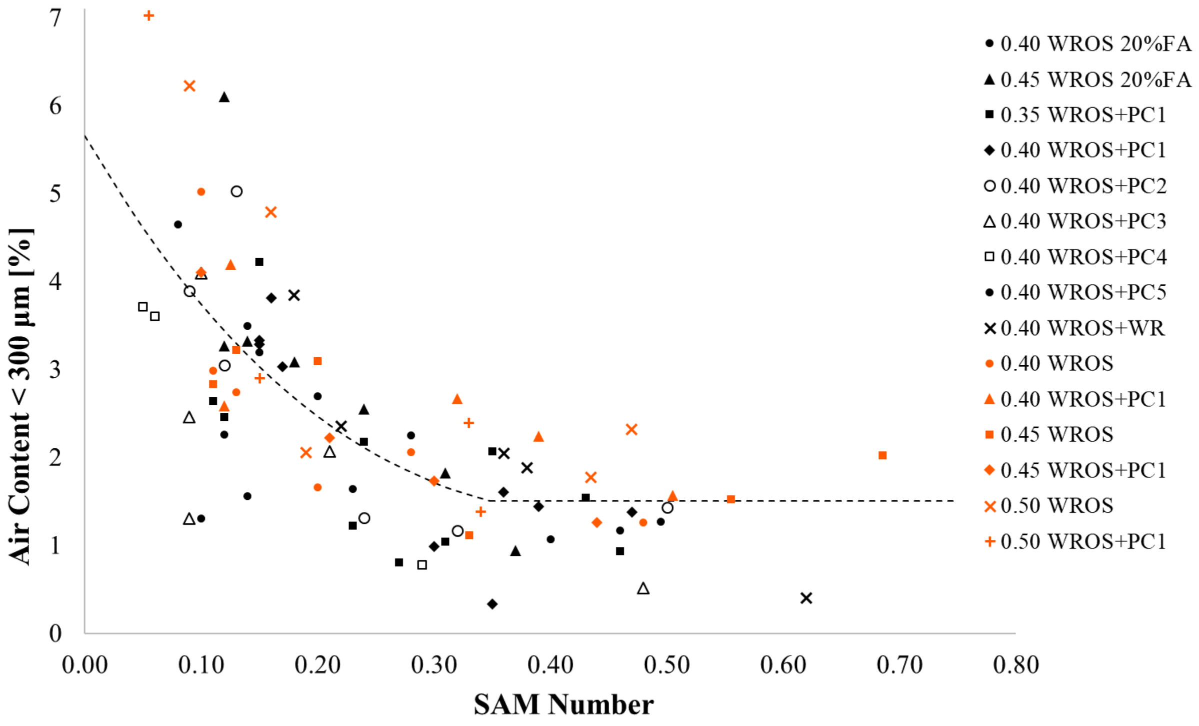

Figure 7 – SAM Number versus air content below 300 µm for 192 laboratory concrete mixtures.

To further show the utility of the SAM Number, Figure 7 shows the relationship between SAM Number and Spacing Factor for 257 laboratory concrete mixtures completed by two different labs. Within this set of data, 75% of the mixtures were completed at Oklahoma State University and 25% of the mixtures were completed at FHWA Turner Fairbanks Highway Research Center [14]. Figure 7 shows that as the SAM Number increases then so does the Spacing Factor. Past recommendations for the Spacing Factor have used a single value to determine if a material is recommended for freeze-thaw durability. This has also been beneficial in aiding industry implementation because it is simple and shows if something is above or below the recommended value.

If target values for the SAM Number and Spacing Factor are used then this will separate the data into four quadrants. The upper right and lower left quadrant show where the SAM Numbers and Spacing Factors agree that the air void system is either satisfactory or unsatisfactory. The upper left and lower right quadrant show where the SAM Number and Spacing Factor do not agree. Past work has suggested that a

SAM Number of 0.20 correctly determines if a Spacing Factor is above or below 200 µm for 88% of the data [5]. For this work, the laboratory data showed 85% agreement.

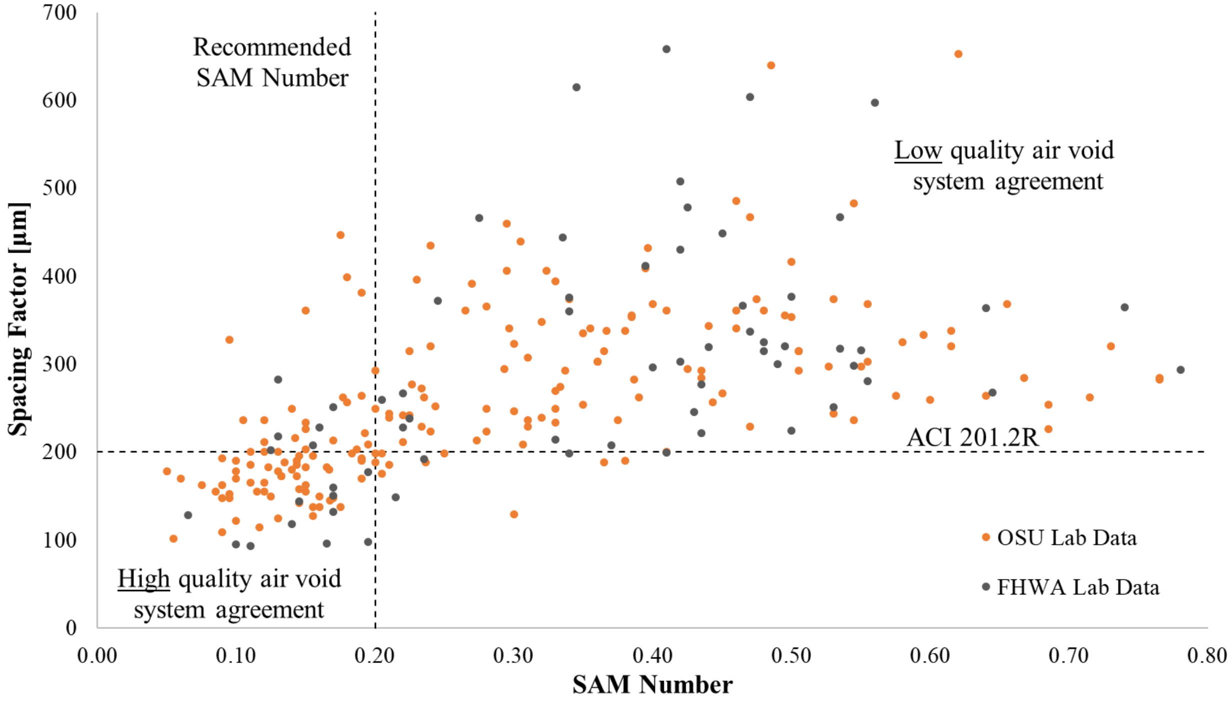

Figure 8 – SAM Number versus Spacing Factor for 257 laboratory concrete mixtures completed by two different research groups. The results show 85% agreement.

Next, to investigate if the SAM is a useful tool for field usage, the test was used to evaluate field mixtures completed by either a Department of Transportation or private testing lab from 21 different States and one Canadian Province for 231 different concrete mixtures from 110 different projects. A hardened sample was also obtained for ASTM C457 analysis. The SAM Number and Spacing Factor are plotted together for the field data in Figure 9. A similar trend is shown in both the laboratory and field data. The Spacing Factor limit of 200 µm from ACI 201.2R-16 [26] is displayed in Figure 9 as well as a SAM Number limit of 0.20. The results show 70% agreement for the field data. While this is slightly lower than the laboratory testing, it shows the SAM Number is a useful tool to provide important insights into the quality of the air void system in fresh concrete. This lower agreement may be caused by the increased variability of the field and differences in testing procedures and materials. With the wide range in field users, this new test may also show variability due to unfamiliarity.

Figure 9 shows the relationship between the SAM Number and the air volume of chords less than 300 µm for field concrete mixtures. This data set represents 112 comparisons with the same cubic and linear trend line as was used previously. The field data that was completed by Kansas, Iowa, Pennsylvania, and the FHWA Turner Fairbanks Highway Research Center with other methods was not included in this analysis due to lack of content in the air volume of chords less than 300 µm. Again, the data shows that the SAM Number is a good indicator of the small voids in the concrete.

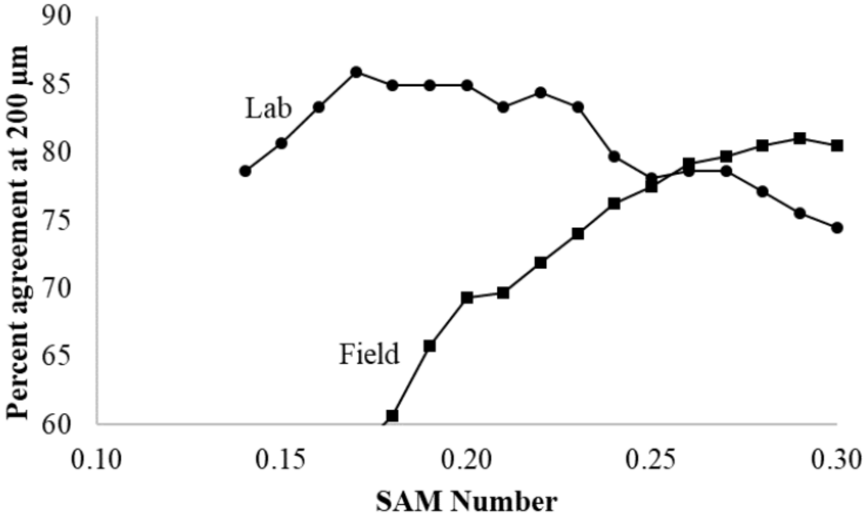

Figure *9* – SAM Number versus air content below 300 µm for 112 field concrete mixtures.

The field data points in the upper right-hand quadrant of Figure 10 represent mixtures that would not be recommended for use in freezing climates and consist of 25% of the data (57 Mixtures). These projects may show a reduced lifespan if they are exposed to moisture and freezing temperatures. If these mixtures could have been identified by the SAM to have a low-quality air void system, then they could be adjusted. If this adjustment could have increased the lifespan of at least one project, then it would make significant savings to the public. This again highlights the limitation of using the air volume to evaluate concrete.

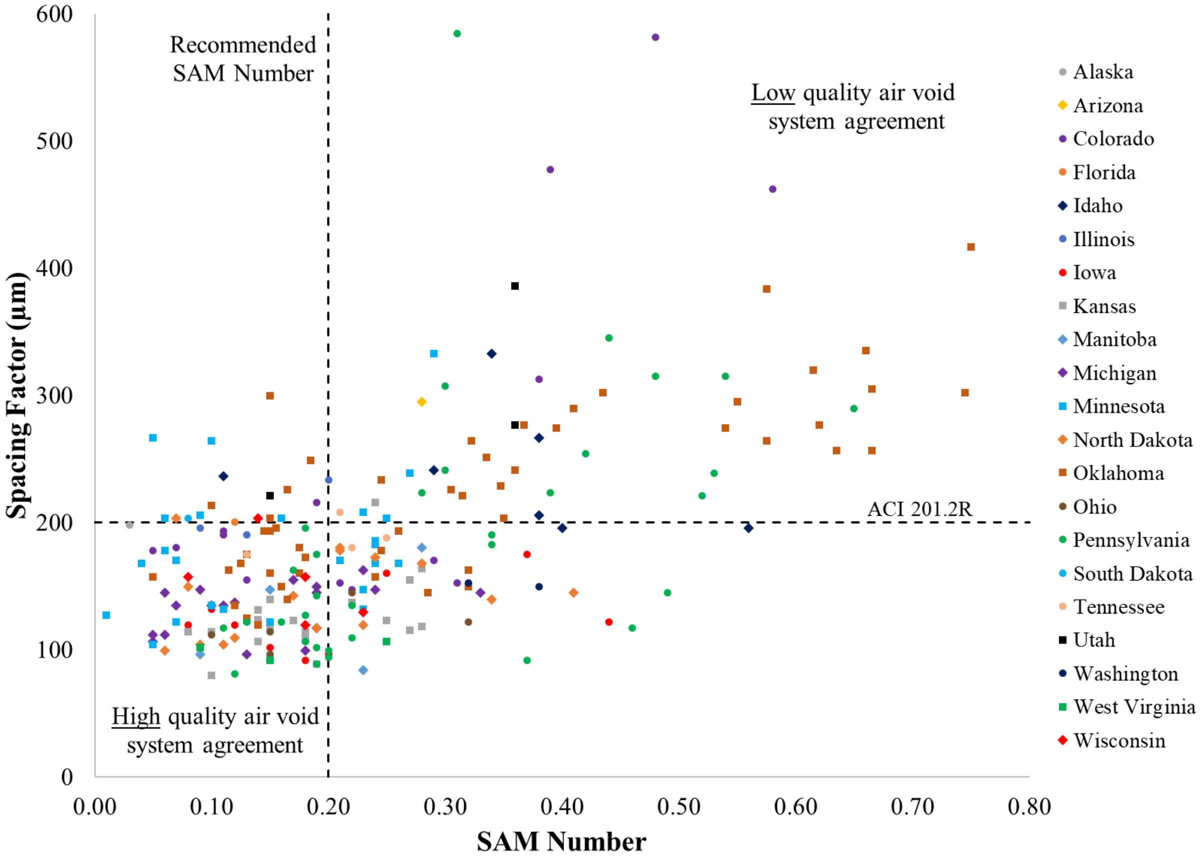

Figure 10 – SAM Number versus Spacing Factor for 231 field concrete mixtures completed by 21 different State DOTs and one Canadian province with various aggregates and admixtures. The results show 70% agreement.

Based on the data in Figure 8 and Figure 10, it is not clear if a SAM Number of 0.20 shows the best correlation with a Spacing Factor of 200 µm. For example, there are a number of data points that are in the lower right quadrant or have a SAM Number greater than 0.20 but a Spacing Factor less than 200 µm in Figure 10. If the SAM Number limit was higher, then this might improve the agreement for the field data. To investigate this further a range of SAM Numbers were chosen and compared to a Spacing Factor of 200 µm for both the lab and field data.

Figure 11 shows the percentage of data points that fall within either the upper right or lower left quadrants. These results show that a SAM Number near 0.20 has an agreement of close to 85% with a

Spacing Factor of 200 μm for the laboratory data. There is a decrease in the agreement for the laboratory data for larger and smaller SAM Numbers. One reason the curve has this shape is that in the laboratory testing the mixtures were designed to have almost equal amounts of low and high-quality air void systems. However, the field mixtures that were sampled did not have a large number of low-quality air void systems as this would not be in the best interest for the durability of the concrete. Because of this, the agreement curve for the field data will not have the same shape. For example, Figure 11 shows that the correlation of that data may be improved if a higher SAM Number is used. As expected the agreement curve for the field data does not have the same shape as the agreement curve for the lab data. However, it is important to note that the improvement in agreement for increasing the SAM Number is not significant. Furthermore, it is conservative to use a lower SAM Number for the design and specification of concrete mixtures. Because of this, a SAM Number of 0.20 remains a satisfactory choice to correlate with a Spacing Factor of 200 μm.

3.3 Practical Implications

Due to shrinking resources and greater demand for long-lasting infrastructure the use of rapid test methods that provide direct measurements of critical parameters in a concrete mixture is in greater demand [27]. The SAM seems to meet these needs and provides a tool that shows great potential to be used as a quality control test where freeze-thaw durable concrete is required.

This work shows that the SAM Number is a more direct measurement of the air void quality in the fresh concrete than using the total air volume. The measurement method has shown good agreement to the Spacing Factor (85% lab, 70% field) for 488 concrete mixtures. The success of this testing with such a wide range of materials, operators, equipment, conditions, and construction procedures is a strong validation of the SAM. Furthermore, 25% of the field data was found to contain air void systems that are not recommended for freeze thaw durability. These mixtures were accepted on their projects based on

their air content but then the SAM showed low quality air void systems. This shows the importance in using the SAM to investigate the quality of the air void systems in the concrete before it is placed.
The SAM is a powerful measurement because it can be completed in less than 10 minutes before the concrete has hardened and it provides more insight than the volume of air within the concrete. This testing method also allows the mixtures to be corrected before they are placed to ensure that satisfactory freeze-thaw durability is obtained. Furthermore, because this tool is portable, it can provide immediate feedback on how mixture ingredients, construction practices, and changes in temperature impact the quality of the air void system in fresh concrete. This can provide important insights into the performance of these concrete mixtures that were not possible to obtain in the past. In addition, because the SAM Number is a more direct measurement than the total volume of air, it will allow the overdesign of the air content for concrete mixtures to be reduced while ensuring long-term durability. This reduction in overdesign of the air content will allow for improvements in the economy and sustainability of the mixture.

4.0 Conclusion

This work compares the correlation between the SAM Number, Spacing Factor, and air content for 257 laboratory mixtures and 231 field mixtures with various admixtures, aggregates, devices, and users. The reliability of the method across a data set this diverse shows the reliability and robustness of the SAM test method.

These specific findings have been made:

- Air contents between 3% and 8% were needed in order to obtain a Spacing Factor of 200 μm. This shows the inability of a specific air volume to correlate with air void quality.
- For 257 laboratory mixtures, the correlation between a SAM Number of 0.20 and a Spacing Factor of 200 μm agrees with 85% of the laboratory data comparisons.
- For 231 field mixtures, the correlation between a SAM Number of 0.20 and a Spacing Factor of 200 μm agrees with 70% of the field data comparisons.

- For 231 field mixtures, 25% or 57 of them that were placed based on their air volume were shown by the Spacing Factor and SAM Number to have an air void distribution that is not recommended for freeze thaw durability.

This work shows that the SAM Number provides a more direct measurement of the air void quality of fresh concrete than the total volume of air, which is important for the freeze-thaw durability of concrete. The almost immediate feedback provided by the SAM in the fresh concrete can benefit material suppliers, producers, contractors, and engineers in their quest to build long lasting and economic infrastructure. The implementation of this procedure also shows promise to give new tools to design concrete mixtures, admixture formulation, and construction practices. These are all areas of examples where the SAM is currently being used in the industry. These will be areas of future publications.

5.0 Acknowledgements

The authors would like to acknowledge funding from the Oklahoma Transportation Center and Pooled Fund TPF-5(297) and the supporting states. Special thanks to Jason Weiss for the discussion over this work. We would also like to thank David Porter, Justin Becker, Brad Woodard, Zane Lloyd, Brendan Barns, Jacob Lavey, Chad Stevenson, Jason Toney, Mark Finnell, Muwanika Jdiobe, Megan Buchanan, Tyler Suder, and Lizzie Long for their assistance in preparing samples.

6.0 References

1. Kosmatka, S.H. and M.L. Wilson, *Design and control of concrete mixtures*. 2016: Portland Cement Assoc.
2. Pigeon, M. and R. Pleau, *Durability of concrete in cold climates*. 1995: CRC Press.
3. Backstrom, J., et al., *Void spacing as a basis for producing air-entrained concrete.* ACI Journ., 1954. **4**: p. 760-761.
4. Powers, T.C. and T. Willis. *The air requirement of frost resistant concrete*. in *Highway Research Board Proceedings*. 1950.

5. Ley, M.T., et al., *Determining the Air-Void Distribution in Fresh Concrete with the Sequential Air Method.* Construction and Building Materials, 2017. **150**: p. 723-737.
6. Scherer, G.W. and J. Valenza, *Mechanisms of frost damage.* Materials science of concrete, 2005. **7**(60): p. 209-246.
7. Kleiger, P., *Studies of the Effect of Entrained Air on the Strength and Durability of Concrete made with Various Maximum Sizes of Aggregate*. 1952: Portland Cement Association.
8. Kleiger, P., *Further Studies on the Effect of Entrained Air on Strength and Durability of Concrete with Various Sizes of Aggregates*. 1956: Portland Cement Association.
9. Ley, M.T., *The Effects of Fly Ash on the Ability to Entrain and Stabilize Air in Concrete* in *Civil, Architectural, and Environmental Engineering*. 2007, University of Texas at Austin
10. *ASTM C138/C138M-17a Standard Test Method for Density (Unit Weight), Yield, and Air Content (Gravimetric) of Concrete*, A. International, Editor. 2017: West Conshohocken, PA.
11. *ASTM C173/C173M-16 Standard Test Method for Air Content of Freshly Mixed Concrete by the Volumetric Method*, A. International, Editor. 2016: West Conshohocken, PA.
12. *ASTM C231/C231M-17a Standard Test Method for Air Content of Freshly Mixed Concrete by the Pressure Method*, A. International, Editor. 2017: West Conshohocken, PA.
13. *AASHTO TP 118 LRFD Bridge Design Specifications*, A.A.o.S.H.a.T. Officials, Editor. 2017: Washington, D.C.
14. Tanesi, J., et al., *Super Air Meter for Assessing Air-Void System of Fresh Concrete.* Advances in Civil Engineering Materials, 2016. **5**(2): p. 22-37.
15. LeFlore, J. *Super Air Meter Test Video*. 2016; Available from: https://www.youtube.com/watch?v=xAcHqMz_m3I.
16. Welchel, D., *Determining the Size and Spacing of Air Bubbles in Fresh Concrete*. 2014, Oklahoma State University.

17. Hover, K.C., *Analytical investigation of the influence of air bubble size on the determination of the air content of freshly mixed concrete.* Cement, concrete and aggregates, 1988. **10**(1): p. 29-34.

18. Klein, W. and S. Walker. *A method for direct measurement of entrained air in concrete*. in *Journal Proceedings*. 1946.

19. M.T. Ley, K.J.F., K.C. Hover, *Observations of Air-Bubbles Escaped From Fresh Cement Paste.* Cement Concrete Research 2009.

20. M.T. Ley, R.C., M. Juenger, K.J. Folliard, *The Physical and Chemical Characteristics of the Shell of Air-Entrained Bubbles in Cement Paste.* Cement Concrete Research 2009.

21. Felice, R., J.M. Freeman, and M.T. Ley, *Durable Concrete with Modern Air-Entraining Admixtures.* Concrete international, 2014. **36**(8): p. 37-45.

22. Ley, M.T. and B. Tabb. *A test method to measure the freeze thaw durability of fresh concrete using overpressure*. in *T&DI Congress 2014: Planes, Trains, and Automobiles*. 2014.

23. Ley, M.T., *The effects of fly ash on the ability to entrain and stabilize air in concrete*. 2007: ProQuest.

24. Jakobsen, U., et al., *Automated air void analysis of hardened concrete—a Round Robin study.* Cement and Concrete Research, 2006. **36**(8): p. 1444-1452.

25. Peterson, K., L. Sutter, and M. Radlinski, *The practical application of a flatbed scanner for air-void characterization of hardened concrete*, in *Recent Advancement in Concrete Freezing-Thawing (FT) Durability*. 2010, ASTM International.

26. 201.2R, A.C. *Guide to Durable Concrete*. 2016. American Concrete Institute.

27. W.J. Weiss, M.T.L., O.B. Isgor, *Toward Performance Specifications for Concrete Durability: Using the Formation Factor for Corrosion and Critical Saturation for Freeze-Thaw.* Transportation Research Board, 2017(17-02543).

TOOLS FOR MIXTURE DESIGN WITH THE SEQUENTIAL AIR METHOD

Concrete is a building material used for a wide range of construction projects all over the world. The quality of concrete mixtures affects the long-term durability and enhanced constructability. With the wide range of materials and admixtures used in modern concrete, the industry needs tools to be able to evaluate the quality of these mixtures as expectations grow. These tools need to be easily understood and provide critical feedback for users to be able to obtain good quality results.

Concrete can become damaged due to critical saturation with a series of freezing and thawing cycles [1, 2]. However, if the air void system is made up of well-distributed air bubbles, the concrete mixture may be able to resist that damage [3-5]. Air-entraining admixtures (AEA) are typically used to achieve well-spaced air bubbles. These air voids create pressure-relief regions for water to move to during freezing [2, 3, 5, 6]. It is important to provide small bubbles that are well-distributed in the fresh concrete that in turn creates a void system with the right size and spacing in the hardened concrete [7-9]. For this work, the quality and efficiency of the air void system will be discussed to describe a satisfactory void size and spacing in the hardened concrete.

1.1 Air Void System Quality and Efficiency

A historic method that determines the air void quality uses a hardened air void analysis to determine a parameter called the Spacing Factor [3, 4]. After the concrete has hardened then it is cut, polished, and the surface is inspected under a microscope to inspect the voids. This method can take weeks to complete, which does not provide immediate feedback needed to modify the fresh concrete. While there are other methods that can measure the volume of air in fresh concrete (ASTM C 231, ASTM C 138, ASTM C 173), the volume of air does not give insight into the quality or efficiency of the air void system.

In Figure 1, there are four abstract concrete samples shown. Each sample represents an air content with various bubble sizes and spacing. The quality of the air void system moves low to high (left to right), and the efficiency of the air void system moves low to high (top to bottom). The low efficiency samples show twice the amount of air as the high efficiency images with similar spacing results. This means that with smaller, well-dispersed bubbles, the air void system provides better results with half the amount of air.

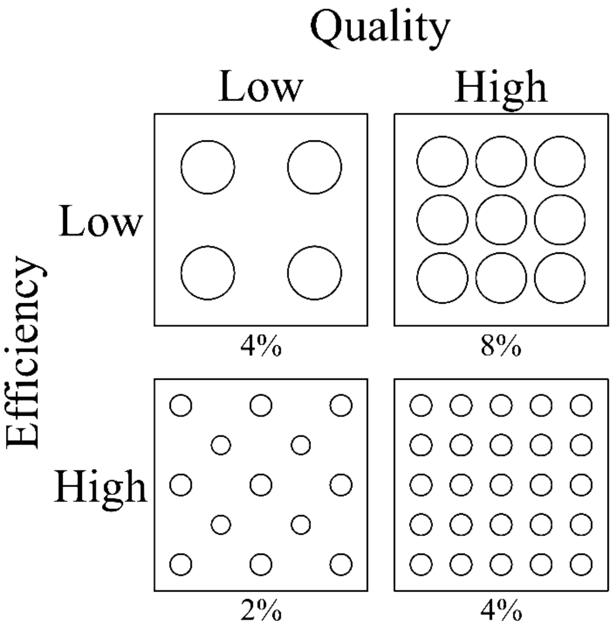

Figure 11 – Quality and efficiency of air void systems in concrete samples.

The current established tests for freeze thaw durability are not able, within fresh concrete, to measure the quality and efficiency of the air void system. While other methods can measure the volume of air in fresh concrete, studies have shown that the air volume is not the only indicator of freeze thaw durability. The small, well-dispersed bubbles improve the quality and efficiency of the air void system. The Spacing Factor has represented the quality of the air void distribution for a concrete mixture; however, measurement of the Spacing Factor requires hardened air void analysis, which is time consuming and can only be conducted on hardened concrete [3, 4].

The efficiency lines on the air content versus SAM Number figures have been established to provide guidelines for users to understand where their concrete mixture stands in relation to a variety of other concrete mixtures in terms of freeze thaw durability. Using these guidelines, new admixtures and aggregates can be studied and adjusted with the SAM Number to figure out how various materials affect the quality of the air-void distribution.

2.0 Experimental Methods

2.1 Laboratory Materials

All of the laboratory concrete mixtures in this research used a Type I cement that met the requirements of ASTM C150. Both the oxide analysis and Bogue calculations for this cement used is shown in Table 1. The aggregates used were locally available crushed limestone and natural sand used in commercial concrete. The crushed limestone had a maximum nominal aggregate size of 19 mm (3/4"). One mixture contained a blend of the coarse and intermediate aggregate as well. Both the crushed limestone and the sand met ASTM C33 specifications. All the admixtures used are described in Table 2, which met the requirements of ASTM C260 and ASTM C494.

Table 4 – Type I cement oxide analysis

Oxide (%)	SiO_2	Al_2O_3	Fe_2O_3	CaO	MgO	SO_3	Na_2O	K_2O	TiO_2	P_2O_5	C_3S	C_2S	C_3A	C_4AF
Cement	21.1	4.7	2.6	62.1	2.4	3.2	0.2	0.3	-	-	56.7	17.8	8.2	7.8
Fly Ash	38.7	18.8	5.8	23.1	5.6	1.2	1.8	0.6	1.5	0.4	-	-	-	-

Table 5 – Admixture references

Short Hand	**Description**	**Application**
WROS	Wood Rosin	Air-entraining agent
SYNTH	Synthetic chemical combination	Air-entraining agent
PC	Polycarboxylate	Superplasticizer
WR	Triethanolamine	Water reducer

The wood rosin (WROS) and synthetic (SYNTH) AEA are two popular commercial AEAs. Twenty-three different mixture designs were investigated and are shown in Table 3. A subset of mixtures was investigated with either a polycarboxylate (PC) superplaticizer meeting ASTM C1017, or a midrange water reducer (WR) meeting ASTM C494. A dose of between 60 and 200 mL/100 kg was used for the superplasticizer to increase the slump of the mixture between 50 mm to 200 mm. Between four and fourteen dosages of AEA were investigated for each mixture to achieve a range of air contents from 2% to

10%. An ASTM C618 Class C fly ash was used in several of the mixtures with a 20% cement replacement by weight.

Table 6 – SSD Mixture proportions

w/cm	Cement kg/m^3	Fly-Ash kg/m^3	Paste Volume (%)	Coarse kg/m^3	Fine kg/m^3	Water kg/m^3	Admixture Used
0.45	362	0	29	1098	714	163	WROS
0.45	362	0	29	1098	714	163	SYNTH
0.53	362	0	32	1053	682	192	WROS
0.41	362	0	28	1127	722	148	WROS
0.39	362	0	27	1140	730	141	WROS
0.45	362	0	29	1098	714	163	WROS + PC1
0.45	362	0	29	1098	714	163	SYNTH + PC1
0.45	290	72	30	1089	709	163	WROS
0.45	223	56	23	785/573*	634	126	WROS
0.40	290	72	28	1115	724	145	WROS
0.40	290	72	28	1115	724	145	WROS + PC1
0.35	290	72	28	1127	768	127	WROS + PC1
0.40	290	72	28	1115	724	145	WROS + PC2
0.40	290	72	28	1115	724	145	WROS + PC3
0.40	290	72	28	1115	724	145	WROS + PC4
0.40	290	72	28	1115	724	145	WROS + PC5
0.40	290	72	28	1115	724	145	WROS + WR
0.40	362	0	28	1098	742	145	WROS
0.40	362	0	28	1098	742	145	WROS+PC1
0.45	335	0	27	1142	742	151	WROS
0.45	335	0	27	1142	742	151	WROS+PC1
0.50	335	0	29	1115	724	167	WROS
0.50	335	0	29	1115	724	167	WROS+PC1

* Mixture used a coarse and intermediate aggregate blend.

2.3 Laboratory Concrete Mixture Procedure and Testing

Aggregates were collected from outside storage piles, and brought into a temperature-controlled room at 23°C for at least 24 hours before mixing. Aggregates were placed in the mixer and spun and a representative sample was taken for a moisture correction. At the time of mixing all aggregate was loaded into the mixer along with approximately two thirds of the mixing water. This combination was mixed for three min to allow the aggregates to approach the saturated surface dry (SSD) condition and ensure that the aggregates were evenly distributed.

Next, the cement, fly ash (if used), and the remaining water was added and mixed for three min. The resulting mixture rested for two min while the sides of the mixing drum were scraped. After the rest period, the mixer was started and the admixtures were added. If the PC or WR was used then it was added first and allowed to mix for 15 seconds to 30 seconds then the AEA was added. After the admixtures were added, the concrete was mixed for three minutes.

Samples were made for hardened air void analysis (ASTM C457). Two 7 L samples were tested with the SAM. These two samples were investigated simultaneously by different operators to determine the average SAM value of a concrete mixture.

2.4 Sequential Air Method

The device used to complete the SAM resembles an ASTM C231 Type B pressure meter with some modifications. The meter uses a digital pressure gauge and six restraining clamps instead of the typical four. These additional clamps are required because of the increased pressures during the SAM test. A picture of an initial version of the device is shown in Figure 2.

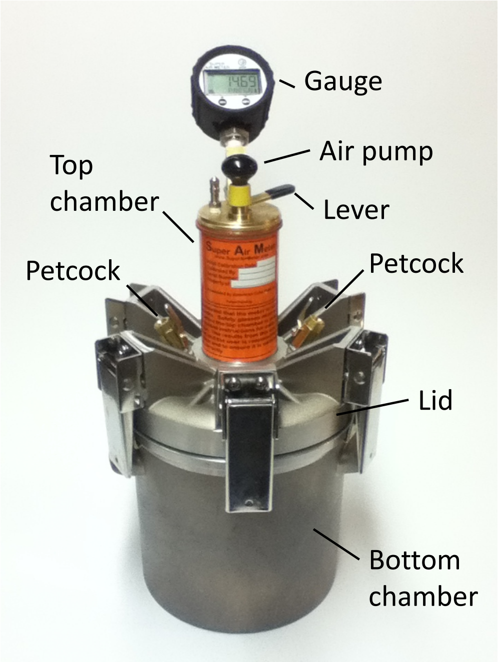

Figure 12 – The device used to complete the SAM.

The test takes between eight to ten min by an experienced user to complete. A video of the test is available [10].

2.4.1 Air Content and Aggregate Correction

The volume of air in the concrete can be determined by using Boyle's Law from the first equilibrium pressure at 100 kPa (14.5 psi). This procedure is discussed in other publications [11-13] and matches the same method and procedure used in the conventional pressure meter (ASTM C231). Past experiments with similar equipment have shown that the air content determined by the SAM closely matched results from the ASTM C231 pressure method [11, 14, 15]. Because the procedures are the same and shown to be equivalent, this is not investigated further in this work.

The calculated air volume with the procedure does not include the aggregate correction factor caused by air contained within the aggregate. The procedure to find the aggregate correction factor is outlined in ASTM C231. Since the SAM Number compares the difference between two sequential pressures, any impact caused by the aggregate on the response to pressure should be removed by subtracting the two pressure responses from each other. The application of this procedure on lightweight aggregates is an area of future research.

2.4.2 Estimating Air Void Size by Comparing the Air Volume and SAM Number

Concrete mixtures that contain large air bubbles have been shown to not provide a stable air-void system and not be as effective at providing freeze thaw durability as mixtures with smaller bubbles [16, 17]. The industry would benefit from a method that provides immediate feedback so that mixtures could be quickly evaluated to determine the current size of bubbles and how different variables affect the size of the bubbles.

One way to determine the average size or quality of the air-void system in concrete is to look at the combination of the volume of air and the SAM Number in the concrete. Since the SAM provides both of these numbers after completing the test, this information could be used to rapidly determine the air-void size distribution in fresh concrete mixtures. For a given air volume, the mixtures with a higher SAM Number have bubbles that are on average larger than mixtures with a smaller SAM Number. However, a user does not always realize if the SAM Number that they are investigating is a large or small value for the air content found. Historic data could be used to provide this guidance.

To analyze the air volume compared to the SAM Number, a quantile regression method was used. A quantile regression takes a set of data and estimates the upper or lower bound of the data. For example, the 50th quantile separates 50% of the data for two different variables. The 85th quantile gives a line where 15% of the data is above and 85% of the data is below. For this work, quantile lines of 85% and 15% provide useful guidance for users to understand where the SAM Number falls in relation to the air content found. The 15th quantile line (lower limit) will be called the high efficiency line and the 85th quantile line (upper limit) will be called the low efficiency line in this paper.

This analysis is useful, as it uses the air content and SAM Number to produce a graph that shows where a typical mixture falls along with mixtures that have on average larger and smaller air voids. This can be helpful for a user to make an immediate evaluation of the average void size of a mixture as both the air content and SAM Number can be measured in the fresh concrete. This immediate feedback can allow users to learn how different ingredients or construction procedures impact the quality of the bubble size and spacing in the concrete.

2.4.3 Variability in Measurement

The variability of the SAM Number was evaluated by using two or three operators to investigate the same concrete mixture simultaneously. To get more insight into the variability of the method, previous testing was also done by two operators by using water and a calibration vessel that provided a reading of 5% air. By only using water and a calibration vessel, this allowed the variability of the test to be examined without including the variability of the concrete [5].

2.5 Hardened Air Sample Preparation

Samples were cut into 19 mm thick slabs, the surface was treated with an acetone and lacquer mixture to harden the surface, and then the samples were lapped with sequentially finer grits. The prepared surface was then inspected under a stereo microscope. After a satisfactory surface was obtained, the hardener was removed with acetone. The sample was then blackened with black permanent marker, the voids were filled with less than 1 µm white barium sulfate powder, and the voids within the aggregates were blackened under a stereo microscope. This process left the surface of the concrete sample black and the voids within the paste white. Sample preparation details can be found in other publications [11, 18]. The surface was then investigated with ASTM C457 method C by using the Rapid Air 457 from Concrete Experts, Inc. A single threshold value of 185 was used for all samples in this research and the results do not include chords smaller than 30 µm. These settings have been shown to provide satisfactory results with the materials and instrument used and match the practices by others [18-20].

3.0 Results and Discussion

3.1 SAM Number and Spacing Factor Relationship

In Figure 3, the relationship between SAM Number and Spacing Factor is represented for 192 laboratory concrete mixtures completed by Oklahoma State University. There seems to be a relationship between the SAM Number and Spacing Factor as shown in Figure 3. As the SAM Number increases then so does the Spacing Factor for the majority of the data. The distributed data could possibly be from variation in test measurements or aggregates and admixture combinations. Past recommendations in freeze thaw analysis have used a single value to determine if a material is recommended for freeze thaw durability. This has also been beneficial in aiding industry implementation. One of the most common values to use is 200 µm. Past work has suggested that a SAM Number of 0.20 correctly determines if a Spacing Factor is above or below 200 µm for 88% of the data [5]. Refer to the appendix for all of the lab mixtures.

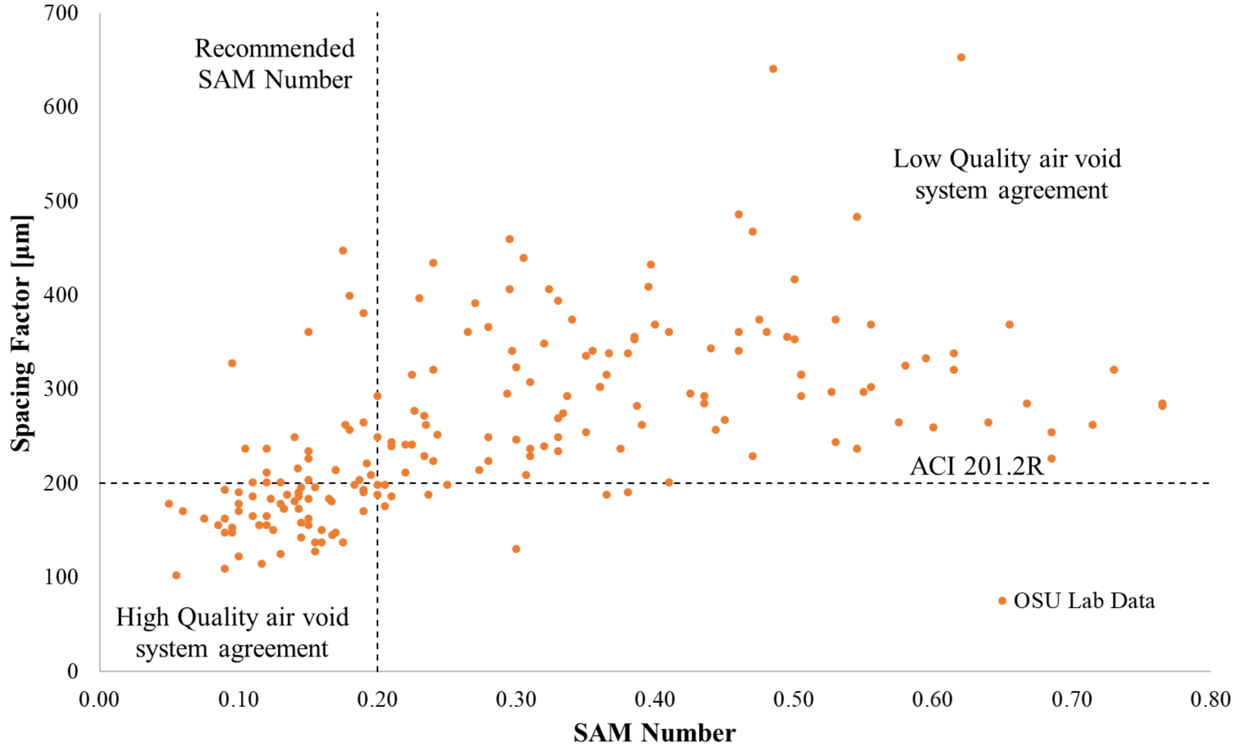

Figure 13 – SAM Number versus Spacing Factor for 192 laboratory concrete mixtures completed by Oklahoma State University.

3.3 SAM Number and Air Content Relationship

While comparing the SAM Number to the Spacing Factor shows the validity of the SAM test, it would be helpful to give immediate feedback to the user about the quality of the air-void system in the concrete. The two parameters that are measured in the SAM test are the air content and the SAM Number. It may be possible to compare these numbers and give users much better insight on the average size distribution of their air bubbles based on historic data.

The relationship between the air content and SAM Number is shown in Figure 4 for laboratory mixtures that were completed at Oklahoma State University. Two cubic polynomial lines are included to show the 85th and 15th quantile. These lines represent the efficiency of the SAM Number at a given air content. 15% of the data falls below the High Efficiency line and 85% of the data falls below the Low Efficiency line. These lines are not limitations to the data set, but rather guidelines for the user to understand whether the concrete mixture is efficient for to the volume of air found in the mixture. These two cubic lines were found to be the best representation of how the data varies. Other trend lines were investigated but they did not provide a useful representation of the investigated data set.

Equation 1 – High Efficiency line:

$$y = -0.0006x^3 + 0.0186x^2 - 0.1888x + 0.6804$$

Equation 2 – Low Efficiency line:

$$y = 0.0014x^3 - 0.0102x^2 - 0.1061x + 0.9213$$

These lines can help SAM users to understand where their concrete mixture falls compared to other SAM Numbers from a wide variety of tests. The closer the SAM Number is to the High Efficiency line, the finer the air-void distribution. If the number is closer the Low Efficiency line, then the air-void distribution is coarser for a specific air volume. These guidelines are based on 192 different concrete mixtures consisting of nine different admixture combinations, seven different water cement ratios (w/cm), and a range of 2% to 10% air contents. It should be noted that these lines are dependent on the mixtures that were investigated. However, the results are helpful as it gives insight into the average size of the bubble system before the concrete has hardened. Due to the wide variety of admixtures, aggregates, and user experience, the two quantile lines help to simplify a range that best represents the SAM Number versus air content instead of a single trend line for all test runs.

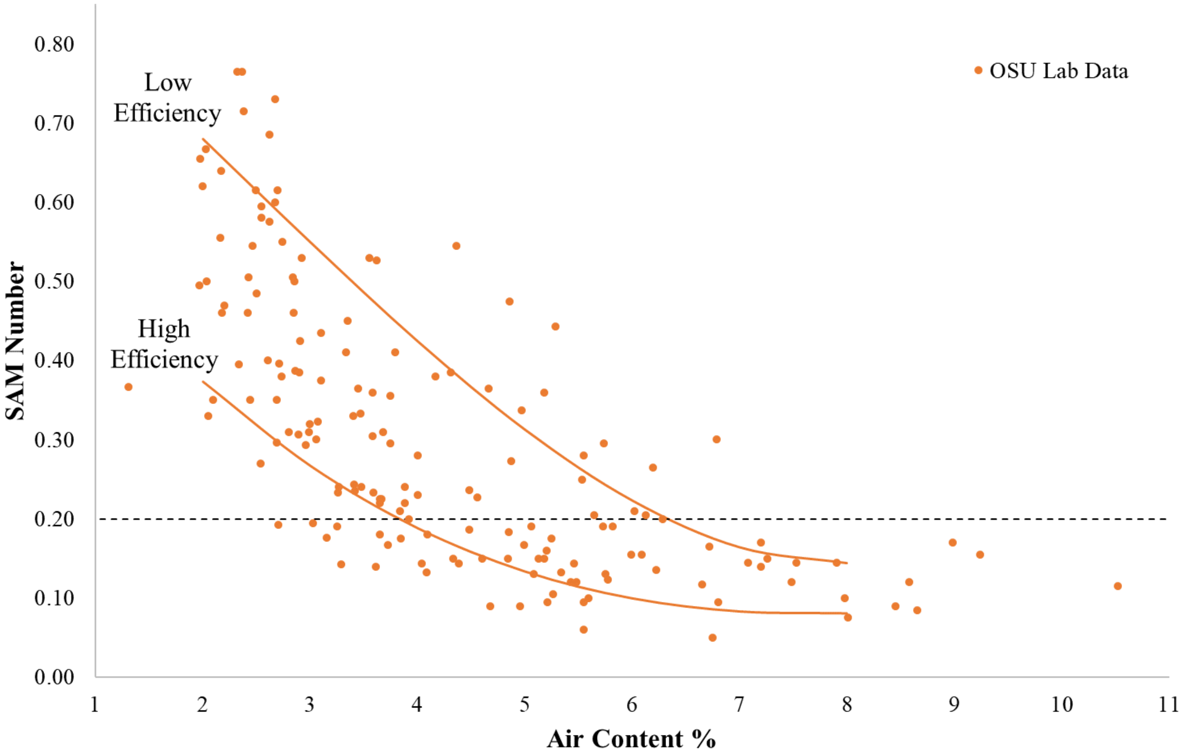

Figure 14 – Air Content versus SAM Number for 192 laboratory concrete mixtures completed by Oklahoma State University.

In Figure 5, the comparison between air content and SAM Number is shown for three concrete mixture designs with three different admixture combinations. The guidelines established from the laboratory data were added to show how these lines are helpful to determine how different admixtures effect the air void distribution within concrete mixtures. The mixture containing only air entrainment shows a trend line that falls along the High Efficiency line. The mixtures containing blends of admixtures show one trend that falls between the high and low efficiency lines (PC5) and one trend closer to the low efficiency line. By adding one admixture to the concrete, the air void system quality drastically changes the air content necessary to pass freeze thaw durability. For example, at 5% air content, the mixture with air entrainment only, passes with a SAM Number of 0.11, the mixture with PC5 passes with a SAM Number of 0.20 and the mixture with PC1 fails with a SAM Number of 0.32. This shows that the mixture with the blend of admixtures using PC1 needs a higher air content to pass the 0.20 limit.

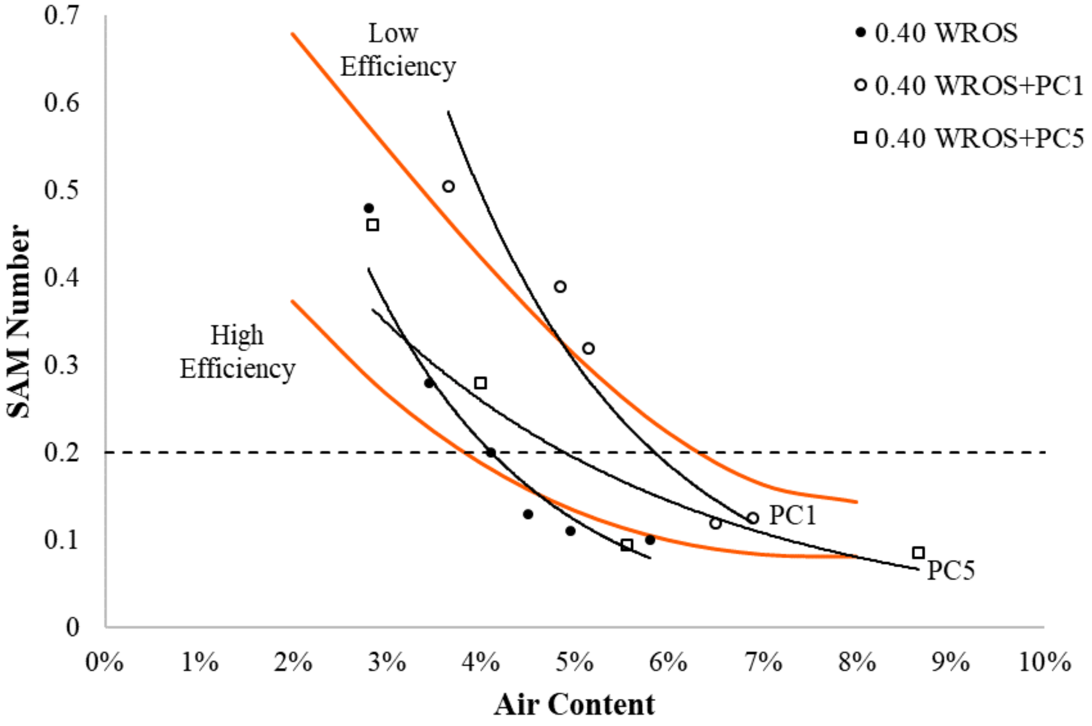

Figure 15 – Air Content versus SAM Number for two laboratory mixture designs with different admixtures.

In Figure 6, the comparison between air content and SAM Number is shown for three concrete mixture designs with three different types of cement. The guidelines established from the laboratory data were added to show how these lines are helpful to determine how different cements effect the air void distribution within concrete mixtures. Two mixtures sets containing different types of cement show trend lines that fall along the High Efficiency line. The mixtures containing a third type of cement shows a trend line that falls closer to the Low Efficiency line. By using different materials, the air void system quality drastically changes the air content necessary to pass freeze thaw durability. For example, the High Efficiency mixtures pass with air contents of 3.5% and 4% while the Low Efficiency mixture passes with an air content of 6.7%. This shows that the mixture with a higher air content is less efficient due to the amount of air entrainment needed to reach a passing freeze thaw durability.

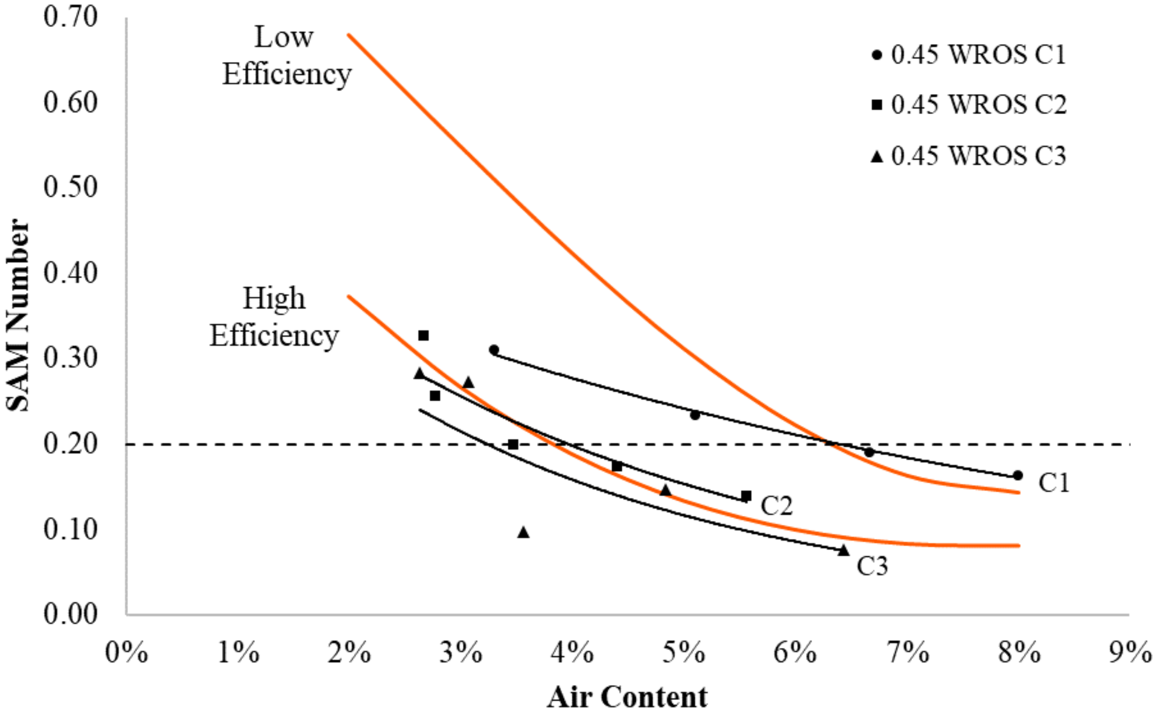

Figure 16 – Air Content versus SAM Number for two laboratory mixture designs with different types of cement.

4.0 Practical Implications

This work studies the implementation of a new method using laboratory data. Using a wide variety of concrete mixtures shows the strength in diversity of the SAM test. The SAM Number provides feedback to the user before the mixture is placed to determine if it needs to be adjusted to meet specification requirements. If the industry were able to adjust concrete mixtures before placement, there would be less rejected concrete mixtures and longer lasting concrete after placement.

The curves on the air content versus SAM Number figures have been established to provide guidelines for users to understand where their concrete mixture stands in relation to a variety of other concrete mixtures in terms of freeze thaw durability. Using these guidelines, new admixtures and aggregates can be studied and adjusted with the SAM Number to figure out how various materials affect the quality of the air-void distribution. This shows great promise to be a tool that can help producers design their concrete, troubleshoot field practices, and provide concrete that has a high confidence of freeze thaw durability.

5.0 Conclusion

This work analyzes laboratory concrete mixtures to determine the reliability of the SAM test method and give guidance to field users. Efficiency lines based on the laboratory data provide helpful insight into the average air void size in fresh concrete mixtures for users to know whether the mixture will meet specifications or not. These curves act as guidelines for field users to relate to data from a wide variety of other mixtures.

These specific findings have been made:

- The SAM Number and the Spacing Factor for laboratory concrete mixtures correlate and there is agreement for a 0.20 SAM Number and a 200µm Spacing Factor.
- For 192 laboratory mixtures, the correlation between a SAM Number of 0.20 and a Spacing Factor of 200 µm agrees with 86% of the laboratory data comparisons.
- Cubic 85% and 15% quantile lines based on the laboratory data provides a useful tool to evaluate the average void size in fresh concrete mixtures. This can be a useful tool for a user to gain immediate feedback on how the concrete mixtures, material changes, and construction practices impact the average void size in their concrete.

The overall study has shown promising results for the SAM method to provide a positive impact in the concrete industry. Because the SAM provides rapid feedback that is useful, it has the ability to impact each phase within the concrete industry for the better, from materials to producers to construction implementation.

6.0 References

1. Kosmatka, S.H. and M.L. Wilson, *Design and control of concrete mixtures*. 2016: Portland Cement Assoc.
2. Pigeon, M. and R. Pleau, *Durability of concrete in cold climates*. 1995: CRC Press.
3. Backstrom, J., et al., *Void spacing as a basis for producing air-entrained concrete.* ACI Journ., 1954. 4: p. 760-761.
4. Powers, T.C. and T. Willis. *The air requirement of frost resistant concrete*. in *Highway Research Board Proceedings*. 1950.
5. Ley, M.T., et al., *Determining the Air-Void Distribution in Fresh Concrete with the Sequential Air Method.* Construction and Building Materials, 2017. 150: p. 723-737.
6. Scherer, G.W. and J. Valenza, *Mechanisms of frost damage.* Materials science of concrete, 2005. 7(60): p. 209-246.
7. Kleiger, P., *Studies of the Effect of Entrained Air on the Strength and Durability of Concrete made with Various Maximum Sizes of Aggregate*. 1952: Portland Cement Association.
8. Kleiger, P., *Further Studies on the Effect of Entrained Air on Strength and Durability of Concrete with Various Sizes of Aggregates*. 1956: Portland Cement Association.
9. Ley, M.T., *The Effects of Fly Ash on the Ability to Entrain and Stabilize Air in Concrete* in *Civil, Architectural, and Environmental Engineering*. 2007, University of Texas at Austin
10. LeFlore, J. *Super Air Meter Test Video*. 2016; Available from: https://www.youtube.com/watch?v=xAcHqMz_m3I.
11. Welchel, D., *Determining the Size and Spacing of Air Bubbles in Fresh Concrete*. 2014, Oklahoma State University.

12. Hover, K.C., *Analytical investigation of the influence of air bubble size on the determination of the air content of freshly mixed concrete.* Cement, concrete and aggregates, 1988. 10(1): p. 29-34.

13. Klein, W. and S. Walker. *A method for direct measurement of entrained air in concrete*. in *Journal Proceedings*. 1946.

14. Tanesi, J., et al., *Super Air Meter for Assessing Air-Void System of Fresh Concrete.* Advances in Civil Engineering Materials, 2016. 5(2): p. 22-37.

15. Ley, M.T. and B. Tabb. *A test method to measure the freeze thaw durability of fresh concrete using overpressure*. in *T&DI Congress 2014: Planes, Trains, and Automobiles*. 2014.

16. Felice, R., J.M. Freeman, and M.T. Ley, *Durable Concrete with Modern Air-Entraining Admixtures.* Concrete international, 2014. 36(8): p. 37-45.

17. Freeman, J.M., *Stability and quality of air void systems in concretes with superplasticizers*. 2012, Oklahoma State University.

18. Ley, M.T., *The effects of fly ash on the ability to entrain and stabilize air in concrete*. 2007: ProQuest.

19. Jakobsen, U., et al., *Automated air void analysis of hardened concrete—a Round Robin study.* Cement and Concrete Research, 2006. 36(8): p. 1444-1452.

20. Peterson, K., L. Sutter, and M. Radlinski, *The practical application of a flatbed scanner for air-void characterization of hardened concrete*, in *Recent Advancement in Concrete Freezing-Thawing (FT) Durability*. 2010, ASTM International.

Effects of Pumping Concrete Based on The Air Void Paramaters in Fresh and Hardened Concrete

1.0 INTRODUCTION

Elevated slabs exposed to the weather, such as concrete bridge decks or parking garages, have been highly susceptible to rapid freezing and thawing damage [1]. The use of entraining air bubbles into the concrete has been the solution to freeze-thaw durability [2, 3]. Yet, the emphasis of air volume has not always been enough to provide freeze-thaw durable concrete [4-7]. The proper air void distribution in concrete must be obtained to provide space for the water to freeze and expand without damaging the concrete [1-9]. Unfortunately, pumping of air-entrained concrete for elevated slabs frequently results in quality control issues due to increased pressures and even rejection of the load due to the loss of air content after the concrete was pumped [10-17]. Regardless, many of these bridges remain standing after excessive freezing and thawing cycles. Therefore, this research used Unit Weight (ASTM C138), Super Air Meter (AASHTO TP 118), Freeze-Thaw Resistance (ASTM C666), and Hardened Air Void Analysis (ASTM C457) to investigate how the air void quality and freeze-thaw durability performance of concrete changes due to pumping.

2.1 EXPERIMENTAL METHODS

2.2 Materials

All of the concrete and grout mixtures described in this work were prepared using an ASTM C150 Type I Portland cement and an ASTM C618 Class C fly ash. The laboratory and field mixtures used the same aggregates. The fine aggregate was a natural sand source and the coarse and intermediate aggregates were quarried from a single dolomitic limestone. Both field and laboratory mixtures used a wood rosin based air-entraining admixture (AEA). The field mixtures and some laboratory mixtures used ASTM C494 Type A/F mid-range water reducer (WR) was dosed at 7 oz./cwt (467 mL/100 kg). However some laboratory mixtures used a ASTM C1017 Polycarboxylate (PC) superplasticizer at a dosage of 2.5 oz./cwt (163 mL/100 kg). Some mixtures in the laboratory used a food grade citric acid at 0.25% weight of the cementitious material as a hydration stabilizer, set retarder, and water reducer. The admixture dosages of these mentioned admixtures in the laboratory were chosen to provide approximately the same slump before pumping for all mixtures.

2.3 Laboratory and Field Mixture Design

All of the concrete mixtures had a water-to-cementitious material ratio (w/cm) of 0.45 and 611 lbs./yd^3 (362 kg./ m^3) of total cementitious material with 20% Class C fly ash replacement by weight. The paste content of each mixture was 28.9%, which the air content was not included in determining the paste content. The mixtures contained 1264 lbs./yd^3 (745 kg./ m^3) of coarse aggregate, 426 lbs./yd^3 (253 kg./ m^3) of intermediate aggregate, and 1471 lbs./yd^3 (873 kg./ m^3) of fine aggregate. However, the proportions of aggregate were slightly adjusted depending on the mixtures to maintain an approximately constant combined aggregate gradation using the Tarantula Curve [17, 18]. This was due to the Tarantula Curve in previous work showing to improve pumpability of concrete and reduce segregation and other workability issues [17, 18].

2.4 Grout Mixtures

The pump and pipe network were primed with grout prior to each laboratory pumping session. Priming consists of lining the walls of the pump and pipe network with a thin lubricating layer of grout. This grout mixture had a 0.40 w/cm, 1006 lbs./yd^3 (597 kg./ m^3) of cement, and 2514 lbs./ yd^3 (1491 kg./ m^3) of sand.

2.5 Mixing Procedure

For the laboratory mixtures, aggregates were brought from outside stockpiles into a temperature-controlled room at 72°F (22°C) for at least 24 hours before mixing. The aggregates spun in a mixing drum for at least three minutes. A representative sample for moisture content testing was used to apply a moisture correction to the mixture. At the time of mixing, all aggregates were loaded into the mixer along with approximately two-thirds of the mixing water. This combination mixed for three minutes to allow the aggregate surface to saturate and ensure the aggregates were evenly distributed. Next, the cement, fly ash, and the remaining water mixed for three minutes. The resulting mixture rested for two minutes while scraping the sides of the mixing drum. After the rest period, the admixtures were added and mixing continued for three minutes.

For field testing the concrete was delivered in 5 cubic yard (3.82 m^3) increments. Field mixing followed ASTM C94 and moisture corrections used probes within the aggregates. All of the concrete tested in the field was truck-mixed.

2.6 Equipment

2.6.1 Concrete Pumps

The Putzmeister TK 50 concrete pump used for the laboratory testing. This pump provides an almost continuous concrete flow by two alternating pistons. One piston draws concrete from the hopper as it retracts, and the second piston pushes concrete out as it extends. An S-valve alternating delivery system shifts from one delivery cylinder to the other. This delivers concrete from the pump as a remixer continually agitates the concrete in the hopper. The pump settings used in this work were 1500 RPM, and the piston volume was 0.57 ft^3 (0.01614 m^3) as determined by previous work [17].

A PumpStar AZ34.5-PS220 truck-mounted concrete pump was used for the field research and has two 9.0 in. (22.86 cm) inside diameter (I.D.) delivery cylinders with an approximate length of 6.5 ft. (16.51 cm). An S-valve delivery system switches between the delivery cylinders. After the S-valve, the pipe diameter reduced to 5.0 in. (12.7 cm) I.D. Following this was approximately 110 ft. (33.5 m) of 5.0 in. (12.7 cm) I.D. double-wall steel pipe. At the end of the boom was a reducer and approximately 10 ft. (304.8 cm) of 4.0 in. (10.2 cm) I.D. rubber hose for easier placement.

2.6.2 Pressure Sensors

Measurements of the concrete pressure near the edge of the pipe was completed for laboratory and field testing with a novel pressure sensor setup developed by previous work[17]. Each pressure sensor consisted of a GE 5000 pressure sensor in conjunction with a buffer chamber filled with hydraulic fluid. The GE 5000 pressure sensor was capable of measuring pressures between 14.5 psi to 500 psi with +/-0.5 psi (3.45 kpa) accuracy. The buffer chamber was required to separate the sensor from the concrete. The buffer chamber consists of a hydraulic fluid-filled chamber with a flexible rubber membrane on one end, with the other end connected to the GE 5000 pressure sensor. As pressures increase on the rubber membrane, the pressures transfer to the fluid in the chamber and to the GE 5000 sensor. The walls of the buffer chamber perpendicular to the rubber membrane were threaded.

To connect the sensor to the pipe, a 1.125 in. (2.86 cm) diameter hole was drilled and a nut was welded to the outside of the pipe. The buffer chamber threads into the nut until the rubber membrane was adjacent to the walls of the pipe. The pressure sensors were rotated approximately 60° from the horizontal to keep aggregate, paste, and water from collecting on top of the flexible rubber membrane. The pressure sensor recorded data every 0.02 seconds.

Calibration of the sensor assembly used a water-filled pipe. A hand pump increased the pressure in the pipe from 0 to 110 psi (758.4 kpa) in systematic steps. By plotting the voltage and water pressure, a calibration curve was created and a linear model was used to fit the data with an average R-value of 0.99.

All measurements used the linear model to determine the pressure at the surface of the pipe. During calibration of the sensor, the y-intercept would shift 0 psi (0 kpa) to 20 psi (137.9 kpa) between measurements, but the slope of the calibration line remained constant. This may be caused by the wear and relaxation of the rubber membrane on the pressure sensor. To account for this, the pressure sensor measured the empty pipe network to determine the 0 psi (0 bar) or atmospheric pressure value before each experiment.

This work used the peak pressure to characterize each mixture. The peak pressure was the maximum pressure recorded from each piston stroke. The maximum pressure measured in the laboratory mixtures was between 50 psi (344.7 kpa) and 120 psi (827.4 kpa). The maximum pressures for the field mixtures was between 150 psi (1034.2 kpa) and 200 psi (1379 kpa).

2.6.3 Pipe Configurations

The laboratory testing used a standard pipe network. 1 shows an overview of the pipe network. The pipe network used 4.0 in. (10.2 cm) I.D. single wall steel pipe. Rubber gaskets and couplings secured the sections of pipe together. The pipe network consists of a 3.3 ft. (1 m) long single wall steel pipe reducer that reduces the 5.0 in. I.D. (12.7 cm) output of the pump to 4.0 in. (10.2 cm). After the reducer, there was 52.5ft. of 4.0 in. (10.2 cm) I.D. steel pipe with three 1.5ft (45.7 cm) radius 90° bends. At the end of the steel pipe network. I.D. flexible rubber hose returns the concrete to the hopper of the pump creating a continuous flow. The total volume of the pipe network was approximately 6.0 ft^3 (0.1699 m^3). Along the pipe network, four sensors measured the pressures at the walls of the pipe during pumping. The locations of the four pressure sensors were in Figure 1.

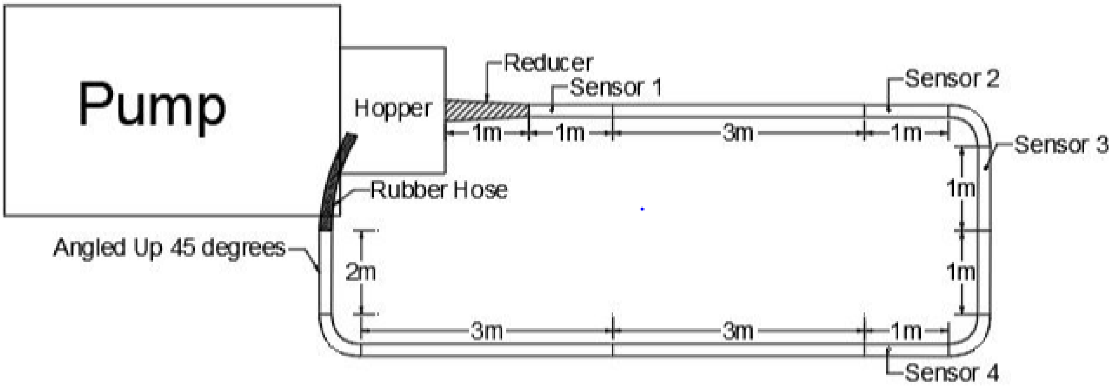

Fig. 1. Plan View of the pipe network.

The field testing used three different configurations of flat, arch, and A-frame arrangements. In the flat configuration, the pipe was placed horizontally to discharge approximately 100 ft. (30.48 m) from the pump. In the arch configuration, the boom followed a curve with the maximum height at approximately 40 ft. (12.19 m) above the ground and the point of discharge at approximately 60 ft. (18.29 m) from the pump. The final configuration was the A-frame. In the A-frame orientation, the boom was in a sharp upward and downward configuration with the maximum height of approximately 50 ft.

(15.24 m) above the ground and the outlet of the pump approximately 30 ft. (9.14 m) from the pump. The first pressure sensor was at the discharge of the piston. The second sensor was before the peak of the arch and A-frame and the third sensor was after the peak.

2.7 Evaluation of Air Entrained Concrete

The properties of air-entrained concrete after pumping was evaluated based on the total air volume, air void quality, and freeze-thaw resistance of the concrete changes. The following tests were run on the concrete before and after adding to the pump: Slump (ASTM C143), Unit Weight (ASTM C138), Super Air Meter (AASHTO TP 118), Freeze-Thaw Resistance (ASTM C666), and Hardened Air Void Analysis (ASTM C457). For this work, durability factors less than 70% after 300 freeze-thaw cycles for ASTM C666 were considered failing and has been consistent with previous work [4-7].

The laboratory testing of the concrete was tested before pumping, tested after one cycle through the pipe network, and then tested every 15 minutes of recirculating the concrete through the pump and pipe network. For each 15 minutes of pumping, the concrete circulated approximately 40 times through the pipe network. This was the same as traveling approximately 2400 ft. (731.5 m) of 4.0 in. (10.16 cm) diameter line and passing through the reducer forty times. The concrete tested after one cycle through the pump was most representative of typical construction applications. The concrete tested after several cycles through the pump provides insight to how excessive pumping affects the properties of the concrete. The pumping session was stopped when the slump was less than 3.0 in. (7.62 cm) to avoid blockages in the line.

For a few laboratory mixtures, the concrete was tested before pumping, immediately after pumping, and then every 20 to 30 minutes without agitation to determine how the slump, unit weight, air volume, and SAM Number changed over time. A sample was also collected for hardened air void analysis. This testing procedure was performed three times using citric acid and twice using a PC. This was done to show how the air void system recovered over time.

In the field, the same tests of Slump (ASTM C143), Unit Weight (ASTM C138), Super Air Meter (AASHTO TP 118), Freeze-Thaw Resistance (ASTM C666), and Hardened Air Void Analysis (ASTM C457) were run before and after the pump in each boom configuration. The concrete was tested simultaneously before and after the pump to ensure measurements were as comparable as possible.

3.1 RESULTS AND DISCUSSION

Figure 2 shows a plot of the air content before and after one cycle through the pump for the laboratory and field mixtures. The plot shows a line of equality. If a mixture had the same air content before and after pumping then it would be on this line. All of the laboratory mixtures with citric acid and WR showed a decrease in air content after pumping. The PC samples and field samples did not show a significant change in air content. Of the 18 field mixtures, five samples showed a 0.5% change in air volume.

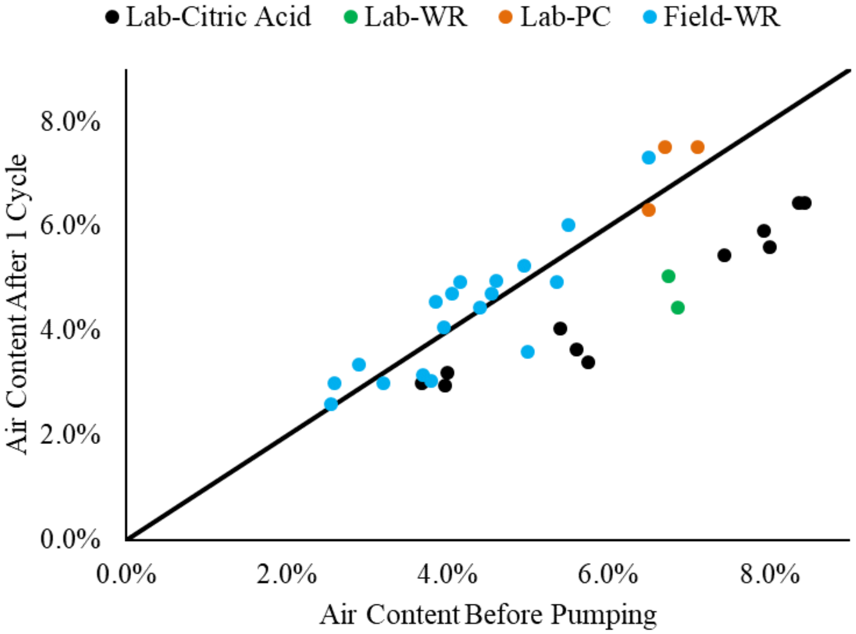

Fig. 2. Plot of Air content before pumping vs. Air content after 1 cycle

3.2 Air Volume and Super Air Meter Results

Figure 3 shows the normalized air content versus the number of cycles through the pump. The normalized air content was the ratio of the air before pumping to the air measured after pumping multiplied by 100. All lab mixtures containing a citric acid and WR showed the most significant decrease in air content between the measurements right after mixing and the measurements after one pumping cycle. After the first pumping cycle, the air content of the citric acid and WR mixtures either decreased at a slower rate or remained approximately constant with additional times through the pump. On average, the citric acid and WR lost approximately 30% of the initial air content after one cycle through the pump with a standard deviation of 4.5% and 7.1% respectively. In contrast, the PC mixture and field mixtures did not show a significant change in air volume after one pumping cycle. These results indicate most of the air lost during pumping occurs during the first cycle for the citric acid and WR mixtures. In addition, the relative proportion of air lost for all citric acid and WR samples was comparable.

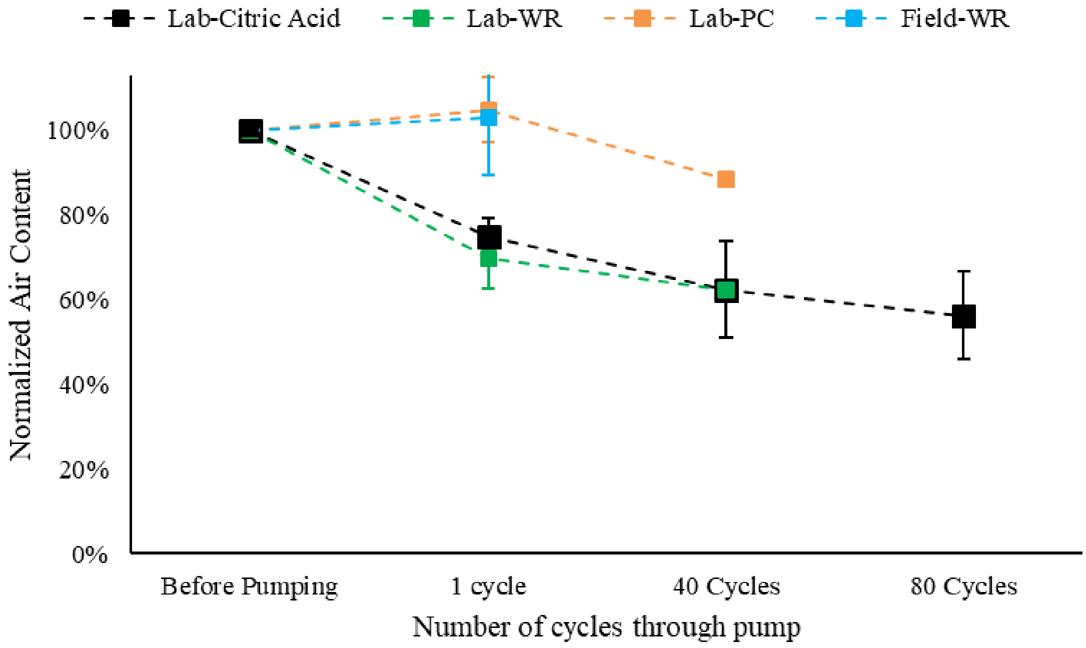

Fig. 3. Plot of Normalized air content vs. Number of cycles through the pump.

Figure 4 shows the SAM Number before pumping compared to the SAM Number after one cycle through the pump and pipe network. In all citric acid, WR, and field mixtures, the SAM Number increased by at least 50% for 87% of the mixtures after one cycle through the pump. In the PC samples, the SAM Number slightly decreased after one pumping cycle.

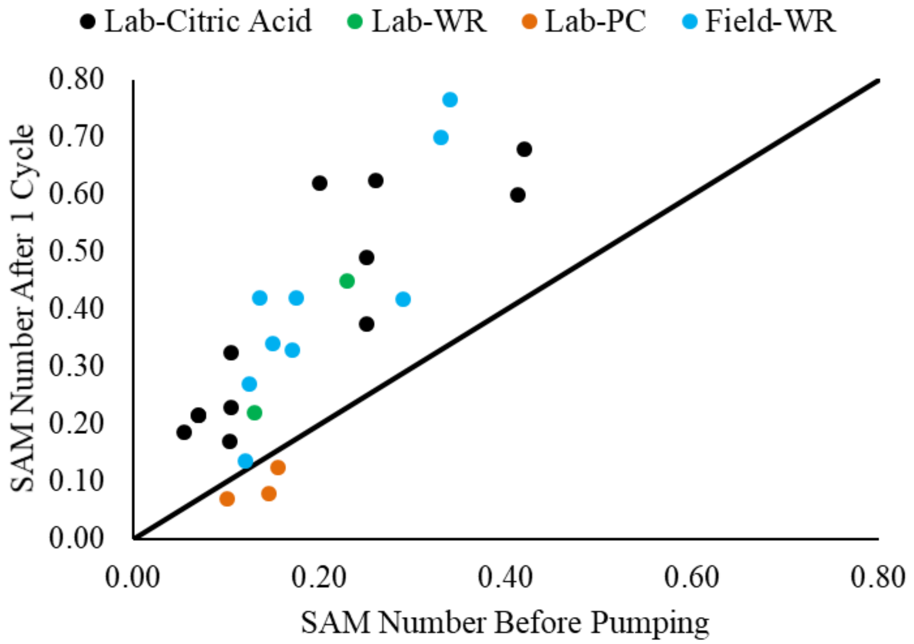

Fig. 4. Plot of SAM Number Before Pumping versus the SAM Number after pumping one cycle through pump and pipe network

Figure 5 plots the Normalized SAM Number vs. number of cycles through the pump for laboratory and field samples. The Normalized SAM Number ratio was the SAM Number after pumping divided by the SAM Number before pumping multiplied by 100. Also the graph shows error bars from one standard deviation. A positive number indicates an increase in SAM Number and a negative number indicates a decrease in SAM Number. After one pumping cycle, the SAM Number for the citric acid, WR, and Field samples increased. PC samples showed a slight decrease in SAM Number after one pumping cycle. With multiple cycles, the SAM Number remained approximately constant or increased for all samples.

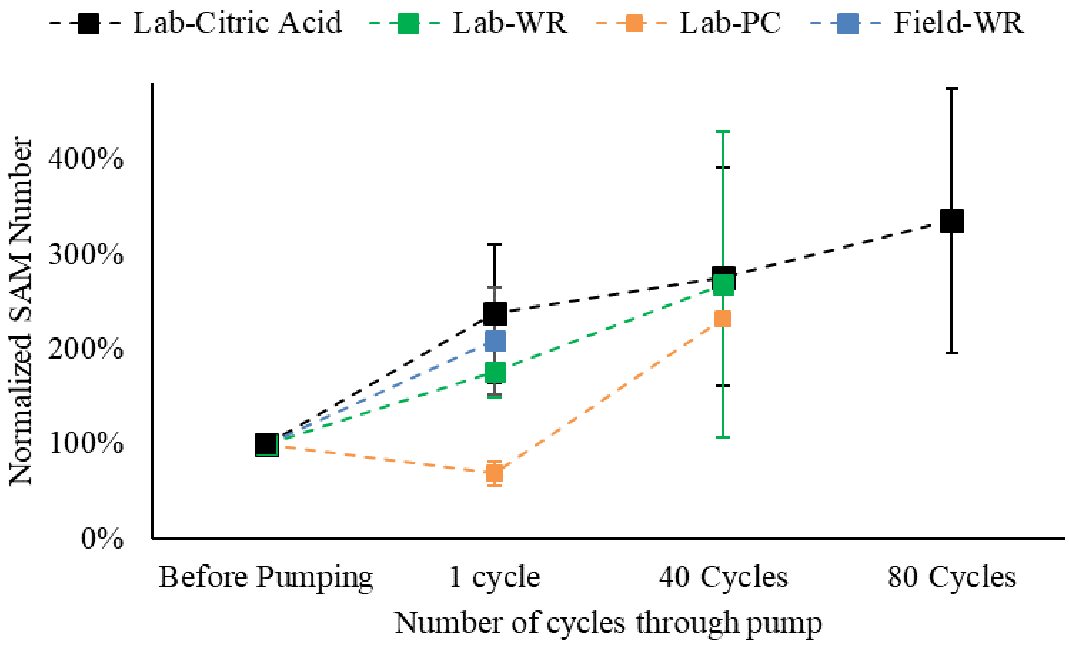

Fig. 5. Plot of SAM Number vs number of cycles through the pump and pipe network.

3.3 Recovery of the air void system

To investigate how the air void system recovered over time. Mixtures were tested every 20-30 minutes after pumping. Figures 6, 7, and 8 show the data at zero minutes corresponds to the measurement taken before pumping. The data at ten minutes corresponds to one cycle through the pipe network. A non-pumped sample has also been included for comparison. The results have been divided into mixtures that lost air during pumping and those that did not. These will be discussed separately.

3.3.1 Mixture with minimal air change from pumping

The mixtures with minimal change in the air volume from pumping were shown in Figure 6 and Figure 7. In these mixtures there was minimal change in the air volume and SAM number over time after pumping. Since the mixtures were not modified by the pumping process then we would not expect these values to change. This data confirms this and acts as a control.

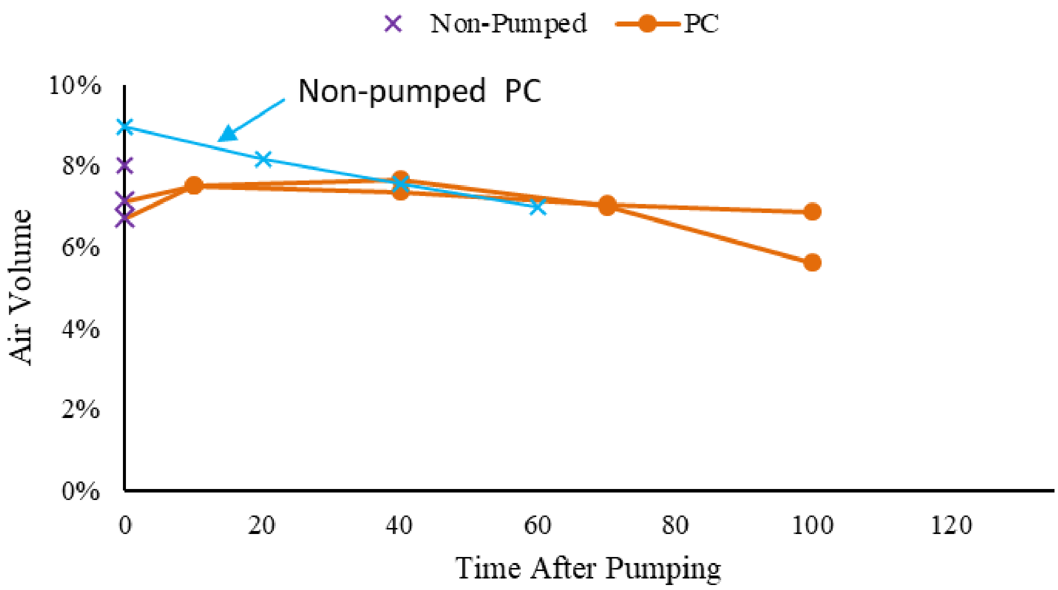

Fig. 6. Plot of fresh air content (%) versus time after pumping one cycle through the pump and pipe network.

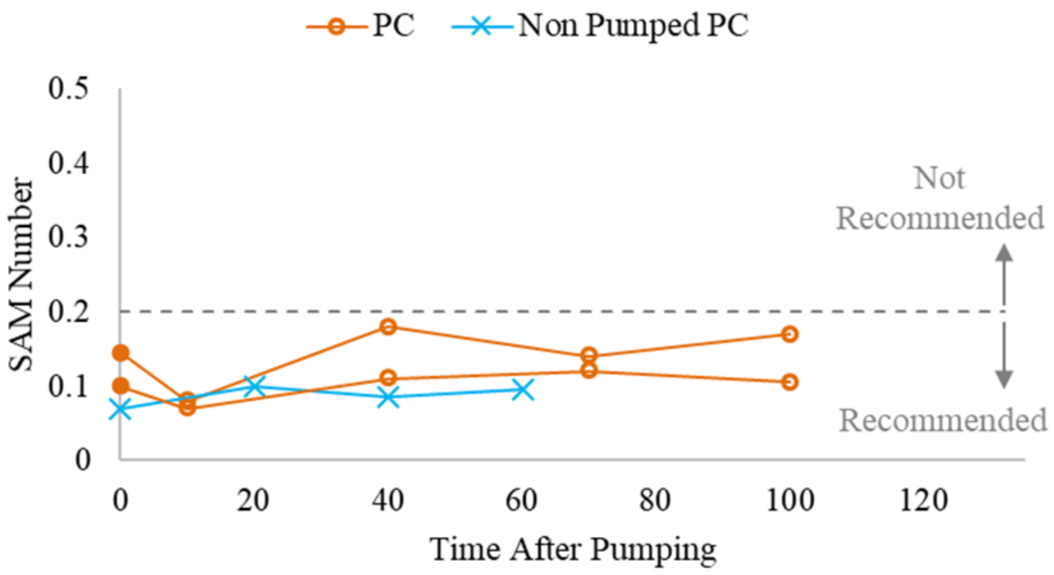

Fig. 7. Plot of SAM Number versus time after pumping one cycle for PC mixtures.

3.3.2 Mixtures with changes from pumping

Figure 8 shows the air volume change and Figure 9 shows the SAM Number change over time for mixtures that lost air after one cycle of pumping. As the concrete sat undisturbed, the SAM Number seems to improve over time. This could be caused by the pumping temporarily dissolving the smaller bubbles from the increased pressures. As the concrete sits statically, these smaller bubbles may reform. This was why the SAM Number improves over time.

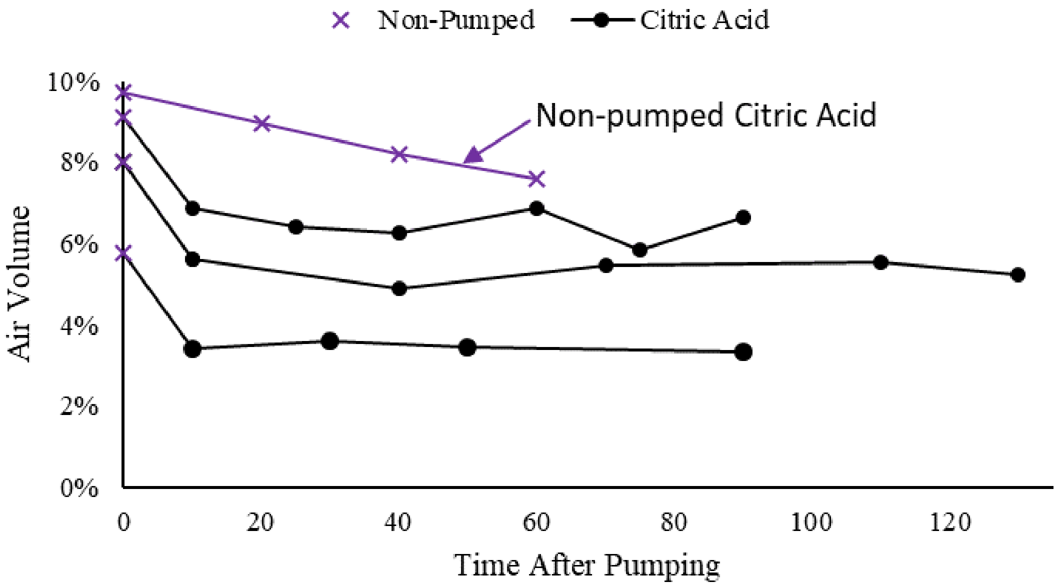

Fig. 8. Plot of fresh air content (%) versus time after pumping one cycle for citric acid mixtures.

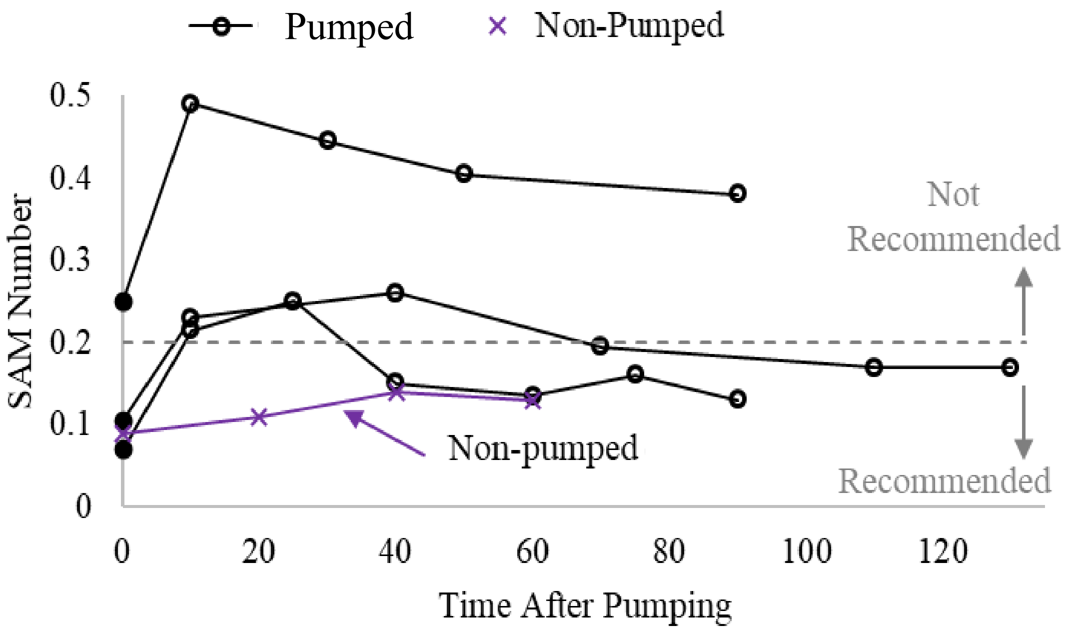

Fig.9. Plot of SAM Number versus time after pumping one cycle for citric acid mixtures.

An important observation was that the improvement in the SAM Number was observed without a significant change in the air volume. This may occur if the dissolved air bubbles are small and do not make a significant contribution to the total air volume but do change the size and spacing of the air void system and so they will impact the SAM Number. This may occur if the voids returning were small and well dispersed. This suggests the air void system measured immediately after pumping was not representative of the hardened concrete for these mixtures.

3.4 Freeze-thaw Durability

Most specifications require air contents to be greater than 4% when freeze-thaw durability was required. In addition, previous research has also shown a SAM Number less than 0.32 correlates to the point of satisfactory performance in ASTM C666 [5-7].

Figure 10 shows the relationship between air content and durability factor. A dashed vertical line shows 4% air content and a durability factor of 70%. The filled circles represent the air content measured before pumping and the open circles represent the air content measured after pumping. In addition, 64 data points are included from previous publications to show the typical relationship between the air content and durability factor for non-pumped samples [5-7]. The previous work used the same cement, fly ash, coarse aggregate, and fine aggregate. Pumping frequently reduced the air content below 4%; however, the ASTM C666 freeze-thaw performance was satisfactory. This shows the air content after pumping does not accurately predict the freeze-thaw performance based on industry standards.

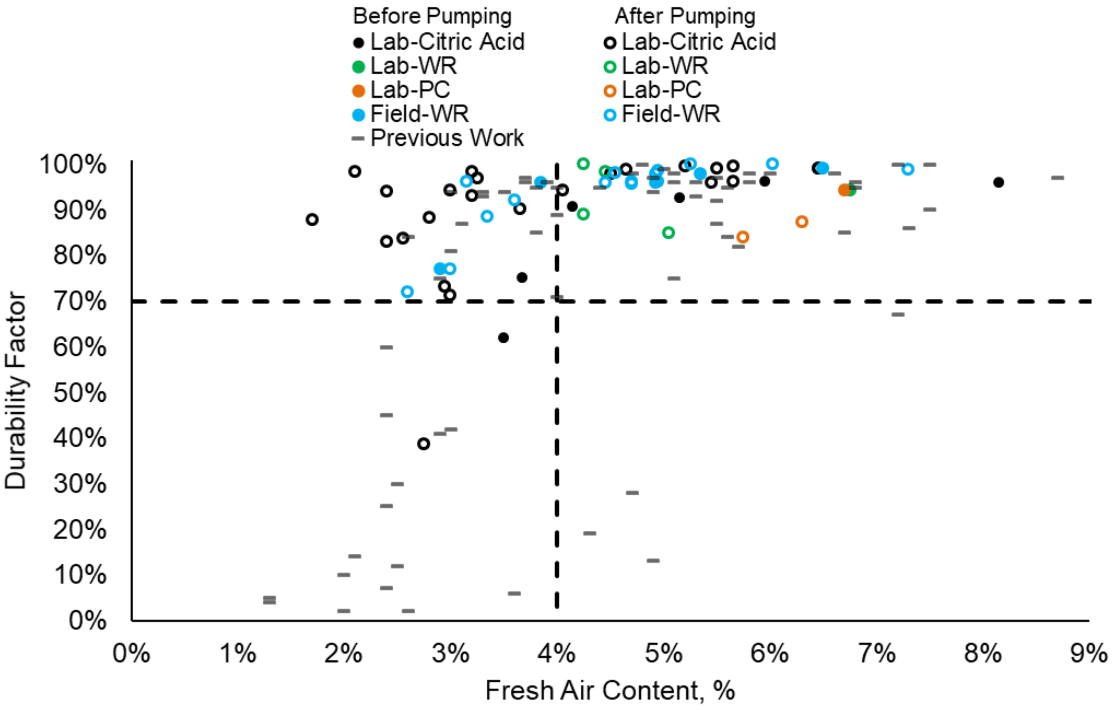

Fig. 17. Plot of fresh air volume measured after pumping versus Durability Factor

Figure 11 shows the relationship between SAM Number and Durability Factor. The closed circles represent points measured before pumping, and the open circles represent points measured after pumping. In addition, 64 data points from previous publications and a recommended limit are included to show the typical relationship between the SAM Number and Durability Factor for non-pumped samples [5-7]. The previous work used the same cement, fly ash, coarse aggregate, and fine aggregate. Figure 11 shows a large difference in freeze thaw performance between the SAM Number measured after pumping and the previously published data set. The previously investigated data points were not pumped and this could explain the large difference in performance. This will be discussed later in this document.

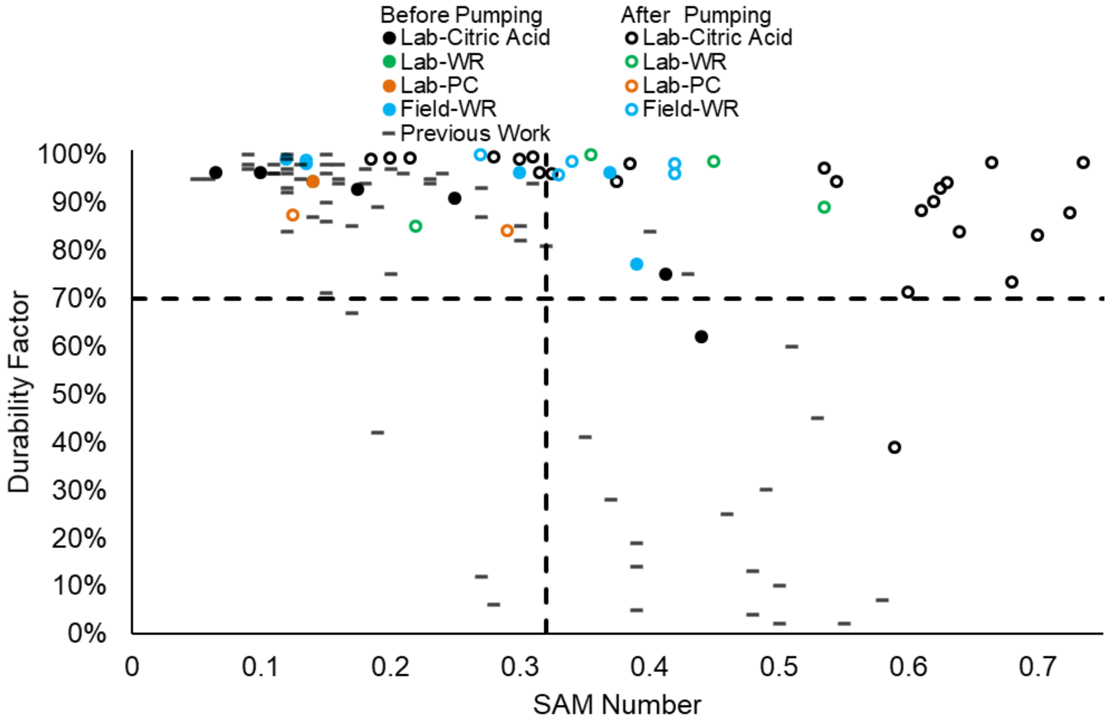

Fig. 18. Plot of SAM Number versus Durability Factor

It was important to recognize that all samples that had an air content > 4% and a SAM Number < 0.32 *prior to pumping* showed satisfactory freeze thaw performance *after pumping*, regardless of the number of cycles through the pump, change in air content, or change in SAM Number due to pumping. For example, 33 samples evaluated with ASTM C666 freeze-thaw had a satisfactory air volume and SAM Number prior to pumping. After pumping 22 of these samples did not have a satisfactory air volume and SAM Number. Regardless, all 33 samples showed satisfactory freeze thaw performance. *This indicates the air void system measured after pumping was not representative of what is present in the hardened concrete.*

3.5 Hardened Air Void Analysis Results

Figure 12 shows a plot of the spacing factor before pumping versus the spacing factor after one pumping cycle for laboratory and field samples. Also shown on the graph is a line of equality and lines representing the accepted coefficient of variation for the hardened air void analysis. Just over 80% of the samples fall within the accepted coefficient of variation. This suggests pumping did not significantly change the spacing factor of the hardened concrete samples.

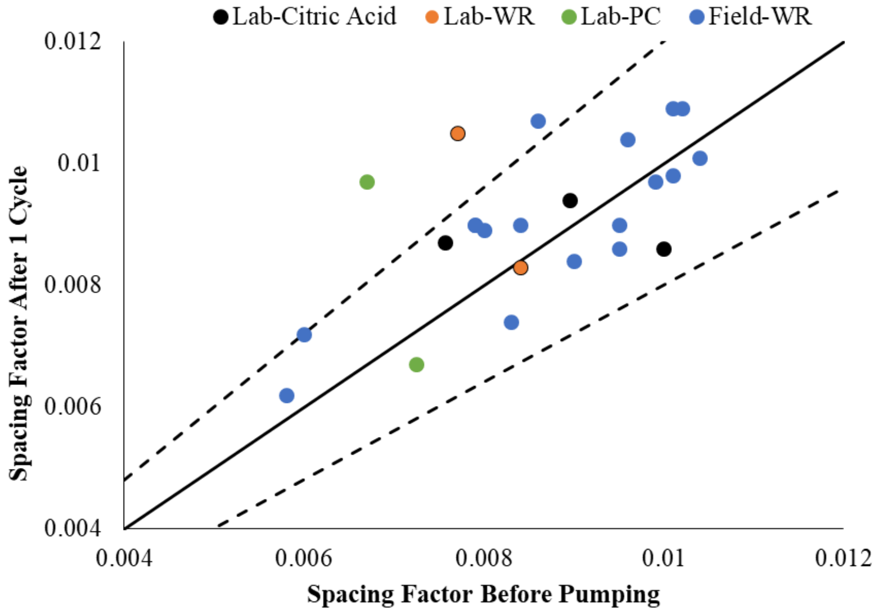

Fig. 12. Plot of spacing factor before pumping versus spacing factor after 1 cycle for laboratory and field samples.

Figure 13 shows a plot of the hardened air volume divided by the fresh air volume for samples before and after pumping. A number above 100% indicates the hardened air volume was higher than the measured fresh air volume. There were 25 samples compared before pumping and 35 samples compared after pumping. The graph shows error bars from one standard deviation. The plot shows that on average, the hardened air volume matched the fresh air volume for the samples before pumping. After pumping, the hardened air content was on average 11% higher than the fresh air content. This shows that on average the hardened air content is higher than the measured fresh air content after pumping. This suggests that the air dissolved during pumping returns over time. This supports previous measurements concerning the air content recovery.

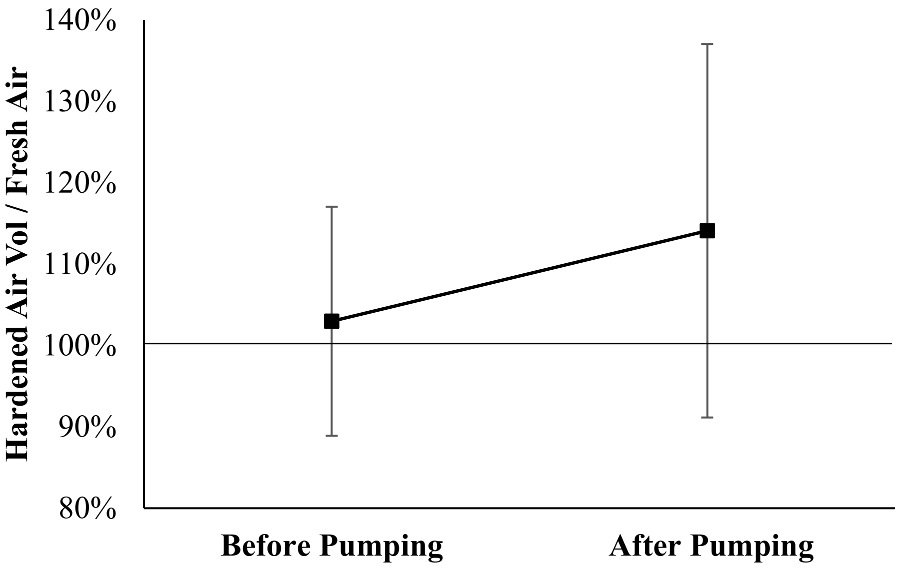

Fig. 13. Plot of hard air/fresh air for samples before pumping and after pumping.

It should be noted that this volume change is not large. For example, a concrete measured at 6% fresh air content after pumping would be expected to increase to 6.7%. Despite this small volume, the returning bubbles may be primarily smaller bubbles and so they may impact the air void spacing and SAM Number and not the volume.

3.6 Predicting Freeze-Thaw Performance for Pumped Concrete

Pumping frequently caused the air contents and SAM Numbers to change due to pumping. Based on the 16 laboratory and 18 field mixtures investigated, 67% of the mixtures showed a change in air content greater than 0.5% and 91% of mixtures showed an increase in SAM Number of 50% due to pumping.

In practice, a high quality air void system is commonly identified as having an air content above 4.0% [1] and a SAM Number below 0.32 [5]. However, these limits do not seem to apply for concrete measured immediately after pumping as these measurements did not reflect the freeze-thaw durability of the hardened concrete for the laboratory and field samples investigated in this study. Furthermore, the measurements of SAM Numbers over time suggest the air is returning to the concrete, the hardened air void analysis shows an average increase in air content of 11% compared to the fresh measurements after pumping, and there is no statistical difference for 83% of the spacing factors investigated before and after pumping.

There were 22 samples that were found to have an air volume < 4% or a SAM Number > 0.32 when sampled after pumping. Based on industry standards these samples would not be expected to be freeze-thaw durable. *However all of these samples showed satisfactory performance in freeze thaw testing.* This was observed regardless of the number of cycles through the pump, change in air content, or change in SAM number due to pumping. This freeze thaw testing combined with the hardened air void analysis and air recovery work suggests that the air returns to the concrete over time and provides a well-distributed bubble system that provides a satisfactory freeze thaw durability.

This suggests the air content and SAM Number measurements after pumping may not be reliable indicators of the freeze-thaw durability for the materials and conditions investigated. This suggests the typical construction practice of investigating the air content after pumping concrete may not reflect the actual freeze-thaw performance of the concrete. This was observed in both laboratory and field testing.

3.7 Practical Significance

Based on the 16 laboratory and 18 field mixtures investigated in this work, it appears that the air that is lost during pumping are primarily smaller bubbles. However, these bubbles appear to return to the concrete over time as a small and well-distributed bubble system with a comparable spacing factor to the concrete prior to pumping. This means that the air volume and SAM Number measurements made after pumping are not representative of what will be within the hardened concrete and should not be used to predict freeze thaw durability of concrete.

This suggests that rejecting concrete after pumping for low air content or a high SAM Number is not a good practice. Instead, it is suggested to test the concrete before it is pumped for both air volume and SAM Number. When the mixtures had an air content > 4% and a SAM Number < 0.32 before pumping, all mixtures showed satisfactory freeze thaw durability regardless of any changes in the fresh air content or SAM Number due to pumping.

4.1 CONCLUSIONS

Pumping frequently caused changes in the air void system of the fresh concrete. Regardless of the change in the air void system of the fresh concrete, the hardened air void parameters and freeze thaw performance did not show substantial change of the air void system due to pumping. Based on the investigation the following conclusions have been made:

- For mixtures containing citric acid and WR, 67% of the mixtures showed a change in the air content of more than 0.5% and 87% showed an increase in SAM Number by 50% after one cycle of pumping.
- Of the three mixtures containing PC, the air content of one mixture was changed by more than 0.5% and no mixtures showed an increase in SAM Number from a single pumping cycle.

- Mixtures that lost air and increase SAM Number from pumping showed an improvement in the SAM Number with measurements over time.
- If a mixture had and an air volume > 4% and SAM Number < 0.32 prior to pumping then the mixture showed satisfactory performance in ASTM C666 testing regardless of the change in the fresh air content or SAM Number from pumping in both the laboratory and field testing regardless of the number of cycles through the pump, the pumping pressure, or the pump configuration.
- When comparing spacing factors before and after pumping, 83% of the data showed changes that were within the variation of the test method.
- There was an average increase in the air volume of 11% from the measured fresh air volume to the hardened air volume after pumping and no difference in the fresh and hardened air volume difference prior to pumping.

These findings indicate the air volume and SAM Number measured immediately after pumping have not been representative of the hardened concrete and measurements of these parameters should not be used to reject concrete for poor freeze-thaw durability. Instead, the air volume and SAM Number of the concrete should be measured prior to pumping.

Care should be taken in extrapolating these findings as only a limited number of materials and mixture ingredients have been investigated. However, the results were consistent for both the lab and the field testing and all measurements suggest that measurement of the concrete prior to pumping was the best indicator of performance. Additional work is underway to expand these findings to a wider range of materials and pumping configurations.

REFERENCES

[1] Kosmatka SH, Wilson ML. Design and Control of Concrete Mixtures. 15th ed. Stokie, Illinois: Portland Cement Association; 2016.

[2] Powers TC, Willis T. The Air Requirement of Frost Resistant Concrete. Highway Research Board Proceedings. 1950.

[3] Scherer GW, Valenza J. Mechanisms of Frost Damage. Materials Science of Concrete, 2005. **7**(60): p. 209-246.

[4] Felice R, Freeman JM, Ley MT. Durable Concrete with Modern Air-Entraining Admixtures. Concrete International, 2014. **36**(8): p. 37-45.

[5] Ley MT, et al., Determining the Air-Void Distribution in Fresh Concrete with the Sequential Air Method. Construction and Building Materials, 2017. **150**: p. 723-737.

[6] Welchel D. Determining the Size and Spacing of Air Bubbles in Fresh Concrete. Oklahoma State University. 2014.

[7] Hall, H. Implementation of the Sequential Air Method in Laboratory and Field Studies. 2015, Oklahoma State University.

[8] Backstrom J, et al., Void Spacing as a Basis for Producing Air-Entrained Concrete. ACI Journal, 1954. **4**: p. 760-761.

[9] Mielenz R., Wolkodoff VE, Backstrom JE, Flack HL. Orgin, Evolution and Effects of the Air Void System in concrete, Part 1 - Entrained Air in Unhardened Concrete. Proceedings, American Concrete Institute, July 1958. **30**(1): p. 95-122.

[10] Elkey W, Janssen DJ, Hover KC. Concrete Pumping Effects on Entrained Air-Voids. Washington State Transortation Center. 1994.

[11] Elkey WD, Janssen DJ, Hover KC. Effects of Admixtures on Air-Void Stability of Concrete Subjected to Pressurization. in Concrete Under Severe Conditions 2. 1998.

[12] Janssen DJ, Dyer RM, Elkey WE. Effect of Pumping on Entrained Air Voids: role of pressure. in CONSEC 95 Concrete Under Severe Conditions. 1995.

[13] Hover K.C., P.R.J. Impact of Concrete Placing Method on Air Content, Air-void System Parameters, and Freeze-Thaw Durability. Transportation Research Record, 1996. **1532**: p. 1-8.

[14] NRMCA Association, CIP21 - Loss of Air Content in Pumped Concrete. NRMCA, 2005.

[15] Janssen DJ, MacDonald KA, Gardiner AJ. Effects of pumping parameters on the stability of entrained air voids. Concrete Under Severe Conditions, 2001. **2**: p. 1344-1351.

[16] Yingling J, Mullings GM, Gaynor RD. Loss of Air Content in Pumped Concrete. Concrete International, October 1992. **14**(10): p. 57-61.

[17] Seader, N. The Pumpability of Optimized Graded Aggregates, in College of Civil and Environmental Engineering. 2016, Oklahoma State University.

[18] Cook, MD. Aggregate Proportioning for Slip Formed Pavements and Flowable Concrete. 2015, Oklahoma State University.

ESTABLISHING A FREEZE-THAW PREDICTION MODEL: ELECTRICAL RESISTIVITY AND FORMATION FACTOR OF AIR-ENTRAINED CONCRETE

Chunyu Qiao, Mehdi Khanzadeh Moradllo, Hope Hall, M. Tyler Ley, and W. Jason Weiss

ABSTRACT

This paper studies the influence of the air content on the electrical resistivity and formation factor of the concrete as these measures are often used in specifications for acceptance and payment. Experimental measurements are conducted on 30 air-entrained concretes with three water-to-cement ratios (w/c=0.40, 0.45 and 0.50) over a large range of air contents (2.5 % - 9.0 %). The porosity of the concrete is measured, which is comparable to the theoretical estimation from the Powers-Brownyard model. Electrical resistivity measurements are performed on saturated concrete samples, and samples submerged in simulated pore solutions. The samples submerged in a bucket of simulated pore solution achieve a degree of saturation that relates to the filling of matrix pores, (i.e., the Nick Point). The degree of saturation at the Nick Point (S_{NK}) decreases as the air content increases. A formation factor (F_{SAT}) is calculated for the saturated concrete, as well as the apparent formation factor (F_{SK}) for the samples submerged which reach Nick Point saturation (S_{NK}) in the simulated pore solution. As the air content increases, F_{SAT} decreases due to the increased porosity (air voids) that are filled with conductive fluid, while F_{NK} is independent on the air content (as the air voids are filled with nonconductive air). As the w/c increases, both F_{SAT} and F_{NK} decrease due to the increased porosity and connectivity. For the concrete with the same w/c, the addition of a high-range water reducing admixture (HRWRA) results in higher values of F_{SAT} and F_{NK} due to the refined microstructure in mixtures containing HRWRA. A saturation

function is used to provide a powerful tool in quality control to back calculate F_{SAT} that relates to different transport properties.

INTRODUCTION

Air entrainment has been widely used to improve the performance of concrete against freeze and thaw damage[1]. The air void system in air-entrained concrete is described by the air content and the average spacing of the air voids. ACI 201 committee recommends the air content of concrete in the range of 3 % - 7 %, which depends on the size and type of aggregates and the severity of freeze thaw cycles[2]. Moreover, previous studies suggest to provide a system that can perform well under freeze and thaw cycling requires the concrete has a spacing factor for the air voids with a typical value that is less than 200-250 μm (7.87×10^{-3}-9.84×10^{-3} in.)[3, 4].

The work by Maclnnis[5] and Fagerlund[6, 7] revealed that freeze-thaw damage depends on the degree of saturation in the concrete. They proposed a critical degree of saturation (S_{CR}) below which freeze-thaw cycles would not cause damage to the concrete. A two-stage sorptivity based model has been established to predict the time to reach S_{CR}[8, 9]. The initial absorption represents the process that water is drawn into gel and capillary pores due to the capillary suction[10]. The completion of the initial absorption usually occurs within days[11], and it is defined as the Nick Point with a degree of saturation denoted as S_{NK}. The secondary absorption represents the process that water is transported into the air voids due to moisture diffusion[12]. The service life of the concrete under freeze-thaw damage is primarily determined by the time to fill the air voids from S_{NK} to S_{CR} [6, 11, 13]. Thus, it is important to clarify the influence of the air content and air void distribution on the value of S_{NK}, which helps incorporate the air content to the sorptivity based service life model.

In general, air voids are considered as isolated inclusions in the matrix due to the large size of air voids ($10 – 10^3$ μm [3.94×10^{-4}-3.94×10^{-2} in.]) compared to the gel pores and capillary pores (10^{-3} - 1 μm [3.94×10^{-8}-3.94×10^{-5} in.]). Air voids have been shown to increase permeability and gas diffusivity of the concrete[14]. The transport properties of the concrete are related to its microstructure. The formation factor has been proposed to quantitatively describe the microstructure of the concrete (the reciprocal of the product of porosity and the connectivity of the pore network) [15] and relate to different transport properties, such as the intrinsic permeability[16, 17] and the chloride diffusion coefficient[15, 18].

Electrical resistivity measurement is increasingly being implemented in specifications and to calculate the formation factor of the concrete[19, 20]. Electrical resistivity measurements are sensitive to the conditioning of concrete which includes leaching and the degree of saturation[20, 21]. The formation factor has been historically calculated from the electrical resistivity of saturated concrete[13, 22]. However, since air voids are usually not fluid filled in practice the practice of using saturated concrete can be question. This paper suggests that an apparent formation factor may better represent the actual saturation state of the concrete and correlate to the service life[23]. This paper quantifys the influence of the air content and air void distribution on both the formation factor of saturated concrete and the apparent formation factor of partially saturated concrete.

This paper examines the influence of the air content on the concrete porosity, electrical resistivity and formation factor of the fully and partially saturated concrete. The experimentally measured porosity is compared with the theoretical calculated porosity based on the mixture proportion and Powers-Brownyard model. The degree of saturation at Nick Point (S_{NK}) is determined by an absorption test on concrete submerged in a simulated pore solution in a bucket (“bucket test”). Electrical resistivity measurements on concrete at two degrees of saturation will be used to calculate: 1) the formation factor (F_{SAT}) at full saturation, and 2) the apparent formation factor (F_{NK}) at S_{NK}. F_{SAT} and F_{NK} will be correlated using a saturation function.

RESEARCH SIGNIFICANCE

This study provides an improved understanding on the influence of the air content on the electrical resistivity and formation factor of the concrete at two important degrees of saturation. An absorption test ("bucket test") is recommended to determine the degree of saturation at Nick Point (S_{NK}), during which a concrete cylinder is submerged in a simulate pore solution. The apparent formation factor at S_{NK} is not influenced by the air content, enabling the bucket test to be more easily implemented in practice for quality control.

MATERIALS AND MIXTURES

Type I ordinary portland cement (ASTM C150-17) was used with a specific gravity of 3.15 and a Blaine fineness of 386 m^2/kg (1885 ft^2/lb). The chemistry and mineral compositions, as provided by material producers, are listed in Table 1.

Table 2 lists the 30 concrete mixtures that were prepared with three water to cement ratios (w/c = 0.40, 0.45 and 0.50) and a wide range of the air contents. The mixture proportions were adjusted to yield.

The fine aggregate was a natural river sand with a specific gravity of 2.61 and an absorption rate of 0.44 %. Two coarse aggregates were used with specific gravity of 2.75 and 2.72. The coarse aggregates were crushed limestone with an absorption of 0.73 % and a maximum size of 19.1 mm (0.75 in.). A wood rosin air entraining admixture (AEA) was used to achieve different air contents as listed in Table 2. In addition, a polycarboxylate (PC)-based high range water reducing admixture (HRWRA) was used as it has been shown to alter the air void distribution[24].

EXPERIMENTAL METHODS

POROSITY

Porosity measurement was conducted on the cylindrical specimens with a diameter of 102 ± 2 mm (4 ± 0.08 in.) and a thickness of 51 ± 1 mm (2 ± 0.04 in.) at the age of 180 days. The volume of permeable pores was determined according to ASTM C642-13 with the exception that the concrete specimens were saturated by vacuum [25], instead of being placed into boiling water. Vacuum saturation has been shown to be a comparable method of sample conditioning which enables to saturate all air voids in the specimen [25]. After the specimens were oven dried at 105 ± 2 °C (212 ± 3.6 °F), the mass was measured and then they were placed into the vacuum chamber with a vacuum level of 933 ± 266 Pa (7 ± 2 Torr) for 3 hours. Lime water was drawn into the vacuum chamber and specimens were maintained in vacuum for another hour. The specimens were kept submerged for another 20 hours after the vacuum session. The mass of the surface-dry samples and their apparent mass under water were measured to calculate the porosity.

UNIAXIAL BULK ELECTRICAL RESISTANCE

The electrical resistivity and formation factor of saturated concrete were measured on the saturated concrete specimen (102 ± 2 mm [4 ± 0.08 in.] in diameter and 51 ± 1 mm [2 ± 0.04 in.] in height) after the porosity measurement[26]. The resistance of the specimens was measured using a Giatec RCON2^{TM} resistivity meter with a frequency of 1 kHz at 23 ± 2 °C (73.4 ± 3.6 °F). Two 102 mm (4 in.) in diameter stainless steel plate electrodes were used with two pieces of sponge with a thickness of 3 mm (0.12 in.). During the test, the sponge was saturated with lime water and placed between specimens and plate electrodes to ensure the electrical connection [27]. The electrical resistivity can be calculated using the measured electrical resistance minus the resistance of two pieces of sponge.

BUCKET TEST

A simplified sorption test (bucket test) was directly performed on the demolded concrete specimens (102 ± 2 mm [4 ± 0.08 in.] in diameter and 203 ± 2 mm [8 ± 0.08 in.] in height) to determine the degree of saturation at the Nick Point (S_{NK}), the corresponding electrical resistivity and apparent formation factor.

For each mixture, two samples were submerged in a 5-gal (18.9 L) bucket containing 13.5 L (3.6 gal) simulated pore solution, which minimizes alkali leaching [28]. The samples were positioned to ensure all surfaces in contact with the liquid. The volume ratio of the sample to storage solution was chosen to be 1:8, which is large enough to ignore the influence of concrete samples on the composition of the simulated pore solution [13].

As shown in Table 3, the pore solution chemistry at the sealed condition was estimated from the pore solution resistivity calculator by the National Institute of Standards and Technology (NIST) [29]. The calculation is based on the alkali contents of the cement (Table 1) and the degree of hydration (*DOH* of 0.75, 0.80 and 0.85 is assumed for the mature concrete with w/c=0.40, 0.45 and 0.50, respectively).

The mass change and electrical resistance were periodically recorded over 91 days of submersion. After the bucket test was completed, the samples were removed from the buckets, and washed with tap water to wash off the simulated pore solution on the surface. The samples were placed in an environmental chamber at 23 ± 2 °C (73.4 ± 3.6 °F) and 50 ± 2 % RH for a week. The samples were then oven dried at 105 ± 2 °C (212 ± 3.6 °F) and weighed. Afterwards, the samples were vacuum saturated with lime water and weighed. The vacuum saturation procedure is the same as in above porosity measurement. The oven dry mass and saturation mass will be used for the calculation of S_{NK}.

RESULTS AND DISCUSSIONS

THEORETICAL CALCULATION OF POROSITY OF AIR-ENTRAINED CONCRETE

The pore space in air-entrained concrete can be considered to include three parts: i) the pores in the hydrated cementitious paste matrix (φ_{PP}); ii) the entrained and entrapped air (φ_{AIR} as listed in Table 2); and iii) the pores of aggregates (φ_{AP}) [25]. The total porosity (φ) of the air-entrained concrete can be expressed as:

$$\varphi = \varphi_{PP} + \varphi_{AIR} + \varphi_{AP} \tag{1}$$

The pores in the hydrated cementitious paste matrix can be categorized as gel pores (φ_{GP}), capillary pores (φ_{CP}) and chemical shrinkage (φ_{CS}) in Powers-Brownyard model [30]:

$$\varphi_{PP} = \varphi_{GP} + \varphi_{CP} + \varphi_{CS} \tag{2}$$

Figure 1 shows Powers-Brownyard model illustrating the pore space evolution in a cement paste as functions of the degree of hydration (DOH), which means[30]:

$$\varphi_{GP} = \phi_{PP} \cdot [0.6 \cdot (1 - x) \cdot DOH] \tag{3a}$$

$$\varphi_{CP} = \phi_{PP} \cdot [x - 1.3 \cdot (1 - x) \cdot DOH] \tag{3b}$$

$$\varphi_{CS} = \phi_{PP} \cdot [0.2 \cdot (1 - x) \cdot DOH] \tag{3c}$$

where, ϕ_{PP} and x are the volume fraction of the paste matrix and the initial porosity of the cement paste with the expressions:

$$x = \frac{V_w}{V_c + V_w} = \frac{m_w/\rho_w}{m_c/\rho_c + m_w/\rho_w} \tag{4a}$$

$$\phi_{PP} = V_c + V_w = m_c/\rho_c + m_w/\rho_w \tag{4b}$$

where, V_c/V_w, m_c/m_w, ρ_c/ρ_w are the volume (m^3 [yd^3]), mass (kg/m^3 concrete [lb/yd^3 concrete], in Table 2) and density (kg/m^3 [lb/yd^3]) of cement and water, respectively.

Assuming the pore volume of the aggregates equals the absorption capacity of the aggregate, the porosity related to aggregates (φ_{AP}) can be calculated as:

$$\varphi_{AP} = \frac{c_{FA} \cdot m_{FA} + c_{CA1} \cdot m_{CA1} + c_{CA2} \cdot m_{CA2}}{\rho_w} \tag{5}$$

where, $c_{FA}/c_{CA1}/c_{CA2}$ and $m_{FA}/m_{CA1}/m_{CA2}$ are the absorption rate and mass (kg/m^3 concrete [lb/yd^3 concrete], in Table 2) of fine aggregate, and coarse aggregates, respectively.

With the mixture proportions (in Table 2) and the assumed *DOH* in the concrete with w/c=0.40, 0.45, and 0.50 at 180 days, the total theoretical porosity is determined using Eq. 1 – Eq. 5. The theoretical and experimental data is shown in Fig. 2. There is a good correlation (within ± 10 % variation) between the theoretical values and the experimental data. However, the theoretical porosity is slightly higher than the experimental data, and the difference is approximately 1.1 - 1.3 % (which is similar to the porosity of the aggregate, φ_{AP}). This may indicate the difficulty to saturate the normal weight aggregates within the hardened concrete even at a high vacuum level (933 ± 266 Pa [7 ± 2 Torr])[31]. It appears reasonable to assume the total porosity as the sum of the paste matrix porosity and air content ($\varphi_{PP} + \varphi_{AIR}$) in the air-entrained concrete with normal weight aggregates; however, more work is needed to confirm this observation.

DETERMINATION OF DEGREE OF SATURATION AT NICK POINT (S_{NK})

The degree of saturation at Nick Point (S_{NK}) was experimentally determined using the bucket test. Figure 3 shows the two-stage absorption from the amount of absorbed water and the electrical resistivity of the concrete as functions of the square root of time from bucket test. The Nick Point occurred at Day 4 - Day 7 for the samples with varying w/c and air content, as illustrated in Fig. 3, and the degree of saturation at Nick Point (S_{NK}) can be calculated as:

$$S_{NK-B} = \frac{m_{NK} - m_{OD}}{m_{SAT} - m_{OD}} \tag{6}$$

where, m_{NK}, m_{OD} and m_{SAT} denote the mass (g [lb]) at S_{NK}, oven dry and saturation, respectively.

In theory, liquids fill all the matrix pores in the concrete (φ_{PP} in Eq. 2) during the initial absorption at S_{NK}, while all the air voids (φ_{AIR}) remain empty. As such, the theoretical value of S_{NK} can be determined using Eq. 7:

$$S_{NK-T} = \frac{\varphi_{PP}}{\varphi_{PP} + \varphi_{AIR}} = \frac{\varphi_{GP} + \varphi_{CP} + \varphi_{CS}}{\varphi_{GP} + \varphi_{CP} + \varphi_{CS} + \varphi_{AIR}} \tag{7}$$

Figure 4 shows that the measured values of S_{NK-B} from the bucket test (Eq. 6) varies in the range of 0.5-0.9, which are comparable to the theoretical values within ± 10% variation. As shown in Fig. 4, the value of S_{NK-B} decreases as the air content increases, since a greater volume of air voids needs to be filled during the secondary absorption. At a similar air content, the concrete with a higher w/c generally has a larger value of S_{NK-B} since a greater volume of matrix pores need to be filled during the initial absorption. For the same w/c concrete, the addition of HRWRA has little influence on the trend of S_{NK-B} for the air contents investigated. This indicates that S_{NK-B} is independent of the air void distribution, at a comparable air content for a given w/c.

ELECTRICAL RESISTIVITY AND FORMATION FACTOR OF SATURATED CONCRETE (*S*=100%)

Figure 5 shows the measured electrical resistivity (ρ_{SAT}, in Ω·m [Ω·in]) of the saturated air-entrained concrete from the bulk electrical resistance measurement. There is a lower value of ρ_{SAT} in the concrete with a higher air content since the larger porosity allows a higher volume of liquids to conduct electricity. As the w/c increases, the value of ρ_{SAT} decreases due to the coarser microstructure. As shown in Fig. 5, the addition of HRWRA results in a higher value of ρ_{SAT}. This can be expected to relate to that PC superplasticizer can refine the microstructure[32, 33]. The increased variation in ρ_{SAT} of the concrete with HRWRA may the result of the coarsened air void distribution by HRWRA[24].

As a microstructural descriptor, a formation factor (F_{SAT}) is defined as the ratio of the electrical resistivity ρ_{SAT} of the saturated concrete to that of the pore solution[15]:

$$F_{SAT} = \frac{\rho_{SAT}}{\rho_{ps-SAT}} = \frac{1}{\varphi \cdot \beta} \tag{8}$$

where, $\rho_{ps\text{-}SAT}$ is the electrical resistivity (Ω·m [Ω·in]) of the pore solution, and β is the connectivity of the pore network. The value of $\rho_{ps\text{-}SAT}$ needs to be determined to calculate F_{SAT} using Eq. 8.

In practice, the pore solution of air-entrained concrete usually only exist in the matrix pores, while leaving the air voids empty. However, when an oven dried air-entrained concrete sample is vacuum saturated with lime water, the air voids can also be saturated[25]. Thus, the ions of the original pore solution transport into the liquids in air voids until a uniform composition is reached. The new pore solution at equilibrium can be considered as a diluted solution from the original pore solution.

The dilution factor is the ratio of total porosity (φ) to the matrix porosity (φ_{PP}). As a first approximation, $\rho_{ps\text{-}SAT}$ can be calculated using Eq. 9:

$$\rho_{ps-SAT} = \rho_{ps-original} \cdot \frac{\varphi_{PP}}{\varphi} = \frac{\rho_{ps-original}}{S_{NK-B}} \quad (9)$$

where, $\rho_{ps\text{-}original}$ is the electrical resistivity (Ω·m [Ω·in]) of the original pore solution.

Considering the small amounts of HRWRA (in Table 2) with the majority bound in hydration products, its addition is assumed to have little influence on the pore solution resistivity. As such, the NIST online pore solution resistivity calculator[29] is used to quantify $\rho_{ps\text{-}original}$ with values of 0.133 (5.236), 0.154 (6.063) and 0.173 (6.811) Ω·m (Ω·in) for the concrete with w/c = 0.40, 0.45, and 0.50, respectively. With Eq. 8 – 9, the values of F_{SAT} can be calculated, as plotted in Fig. 6. As the air content increases, the value of F_{SAT} linearly decreases due to the increased porosity. As the w/c increases, F_{SAT} decreases due to the increased porosity and pore connectivity. For the same w/c concrete, the addition of HRWRA leads to a higher value of F_{SAT} (in Fig. 6b). This is related to the refined microstructure by adding HRWRA[32, 33].

ELECTRICAL RESISTIVITY AND APPARENT FORMATION FACTOR OF PARTIALLY-SATURATED CONCRETE (S=S_{NK})

As shown in Fig. 3, the concrete electrical resistivity dramatically decreases during the initial absorption of the bucket test. Then the concrete electrical resistivity only changed slightly over time during the secondary absorption stage. The measured electrical resistivity at Nick Point (ρ_{NK}, in Ω·m [Ω·in]) is obtained from the bucket test, and it is plotted in Fig. 7.

The empty air voids in the concrete at the Nick Point results in the higher value of ρ_{NK} (in Fig. 7), compared to that of ρ_{SAT} (in Fig. 5). As the w/c increases, the value of ρ_{NK} decreases due to the increased connectivity and porosity of the concrete. For the same w/c concrete, the refined microstructure by adding HRWRA[32, 33] leads to a higher value of ρ_{NK}, as shown in Fig. 7b. The significant difference between ρ_{SAT} (in Fig. 5) and ρ_{NK} (in Fig. 7) is that the value of ρ_{NK} is independent of the air content of the concrete. The independence of ρ_{NK} on the air content is expected since the pore solution at S_{NK} only occupies the matrix pores which are similar in volume and microstructure in the same group of concrete.

Similar to definition of F in Eq. 8, an apparent formation factor (F_{NK}) is defined as the ratio of the concrete electrical resistivity at Nick Point to the pore solution resistivity:

$$F_{NK} = \frac{\rho_{NK}}{\rho_{ps-NK}} \tag{10}$$

where, ρ_{ps-NK} is the electrical resistivity (Ω·m [Ω·in]) of the pore solution at S_{NK} (in Table 3). The values of F_{NK} are calculated using Eq. 10, as plotted in Fig. 8. F_{NK} has the similar trends as those discussed about ρ_{NK} (Fig. 7) and it is also independent on the air content.

THE RELATIONSHIP BETWEEN *F* AND *F_{NK}*: *F*(*S_{NK}*)

To better understand the influence of the air content on electrical resistivity, it is meaningful to relate F_{SAT} to F_{NK} via the degree of saturation. In practice, the ratio of F_{SAT} to F_{NK} is simplified as a saturation function with a form of a basic power function [20, 22]:

$$f(S_{NK}) = \frac{F_{SAT}}{F_{NK}} = S_{NK}{}^{n} \tag{11}$$

The experimental data of $f(S_{NK})$ is fitted using Eq. 11, as plotted in Fig. 9. The fitted value of exponent n is 2.97 (approximately 3), and the majority of the experimental data lies within ± 15%

variation. And the fitted n value is similar to that of 2.41 previously obtained by Barrett for plain concrete with different w/c, paste volume and air contents[22]. A similar form of saturation function has also been defined to quantify the ionic diffusion coefficient as a function of the degree of saturation (S) in partially saturated cementitious materials with an n value in the range of 3.5-6 [20, 34, 35].

The saturation function in Eq. 11 has significant implications in engineering practice. Coupled with the value of F_{NK} that can be easily obtained from the bucket test, Eq. 11 can be used to back calculate the value of F_{SAT} when vacuum saturation is not available. This provides a powerful tool in quality control to obtain F_{SAT} that relates to different transport properties by using simple test procedures and equipment that should be widely available. This in turn can make it easier for these methods to implement in practice.

CONCLUSIONS

This paper reports porosity and electrical resistivity measurements for the concrete made with three w/c over a wide range of air contents (2.5 % to 9.0 %) with and without HRWRA. Electrical resistivity measurements were performed at two important moisture states and were used to calculate: i) the formation factor (F_{SAT}) at full saturation, and ii) the apparent formation factor (F_{NK}) at matrix saturation. Matrix saturation, also known as the Nick Point, were obtained using concrete submerged in a simulated pore solution after a specific period.

The theoretical porosity of the air-entrained concrete can be estimated based on the mixture proportions and Powers-Brownyard model. The theoretical porosity was found to be comparable to the experimental data.

The degree of saturation at the Nick Point (S_{NK}) decreases as the air content increases. The experimentally measured values of S_{NK} is comparable to the theoretical values (i.e., ± 10 % variation).

As the air content increases, the formation factor F_{SAT} of saturated concrete decreases due to a higher volume of fluid filled air voids that conducts electricity. As the w/c increases, F_{SAT} decreases due to the increased matrix porosity and connectivity. The addition of HRWRA (at the same w/c) results in a higher value of F_{SAT}, which appears to be related to the refined microstructure that reduces connectivity of the pore network.

The apparent formation factor F_{NK} of concrete at Nick Point (S_{NK}) is independent on the air content. F_{SAT} and F_{NK} can be correlated using a saturation function in a form of a power function with a fitted exponent of approximately 3.

ACKNOWLEDGEMENTS

The authors gratefully acknowledge support for this work through the pooled fund study (Project No. U1117C) managed by the Oklahoma Department of Transportation. The authors would like to thank Mr. Myo Thiha Zaw for his assistance with conducting of the experiments.

REFERENCES

1. Scherer GW, Valenza JJ, "Mechanisms of frost damage," Materails Science of Concrete, Vol VII, Skalny J, Young JF, eds., American Ceramic Scociety, 2005, pp. 209-246.

2. 201 AC, "201.2R-16 Guide to Durable Concrete," Farmington Hills, MI: 2016, pp. 84.

3. Powers TC, "Void Space as a Basis for Producing Air-Entrained Concrete," Journal Proceedings, V. 50, No. 5. 1954, pp. 741-760.

4. Hover K, "Some Recent Problems with Air-Entrained Concrete," Cement, Concrete and Aggregates, V. 11, No. 1. 1989, pp. 67-72.

5. Maclnnis C, Becaudoin JJ, "Effect of Degree of Saturation on the Frost Resistance of Mortar Mixes," ACI Journal, V. 65, No. 3. 1968, pp. 203-208.

6. Fagerlund G, "The Signifcance of Critical Degrees of Saturation at Freezing of Porous and Brittle Materials," ACI Special Publication, V. 47. 1975, pp. 13-66.

7. Fagerlund G, "The international cooperative test of the critical degree of saturation method of assessing the freeze/thaw resistance of concrete," Matériaux et Construction, V. 10, No. 4. 1977, pp. 231-253.

8. Bentz DP, Ehlen MA, Ferraris CF, Garboczi EJ, "Sorptivity-based service life predictions for concrete pavements," International Society for Concrete Pavements, Orlando, FL, 2001, pp. 181-193.

9. Fagerlund G, "A service life model for internal frost damage in concrete (Report TVBM; Vol. 3119)," Division of Building Materials, LTH, Lund University: 2004.

10. Baroghel-Bouny V, Mainguy M, Lassabatere T, Coussy O, "Characterization and identification of equilibrium and transfer moisture properties for ordinary and high-performance cementitious materials," Cement and concrete research, V. 29, No. 8. 1999, pp. 1225-1238.

11. Li W, Pour-Ghaz M, Castro J, Weiss J, "Water Absorption and Critical Degree of Saturation Relating to Freeze-Thaw Damage in Concrete Pavement Joints," Journal of Materials in Civil Engineering, V. 24, No. 3. 2012, pp. 299-307.

12. Hall C, Hoff WD, "Topics in water transport," Water Transport in Brick, Stone and Concrete, CRC Press, 2011, pp. 221-288.

13. Todak HN, "Durability assessments of concrete using electrical properties and acoustic emission testing," Purdue University, West Lafayette: 2015.

14. Wong HS, Pappas AM, Zimmerman RW, Buenfeld NR, "Effect of entrained air voids on the microstructure and mass transport properties of concrete," Cement and Concrete Research, V. 41, No. 10. 2011, pp. 1067-1077.

15. Snyder KA, "The relationship between the formation factor and the diffusion coefficient of porous materials saturated with concentrated electrolytes: theoretical and experimental considerations," Concrete Science and Engineering, V. 3, No. 12. 2001, pp. 216-224.

16. Katz AJ, Thompson AH, "Quantitative prediction of permeability in porous rock," Physical Review B, V. 34, No. 11. 1986, pp. 8179-8181.

17. Moradllo MK, Qiao C, Isgor B, Reese S, Weiss WJ, "Relating the formation factor of concrete to water absorption," ACI Materials Journal, V. Accepted. 2018.

18. Qiao C, Coyle A, Isgor B, Weiss J, "Prediction of Chloride Ingress in Saturated Concrete Using Formation Factor and Chloride Binding Isotherm," Advances in Civil Engineering Materials, V. 7, No. 1. 2018, pp. 206-220.

19. Spragg R, Qiao C, Barrett T, Weiss J, "Assessing a concrete's resistance to chloride ion ingress using the formation factor," Corrosion of Steel in Concrete Structures, Woodhead Publishing, Oxford, 2016, pp. 211-238.

20. Weiss J, Suyder K, Bullard J, Bentz D, "Using a saturation function to interpret the electrical properties of partially saturated concrete," Journal of Materials in Civil Engineering, V. 25, No. 8. 2013, pp. 1097-1106.

21. Bu Y, Weiss J, "Saturation of Air Entrained Voids and Its Implication on the Transport of Ionic Species in Concrete," Purdue University, West Lafayette, IN, United States, 2014, pp. 182-189.

22. Barrett TJ, "Improving service life of concrete structures through the use of internal curing: Impact on practice," Purdue University, West Lafayette, IN: 2015.

23. Weiss W, Barrett T, Qiao C, Todak H, "Toward a Specification for Transport Properties of Concrete Based on the Formation Factor of a Sealed Specimen," Advances in Civil Engineering Materials, V. 5, No. 1. 2016, pp. 179-194.

24. Ley MT, Welchel D, Peery J, Khatibmasjedi S, LeFlore J, "Determining the air-void distribution in fresh concrete with the Sequential Air Method," Construction and Building Materials, V. 150. 2017, pp. 723-737.

25. Bu Y, Spragg R, Weiss WJ, "Comparison of the Pore Volume in Concrete as Determined Using ASTM C642 and Vacuum Saturation," Advances in Civil Engineering Materials, V. 3, No. 1. 2014, pp. 308-315.

26. "AASHTO TP 119 Standard method of test for electrical resistivity of a concrete cylinder tested in a uniaxial resistance test," American Association of State Highway and Transportation Officials, Washiongton D.C., 2015, pp. 12.

27. Spragg RP, "The rapid assessment of transport properties of cementitious materials using electrical methods," Purdue University: 2013.

28. Spragg R, Bu Y, Snyder KA, Bentz DP, Weiss J, "Electrical testing of cement-based materials: Role of testing techniques, sample conditioning, and accelerated curing," 2013.

29. National Institute of Standards and Technology, "Estimation of pore solution conductivity," 2017. https://www.nist.gov/el/materials-and-structural-systems-division-73100/inorganic-materials-group-73103/estimation-pore.

30. Powers TC, Brownyard TL, "Studies of the physical properties of hardened portland cement paste." Chicago: Research Laboratories of the Portland Cement Association; 1948.

31. Castro J, Bentz D, Weiss J, "Effect of sample conditioning on the water absorption of concrete," Cement and Concrete Composites, V. 33, No. 8. 2011, pp. 805-813.

32. Sakai E, Kasuga T, Sugiyama T, Asaga K, Daimon M, "Influence of superplasticizers on the hydration of cement and the pore structure of hardened cement," Cement and Concrete Research, V. 36, No. 11. 2006, pp. 2049-2053.

33. Huang H, Qian C, Zhao F, Qu J, Guo J, Danzinger M, "Improvement on microstructure of concrete by polycarboxylate superplasticizer (PCE) and its influence on durability of concrete," Construction and Building Materials, V. 110. 2016, pp. 293-299.

34. Francy O, "Modelling of chloride ions ingress in partially water saturated mortars," Paul Sabatier University, Toulouse, France: 1998.

35. Olsson N, Baroghel-Bouny V, Nilsson L-O, Thiery M, "Non-saturated ion diffusion in concrete – A new approach to evaluate conductivity measurements," Cement and Concrete Composites, V. 40. 2013, pp. 40-47.

Table 1. Composition of raw materials (in % wt.)

	Type I cement
Chemical Data	
SiO_2	21.1
Al_2O_3	4.7
Fe_2O_3	2.6
CaO	62.1
MgO	2.4
SO_3	3.2
Na_2O	0.2
K_2O	0.3
Na_2O_{eq}	0.4
Loss on ignition	2.70
Bogue Phase Calculation	
C_3S	56.7
C_2S	17.8
C_3A	8.2
C_4AF	7.8

Table 2. The mixture proportion (saturated surface dry condition) of concrete (in kg/m^3 [lb/yd^3])

w/c	Mixture	Coarse aggregate 1	Coarse aggregate 2	Fine aggregate	Type I cement	Water	AEA (g/m^3) [oz/yd^3]	HRWRA (g/m^3) [oz/yd^3]	Air content (%)
0.40	M1	677.3 (1141.6)	451.5 (761.0)	762.7 (1285.6)	372.8 (628.4)	149.1 (251.3)	6.46 (0.17)	-	2.8
	M2	672.4 (1133.4)	448.3 (755.6)	757.2 (1276.3)	370.1 (623.8)	148.1 (249.6)	14.41 (0.39)	-	3.5
	M3	668.2 (1126.3)	445.5 (750.9)	752.5 (1268.4)	367.8 (619.9)	147.1 (247.9)	32.95 (0.89)	-	4.1
	M4	665.4 (1121.6)	443.6 (747.7)	749.4 (1263.2)	366.3 (617.4)	146.5 (246.9)	33.18 (0.89)	-	4.5
	M5	661.9 (1115.7)	441.3 (743.8)	745.5 (1256.6)	364.4 (614.2)	145.8 (245.8)	33.94 (0.92)	-	5.0
	M6	656.4 (1106.4)	437.6 (737.6)	739.2 (1246.0)	361.3 (609.0)	144.5 (243.6)	52.41 (1.41)	-	5.8
0.45	M1	697.3 (1175.3)	464.9 (783.6)	754.7 (1272.1)	340.5 (573.9)	153.3 (258.4)	6.66 (0.18)	-	2.5
	M2	693.7 (1169.3)	462.5 (779.6)	750.8 (1265.5)	338.8 (571.1)	152.5 (257.0)	9.82 (0.26)	-	3.0
	M3	690.2 (1163.4)	460.1 (775.5)	747.0 (1259.1)	337.0 (568.0)	151.7 (255.7)	16.28 (0.44)	-	3.5
	M4	685.2 (1154.9)	456.8 (770.0)	741.5 (1249.8)	334.6 (564.0)	150.6 (253.8)	29.61 (0.80)	-	4.2
	M5	674.4 (1136.7)	449.6 (757.8)	729.9 (1230.3)	329.3 (555.1)	148.2 (249.8)	40.93 (1.10)	-	5.7
	M6	670.1 (1129.5)	446.8 (753.1)	725.3 (1222.5)	327.2 (551.5)	147.3 (248.3)	52.66 (1.42)	-	6.3
0.50	M1	680.2 (1146.5)	453.5 (764.4)	735.7 (1240.1)	340.1 (573.3)	170.1 (286.7)	5.56 (0.15)	-	2.6
	M2	674.0 (1136.1)	449.3 (757.3)	728.9 (1228.6)	337.0 (568.0)	168.5 (284.0)	10.49 (0.28)	-	3.5
	M3	666.3 (1123.1)	444.1 (748.6)	720.6 (1214.6)	333.1 (561.5)	166.6 (280.8)	18.19 (0.49)	-	4.6
	M4	653.7 (1101.8)	435.8 (734.6)	707.0 (1191.7)	326.9 (551.0)	163.4 (275.4)	28.97 (0.78)	-	6.4
	M5	644.6 (1086.5)	429.7 (724.3)	697.2 (1175.2)	322.3 (543.3)	161.2 (271.7)	32.95 (0.89)	-	7.7
0.40	M1	671.0 (1131.0)	447.3 (753.9)	755.7 (1273.8)	369.4 (622.6)	147.8 (249.1)	14.01 (0.38)	130.11 (3.51)	3.7
	M2	662.6 (1116.8)	441.8 (744.7)	746.3 (1257.9)	364.8 (614.9)	145.9 (245.9)	19.57 (0.53)	130.01 (3.51)	4.9
	M3	660.5 (1113.3)	440.4 (742.3)	743.9 (1253.9)	363.6 (612.9)	145.4 (245.1)	23.46 (0.63)	129.29 (3.49)	5.2
	M4	651.5 (1098.1)	434.3 (732.0)	733.7 (1236.7)	358.6 (604.4)	143.5 (241.9)	27.91 (0.75)	130.21 (3.51)	6.5
	M5	648.7 (1093.4)	432.5 (729.0)	730.6 (1231.5)	357.1 (601.9)	142.8 (240.7)	31.84 (0.86)	128.65 (3.47)	6.9
0.45	M1	686.6 (1157.3)	457.7 (771.5)	743.1 (1252.5)	335.3 (565.2)	150.9 (254.4)	5.39 (0.15)	112.69 (3.04)	4.0
	M2	678.7 (1144.0)	452.5 (762.7)	734.6 (1238.2)	331.4 (558.6)	149.2 (251.5)	13.83 (0.37)	112.39 (3.03)	5.1

	M3	670.8 (1130.7)	447.2 (753.8)	726.1 (1223.9)	327.6 (552.2)	147.4 (248.5)	17.68 (0.48)	102.19 (2.76)	6.2
	M4	666.6 (1123.6)	444.4 (749.1)	721.4 (1216.0)	325.5 (548.6)	146.5 (246.9)	21.46 (0.58)	102.15 (2.75)	6.8
0.50	M1	679.5 (1145.3)	453.0 (763.6)	735.0 (1238.9)	339.8 (572.8)	169.9 (286.4)	2.69 (0.07)	51.87 (1.40)	2.7
	M2	661.4 (1114.8)	440.9 (743.2)	715.3 (1205.7)	330.7 (557.4)	165.3 (278.6)	5.94 (0.16)	51.93 (1.40)	5.3
	M3	653.0 (1100.7)	435.3 (733.7)	706.3 (1190.5)	326.5 (550.3)	163.3 (275.3)	6.64 (0.18)	52.21 (1.41)	6.5
	M4	635.5 (1071.2)	423.7 (714.2)	687.4 (1158.7)	317.8 (535.7)	158.9 (267.8)	9.09 (0.25)	51.40 (1.39)	9.0

Table 3. Chemical composition (in g/L [oz/gal]) and electrical resistivity of the simulated pore solutions for bucket test

w/c	NaOH	KOH	$Ca(OH)_2$	Resistivity (Ω・m [Ω·in])
0.40	8.4 (1.1)	11.8 (1.6)	2.0 (0.3)	0.115 (4.528)
0.45	7.6 (1.0)	10.6 (1.4)	2.0 (0.3)	0.128 (5.039)
0.50	6.8 (0.9)	9.0 (1.2)	2.0 (0.3)	0.145 (5.709)

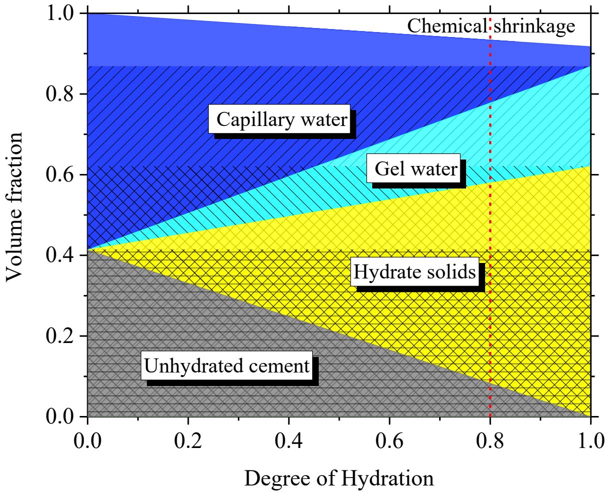

Fig. 1 Illustration of Powers-Brownyard model (w/c=0.45)

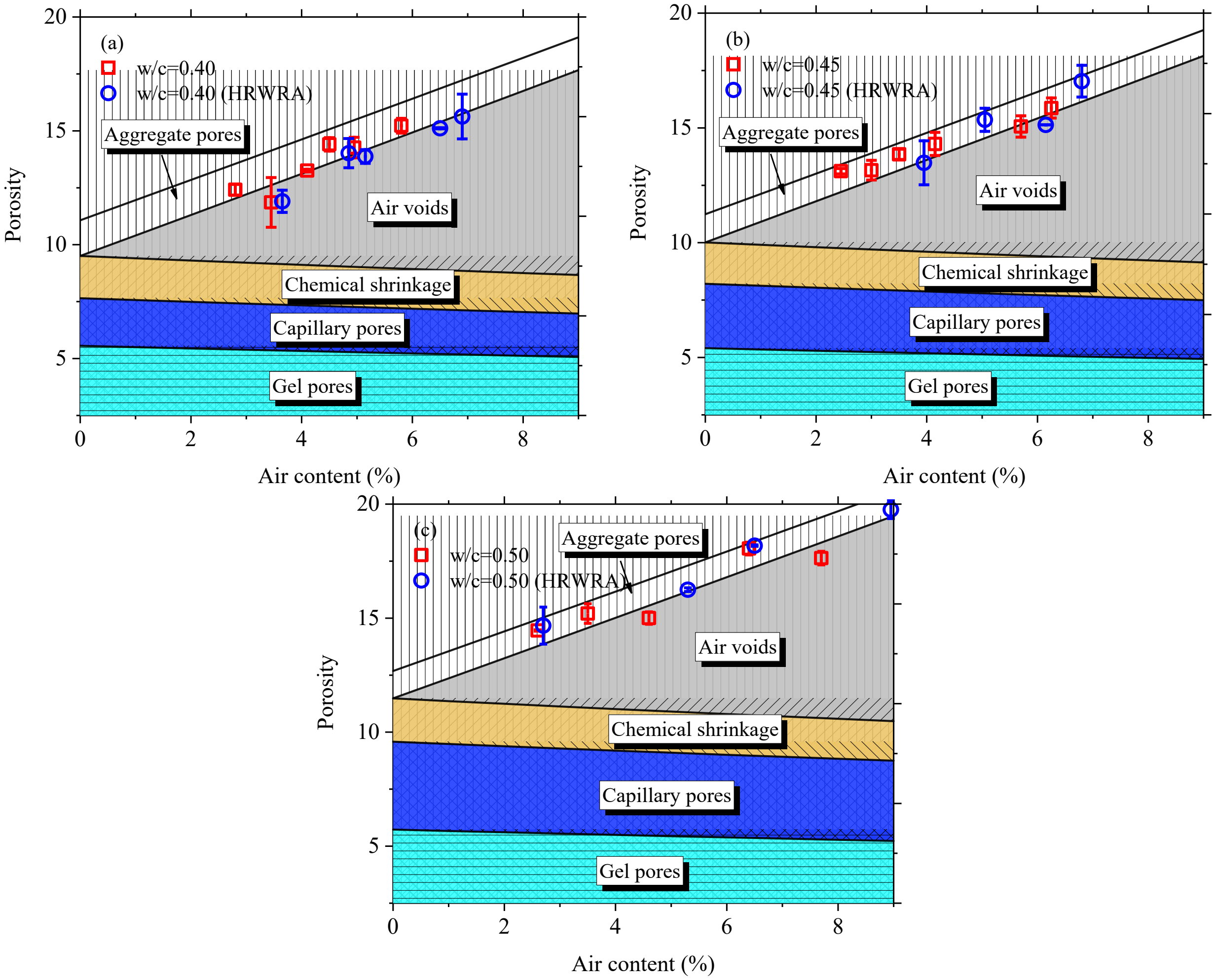

Fig. 2 The comparison of theoretical and experimentally measured porosity of the concrete with different air contents

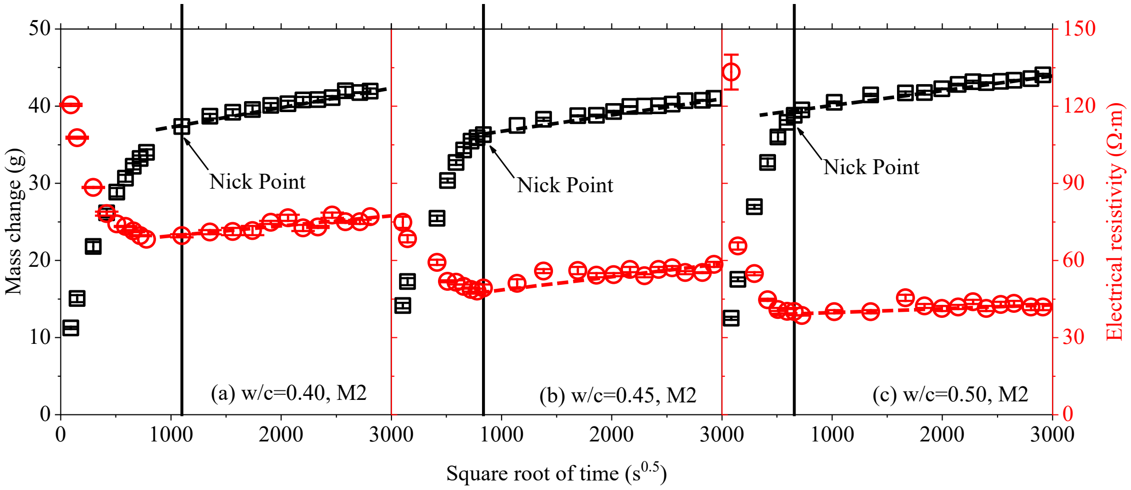

Fig. 3 Determination of S_{NK} during the 91-day bucket immersion test

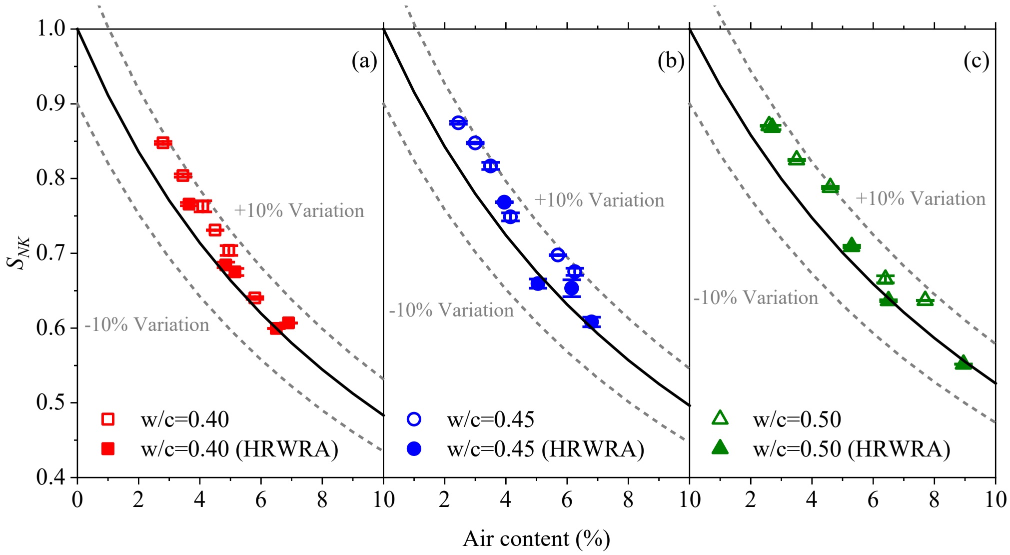

Fig. 4 The measured S_{NK-B} from bucket test (The solid lines represent the theoretical values S_{NK-T} using Eq. 7)

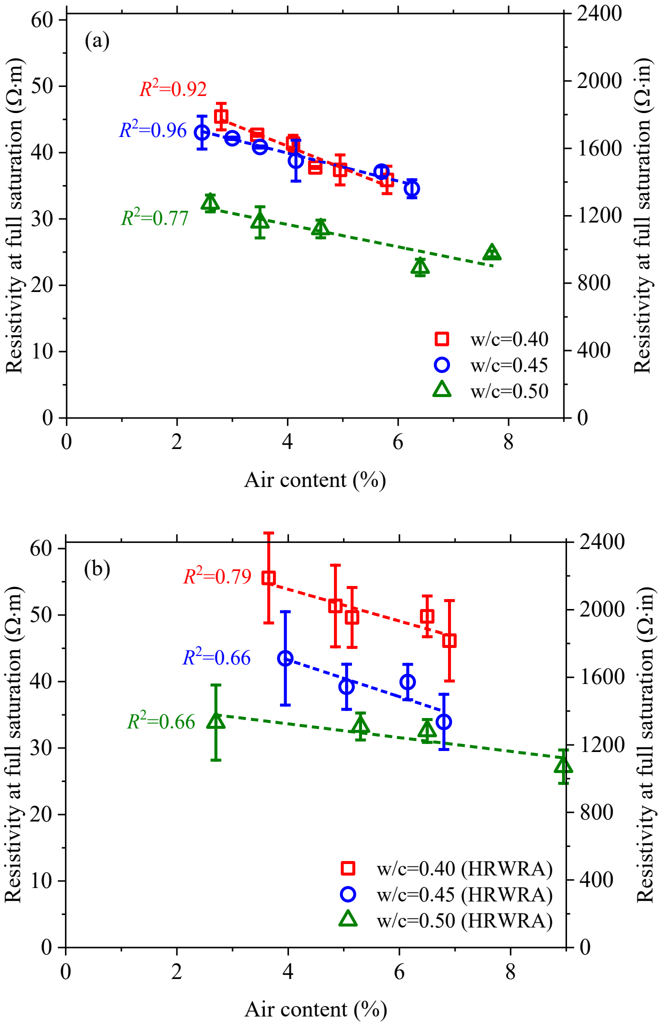

Fig. 5 Electrical resistivity ρ_{SAT} of saturated concrete (S=100%)

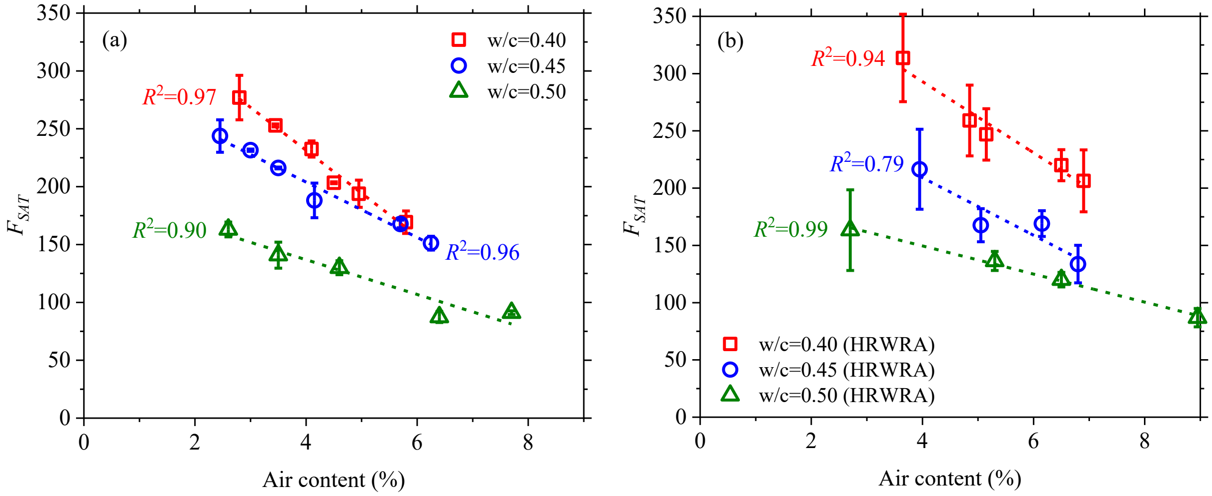

Fig. 6 Formation factor F_{SAT} of saturated concrete (S=100%) as a function of air content

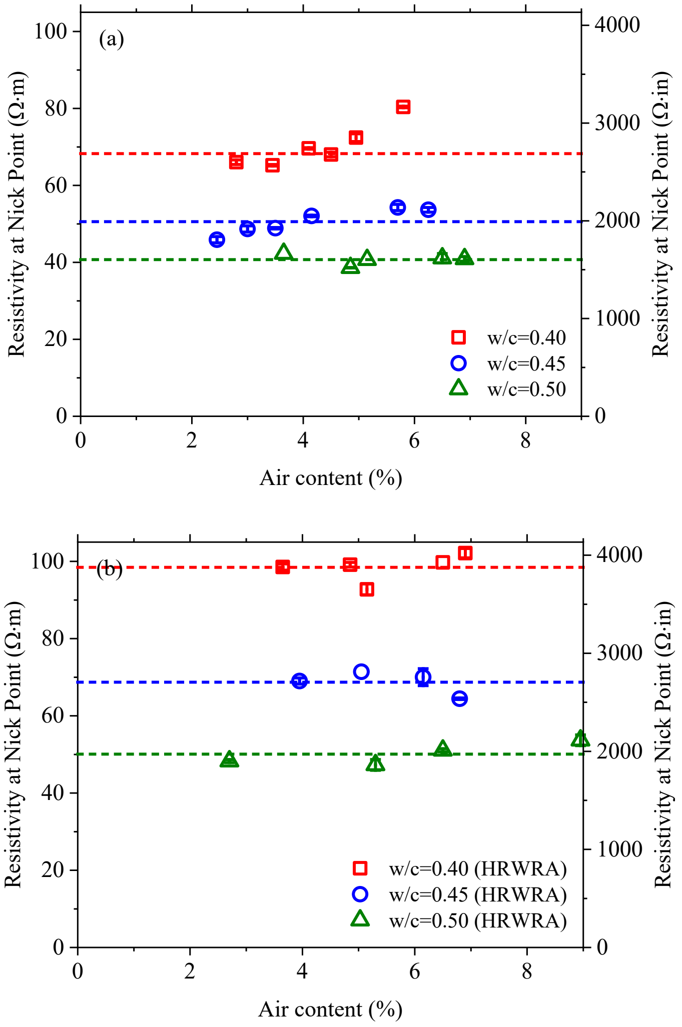

Fig. 7 Electrical resistivity of concrete with different air contents at Nick Point (S=S_{NK})

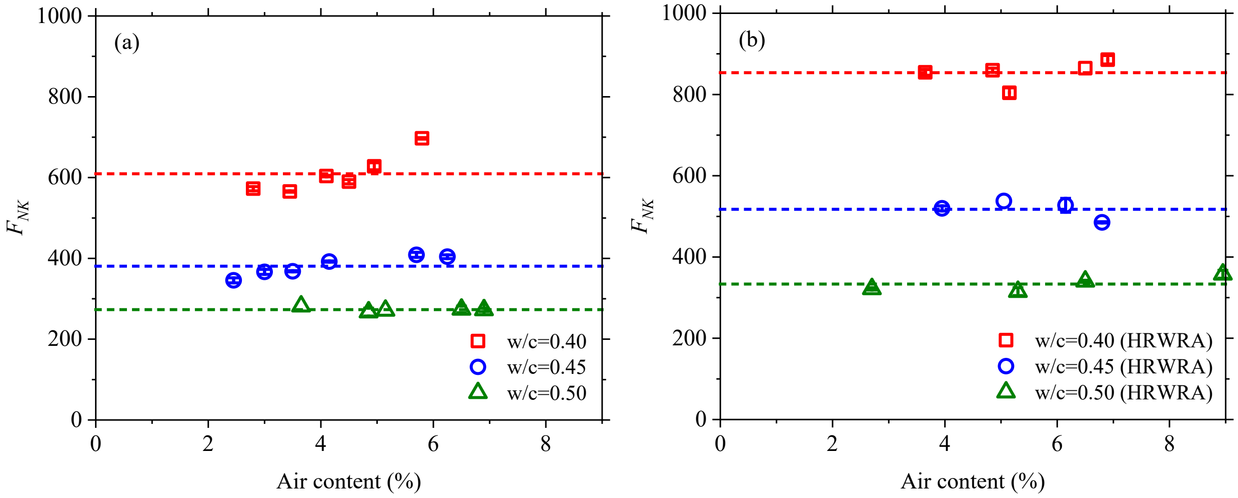

Fig. 8 The apparent formation factor F_{NK} of concrete at Nick Point (S=S_{NK})

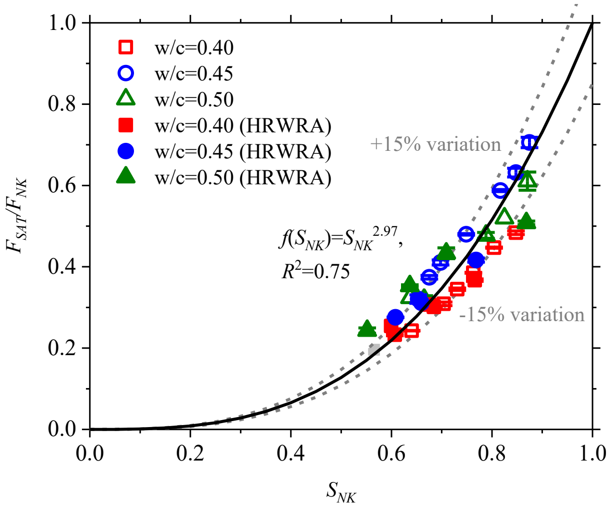

Fig. 9 The relationship between F_{SAT} and F_{NK} as a function of degree of saturation at Nick Point (S=S_{NK})

ESTABLISHING A FREEZE-THAW PREDICTION MODEL: QUANTIFYING FLUID ABSORPTION IN AIR-ENTRAINED CONCRETE USING NEUTRON RADIOGRAPHY

Mehdi Khanzadeh Moradllo, Chunyu Qiao, Mitchell Keys, Hope Hall, M. Tyler Ley, Steven Reese, and W. Jason Weiss

ABSTRACT

The absorption of fluid in concrete is often useful in the prediction of durability. Studies on the influence of entrained air voids (air content and quality) on fluid absorption in concrete are unfortunately very limited. This paper investigates fluid (water) absorption in air entrained concrete mixtures with three water-to-cement ratios (w/c = 0.40, 0.45 and 0.50) and a range of air contents (2.5% – 9.0%) with and without high range water reducer. Neutron radiography is used to measure the time-dependent depth of water penetration, water absorption, and the degree of saturation. In addition, water absorption is related to the apparent formation factor, which is determined from electrical resistivity measurements on concrete samples immersed in a simulated pore solution. Results show that the air content has a minimal impact on the rate of water absorption of the matrix. However, the air content significantly alters the degree of saturation with higher air contents having a lower degree of saturation. As the w/c decreases, the rate of water absorption is reduced due to the refined microstructure. For the given w/c, the addition of the high range water reducer has a slight reduction in the rate of water absorption. Results indicate a linear relationship between sorptivity (initial and secondary) and the reciprocal of the square root of the apparent formation factor. This relationship can provide a powerful tool in quality control to obtain the apparent formation factor.

INTRODUCTION

Concrete is susceptible to damage caused by freezing and thawing cycles in cold environments[1-6]. Air entrainment has been successfully used in concrete to improve frost resistance of concrete and extend its service life.[3, 5-9] The concept of air-entrained concrete is well established and has been used for nearly 90 years.[3, 6, 8] The entrained air voids are connected through the pore system (gel and capillary pores) of the cement paste matrix.[10, 11] Fluid absorption in air voids is a very slow process.[11-14] Entrained air lowers the degree of saturation (DoS) in concrete and delays the time to reach a critical degree of saturation (DoS_{CR}). Accordingly, the long time to reach DoS_{CR} extends the service life of concrete in cold environment.

Extensive studies have been conducted to investigate the mechanisms by which air entrainment improves the performance of concrete.[3, 6, 8] Additional studies have focused on how to specify the air void system characteristics for frost protection.[1, 3, 6, 12] However, systematic studies on the impact of entrained air voids (air content and quality) on fluid transport in concrete are very limited.[11, 15-17] This is particularly important for capillary absorption which can be linked to concrete durability.[18-20]

A study by Wong et al.[11] revealed that the entrained air voids can alter fluid and gas transport properties. This impact of entrained air voids depends on the moisture state of the air voids and the transport mechanism being considered. Entrained air voids facilitate gaseous transport (oxygen permeation and diffusion) when they are vapor filled. This was attributed to the air voids acting as conductors during gaseous transport.[11] The effect of entrained air on capillary water absorption was not consistent.[11] Van den Heede et al.[16] evaluated the influence of air entrainment on transport properties of high-volume fly ash concrete, and found no significant difference in capillary water absorption between the non-air entrained and air entrained concrete mixtures. Li et al.[12] examined the influence of entrained air content (6 – 14% by volume of mortar) on the rate of water absorption in mortar mixtures with a w/c of 0.42 preconditioned at different relative humidities (RHs). Similar water absorption was observed for mixtures with different air contents initially (absorption period less than 25 d); however, over time the specimens with higher volumes of air absorbed more water.[12] The initial and secondary absorption rates correspond to the filling of matrix pores (gel, chemical shrinkage, and capillary pores) and air voids, respectively.[21] However, more research is needed to examine the influence of air content and quality on capillary fluid absorption in modern concrete with varying mixture proportions.

The aim of the current study is to systematically investigate the influence of entrained air voids on capillary water absorption of concrete with varying water-to-cement (w/c) ratios. A high range water reducer (HRWR) was used to modify the air void size and air void distribution (i.e., air void quality). In addition, this study will relate the formation factor (derived from electrical resistivity measurement) to the water absorption in hardened concrete. This study examines whether the formation factor can provide an alternative to the water absorption test thereby saving substantial time in sample preparation and testing.[19] The formation factor was measured under a non-saturated condition (i.e., an apparent formation factor (F_{AP})) which better correlates to the actual saturation state of concrete in the field where the matrix pores are saturated and the air voids are usually empty or only partially filled with fluid.[14, 22]

This study uses neutron radiography (NR) to measure the water absorption. NR provides water content measurements with spatial information that cannot be obtained from the conventional mass measurements.[19, 23] In NR tests, a portion of neutron beam passes through the sample and a portion of the beam is attenuated. The extent of attenuation is primarily related to the neutron cross section (a term used to express the likelihood that an incident neutron will interact with the target nucleus).[23] The neutron scattering and absorption cross sections are particularly large for the first isotope of hydrogen (H-1), which composes 99.9885% of all hydrogen found in nature.[23] Therefore, NR has an advantage over other techniques in measuring the depth of water penetration, mass change from water, and DoS profiles. NR has been used to study the drying process, fluid absorption, plastic shrinkage, internal and external curing, and cracking in cementitious materials.[19, 24-29]

This study has three objectives: i) demonstrate the use of NR to quantify the time-dependent water absorption and DoS in air-entrained concrete, ii) illustrate the influence of air content and quality on water depth of penetration, water absorption, and DoS in air entrained concrete with varying w/c, iii) relate the calculated initial and secondary sorptivities based on NR to the reciprocal of the square root of the apparent formation factor.

RESEARCH SIGNIFICANCE

Studies on the influence of entrained air voids on fluid absorption in concrete are very limited. Findings of this study improve our understanding of the fluid absorption process in air entrained concrete by investigating the influence of w/c, entrained air content, and entrained air quality (spacing) on time-dependent depth of water penetration, water absorption, and the degree of saturation in concrete samples using neutron radiography. In addition, results of this study indicate a linear relationship between fluid absorption and the reciprocal of the square root of the apparent formation factor (derived from electrical resistivity measurement). This relationship can provide a powerful tool in quality control to obtain the apparent formation factor and relate it to absorption properties by using a simple immersion test rather than performing the conventional absorption tests.

EXPERIMENTAL PROGRAM

3.1. MATERIALS AND MIXTURE PROPORTIONS

Type I ordinary portland cement (ASTM C150-17) was used with a specific gravity of 3.15 and a Blaine fineness of 386 m^2/kg (1885 $ft^2/lb.$). The chemical and mineral compositions of the cement are provided in Table 1. The fine aggregate was a natural river sand with a specific gravity of 2.61, and an absorption of 0.44%. Two coarse aggregates were used with specific gravity of 2.75 and 2.72. The coarse aggregates have an absorption of 0.73% and a maximum size of 19.1 mm (0.75 in.).

Thirty concrete mixtures were prepared. The mixtures consisted of three different water to cement ratios (w/c = 0.40, 0.45, and 0.50). The mixtures contained a wide range of air contents (2.5 – 9.0%) and air void quality (air size and distribution) as measured with the Sequential Air Method (SAM) Number[30-31] (0.06 – 0.68). The admixtures used include a wood rosin air entraining admixture (AEA) and a polycarboxylate (PC)-based high range water reducing admixture (HRWR) which was added to alter the air void size and its distribution.[30-33] The mixture proportions are provided in Table 2. The mixture proportions were adjusted to yield.

The mixtures were prepared at Oklahoma State University using the procedure described in.[31] The air content and SAM Number of the freshly mixed concrete was measured according to AASHTO TP 118-17. Concrete specimens were sealed and cured in plastic cylindrical molds with inside dimensions of 102 mm [4 in.] (diameter) × 203 mm [8 in.] (height) at 23 ± 2 °C (73.4 ± 3.6 °F) for 180 days. Three cylinders of each mixture were tested for water absorption by NR.

3.2. PREPARATION AND CONDITIONING OF SAMPLES FOR NR

After 180 d of curing, samples were cut from cylindrical samples with dimensions of 30.0 mm [1.2 in.] (height) × 102.0 mm [4 in.] (diameter) using a wet saw (Fig. 1a). Prismatic slices (76.0 mm [3.0 in.] (height) × 60.0 mm [2.4 in.] (width) × 30.0 mm [1.2 in.] (thickness)) were then cut from the cylindrical slices for the NR experiment (Fig. 1b). The prismatic slices were conditioned at 50 ± 2 % RH and 25 ± 1 °C (77.0 ± 1.8 °F) to use in measuring the absorption by NR. Sample mass was measured daily until there was less than 0.01% change in mass over a 24 h period. The samples with a w/c of 0.50 and 0.45 approached mass equilibrium after approximately 60 d conditioning at 50% RH. The samples with w/c of 0.40 required ≈80 d to approach mass equilibrium at 50% RH.

3.3. EXPERIMENTAL METHODS

3.3.1. Absorption by Neutron Radiography (NR)

3.3.1.1. Method Description

After the conditioning period, the side surfaces of samples were sealed with aluminum tape, to avoid evaporation from the sample during testing. Aluminum tape was selected since it has low neutron attenuation. The bottom surface of samples was exposed to water during the absorption test. Three samples were tested for each mixture.

A water reservoir with dimensions of 25.0 mm [1.0 in.] (depth) × 60.0 mm [2.4 in.] (width) × 76.0 mm [3.0 in.] (length) was made from aluminum to conduct absorption tests, as shown in Fig. 1c. Thin (2 mm [0.08 in.]) supports were made inside the reservoir to hold sample during the test. The water level was 2 ± 1 mm (0.08 ± 0.04 in.) above the top of the supports. The water level was kept constant for all concrete samples during the tests.

The absorption experiment was conducted inside an environmental chamber positioned in the beamline (Fig. 2). The environmental chamber was maintained at 50 ± 2 % RH and a temperature of 25 ± 1 °C (77.0 ± 1.8 °F). A linear motion stage was used to move the samples into the beam (Fig. 2c). This stage re-positions the samples during imaging over the duration of the test period. Five hours (5 h) after exposure to water, the samples were moved inside a larger container in order to start the absorption experiment for the other sets of samples. Two spacers (steps) were placed under the sample to provide a water flow between the bottom of the container and the lower surface of the sample. The larger containers were also stored in the environmental chamber at 50 ± 2 % RH and 25 ± 1 °C (77.0 ± 1.8 °F). A three channel digital peristaltic pump was used to keep water level constant in large containers during the tests. The samples were monitored by NR until water reached the top surface of the sample. The samples were weighed both before and during the absorption experiment to determine the water absorption over time and compare the result with calculations based on radiographs. The samples were oven-dried at 65 ± 1 ºC (149.0 ± 1.8 °F) and vacuum saturated after the absorption test to measure the initial and time-dependent DoS in the samples.

Neutron imaging was conducted at the Neutron Radiography Facility (NRF) at Oregon State University (OSU) Radiation Center (Fig. 2a). This facility utilizes a 1.1 MW (1043 Btu/s) water-cooled research reactor. The beam within the NRF has a collimation ratio (L/D) of 115 ± 4 and a thermal neutron flux of $9.4\times10^{5} \pm 1.6\times10^{4}$ cm^{-2} s^{-1} ($6.1\times10^{6} \pm 1.0\times10^{5}$ in.$^{-2}$ s^{-1}). The NRF at OSU uses an image intensifier coupled with a light-tight right angle adapter to a charge-coupled device (CCD) camera as a neutron detection scheme. A Nikon D610 camera with 50 mm f/1.2 lens was used to capture images through the scintillator with a spatial resolution of approximately 90 μm (3.54×10^{-3} in.). The diameter of field of view (FOV) is approximately 150 mm (5.9 in.). Five radiographs of the concrete samples were taken before exposing the sample to water. The average of these radiographs was used as a reference image. Radiographs were also taken to track the water penetration over time after the sample was exposed to water. Three images of each sample were taken with an exposure time of 1 second. Radiographs were also captured from samples in the oven-dried and vacuum saturated conditions to calculate the DoS profiles. In addition, multiple images were taken from the background (detector's FOV) with open beam (flat-field image) and with closed beam (dark-field image) for the background correction. The following section describes the details of image analysis and water penetration depth, water mass, degree of saturation and sorptivity calculation from NR measurements.

3.3.1.2. Water calibration

A water attenuation coefficient (μ_W) was determined to quantify the water distribution in the samples based on the raw radiographic images. The attenuation coefficient of water was calculated by scanning the empty and water-filled stepped cells with different water thicknesses and developing a relationship between water thickness (X_w) and optical density ($OD = \ln(I_0/I_t)$) based on Eq. 1[34], as shown in Fig. 3.

$$Ln\left(\frac{I_0}{I_t}\right) = \mu_w X_w + \beta X_w^2 \tag{1}$$

where, I_0 and I_t are the average transmitted intensity on the empty and water-filled stepped cells, respectively; β is the correction parameter to empirically correct for the beam hardening and scattering effects[34, 35] and X_w is the thickness of water. The measured values of μ_W and β are summarized in Table 3.

Equation 1 is the modified version of the Beer-Lambert Law to empirically correct for beam hardening and scattering effects.[34, 35] In addition, this water calibration experiment has been conducted in front of the samples after drying them in oven at 65 ± 1 °C (149.0 ± 1.8 °F) to account for the impact from non-evaporable water and other constituents of mortar on optical density values and consequently on attenuation coefficient of water (Fig. 3).

The calculated water attenuation coefficient based on water cells in front of oven-dried samples varies from 0.0782 mm^{-1} (1.99 $in.^{-1}$) to 0.0970 mm^{-1} (2.46 $in.^{-1}$) based on mixtures tested. In addition to using the water steps, large water films were made with dimensions of 150 mm ×

150 mm (5.9 in. × 5.9 in.) and varying thicknesses (2, 3, 4, and 6 mm) to be placed in front of the entire FOV and oven-dried samples with different w/c and air content while imaging. This provides more representative results for optical density versus water thickness values and allows to verify the results based on stepped water cells for each sample.

3.3.1.3. Image processing

The images from NR were processed and analyzed with ImageJ software.[36] This process includes a background correction and calculation of intensity in the region of interest. The raw images were normalized with respect to open and closed beam images to correct for background noise based on Eq. 2.[35]

$$I_{corrected} = \frac{I_{raw\ image} - I_{dark\ field}}{I_{flat\ field} - I_{dark\ field}} \tag{2}$$

A median filter was used to combine three images of a sample to eliminate the artifacts due to the gamma rays.[28, 34] This averaging also reduces the variation in the measured intensities.[37] The average of the first three radiographs was used as a reference image. After a background correction, an average intensity profile was calculated through the sample depth for reference and time-dependent images (Fig. 4a).

The second order solution of modified Beer-Lambert Law (Eq. 1)[19, 34], as shown in Eqs. 3 and 4, was used to calculate a change in attenuation from absorbed water (absorbed water thickness) and volumetric water content (θ) at different depths of the sample (Fig. 4b).

$$X_w(mm[in.]) = -\frac{\mu_w}{2\beta} - \sqrt{\left(\frac{\mu_w}{2\beta}\right)^2 - \frac{1}{\beta} ln\left(\frac{I_t}{I_0}\right)} \tag{3}$$

$$\theta(\frac{mm^3}{mm^3}\ [\frac{in.^3}{in.^3}]) = \frac{X_w}{X_s}\frac{pixel\ area}{pixel\ area} = \frac{X_w}{X_s} \tag{4}$$

where, I_0 and I_t are the average transmitted intensity at depth d_i on the reference profile and time-dependent profile, respectively; β is the correction parameter; X_w and X_s are the thickness of water and the sample, respectively; and θ is the average volumetric water content at depth d_i.

The following steps can be taken to calculate mass change profiles and the cumulative mass change over the time based on NR measurements. This allows the calculation of the initial and secondary absorption rates (S_1 and S_2, respectively) based on the ASTM C 1585-13 definition.

The time-dependent absorbed water mass per pixel (m) can be computed over the sample depth (Fig. 4c).

$$m \ = \theta\left(A_{pixel} X_S\right) \rho_w \tag{5}$$

where, A_{pixel} is the pixel area (0.0081 mm^2 [1.26×10^{-5} $in.^2$]) and ρ_w is the density of water (0.001 g/mm^3 [62.43 $lb./ft^3$]).

The change in sample mass (Δm) (cumulative mass change) was calculated based on Eq. 6 using NR measurements (Fig. 4d).

$$\Delta m \ = \sum m \ . \ n \tag{6}$$

where, Σm is the sum of the evaporated water mass over sample depth; and n is the number of pixels in the width of the sample.

ASTM C 1585-13 identifies absorption as the change in mass divided by the product of the exposed area of the sample and density of water (Fig. 4e). This formulation is shown in Eq. 7.

$$i = \frac{\Delta m}{\rho_w \, A} \tag{7}$$

where, i is the absorption and A is the cross-sectional area of the flow (i.e., the exposed area of the sample to water).

Equations 8 and 9 were used to determine S_1 and S_2 of the samples. S_1 and S_2 are determined as the slope of the absorption versus $\sqrt{t}$ curves during the first 5 h and 1 d – 7 d, respectively (ASTM C 1585-13 definition).

$$i\left(t_{5min}^{5h}\right) = S_1\sqrt{t} \tag{8}$$

$$i\left(t_{7d}^{1d}\right) = S_2\sqrt{t} + B_1 \tag{9}$$

where, t is the time and B_1 is the regression constant.

The time-dependent DoS was calculated based on Eq. 10.

$$DoS = \frac{\Delta m_t}{m_{Sat} - m_{OD}} \times 100 + DoS_{Initial} \tag{10}$$

where, m_{sat} and m_{OD} are the mass of the saturated and oven-dried samples, respectively; and $DoS_{Initial}$ is the initial DoS of the sample before start of the absorption test.

The time-dependent water penetration depths (*d*(t)) were calculated based on volumetric water content profiles (Fig. 5) from NR where the water content reaches the 1.5x of average background water level ($\theta_{d(t)} = 1.5 \times \theta_{Average,\ Ref}$), as shown in Fig. 5b. This value was chosen so that it was statistically greater than the background water content. The water penetration depth is plotted against $\sqrt{t}$ and these curves were used to compute the initial and secondary sorptivities (S_1' and S_2', respectively) based on Eqs. 11 and 12 (Fig. 5c).[18, 19] For the regression analysis, all data points from 5 min to 5 h and from 1 d to 7 d were used to determine S_1' and S_2', respectively (Fig. 5c).

$$d\left(t_{5min}^{5h}\right) = S_1'\sqrt{t} + B_2 \tag{11}$$

$$d\left(t_{7d}^{1d}\right) = S_2'\sqrt{t} + B_3 \tag{12}$$

where, B_2 and B_3 are the regression constants.

3.3.2. Apparent formation factor from immersion test

A simplified immersion test (previously called the bucket test) was performed on the demolded concrete samples (102 mm [4 in.] (diameter) × 203 [8 in.] (height)) to determine F_{AP}.

For each mixture, two samples were submerged in a 19 L (5 gal) bucket containing 13.5 L (3.5 gal) simulated pore solution, which minimizes alkali leaching.[38, 39] The samples were positioned to ensure all surfaces in contact with the liquid (Fig. 6a). The detail on simulated pore solution design can be found in.[22]

The mass change and electrical resistance were periodically recorded over 91 days of submersion. The impedance of the specimens was measured using a resistivity meter with a frequency of 1 kHz at 23 ± 2 °C (73.4 ± 3.6 °F) according to AASHTO TP 119-17 (with the aforementioned difference in conditioning the samples). Two 102 mm (4 in.) diameter stainless steel plate electrodes were used at each end with a thin sponge placed between the concrete and the electrode. During the tests, the sponge was saturated with lime water and placed between samples and plate electrodes to ensure a good electrical connection.[40, 41] The bulk electrical resistivity can be calculated by computing the electrical resistance from measured impedance and subtracting the resistance of the two sponges on the end of the sample.

The electrical resistivity of the pore solution is required to calculate the formation factor (F) based on Eq. 13. In this study, the approach presented by Snyder et al.[42, 43] was used to estimate the electrical conductivity (the reciprocal of the electrical resistivity) of pore solution based on OH^-, K^+ and Na^+ concentrations. More details can be found in.[22]

$$F = \frac{\rho_T}{\rho_{PS}} \tag{13}$$

where, ρ_T is the measured electrical resistivity (Ω·m [Ω·in]) of the bulk concrete and ρ_{PS} is the electrical resistivity (Ω·m [Ω·in]) of the pore solution.

The immersion test shows the two-stage absorption from the amount of absorbed water as function of $\sqrt{t}$, as shown in Fig. 6b. Based on previous studies[12, 14, 22], the initial absorption from the immersion test represents the process that water is drawn into matrix pores (i.e., gel and capillary pores) and the secondary absorption represents the process that water is transported into the large entrained and entrapped air voids. Therefore, in the current study, the measured formation factor at completion point of the initial absorption is defined as apparent formation factor (F_{AP}) since the majority of air voids are empty. This point is defined as the Nick Point or matrix saturation in the literature.[14, 22] This point occurred within 4 - 7 d for the samples with varying w/c and air contents.

EXPERIMENTAL RESULTS AND DISCUSSION

4.1. TIME-DEPENDENT DEPTH OF PENETRATION

The calculated time-dependent depth of water penetration based on NR measurements for mixtures with varying w/c and air contents is presented in Fig. 7. As defined in a previous section, the slope of the depth of penetration versus $\sqrt{t}$ curves during the first 5 h and 1 d – 7 d indicate the S_1' and S_2', respectively (Fig. 5c). Figure 8 shows the S_1' and S_2' versus air content calculated based on Eqs. 11 and 12 for concrete mixtures with varying w/c.

As shown in Fig. 7, it takes longer time for water to reach the edge of the sample with the w/c of 0.40 when compared to the samples with w/c of 0.45 and 0.50 (≈ 40 d to 100 d for 0.40 samples compared to ≈ 10 d to 40 d for other mixtures). Moreover, for the samples with the same w/c, the air content has no significant impact on time-dependent water depth of penetration. This suggests that during the water absorption test, the air voids remain primarily empty.[11] In addition, it can be concluded that increasing the air content has little impact on the matrix porosity of the samples with the same w/c. However, the addition of the HRWR delays the progress of water in the samples irrespective of w/c. This can be attributed to the refined microstructure that reduces connectivity of the pore network.[15, 44] Moreover, the addition of the HRWR can modify the distribution of air voids in the matrix so that the water transport path becomes more tortuous since air voids act as non-permeable obstructions during the absorption test.

Based on Fig. 8, reducing the w/c of mixture lowers the S_1’ and S_2’ due to the refined pore structure. The S_1’ and S_2’ values are constant irrespective of the air content of the concrete for a given w/c; however, the results show variability between the samples. This is expected since the water primarily infiltrates through the matrix pores during the absorption test which are similar in volume and microstructure in the same group of concrete (i.e., similar w/c). For the given w/c, the average S_1’ and S_2’ values decreased by addition of HRWR, particularly in samples with a lower w/c (≈ 25% to 33% reduction in the samples with w/c of 0.40 and 0.45).

4.2. TIME-DEPENDENT WATER ABSORPTION BY NR

A comparison between the mass change results determined from NR (calculated based on Eq. 6) and gravimetric measurements is shown in Fig. 9. Agreement is observed between results from NR and gravimetric measurements with a correlation coefficient of 0.99.

The time-dependent cumulative water absorption was calculated (based on Eq. 7, ASTM C 1585-13 definition) as illustrated in Fig. 10. Based on Eqs. 8 and 9, the slopes of water absorption versus $\sqrt{t}$ curves from 5 min to 5 h and from 1 d to 7 d were used to determine S_1 and S_2 respectively, as shown in Fig. 11. Figure 12 shows the average S_1 and S_2 from samples with different air contents versus w/c.

As shown in Fig. 10, samples with a greater w/c absorb more water (at a given time) as compared to the samples with a lower w/c due to the increased porosity and increased connectivity of pores in concrete. The addition of HRWR reduces the amount of absorbed water at low w/c mixtures (w/c=0.40 and 0.45). This is presumable due to a refined microstructure with less flocculated cement and less entrapped air. Moreover, increasing the air content has little impact on amount of absorbed water over the time in the samples with the same w/c. The results from mass change are consistent with the findings from water depth of penetration curves.

Based on Figs. 11 and 12, S_1 and S_2 calculated from absorption curves (ASTM C 1585-13) have the similar trends as those discussed about S_1' and S_2' determined from depth of penetration curves (Fig. 8), and these parameters are also independent of the air content. The addition of HRWR lowers the mean S_1 and S_2 approximately by 25% for mixtures with the same w/c (at low w/c). As shown in Fig. 12, S_1 and S_2 show higher rate of increase (≈ 60% increase) as the w/c increases from 0.45 to 0.50, compared to the difference between samples with w/c of 0.40 and 0.45 (≈ 25% increase). This is attributed to the refined pore network and the high tortuosity of the pore structure in mixtures with w/c of less than 0.45.[45]

4.3. TIME-DEPENDENT DEGREE OF SATURATION

Figure 13 illustrates the time-dependent DoS (calculated based on Eq. 10) as a function of $\sqrt{t}$ for the mixtures with varying w/c and air contents. As shown in Fig. 13, the increased air content results in a reduction in the DoS. Increasing the air content from 2.5% to 6.2% reduces the DoS by approximately 30% when the water penetration front reaches edge of the sample, regardless of the w/c. As previously mentioned, the air voids primarily remain empty during absorption testing and make little or no contribution to the capillary water absorption of concrete. Therefore, concrete with a lower air content has a higher initial DoS (i.e., DoS_{Matrix}). By increasing the air content of the concrete, the amount of water that needs to be absorbed to reach DoS_{CR} increases. This results in an increase in the time to reach a DoS_{CR}. Concretes that take a longer time to reach a DoS_{CR} have a longer service life when exposed to freezing.[11, 12, 14] The DoS_{CR} appears to be related to the quality of the air with lower air void spacing typically having a higher DoS_{CR}.[14]

At low w/c, the samples with HRWR slightly show lower DoS at a given air content. This is because the addition of HRWR reduces the rate of water absorption (Fig. 10). At a similar air content, the concrete with a higher w/c generally has a greater DoS since a greater volume of matrix pores exist and need to be filled during the absorption.[14]

4.4. RELATING WATER ABSORPTION TO THE APPARENT FORMATION FACTOR

According to a previous study[19], a linear relationship exists between the rate of water absorption and the reciprocal of the square root of the formation factor ($\sqrt{(1/F)}$) based on both theoretical derivations and experimental measurements. Figure 14 shows S_1', S_2', S_1, and S_2 versus the apparent formation factor measured from the immersion test. Figure 14 exhibits a linear relationship between S_1', S_2', S_1, S_2 and $\sqrt{(1/F)}$. This linear relationship is insensitive to air content. These results are consistent with findings of previous study on mortar samples by Khanzadeh Moradllo et al.[19]. Based on the latter[19], the slope of S_1' versus $\sqrt{(1/F)}$ is equal to 3.04 for the mortar samples (w/c=0.35-0.60) that were conditioned at 50% RH which is similar to the slope value of 2.78 obtained in Fig 14a. This linear relationship can be used to predict S_1', S_2', S_1, and S_2 based on F_{AP} and thereby saving substantial time in sample preparation and testing. This relationship provides a powerful tool in quality control to obtain F_{AP} that relates to absorption properties by using a simple immersion test. The fluid absorption properties are key parameters in service life prediction of concrete structures subjected to freeze-thaw cycles.

CONCLUSIONS

This paper used NR to examine the influence of w/c (0.40, 0.45, and 0.50), air content (2.5 – 9%) and HRWR on the capillary water absorption of concrete. The time-dependent water depth of penetration, amount of absorbed water, and DoS with high spatial resolution (≈90 µm) were measured. The apparent formation factor was also determined using electrical resistivity measurements on concrete samples immersed in a simulated pore solution after a specific period. This study relates water absorption to the apparent formation factor. The following conclusions can be drawn:

- Samples with a lower w/c (0.40) showed a lower rate of water penetration and absorption than sample with a higher w/c due to the refined microstructure (water takes ≈ 40 d to 100 d to reach the edge of a sample prepared with w/c of 0.40 compared to a ≈ 10 d to 40 d for the other mixtures).
- The initial and secondary absorption rates are independent of air content since the air voids primarily remain empty during the first 7 day absorption.
- The addition of HRWR reduces the mean initial and secondary sorptivities and absorption rates at a given w/c, particularly at low w/c mixtures. This can be attributed to the refined microstructure that reduces connectivity of the pore network.
- The increased air content leads to a reduction in the time-dependent DoS. By increasing the air content of the concrete, the amount of water that needs to be absorbed to reach DoS_{CR} increases. This results in an increase in the time to reach a DoS_{CR} since the filling of air voids is a slow process. Therefore, concretes that take a longer time to reach a DoS_{CR} have a longer service life when exposed to freezing.
- A linear relationship exists between the initial and secondary sorptivities and the reciprocal of the square root of the apparent formation factor. This relationship is not sensitive to the air content. The apparent formation factor can be used to predict the water absorption and may serve as a replacement of the water absorption test.
- Mass change calculated from NR and gravimetric measurements show good agreement with a correlation coefficient of 0.99. This indicates that the NR technique is suitable for measuring water mass change in materials similar to the ones studied.

ACKNOWLEDGEMENTS

The authors gratefully acknowledge support for this work through the pooled fund study (Project No. U1117C) managed by the Oklahoma Department of Transportation. The authors would like to thank Mr. Myo Thiha Zaw for his assistance with conducting of the immersion experiment.

REFERENCES

1. Backstrom, J., Burrows, R., Wolkodoff, V., and Powers, T., "Void Spacing as a Basis for Producing Air-Entrained Concrete," *Journal of American Concrete Institute,* V. 49. 1954, pp. 740-61.

2. Beaudoin, J.J., and MacInnis, C., "The Mechanism of Frost Damage in Hardened Cement Paste," *Cement and Concrete Research*, V. 4, No. 2. 1974, pp. 139-47.

3. Du, L., and Folliard, K.J., "Mechanisms of Air Entrainment in Concrete," *Cement and Concrete Research*, V. 35, No. 8. 2005, pp. 1463-71.

4. Fagerlund, G., "The International Cooperative Test of the Critical Degree of Saturation Method of Assessing the Freeze/Thaw Resistance of Concrete," *Matériaux et Construction*, V. 10, No. 4. 1977, pp. 231-53.

5. Pigeon, M., Marchand, J., and Pleau, R., "Frost Resistant Concrete," *Construction and Building Materials*, V. 10, No. 5. 1996, pp. 339-48.

6. Powers, T.C., and Willis, T., "The Air Requirement of Frost Resistant Concrete," *Highway Research Board Proceedings*, V. 29, 1950, pp. 184-211, Washington, D.C.

7. Klieger, P., "Effect of Entrained Air on Strength and Durability of concrete Made with Various Maximum Sizes of Aggregate," *Proceedings of the Thirty-First Annual Meeting of the Highway Research Board*, Washington, D.C., January 15-18, 1952, V. 31, pp. 177-201.

8. Powers, T.C., and Helmuth, R., "Theory of Volume Changes in Hardened Portland-Cement Paste During Freezing," *Proceedings of the Thirty-Second Annual Meeting of the Highway Research Board*, Washington, D.C., January 13-16, 1953, V. 32, pp. 285-297.

9. Sun, Z., and Scherer, G.W., "Effect of Air Voids on Salt Scaling and Internal Freezing," *Cement and Concrete Research*, V. 40, No. 2. 2010, pp. 260-70.

10. Bu, Y., and Weiss, J., "Saturation of Air Entrained Voids and Its Implication on the Transport of Ionic Species in Concrete." *4th International Conference on the Durability of Concrete Structures*, Purdue University, West Lafayette, IN, USA, 2014, pp. 182-189.

11. Wong, H., Pappas, A., Zimmerman, R., and Buenfeld, N., "Effect of Entrained Air Voids on the Microstructure and Mass Transport Properties of Concrete," *Cement and Concrete Research*, V. 41, No. 10. 2011, pp. 1067-77.

12. Li, W., Pour-Ghaz, M., Castro, J., and Weiss, J., "Water Absorption and Critical Degree of Saturation Relating to Freeze-Thaw Damage in Concrete Pavement Joints," *Journal of Materials in Civil Engineering*, V. 24, No. 3. 2011, pp. 299-307.

13. Li, W., Pour-Ghaz, M., Trtik, P., Wyrzykowski, M., Münch, B., Lura, P., et al., "Using Neutron Radiography to Assess Water Absorption in Air Entrained Mortar," *Construction and Building Materials*, V. 110. 2016, pp. 98-105.

14. Todak, H.N., "Durability Assessments of Concrete Using Electrical Properties and Acoustic Emission Testing," MSc Thesis, Purdue University, West Lafayette, IN, 2015, 150 p.

15. Huang, H., Qian, C., Zhao, F., Qu, J., Guo, J., and Danzinger, M., "Improvement on Microstructure of Concrete by Polycarboxylate Superplasticizer (PCE) and Its Influence on Durability of Concrete," *Construction and Building Materials*, V. 110. 2016, pp. 293-9.

16. Van den Heede, P., Furniere, J., and De Belie, N., "Influence of Air Entraining Agents on Deicing Salt Scaling Resistance and Transport Properties of High-Volume Fly Ash Concrete," *Cement and Concrete Composites*, V. 37. 2013, pp. 293-303.

17. Yang, R., Gui, Q., Lemarchand, E., Fen-Chong, T., and Li, K., "Micromechanical Modeling of Transport Properties of Cement-Based Composites: Role of Interfacial Transition Zone and Air Voids," *Transport in Porous Media*, V. 110, No. 3. 2015, pp. 591-611.

18. Hall, C., and Hoff, W.D., "Water Transport in Brick, Stone and Concrete." New York: Spon Press, Taylor & Francis Group; 2002, 374 p.

19. Khanzadeh Moradllo, M., Qiao, C., Isgor, B., Reese, S., and Weiss, W.J., "Relating the Formation Factor of Concrete to Water Absorption," *ACI Materials Journal*, V. 115, No. 6, 2018, pp. 887-898.

20. Khanzadeh Moradllo, M., and Ley, M.T., "Quantitative Measurement of the Influence of Degree of Saturation on Ion Penetration in Cement Paste by Using X-ray Imaging," *Construction and Building Materials*, V. 141. 2017, pp. 113-29.

21. Lucero, C,L,, "Quantifying Moisture Transport in Cementitious Materials Using Neutron Radiography." MSc Thesis, Purdue University, West Lafayette, IN, 2015, 110 p.

22. Qiao, C., Khanzadeh Moradllo, M., Hall, H., Ley, T., and Weiss, J., "Electrical Resistivity and Formation Factor of Air Entrained Concrete," *ACI Materials Journal*. V. 116, No. 3, 2019, in press.

23. Sears, V.F., "Neutron Scattering Lengths and Cross Sections," *Neutron news*, V. 3, No. 3. 1992, pp. 26-37.

24. De Beer, F., Strydom, W., and Griesel, E., "The Drying Process of Concrete: a Neutron Radiography Study," *Applied Radiation and Isotopes*, V. 61, No. 4. 2004, pp. 617-23.

25. Kanematsu, M., Maruyama, I., Noguchi, T., Iikura, H., and Tsuchiya, N., "Quantification of Water Penetration into Concrete Through Cracks by Neutron Radiography," *Nuclear Instruments and Methods in Physics Research Section A: Accelerators, Spectrometers, Detectors and Associated Equipment,* V. 605, No. 1-2. 2009, pp. 154-8.

26. Lucero, C.L., Spragg, R.P., Bentz, D.P., Hussey, D.S., Jacobson, D.L., and Weiss, W.J., "Neutron Radiography Measurement of Salt Solution Absorption in Mortar," *ACI materials journal*, V. 114, No. 1. 2017, pp. 149-159.

27. Khanzadeh Moradllo, M., Reese, S., and Weiss, J., "Using Neutron Radiography to Quantify the Settlement of Fresh Concrete " *Advances in Civil Engineering Materials*, Vol. 8, No. 1, 2019, pp. 71-87.

28. Khanzadeh Mordallo, M., Montanari, L., Suraneni, P., Reese, S.R., and Weiss, J., "Examining Curing Efficiency Using Neutron Radiography," *Transportation Research Record: Journal of the Transportation Research Board*. V. 2672, No. 27, 2018, pp. 13-23. https://doi.org/10.1177/0361198118773571

29. Trtik, P., Münch, B., Weiss, W., Kaestner, A., Jerjen, I., Josic, L., et al., "Release of Internal Curing Water from Lightweight Aggregates in Cement Paste Investigated by Neutron and X-Ray Tomography," *Nuclear*

Instruments and Methods in Physics Research Section A: Accelerators, Spectrometers, Detectors and Associated Equipment, V. 651, No. 1. 2011, pp. 244-9.

30. Felice, R., Freeman, J.M., and Ley, M.T., "Durable Concrete with Modern Air-Entraining Admixtures," *Concrete International*, V. 36, No. 8. 2014, pp. 37-45.

31. Ley, M.T., Welchel, D., Peery, J., Khatibmasjedi, S., and LeFlore, J., "Determining the Air-Void Distribution in Fresh Concrete with the Sequential Air Method," *Construction and Building Materials*, V. 150. 2017, pp. 723-37.

32. Mielenz, R.C., and Sprouse, J.H., "High-Range Water-Reducing Admixtures; Effect on the Air-Void System in Air-Entrained and Non-Air-Entrained Concrete," Special Publication, V. 62. 1979, pp. 167-92.

33. Plante, P., Pigeon, M., and Foy, C., "The Influence of Water-Reducers on the Production and Stability of the Air Void System in Concrete," *Cement and Concrete Research*, V. 19, No. 4. 1989, pp. 621-33.

34. Hussey, D.S., Spernjak, D., Weber, A.Z., Mukundan, R., Fairweather, J., Brosha, E.L., et al., "Accurate Measurement of the Through-Plane Water Content of Proton-Exchange Membranes Using Neutron Radiography," *Journal of Applied Physics*, V. 112, No. 10. 2012, pp. 104906 (1-13).

35. Kang, M., Bilheux, H.Z., Voisin, S., Cheng, C., Perfect, E., Horita, J., et al., "Water Calibration Measurements for Neutron Radiography: Application to Water Content Quantification in Porous Media," *Nuclear Instruments and Methods in Physics Research Section A: Accelerators, Spectrometers, Detectors and Associated Equipment*, V. 708. 2013, pp. 24-31.

36. Schneider, C.A., Rasband, W.S., and Eliceiri, K.W., "NIH Image to ImageJ: 25 Years of Image Analysis," *Nature methods*, V. 9, No. 7. 2012, pp. 671-5.

37. Weiss, J., Geiker, M.R., and Hansen, K.K., "Using X-Ray Transmission/Attenuation to Quantify Fluid Absorption in Cracked Concrete," *International Journal of Materials and Structural Integrity*, V. 9, No. 1-3. 2015, pp. 3-20.

38. Spragg, R., Jones, S., Bu, Y., Lu, Y., Bentz, D., Snyder, K., et al., "Leaching of Conductive Species: Implications to Measurements of Electrical Resistivity," *Cement and Concrete Composites*, V. 79. 2017, pp. 94-105.

39. Spragg, R., Villani, C., Snyder, K., Bentz, D., Bullard, J., and Weiss, J., "Factors that Influence Electrical Resistivity Measurements in Cementitious Systems," *Transportation Research Record: Journal of the Transportation Research Board*, No. 2342. 2013, pp. 90-8.

40. Bu, Y., Spragg, R., and Weiss, W., "Comparison of the Pore Volume in Concrete as Determined Using ASTM C642 and Vacuum Saturation," *Advances in Civil Engineering Materials*, V. 3, No. 1. 2014, pp. 308-15.

41. Bu, Y., and Weiss, J., "The Influence of Alkali Content on the Electrical Resistivity and Transport Properties of Cementitious Materials," *Cement and Concrete Composites*, V. 51. 2014, pp. 49-58.

42. Snyder, K.A., "The Relationship Between the Formation Factor and the Diffusion Coefficient of Porous Materials Saturated with Concentrated Electrolytes: Theoretical and Experimental Considerations." C*oncrete Science and Engineering*, V. 3 No. 12. 2000, pp. 216-224.

43. Snyder, K.A., Feng, X., Keen, B., and Mason, T., "Estimating the Electrical Conductivity of Cement Paste Pore Solutions from OH−, K+ and Na+ Concentrations," *Cement and Concrete Research*, V. 33, No. 6. 2003, pp. 793-8.

44. Sakai, E., Kasuga, T., Sugiyama. T., Asaga, K., and Daimon, M., "Influence of Superplasticizers on the Hydration of Cement and the Pore Structure of Hardened Cement," *Cement and Concrete Research*, V. 36, No. 11. 2006, pp. 2049-53.

45. Powers, T.C., and Brownyard, T.L., "Studies of the Physical Properties of Hardened Portland Cement Paste," Book Studies of the Physical Properties of Hardened Portland Cement Paste," *Portland Cement Association,* Skokie, IL, V. 43, 1946, pp. 101-32.

Table 1. Composition of cement (in % w.t.)

	Type I cement
Chemical Data	
SiO_2	21.1
Al_2O_3	4.7
Fe_2O_3	2.6
CaO	62.1
MgO	2.4
SO_3	3.2
Na_2O	0.2
K_2O	0.3
Loss on ignition	2.70
Bogue Phase Calculation	
C_3S	56.7
C_2S	17.8
C_3A	8.2
C_4AF	7.8

Table 2. The mixture proportions (SSD) of concrete (in kg/m^{3} *)

w/c	Mixture	Coarse aggregate 1	Coarse aggregate 2	Fine aggregate	Cement	Water	AEA (g/m^3)	HRWR (g/m^3)	Air content (%)	SAM Number
0.40	M1	677.3	451.5	762.7	372.8	149.1	6.46	-	2.8	0.48
	M2	672.4	448.3	757.2	370.1	148.1	14.41	-	3.5	0.28
	M3	668.2	445.5	752.5	367.8	147.1	32.95	-	4.1	0.20
	M4	665.4	443.6	749.4	366.3	146.5	33.18	-	4.5	0.13
	M5	661.9	441.3	745.5	364.4	145.8	33.94	-	5.0	0.11
	M6	656.4	437.6	739.2	361.3	144.5	52.41	-	5.8	0.10
0.45	M1	697.3	464.9	754.7	340.5	153.3	6.66	-	2.5	0.56
	M2	693.7	462.5	750.8	338.8	152.5	9.82	-	3.0	0.68
	M3	690.2	460.1	747.0	337.0	151.7	16.28	-	3.5	0.33
	M4	685.2	456.8	741.5	334.6	150.6	29.61	-	4.2	0.20
	M5	674.4	449.6	729.9	329.3	148.2	40.93	-	5.7	0.11
	M6	670.1	446.8	725.3	327.2	147.3	52.66	-	6.3	0.11
0.50	M1	680.2	453.5	735.7	340.1	170.1	5.56	-	2.6	0.44
	M2	674.0	449.3	728.9	337.0	168.5	10.49	-	3.5	0.47
	M3	666.3	444.1	720.6	333.1	166.6	18.19	-	4.6	0.19
	M4	653.7	435.8	707.0	326.9	163.4	28.97	-	6.4	0.16
	M5	644.6	429.7	697.2	322.3	161.2	32.95	-	7.7	0.09
0.40	M1	671.0	447.3	755.7	369.4	147.8	14.01	130.11	3.7	0.50
	M2	662.6	441.8	746.3	364.8	145.9	19.57	130.01	4.9	0.39
	M3	660.5	440.4	743.9	363.6	145.4	23.46	129.29	5.2	0.32
	M4	651.5	434.3	733.7	358.6	143.5	27.91	130.21	6.5	0.12
	M5	648.7	432.5	730.6	357.1	142.8	31.84	128.65	6.9	0.13
0.45	M1	686.6	457.7	743.1	335.3	150.9	5.39	112.69	4.0	0.44
	M2	678.7	452.5	734.6	331.4	149.2	13.83	112.39	5.1	0.30
	M3	670.8	447.2	726.1	327.6	147.4	17.68	102.19	6.2	0.21
	M4	666.6	444.4	721.4	325.5	146.5	21.46	102.15	6.8	0.10
0.50	M1	679.5	453.0	735.0	339.8	169.9	2.69	51.87	2.7	0.34
	M2	661.4	440.9	715.3	330.7	165.3	5.94	51.93	5.3	0.33
	M3	653.0	435.3	706.3	326.5	163.3	6.64	52.21	6.5	0.15
	M4	635.5	423.7	687.4	317.8	158.9	9.09	51.40	9.0	0.06

*The conversion factor from kg/m^3 to lb/yd^3 is 1.6855.

Table 3. The water attenuation coefficient and the correction parameter measured in front of oven-dried samples

w/c	Mixture	Air content (%)	μ_w (mm^{-1})	β (mm^{-2})
0.40	M1	2.8	0.0830	-0.0031
	M2	3.5	0.0782	-0.0024
	M3	4.1	0.0838	-0.0031
	M4	4.5	0.0972	-0.0043
	M5	5.0	0.0879	-0.0034
	M6	5.8	0.0868	-0.0030
0.45	M1	2.5	0.0896	-0.0036
	M2	3.0	0.0956	-0.0041
	M3	3.5	0.0906	-0.0034
	M4	4.2	0.0874	-0.0032
	M5	5.7	0.0950	-0.0037
	M6	6.3	0.0962	-0.0043
0.50	M1	2.6	0.0823	-0.0030
	M2	3.5	0.0941	-0.0039
	M3	4.6	0.0951	-0.0039
	M4	6.4	0.0841	-0.0028
	M5	7.7	0.0936	-0.0036
0.40 – HRWR	M1	3.7	0.0893	-0.0035
	M2	4.9	0.0786	-0.0026
	M3	5.2	0.0801	-0.0031
	M4	6.5	0.0807	-0.0028
	M5	6.9	0.0806	-0.0028
0.45 – HRWR	M1	4.0	0.0818	-0.0023
	M2	5.1	0.0935	-0.0041
	M3	6.2	0.0827	-0.0026
	M4	6.8	0.0923	-0.0041
0.50 – HRWR	M1	2.7	0.0925	-0.0037
	M2	5.3	0.0816	-0.0027
	M3	6.5	0.0877	-0.0033
	M4	9.0	0.0970	-0.0043

[*] The conversion factor from mm^{-1} to $in.^{-1}$ is 25.4.

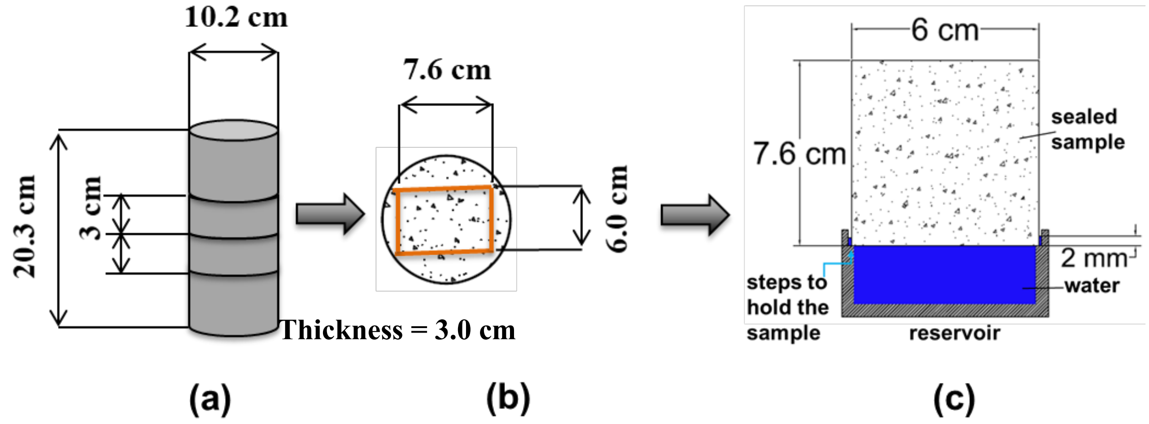

Fig. 1 – Preparation and testing of the samples for absorption by NR: (a) cutting 3.0 cm thick slices from concrete cylinders (b) cutting 7.6 × 6.0 × 3.0 cm prismatic samples from slices (c) a schematic of absorption set up.

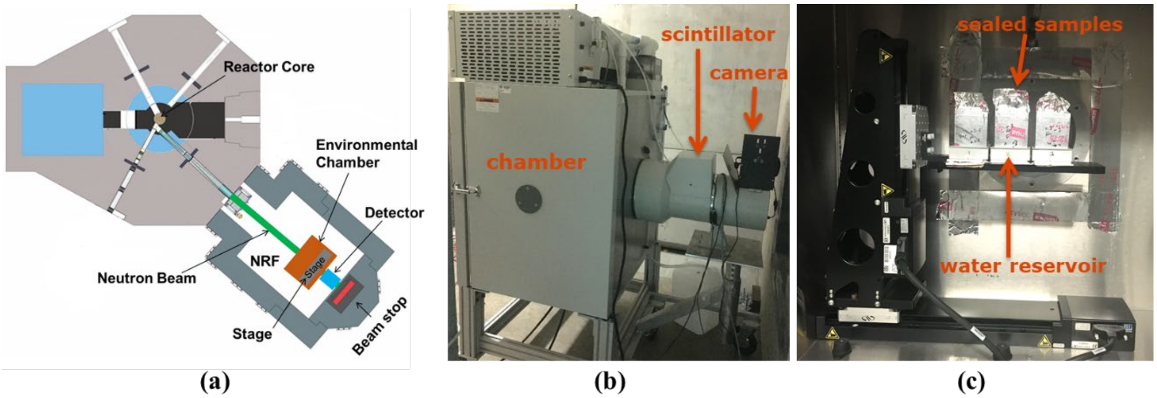

***Fig. 2** – NR experimental set up: (a) plan view of NRF at OSU (adopted from https://radiationcenter.oregonstate.edu/oregon-state-triga-reactor-0) (b) chamber with scintillator at the back (neutron beam is parallel to the scintillator) (c) translating stage inside the chamber.*

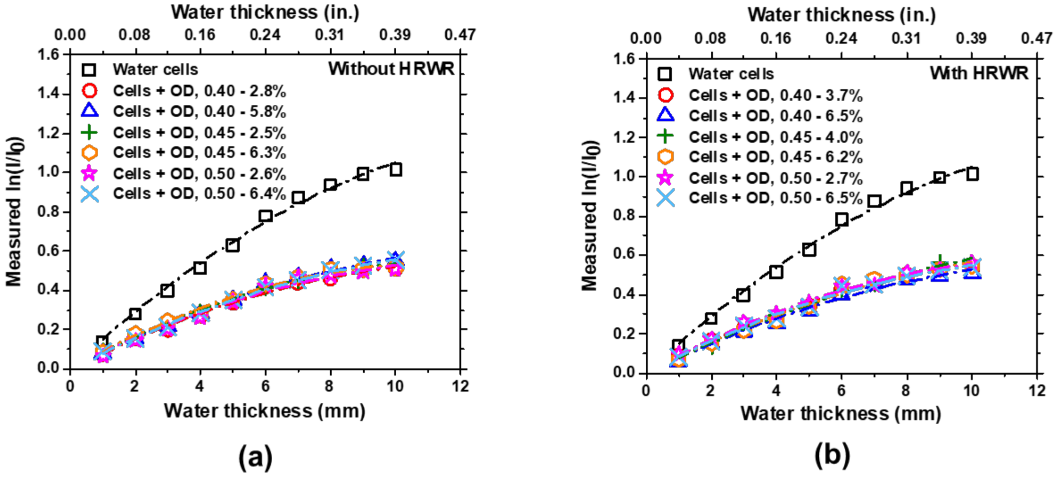

Fig. 3 *– Optical density versus water thickness for the samples with varying w/c and air content: (a) without HRWR and (b) with HRWR.*

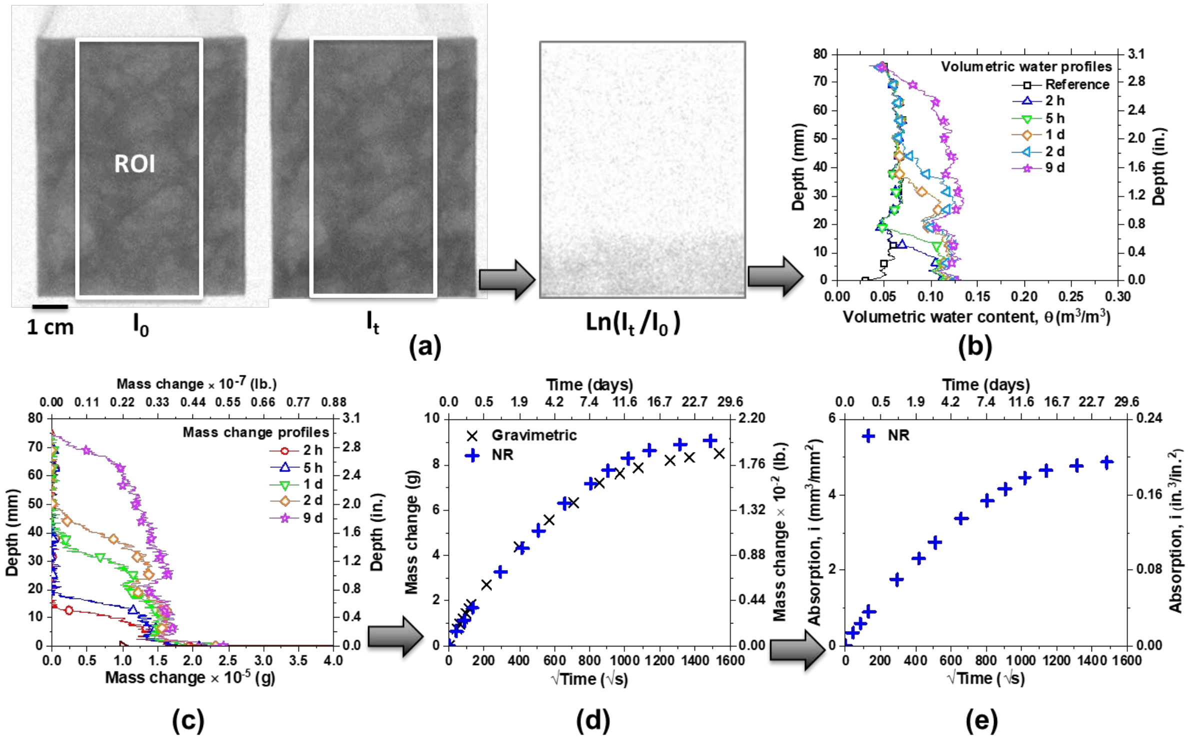

***Fig. 4** – An example of: (a) background corrected images from NR and a normalized image based on the reference radiograph (b) determining volumetric water content profile from NR, (c) determining mass change profile from NR, (d) determining cumulative mass change curve based on time-dependent mass change profiles, and (e) calculating absorption curve from NR results based on ASTM C 1585-13 definition. (Note: ROI=Region of Interest)*

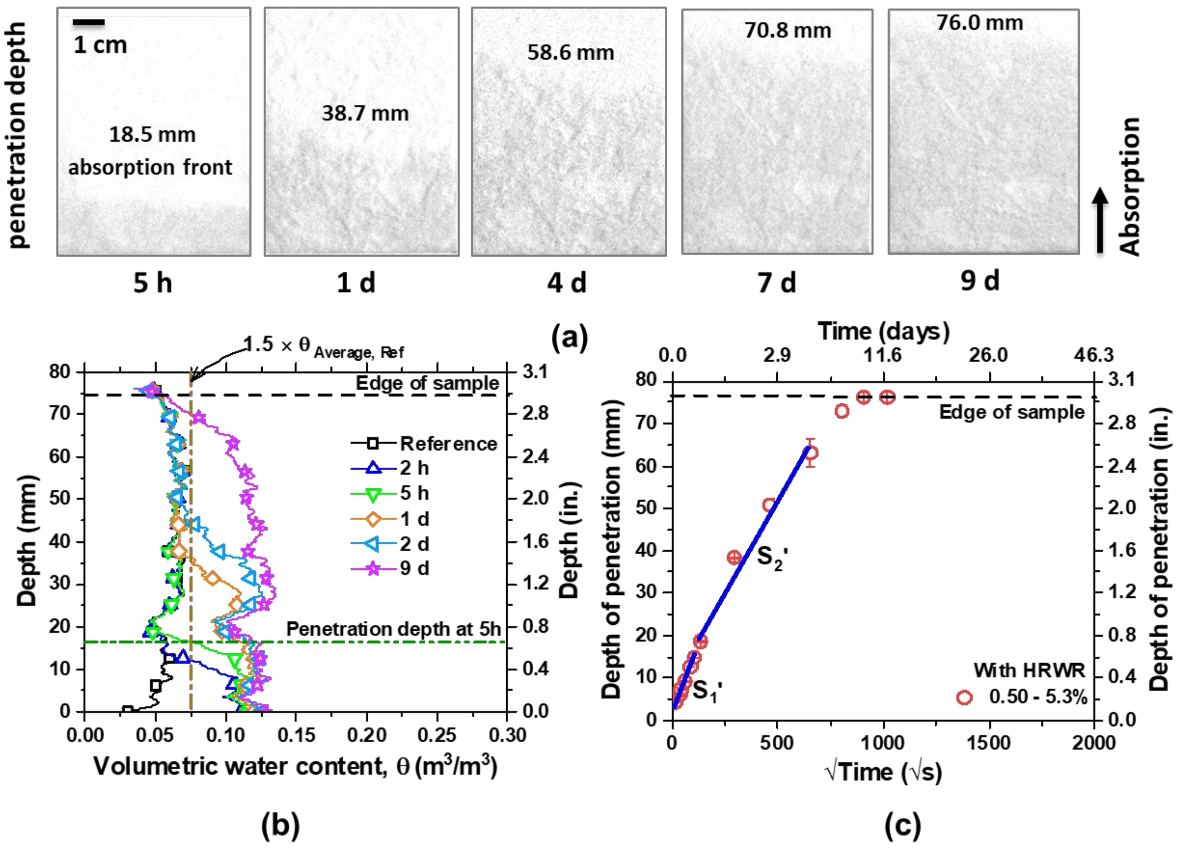

Fig. 5 *– An example of: (a) time-dependent depth of penetration images from NR (b) determining water depth of penetration based on θ profiles, and (c) time-dependent water depth of penetration.*

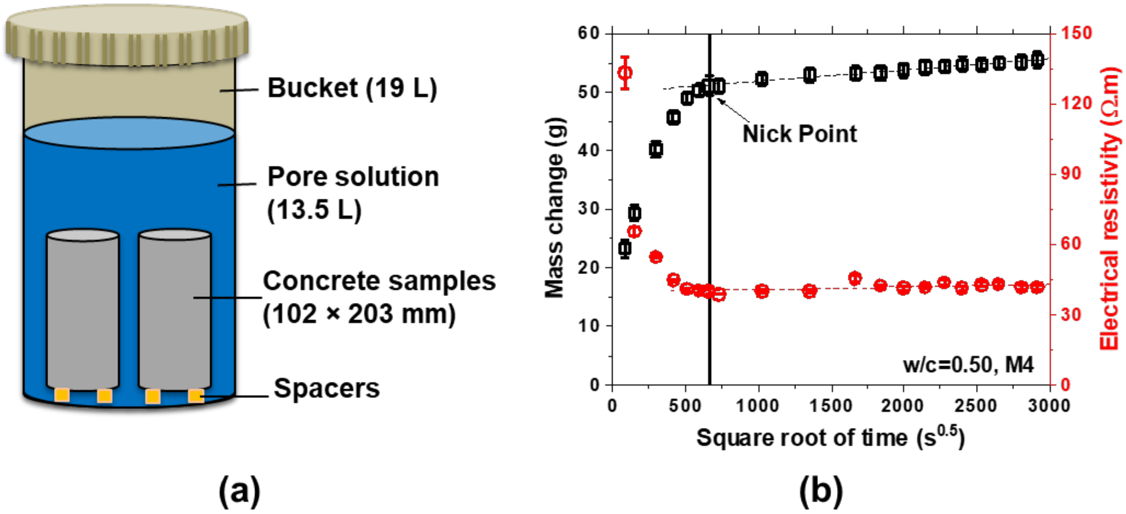

***Fig. 6** – (a) A schematic of the immersion test setup and (b) an example of time-dependent mass change and electrical resistivity values from the immersion test.*

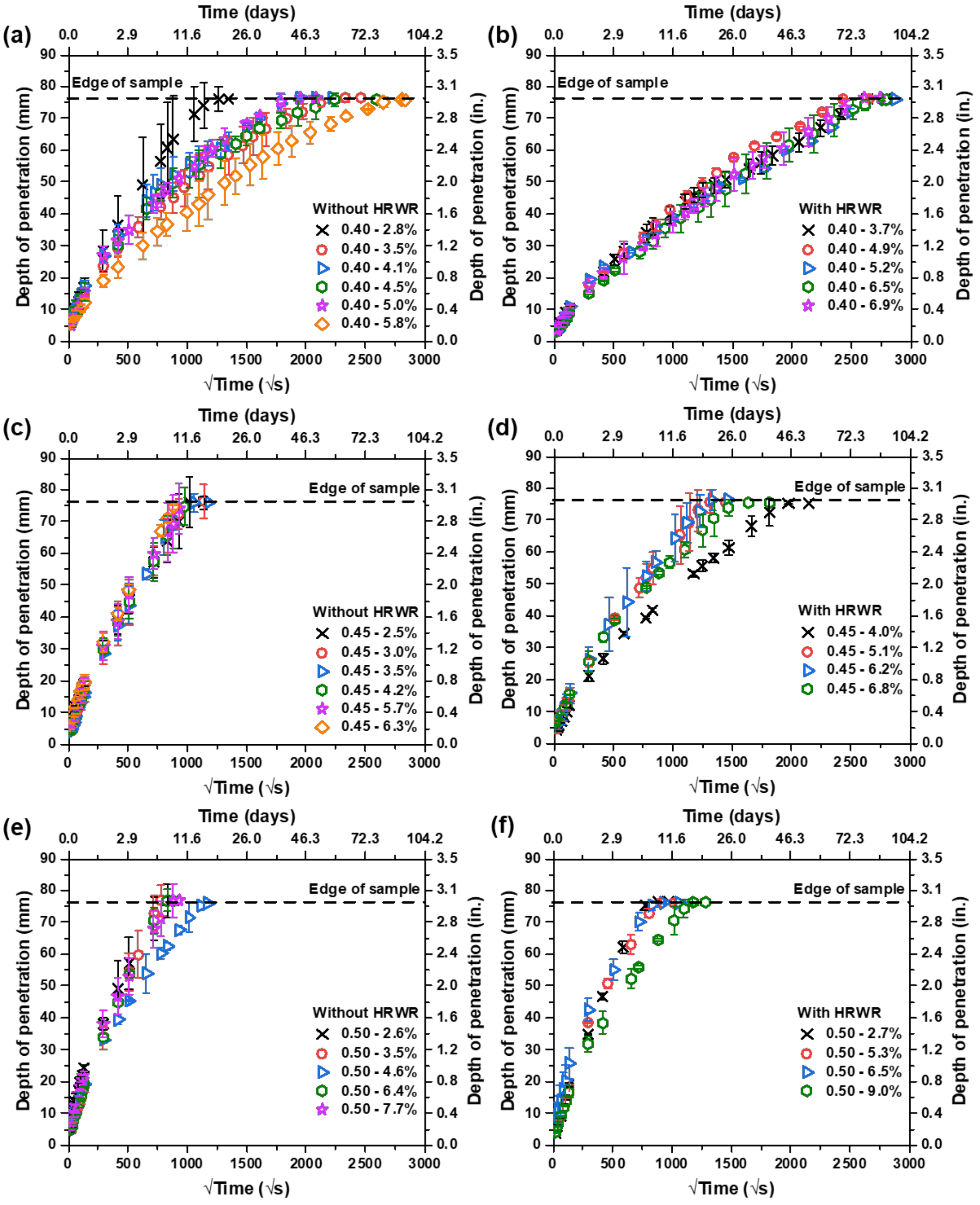

Fig. *7 – Time-dependent water depth of penetration for concrete samples with varying w/c and air content with and without HRWR by NR.*

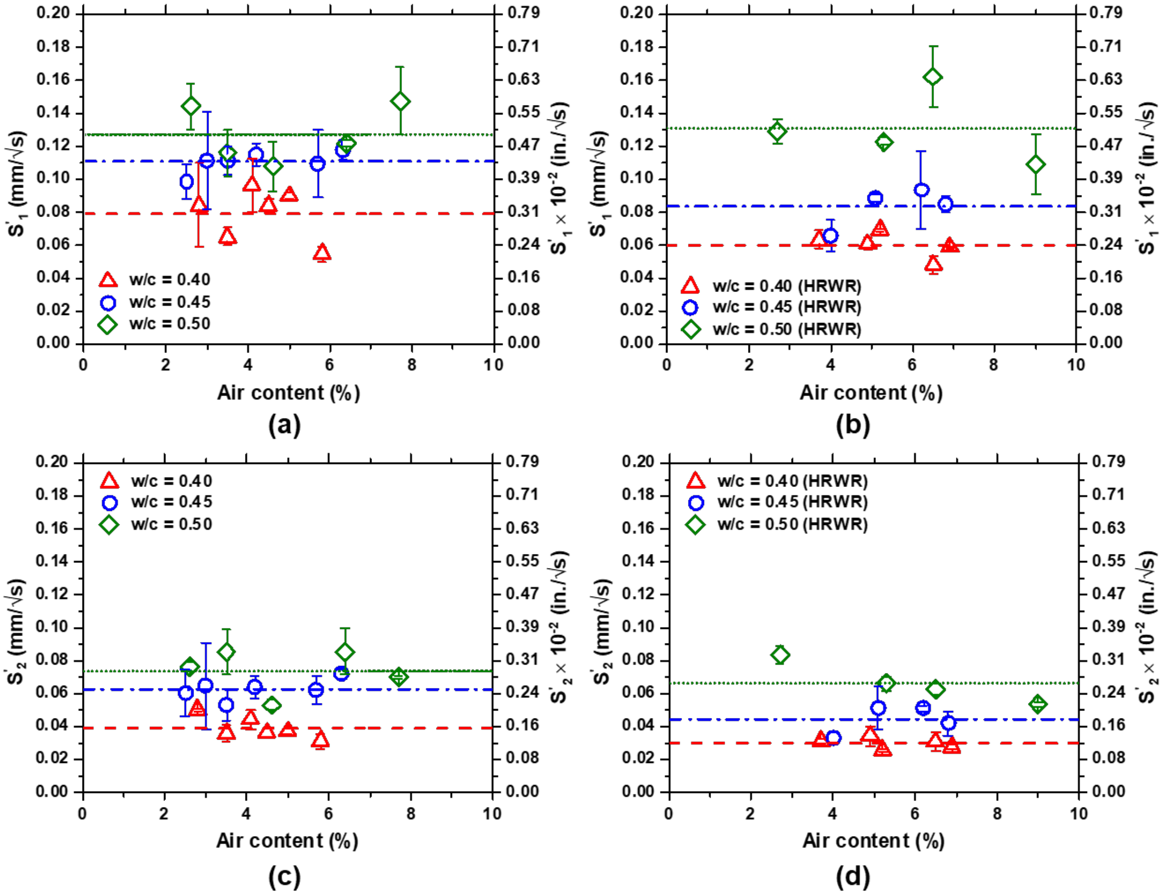

Fig. 8 *– Initial and secondary sorptivity versus air content for the samples with varying w/c with and without HRWR based on depth of penetration vs.* $\sqrt{t}$ *(*S_1'*,* S_2'*).*

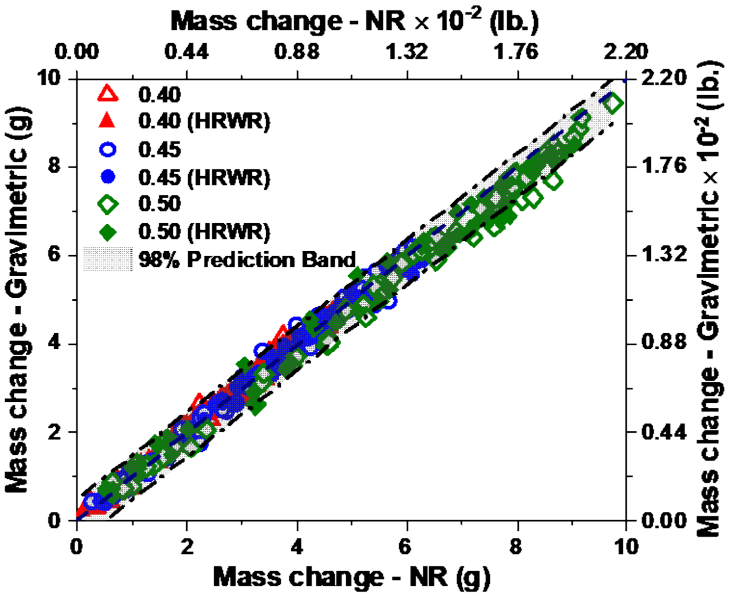

Fig. 9 *– Comparison of mass change values from NR and gravimetric measurements (R^2=996).*

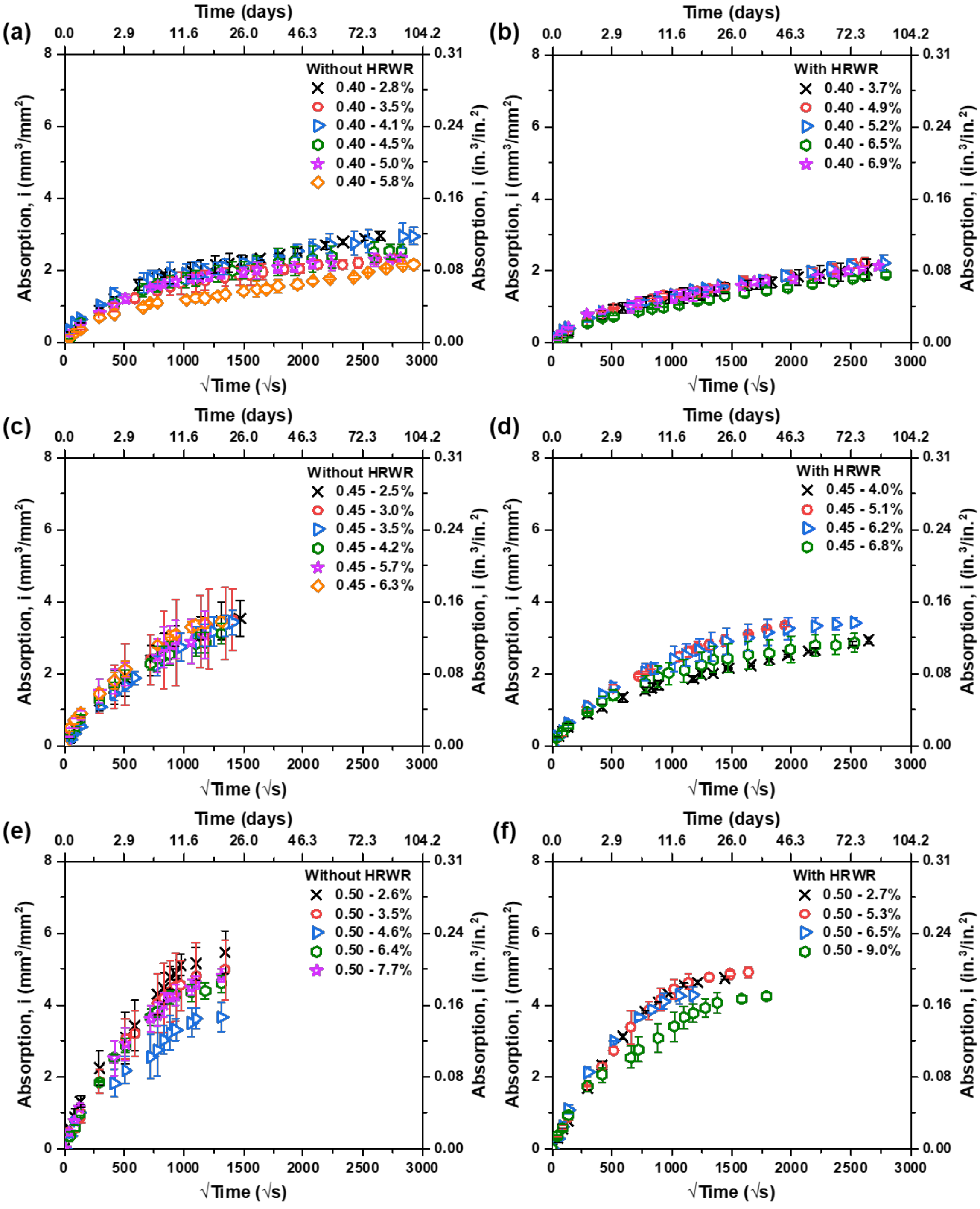

Fig. 10 *– Time-dependent water absorption based on ASTM C 1585-13 definition for concrete samples with varying w/c and air content with and without HRWR by NR.*

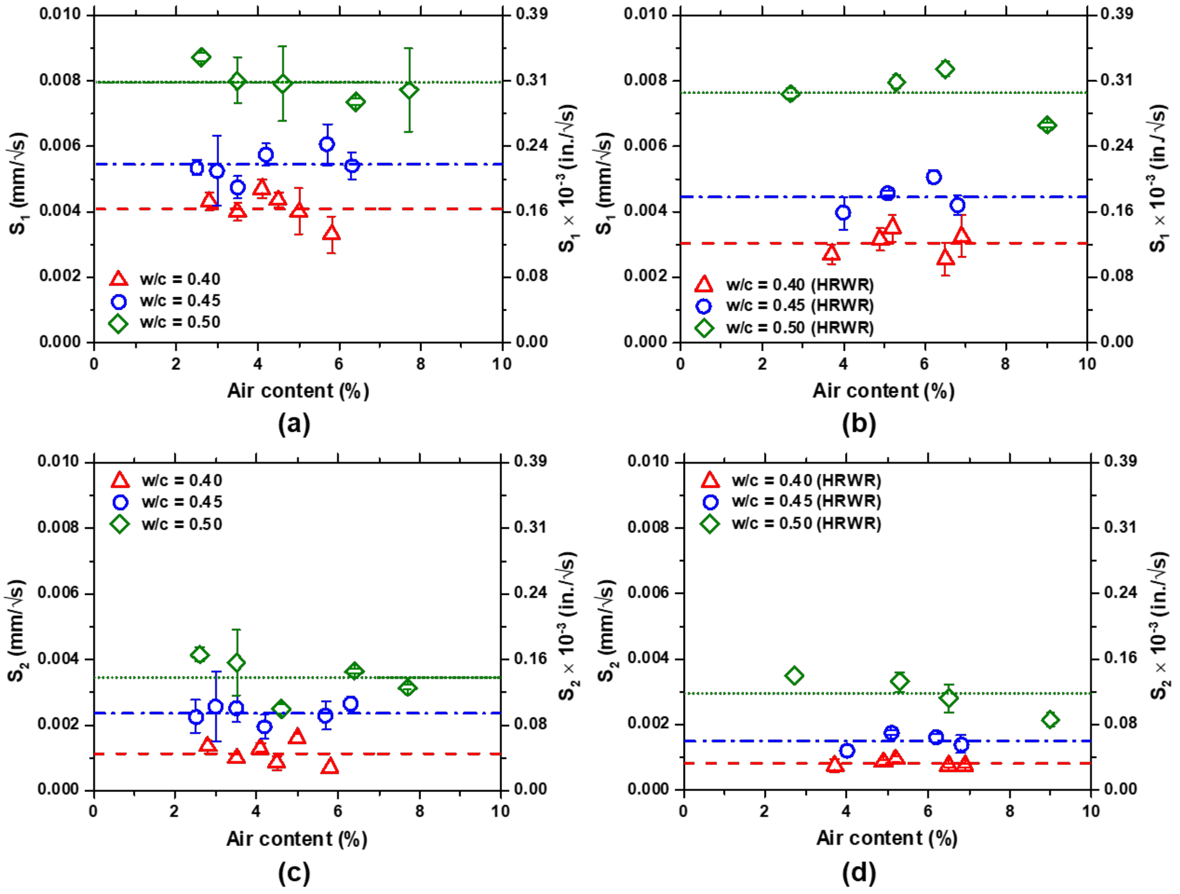

Fig. 11 *– Initial and secondary absorption rate versus air content for the samples with varying w/c with and without HRWR based on absorption vs.* $\sqrt{t}$ *curves* (S_1, S_2) *– ASTM C 1585-13 definition. (Note: the "mm" in* S_1 *and* S_2 *units is not representative of actual depth of penetration.)*

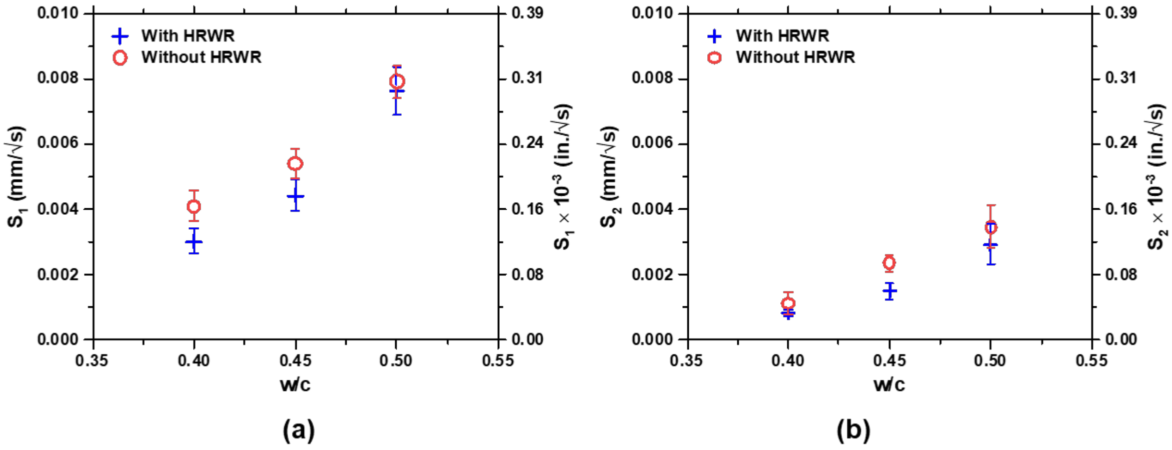

Fig. 12 *– Initial and secondary absorption rate versus w/c for the samples with varying air content with and without HRWR.*

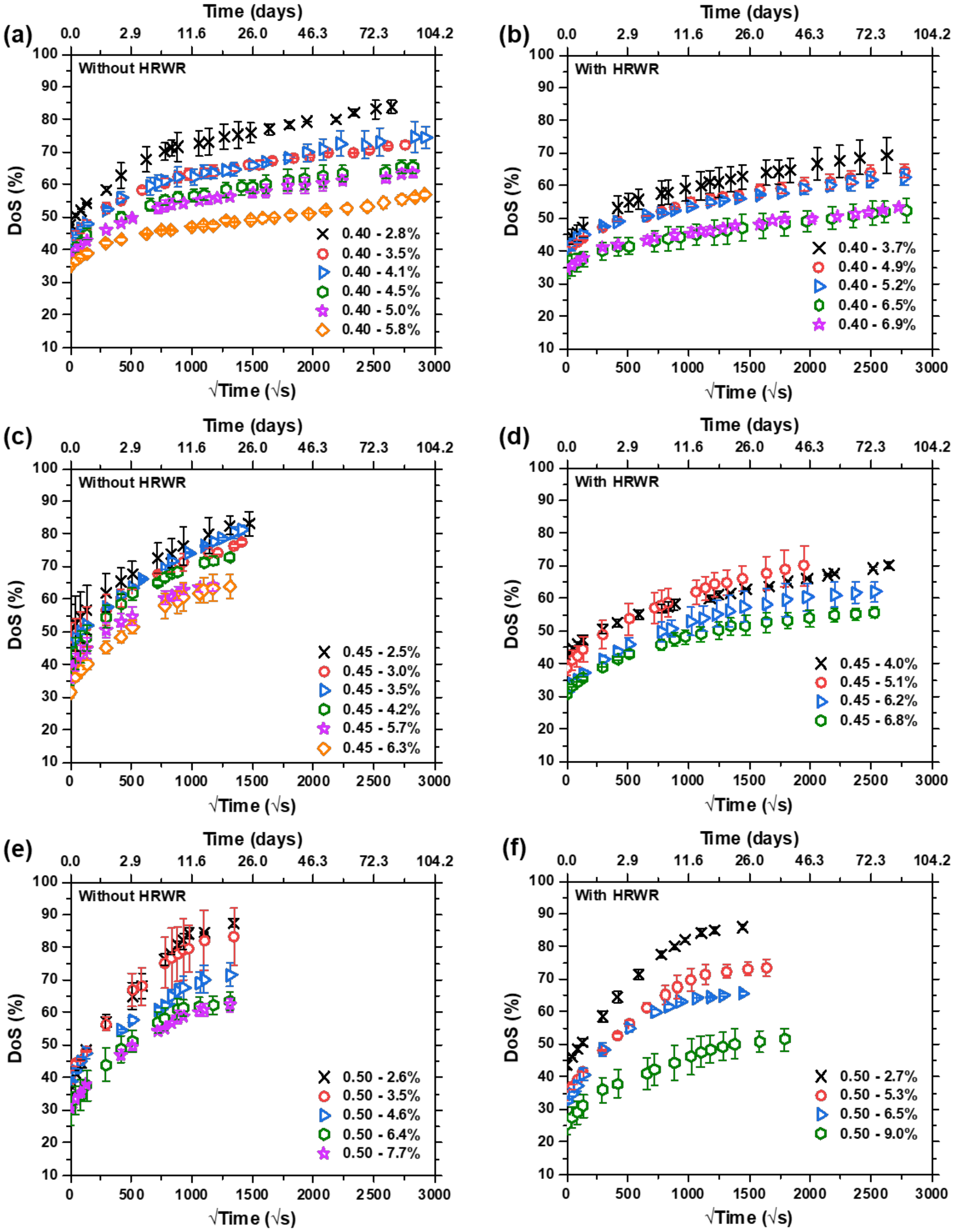

Fig. 13 – Time-dependent degree of saturation for concrete samples with varying w/c and air content with and without HRWR by NR.

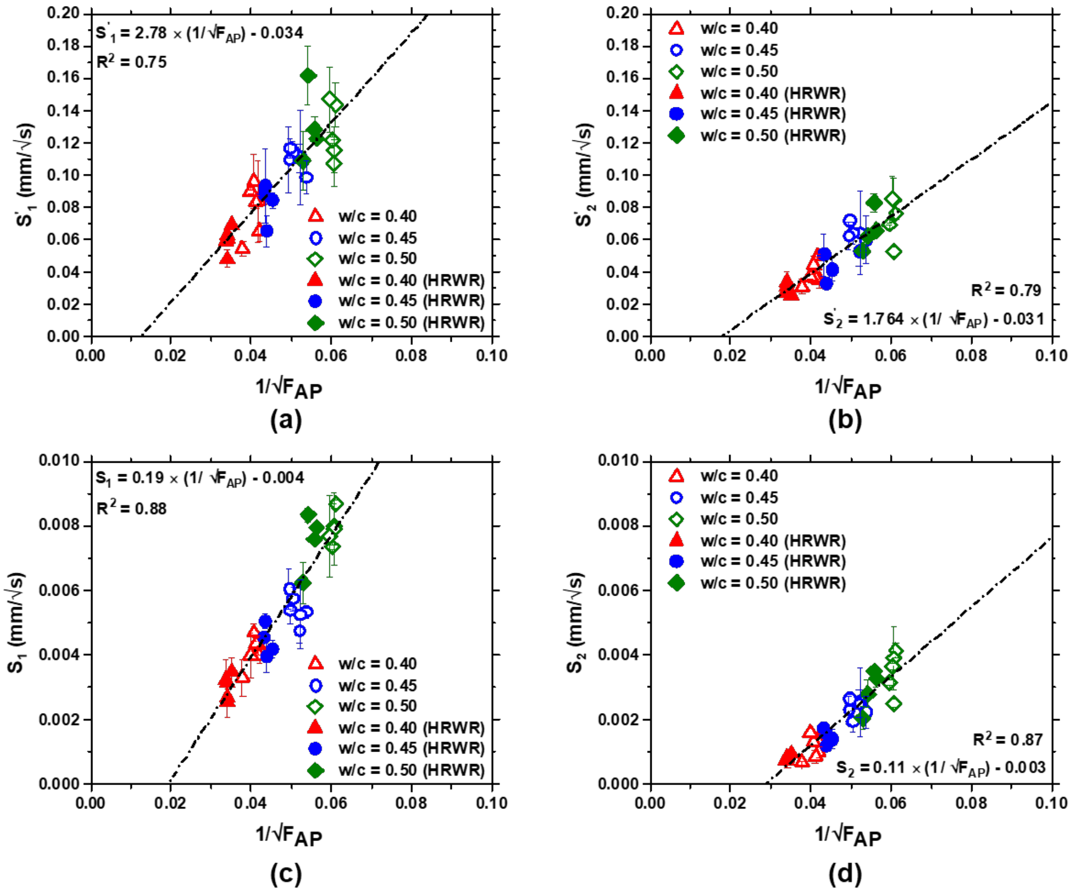

Fig. 14 – (a) and (b): Initial and secondary sorptivities versus apparent formation factor calculated based on depth of penetration vs. $\sqrt{t}$ and (c) and (d) initial and secondary absorption rates vs. apparent formation factor calculated based on absorption vs. $\sqrt{t}$ curves for the samples with varying w/c and air content with and without HRWR. (Note: the "mm" in S_1 and S_2 units is not representative of actual depth of penetration.)

ESTABLISHING A FREEZE-THAW PREDICTION MODEL: QUANTIFYING FLUID FILLING OF THE AIR VOIDS IN AIR ENTRAINED CONCRETE USING NEUTRON RADIOGRAPHY

Mehdi Khanzadeh Moradllo[1], Chunyu Qiao[2], Hope Hall[3], M. Tyler Ley[3], Steven R. Reese[4], and W. Jason Weiss[1]

1. School of Civil and Construction Engineering, Oregon State University, Corvallis, OR 97331, USA

2. DRP, A Twining Company, Boulder, CO 80301, USA

3. School of Civil & Environmental Engineering, Oklahoma State University, Stillwater, OK 74078, USA

4. School of Nuclear Science and Engineering, Oregon State University, Corvallis, OR 97333, USA

ABSTRACT

Knowledge of the degree of saturation in concrete is useful for predicting service-life in a freeze-thaw environment. The degree of saturation increases as a result of fluid absorption. Conventional testing methods to determine fluid absorption (e.g., gravimetric mass measurements) measure cumulative fluid uptake; however, they cannot provide information on the spatial distribution of the absorbed fluid in the sample. Further, conventional test methods cannot determine the degree of saturation at each point in the sample. This paper uses neutron radiography to overcome these limitations and to quantify the volume of water and degree of saturation at each location in the sample. The Powers-Brownyard model is used to calculate pore volume (i.e., matrix pores) that are filled during 1-D capillary water absorption in air-entrained concrete. This information is used to quantify the volume of water in the matrix pores (capillary, chemical shrinkage and gel pores) and the volume of water in the air voids, and subsequently the rate of filling of each pore. This study examined the fluid absorption in concrete mixtures with three different water-to-cement (w/c) ratios (0.40, 0.45 and 0.50) and a range of air contents (2.5% – 9.0%) with and without high

range water reducer. Results show that the air voids filling process is slower than the filling of the matrix pores. The air content has negligible impact on the rate of water ingress in air voids at a given w/c. However, reducing the w/c of a mixture lowers the volume of filled air voids for a comparable period of water ingress due to the lower matrix permeability. As the air content increases, the time-dependent percentage of the air void that is filled (i.e., degree of saturation of air voids) decreases regardless of the w/c.

INTRODUCTION

Concrete is susceptible to damage caused by freezing and thawing [1-6]. The degree of saturation (DoS) of concrete is a key parameter in assessing mixtures susceptibility to freeze-thaw damage [7-10]. It has been shown [8, 9] that a critical degree of saturation (DoS_{CR}) can be defined for each mixture and when the DoS in the concrete exceeds DoS_{CR}, damage will develop during freezing-thawing. The DoS of concrete changes as it dries or absorbs external fluid. As such, improving our understanding of fluid absorption is important for improving of our knowledge of freeze-thaw damage [8, 9, 11, 12].

In air entrained concrete, the fluid absorption can be divided into two parts: 1) water that is absorbed by the matrix pores (capillary, chemical shrinkage and gel pores) and 2) water that is absorbed in the entrained and entrapped air voids [12, 13].

Conventional testing methods for measuring fluid absorption (e.g., ASTM C 1585-13) measure the total cumulative fluid uptake into the concrete. However, conventional test methods do not provide information about the spatial distribution of the fluid in the sample [14]. As such, ASTM C 1585-13 is not able to measure the volume of water that is absorbed by the different types of pores (i.e., matrix pores and entrained air voids) in the concrete. The initial absorption that occurs in the ASTM C 1585-13 test has in the past been assumed to roughly relate to water penetration into the matrix pores and the secondary absorption roughly corresponds to the filling of the air voids; however, the filling of pores is not this simple. The filling process of matrix pores and air voids can overlap. This is because different parameters such as the permeability of the system (i.e., connectivity of pores), distribution of the air voids, and the geometry of the sample can alter the accessibility of the matrix pores or air voids to be filled with fluid during absorption. Therefore, it is useful to provide information about the spatial distribution of filled pores in the concrete to better understand this two-part absorption progress and its influence on time-dependent DoS.

This study uses neutron radiography (NR) to quantify the rate of water absorption (1-D) in concrete samples with varying w/c (0.40, 0.45 and 0.50) and a range of air contents (2.5 – 9.0%). NR has an advantage over other techniques in measuring water movement and distribution due to the large interaction of hydrogen with a thermal neutron beam (i.e., large neutron scattering and absorption cross sections) [15, 16]. NR has been used to study the drying process, fluid absorption, plastic settlement, internal and external curing, and cracking in cementitious materials [17-24].

This study has four objectives. First, it describes how NR can be used to quantify the time-dependent water absorption in concrete. Second, it uses the Beer-Lambert Law [15] to quantify the volume of water at each location in the sample. Third, it applies the Powers-Brownyard model [25] to quantify the volume of matrix pores (capillary, chemical shrinkage and gel pores). Finally, simple equations are used to determine the rate of water absorption by the matrix pores and the air voids.

EXPERIMENTAL PROGRAM

Thirty concrete mixtures were tested with three different w/c (0.40, 0.45, and 0.50), a wide range of air contents (2.5 – 9.0%), and a wide range of air qualities (air size and distribution). The air quality was altered by using a polycarboxylate based high range water reducing admixture (HRWR). The samples were cured for 180 d in a sealed condition at 23 ± 1 ºC. After curing, 76.0 mm (height) × 60.0 mm (width) × 30.0 mm (thickness) prismatic slices were cut from 203.0 mm (height) × 102.0 mm (diameter) cylindrical samples for 1-D absorption experiments using NR. The thickness of the prismatic samples (30 mm) is 60% larger than the maximum size of coarse aggregates (19 mm) in the concrete mixtures. Three samples were tested at a given w/c and air content. The samples were monitored by NR until water reached the top surface of the sample (≈10-100 d depending on w/c). The samples were dried at 65 ± 1 ºC and then vacuum saturated after the absorption test to measure the initial and time-dependent DoS of samples. More details on the preparation, preconditioning, and testing of the samples can be found in [26].

A simplified immersion test was performed on the concrete samples (102 ± 2 mm (diameter) × 203 ± 2 mm (height)) to determine apparent formation factor (F_{AP}) derived from electrical resistivity measurement. For each mixture, two samples were submerged in a 19 L bucket containing 13.5 L simulated pore solution. The electrical resistance was periodically recorded over 91 days of submersion. The impedance of the specimens was measured using a bulk resistivity meter with a frequency of 1 kHz at 23 ± 2 °C according to AASHTO TP 119-17. The detail on testing procedure and calculation of F_{AP} can be found in [11, 26].

Neutron imaging was conducted at the Neutron Radiography Facility (NRF) at Oregon State University (OSU) Radiation Center [21-23, 26]. Five radiographs were taken of the concrete samples before exposing the sample to water. For the setting used in this test, a spatial resolution of approximately 90 μm was obtained. The average of these radiographs was used as a reference image. Radiographs were also taken over time after the sample was exposed to water to track the water penetration into the sample. A linear motion stage with accuracy of 2.0 μm was used to re-positions the samples during imaging over the duration of the test period [26]. Radiographs were also captured from samples in the oven-dried and vacuum saturated conditions to calculate the DoS profiles by NR. In addition, multiple images were taken from the background (detector's FOV) with open beam (flat-field image) and with closed beam (dark-field image) for the background correction.

A water attenuation coefficient (μ_W) is required to quantify the water distribution in the samples based on the raw radiographic images. The μ_W was determined by scanning the empty and water-filled stepped cells with different thicknesses (1-10 mm) in front of the absorption samples after drying them at 65 ± 1 °C and developing a relationship between water thickness (X_w) and optical density ($OD = \ln(I_0/I_t)$) based on Eq. 1 [15, 27]. Equation 1 is the modified version of the Beer-Lambert Law to empirically correct for beam hardening and scattering effects [15, 27]. Equation 1 was fitted to the experimental results (X_w vs. $\ln(I_0/I_t)$) to determine μ_W for different samples [26]. The μ_W was determined in front of the dry samples to account for the impact from non-evaporable water and other constituents of concrete on optical density values and consequently on μ_W [21].

$$Ln(\frac{I_0}{I_t}) = \mu_w X_w + \beta X_w^2 \tag{1}$$

where, I_0 and I_t are the average transmitted intensity on the empty and water-filled cells, respectively and β (mm^{-2}) is the correction parameter to empirically correct for the beam hardening and scattering effects [15, 27]. The measured values of μ_W (mm^{-1}) and β and relevant figures are reported in [26].

DATA PROCESSING

3.1. Image Processing

The NR images were processed and analyzed with ImageJ® software [28]. The raw images were normalized with respect to the flat field (open beam) and dark field (closed beam) images to correct for background noise based on Eq. 2 [27]. A median filter was used for three images of a sample to eliminate the artifacts due to the gamma rays [15]. This filtering also reduces the variation in the measured intensities [29]. After a background correction, an average intensity profile was calculated through the sample depth for reference and time-dependent images.

$$I_{corrected} = \frac{I_{raw\ image} - I_{dark\ field}}{I_{flat\ field} - I_{dark\ field}} \tag{2}$$

The second order solution of the Beer-Lambert Law [15, 27], as shown in Eqs. 3 and 4, was used to calculate a change in attenuation from absorbed water (absorbed water thickness) and volumetric water content (θ) at different depth of sample (Fig. 1a).

$$X_w(mm) = -\frac{\mu_w}{2\beta} - \sqrt{\left(\frac{\mu_w}{2\beta}\right)^2 - \frac{1}{\beta} ln\left(\frac{I_t}{I_0}\right)} \tag{3}$$

$$\theta(\frac{mm^3}{mm^3}) = \frac{X_w}{X_s}\frac{pixel\ area}{pixel\ area} = \frac{X_w}{X_s} \tag{4}$$

where, I_0 and I_t are the average transmitted intensity at depth d_i on the reference profile and time-dependent profile, respectively; μ_W (mm^{-1}) is the attenuation coefficient of water; β (mm^{-2}) is the correction parameter; X_w (mm) and X_s (mm) are the thickness of water and the sample, respectively; and θ is the average volumetric water content at depth d_i (mm).

In Fig. 1a, the initial volumetric water content ($\theta_{Initial}$) over depth was calculated from the reference radiographs before exposing the sample to water based on Eqs. 3 and 4. This initial water content is a measure of water in the hydrated products, interlayer water, and water in the gel pores. The average volume of matrix pores is calculated based on Powers-Brownyard model [25]. The difference between average volume of matrix pores and average initial volume of water content (i.e., average $\theta_{Initial}$) is added to the initial volume of water content at depth d_i to determine the volume of matrix pores over the sample depth, as shown in Fig. 1a. This procedure accounts for the variation of the matrix pores (i.e., amount of paste) over the sample depth. However, it assumes that the degree of hydration and the desorption isotherm are constant for the mortar throughout the depth. The total volumetric water content (i.e., total porosity) was calculated as the difference between the vacuum-saturated and oven-dried images over depth, as presented in Fig. 1a. It is worth noting that the fluctuations in the moisture profiles over depth (Fig. 1a) are due to spatial variability in the sample (i.e., change in porosity and aggregate content) not due to noise from NR measurements. The maximum calculated repeatability standard deviation (i.e., noise) of volumetric water content over depth from three images of individual sample carried out under the same measurement condition is 0.007. The time-dependent θ profiles, the estimated volume of matrix pores, and the measured total porosity over depth were used to determine the time-dependent volume and percentage of filled air voids, as discussed in the next section and presented in Fig. 1b and 1c.

The time-dependent DoS (%) was calculated based on Eq. 5 (Fig. 1d).

$$DoS = \frac{\Delta m_t}{m_{Sat} - m_{OD}} \times 100 + DoS_{Initial} \tag{5}$$

where, m_{sat} (g) and m_{OD} (g) are the mass of the saturated and oven-dried samples, respectively; and $DoS_{Initial}$ (%) is the initial DoS of the sample before start of the absorption test. The DoS_{Matrix} is determined based on calculated volume of matrix pores, as shown in Fig. 1d.

The following steps can be taken to calculate mass change profiles and the cumulative mass change over the time based on NR measurements.

The time-dependent absorbed water mass per pixel (m [g]) can be computed over the sample depth.

$$m = \theta\left(A_{pixel}X_S\right)\rho_w \tag{6}$$

where, A_{pixel} is the pixel area (0.0081 mm^2) and ρ_w is the density of water (0.001 g/mm^3).

The change in sample mass (Δm [g]) (cumulative mass change) was calculated based on the following equation using NR measurements.

$$\Delta m = \sum m \, . \, n \tag{7}$$

where, Σm (g) is the sum of the absorbed water mass over sample depth; and n is the number of pixels in the width of the sample.

3.2. Determining the Volume of Water Filled Air Voids

As mentioned, in air entrained concrete, water is absorbed by the matrix pores and the entrained and entrapped air voids. The following steps can be taken to quantify the volume of water absorbed by each type of pore by using 1-D absorption results from NR.

Figures 2 and 3 outline the steps to determine the volume fraction of pores filled with fluid. Figure 2 (a to c) provides a schematic diagram of time-dependent volumetric water content profiles obtained from NR. Figure 2 illustrates the volume of pores initially filled with water (i.e., volume of filled pores after conditioning at 50% RH), volume of matrix pores, and the total volume of pores. The volume of initially filled pores ($\theta_{Initial}$) and total pores (θ_{Total}) are determined from reference and vacuum-saturated radiographs, respectively. The volume of matrix pores (θ_{Matrix}) is calculated based on Powers-Brownyard model [25]. The details on application of this model for air entrained concrete can be found in [11]. As discussed previously, the difference between average volume of matrix pores and average initial volume of water content (i.e., average $\theta_{Initial}$) is added to the initial volume of water content at depth d_i to determine the volume of matrix pores over the sample depth. This procedure accounts for the variation of the matrix pores over the sample depth. Figure 2b shows the initial sharp water front that moves into the sample upon wetting. The initial absorbed water content is below the θ_{Matrix}. Therefore, the area shown in Fig. 2b between $\theta_{Initial}$ and the time-dependent θ profile (θ_t) represents the volume of water filled matrix pores ($\theta_{Matrix\text{-}Fill}$). Water infiltrates the air voids when the θ_t values are larger than the θ_{Matrix} (Fig. 2c). The volume of water filled air voids ($\theta_{Air\text{-}Fill}$) can be determined by subtracting the θ_{Matrix} from θ_t over the sample depth (green area, Fig. 2c). The mathematical expressions of the volume of water filled matrix pores and air voids are presented in Eqs. 8a and 8b. As shown in Figs. 1 and 2, the air voids filling process is slower than the filling of the matrix pores. The water absorption front by matrix pores is significantly sharper than that of the air voids. This is attributed to the higher capillary pressure in matrix pores when compared to the air voids.

$$\theta_{Matrix-Fill} = \theta_t - \theta_{Initial} \;\; \boldsymbol{and} \;\; \theta_{Air-Fill} = 0 \;\; \boldsymbol{if} \;\; \theta_t \leq \theta_{Matrix} \tag{8a}$$

$$\theta_{Matrix-Fill} = \theta_{Matrix} - \theta_{Initial} \;\; \boldsymbol{and} \;\; \theta_{Air-Fill} = \theta_t - \theta_{Matrix} \;\; \boldsymbol{if} \;\; \theta_t > \theta_{Matrix} \tag{8b}$$

where, θ_t and $\theta_{Initial}$ are the time-dependent and initial volumetric water contents of the sample at depth d_i (measured by NR), respectively; and θ_{Matrix} is the calculated volume of matrix pores based on the Powers-Brownyard model.

A simulation of the time-dependent volume of water filled air voids profiles (i.e., smoothed version of the Fig. 1b) is presented in Fig. 3a. To determine the percentage of filled air voids (i.e., DoS of air voids), the volume of filled air voids was divided by the estimated volume of air voids over the sample depth (Fig. 3b). The volume of air voids at each pixel (θ_{Air}) was calculated based on Eq. 9. It is worth mentioning that the calculated volumetric water content in air voids at different locations (from NR) is the average value through the sample thickness. Therefore, the amount of absorbed water in both partially and fully filled air voids is considered in the calculation of the volume and percentage of filled air voids.

$$\theta_{Air} = \theta_{Total} - \theta_{Matrix} \tag{9}$$

where, θ_{Total} is the volumetric water content of vacuum-saturated sample at depth d_i (measured by NR, Fig. 1a).

Equations 5 and 6 were used to interpret the time-dependent absorbed water mass by matrix pores and air voids (Fig. 4). The volumetric water content (θ) in Eq. 5 was replaced by time-dependent $\theta_{Matrix\text{-}Fill}$ or $\theta_{Air\text{-}Fill}$ to calculate the absorbed mass by matrix pores and air voids over time, respectively. The time-dependent $\theta_{Matrix\text{-}Fill}$ or $\theta_{Air\text{-}Fill}$ were determined from time-dependent volumetric water content profiles (Fig. 1a) using Eq. 8.

It is worth noting that the heterogeneity of concrete samples due to the distribution of coarse aggregates over the depth can impact the fluid absorption properties in concrete [29]. Based on the calculation presented in appendix A, the volume fraction of coarse aggregate over depth in NR samples is illustrative of the average value from the mixture proportions. However, the influence of the spatial distribution of coarse aggregate in concrete on the fluid absorption (e.g., impact from the aggregate blocking, dilution, and interfacial transition zone) is not examined in this study.

Equation 10 was used to determine the rate of fluid absorption by air voids. The water absorption rate by air voids (S_2') is determined as the slope of the absorbed water by air voids versus the square root of time curve during the 3 d – 40 d (Fig. 4). The initial and secondary absorption rates (S_1 and S_2) based on ASTM C 1585-14 definition are shown in Fig. 4a.

$$m_a\left(t_{40d}^{3d}\right) = S_2'\sqrt{t} + B_1 \tag{10}$$

where, m_a (g) is the time-dependent mass of water absorbed by air voids; t (s) is the time; and B_1 is the regression constant.

EXPERIMENTAL RESULTS AND DISCUSSION

4.1. TIME-DEPENDENT AMOUNT OF FLUID ABSORBED BY AIR VOIDS

The calculated time-dependent fluid absorbed by air voids for mixtures with varying w/c and air contents is presented in Fig. 5, which indicates that reducing the w/c of mixture lowers the amount of water absorbed by air voids for a given period of fluid absorption. Figure 7a shows the average amount of water absorbed by air voids after 20 d versus w/c for the samples with varying air content with and without HRWR. The average amount of water absorbed by air voids after 20 d in the samples with w/c of 0.40 is 83% less and with w/c of 0.45 is 67% less than that of the samples with w/c of 0.50, as shown in Fig. 6a. However, the measurements at a w/c of 0.45 and 0.50 have a high variability. The reduction in the volume of filled voids in the low w/c samples can be attributed to a microstructure which is more dense. The high sample to sample variability in the high w/c samples can be attributed to the variability in the total volume of air voids over the sample depth, as shown in Fig.1a. In addition, it is worth noting that air void filling is a very slow process (i.e., little amount of water absorption by air voids when compared to total absorption, as shown in Fig. 4b). So, even a small difference in the absorption values causes a very high variability. However, more work is underway to further understand the cause of this variability. The air content appears to have a minimal impact on time-dependent amount of water absorbed by air voids at a given w/c. The addition of HRWR reduced the amount of water absorbed by air voids (≈60% at 20 d) in the samples with w/c of 0.45. As shown in Fig. 6a, the impact from the addition of HRWR is not significant in the samples with w/c of 0.40 and 0.50. This difference in the amount of water absorbed by air voids between the w/c=0.45 samples with and without HRWR is likely related to the variability of the pore structure in the matrix of these mixtures (i.e., variability in distribution of the flocculted cement particles and the pore refinement that would impact pore connectivity).

The amount of water absorbed by air voids after 20 d absorption (m_{20}) versus the inverse of apparent formation factor (F_{AP}) (derived from electrical resistivity measurement) for the samples with varying w/c and air content and quality is shown in Fig. 6b. The apparent formation factor was measured under a non-saturated condition (i.e., matrix saturation) which correlates to the saturation state of concrete in the field [11, 26]. Based on Fig. 6b, the m_{20} increases with an increase in the F_{AP}. This relationship also shows that the interconnectivity of matrix pores (i.e., permeability) has a significant impact on the amount of fluid absorbed by air voids.

4.2. TIME-DEPENDENT VOLUME OF WATER FILLED AIR VOIDS

Figure 7 shows the volume and percentage of water filled air voids over the sample depth for the samples with varying w/c and air contents. Figures 7a, c, and e present the volume of filled air voids over the depth for the samples with varying w/c and air contents at a comparable time period, while the Figs. 7b, d, and f compare the percentage of filled air voids (i.e., DoS of air voids) for the same set of samples. The air content has a minimal impact on the volume of filled air voids over the depth at a given w/c and at a comparable time (Figs. 7a, c, and e), while it significantly influences the percentage of filled air voids over depth (i.e., DoS of air voids) (Figs. 7b, d, and f). As the air content increases, the percentage of fluid filled air voids decreases regardless of the w/c. This is expected since there is a larger amount of air voids need to be filled with fluid in the samples with a higher air content. However, the sample with a higher air content has a higher fraction of empty voids which result in a lower DoS. The lower DoS in concrete with high air content delays the time to reach a critical DoS [9, 12].

The time-dependent percentage of water filled air voids is compared for samples with different air contents and w/c in Fig. 8. Based on the results for samples with a w/c of 0.40, the percentage of filled air voids is lower than the samples with w/c of 0.45 which is less than the w/c of 0.50

regardless of the air content. However, the results show higher variability in the samples with w/c of 0.45 and 0.50 at a given air content. The air voids filling process is slower and limited to the first 25 mm of the sample depth in the samples with a w/c of 0.40, while the filling of air voids progresses to the inner depths (≈40-70 mm) in the samples with a higher w/c. This can be attributed to the lower permeability of the samples with a w/c of 0.40 due to the refined microstructure. For the samples with a w/c of 0.40, it takes a longer time for water to penetrate through the entire depth of the sample when compared to the samples with a higher w/c (≈40-100 d for the samples with a w/c of 0.40 compared to a ≈10-15 d for the samples with a w/c of 0.50) [26].

Based on Fig. 8, the addition of HRWR slightly increases the percentage of filled air voids in the samples with a w/c of 0.50, while the percentage of filled air voids decreases by addition of HRWR in samples with a w/c of 0.45. As previously mentioned, this inconsistency can be attributed to the variability in the quality of the mixtures (i.e., variability in distribution of the flocs of cement and the pore refinement) with a w/c of 0.45 by addition of the HRWR. Previous studies found that the addition of HRWR alters the fluid absorption properties in air entrained concrete, particularly at low w/c mixtures (i.e., w/c=0.40 and 0.45) [11, 26].

4.3. RATE OF WATER ABSORPTION BY AIR VOIDS (S_2')

Figure 9 shows the S_2' versus air content and SAM number calculated based on Eq. 10 for concrete mixtures with varying w/c with and without HRWR. As shown in Fig. 9, reducing the w/c of the mixture lowers the value of S_2'. As mentioned, this can be attributed to the refined microstructure of the sample with a lower w/c where the fluid progress through the capillary pores is slow. The entrained air voids are connected by the capillary pore system of the cement paste matrix [30, 31]. Therefore, the process of air void filling will require a longer time in a low w/c mixture.

Figure 9 also indicates that the impact of air content on S_2’ is minimal, while the S_2’ decreases with reduction of the SAM number. The relationship between S_2’ and SAM number is stronger in the samples with HRWR. A lower SAM number is shown to correlate to better air void quality (i.e., lower spacing factor) [32]. The addition of HRWR increases the mean value of S_2’ in the samples with a w/c of 0.50. However, the mean value of S_2’ decreased by addition of HRWR in samples with a w/c of 0.45 most likely due to the variability in the quality of these mixtures (i.e., variability in distribution of the flocs of cement and the pore refinement).

The slope of the “S_2’ versus SAM number” (calculated from Figs. 9c and d) versus the inverse of the apparent formation factor for the samples with varying w/c is shown in Fig. 10. Fig. 10 shows that when the $1/F_{AP}$ is high (i.e., high permeability), the SAM number significantly impacts S_2’. However, the impact from SAM number on S_2’ is difficult to determine due to the low amount of fluid ingress for the samples with a low $1/F_{AP}$ for the 100 days of ponding investigated in this testing. This may be attributed to the lower fluid infilling rate in the samples with a low $1/F_{AP}$ and for samples with low w/c requiring a longer time for the air voids to fill. The relationship between S_2’, $1/F_{AP}$, and SAM number needs to be examined for longer time periods of water exposure and for mixtures with a wide range of materials, w/c and air qualities before this can be implemented in service life modeling of concrete exposed to freeze-thaw cycles.

CONCLUSIONS

This paper developed a method to estimate the water absorption by the matrix pores and air voids of concrete mixtures with varying w/c (0.40, 0.45, and 0.50) and air contents (2.5% – 9%) with and without HRWR using NR. The following conclusions can be drawn:

- Samples with a w/c of 0.40 showed a lower percentage of water filled air voids and a lower rate of absorption by air voids (S_2’) when compared to the samples with higher w/c (0.45 and 0.50). In addition, the amount of water absorbed by air voids reduces with an increase in the apparent formation factor. This is due to the lower permeability of the matrix in low w/c samples (i.e., samples with higher F_{AP}).

- The air void filling process is slower than the filling of the matrix pores. The water absorption front by matrix pores is significantly sharper than that of the air voids. This is attributed to the higher capillary pressure in matrix pores when compared to the air voids.
- The air volume has a minimal impact on rate of air void filling at a given w/c. However, as the air content increases, the percentage of the air void volume that is filled decreases regardless of the w/c for a given period of exposure. This lowers the DoS in the sample and delays the time to reach a DoS_{CR}. Accordingly, the long time to reach DoS_{CR} extends the service life of concrete in cold environment.
- The addition of HRWR reduced the amount of water absorbed by air voids in the samples with w/c of 0.45. However, the impact from the addition of HRWR is not significant in the samples with w/c of 0.40 and 0.50. This difference is likely related to the variability of the pore structure in the matrix of the mixtures with w/c of 0.45 (i.e., variability in distribution of the flocculted cement particles and the pore refinement that would impact pore connectivity).
- The impact of SAM number on S_2' appears to depend on the quality of the matrix. For very high F_{AP} (i.e., low permeability), the impact can not be seen since the absorption rate is so low. However, the impact from SAM number on S_2' is significant in the samples with a low F_{AP} (i.e., high permeability) due to the higher fluid infilling rate. Result shows that the sample with good air quality or low SAM number has a lower rate of fluid absorption by air voids.

The method described in this study can help to improve the predictive capabilities of service life modeling methods for concrete elements and structures subjected to freeze-thaw cycles. This is because while the filling rate of air voids is a crucial factor in estimating service life of air-entrained concrete in cold environments, there is lack of previous studies to quantify this factor.

ACKNOWLEDGEMENTS

The authors gratefully acknowledge support for this work through the pooled fund study (Project No. U1117C) managed by the Oklahoma Department of Transportation. This paper is the 3rd in a series with [11] and [26].

Declarations of interest: none.

APPENDIX A

Volume of Coarse Aggregates in NR Samples

The heterogeneity of concrete samples due to the distribution of coarse aggregates over the depth can impact the fluid absorption properties in concrete [29]. Therefore, it is essential to determine the volume fraction of coarse aggregates at a given location in thin concrete samples. The volume fraction of coarse aggregates at a given location in NR samples was estimated using Eq. A.1 [29]. A combination of Beer's law and a simple rule of mixtures approach has been used to develop Eq. A.1 [29].

$$V_{Coarse\ Agg} = \frac{\mu_{Mortar} - \mu_{Concrete}}{\mu_{Mortar} - \mu_{Coarse\ Agg}} \times 100\% \tag{A.1}$$

where, μ_{Concrete} (mm^{-1}) is the measured attenuation coefficient at a given depth in saturated concrete sample; μ_{Mortar} (mm^{-1}) and $\mu_{\text{Coarse Agg}}$ (mm^{-1}) are the attenuation coefficients for a sample of pure mortar and a sample of pure coarse aggregate in a saturated condition respectively; and $V_{\text{Coarse Agg}}$ is the volume fraction of the coarse aggregate at a given depth in concrete sample.

Figure A.1 shows an example of the calculated volume fraction of coarse aggregate over the depth of concrete sample and the comparison with the average volume fraction of coarse aggregates from the mixture proportions. Based on the results from tested NR samples, the calculated average volume fraction of coarse aggregate for NR samples is approximately 3-10% higher than the average value from the mixture proportions. In addition, the maximum difference between the calculated volume fraction of coarse aggregate and the average value from the mixture proportions is approximately 20% at a given depth of the sample. In other words, the minimum volume fraction of mortar in tested NR samples is ≈40% at a given depth (i.e., volume fraction of coarse aggregate is ≈30-60%). Therefore, the volume fraction of coarse aggregate over depth in NR samples is illustrative of the average value from the mixture proportions.

REFERENCES

[1] J. Backstrom, R. Burrows, V. Wolkodoff, T. Powers, Void spacing as a basis for producing air-entrained concrete, J. Am. Concrete Inst. 49 (1954) 16-1.

[2] J.J. Beaudoin, C. MacInnis, The mechanism of frost damage in hardened cement paste, Cement and Concrete Research 4(2) (1974) 139-147.

[3] L. Du, K.J. Folliard, Mechanisms of air entrainment in concrete, Cement and Concrete Research 35(8) (2005) 1463-1471.

[4] M. Pigeon, J. Marchand, R. Pleau, Frost resistant concrete, Construction and Building Materials 10(5) (1996) 339-348.

[5] T.C. Powers, R. Helmuth, Theory of volume changes in hardened portland-cement paste during freezing, Highway research board proceedings, 1953.

[6] T.C. Powers, T. Willis, The air requirement of frost resistant concrete, Highway Research Board Proceedings, 1950.

[7] G. Fagerlund, The international cooperative test of the critical degree of saturation method of assessing the freeze/thaw resistance of concrete, Matériaux et Construction 10(4) (1977) 231-253.

[8] G. Fagerlund, The critical degree of saturation method of assessing the freeze/thaw resistance of concrete, Matériaux et Construction 10(4) (1977) 217-229.

[9] W. Li, M. Pour-Ghaz, J. Castro, J. Weiss, Water absorption and critical degree of saturation relating to freeze-thaw damage in concrete pavement joints, Journal of Materials in Civil Engineering 24(3) (2011) 299-307.

[10] C. Maclnnis, J.J. Becaudoin, Effect of degree of saturation on the frost resistance of mortar mixes, Journal Proceedings, 1968, pp. 203-208.

[11] C. Qiao, M.K. Moradllo, H. Hall, T. Ley, J. Weiss, Electrical Resistivity and Formation Factor of Air Entrained Concrete, ACI Materials Journal (2018) in press.

[12] H.N. Todak, Durability assessments of concrete using electrical properties and acoustic emission testing, Purdue University, 2015.

[13] G. Fagerlund, Predicting the service life of concrete exposed to frost action through a modelling of the water absorption process in the air-pore system, The modelling of microstructure and its potential for studying transport properties and durability, Springer1996, pp. 503-537.

[14] M.K. Moradllo, M.T. Ley, Quantitative measurement of the influence of degree of saturation on ion penetration in cement paste by using X-ray imaging, Construction and Building Materials 141 (2017) 113-129.

[15] D.S. Hussey, D. Spernjak, A.Z. Weber, R. Mukundan, J. Fairweather, E.L. Brosha, J. Davey, J.S. Spendelow, D.L. Jacobson, R.L. Borup, Accurate measurement of the through-plane water content of proton-exchange membranes using neutron radiography, Journal of Applied Physics 112(10) (2012) 104906.

[16] V.F. Sears, Neutron scattering lengths and cross sections, Neutron news 3(3) (1992) 26-37.

[17] F. De Beer, W. Strydom, E. Griesel, The drying process of concrete: a neutron radiography study, Applied Radiation and Isotopes 61(4) (2004) 617-623.

[18] M. Kanematsu, I. Maruyama, T. Noguchi, H. Iikura, N. Tsuchiya, Quantification of water penetration into concrete through cracks by neutron radiography, Nuclear Instruments and Methods in Physics Research Section A: Accelerators, Spectrometers, Detectors and Associated Equipment 605(1-2) (2009) 154-158.

[19] C.L. Lucero, Quantifying moisture transport in cementitious materials using neutron radiography, (2015).

[20] C.L. Lucero, R.P. Spragg, D.P. Bentz, D.S. Hussey, D.L. Jacobson, W.J. Weiss, Neutron Radiography Measurement of Salt Solution Absorption in Mortar, ACI materials journal 114(1) (2017) 149.

[21] M.K. Moradllo, C. Qiao, B. Isgor, S. Reese, W.J. Weiss, Relating the Formation Factor of Concrete to Water Absorption, ACI Materials Journal 115(6) (2018) 887-898.

[22] M.K. Moradllo, S. Reese, J. Weiss, Using Neutron Radiography to Quantify the Settlement of Fresh Concrete, Advances in Civil Engineering Materials 8(1) (2019).

[23] M.K. Mordallo, L. Montanari, P. Suraneni, S.R. Reese, J. Weiss, Examining Curing Efficiency Using Neutron Radiography, Transportation Research Record: Journal of the Transportation Research Board 2672(27) (2018) 13-23.

[24] P. Trtik, B. Münch, W. Weiss, A. Kaestner, I. Jerjen, L. Josic, E. Lehmann, P. Lura, Release of internal curing water from lightweight aggregates in cement paste investigated by neutron and X-ray tomography, Nuclear Instruments and Methods in Physics Research Section A: Accelerators, Spectrometers, Detectors and Associated Equipment 651(1) (2011) 244-249.

[25] T.C. Powers, T.L. Brownyard, Studies of the physical properties of hardened Portland cement paste, Journal Proceedings, 1946, pp. 101-132.

[26] M.K. Moradllo, C. Qiao, M. Keys, H. Hall, M.T. Ley, S. Reese, W.J. Weiss, Quantifying Fluid Absorption in Air Entrained Concrete Using Neutron Radiography, ACI Materials Journal (2019) in press.

[27] M. Kang, H.Z. Bilheux, S. Voisin, C. Cheng, E. Perfect, J. Horita, J. Warren, Water calibration measurements for neutron radiography: Application to water content quantification in porous media, Nuclear Instruments and Methods in Physics Research Section A: Accelerators, Spectrometers, Detectors and Associated Equipment 708 (2013) 24-31.

[28] C.A. Schneider, W.S. Rasband, K.W. Eliceiri, NIH Image to ImageJ: 25 years of image analysis, Nature methods 9(7) (2012) 671-675.

[29] J. Weiss, M.R. Geiker, K.K. Hansen, Using X-ray transmission/attenuation to quantify fluid absorption in cracked concrete, International Journal of Materials and Structural Integrity 9(1-3) (2015) 3-20.

[30] Y. Bu, J. Weiss, Saturation of air entrained voids and its implication on the transport of ionic species in concrete, (2014).

[31] H. Wong, A. Pappas, R. Zimmerman, N. Buenfeld, Effect of entrained air voids on the microstructure and mass transport properties of concrete, Cement and Concrete Research 41(10) (2011) 1067-1077.

[32] M.T. Ley, D. Welchel, J. Peery, S. Khatibmasjedi, J. LeFlore, Determining the air-void distribution in fresh concrete with the Sequential Air Method, Construction and Building Materials 150 (2017) 723-737.

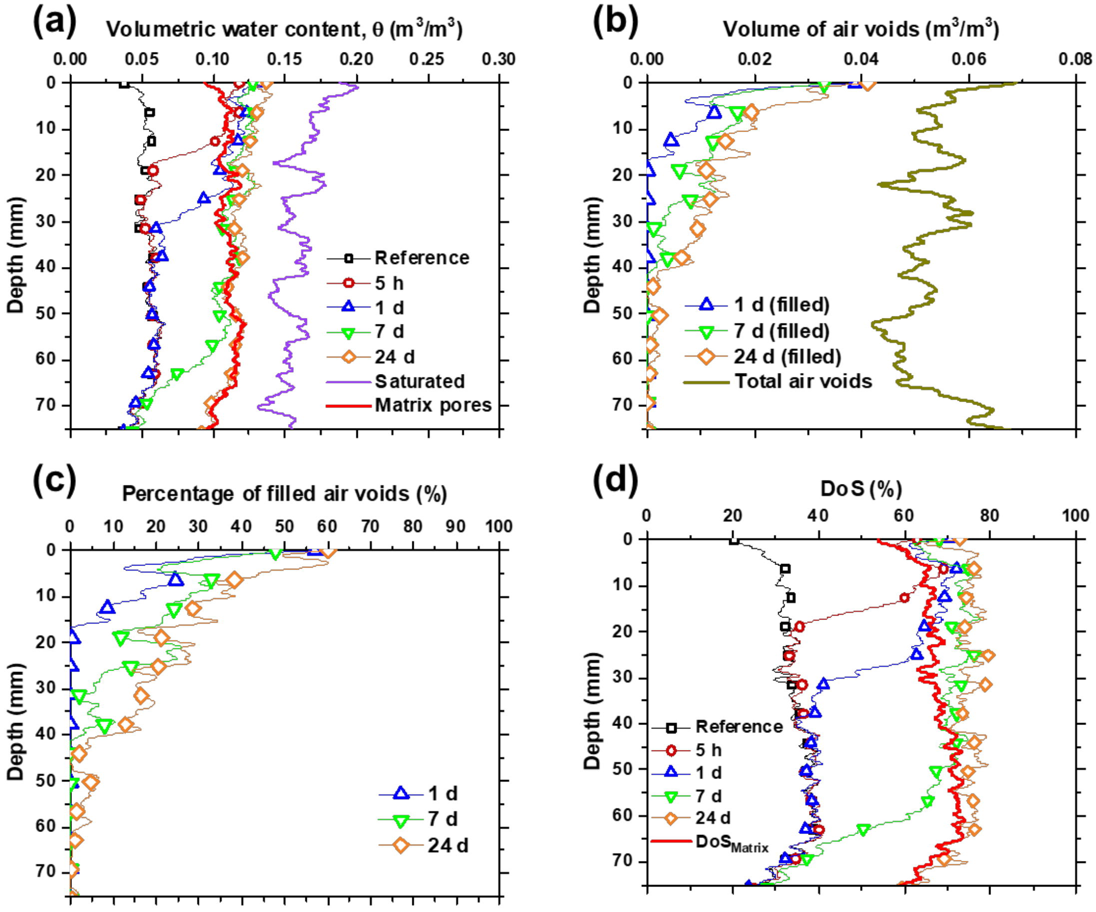

Fig. 1 – An example of time-dependent profiles of: (a) volumetric water content (b) volume of filled air voids, (c) percentage of filled air voids, and (d) degree of saturation over depth from NR.

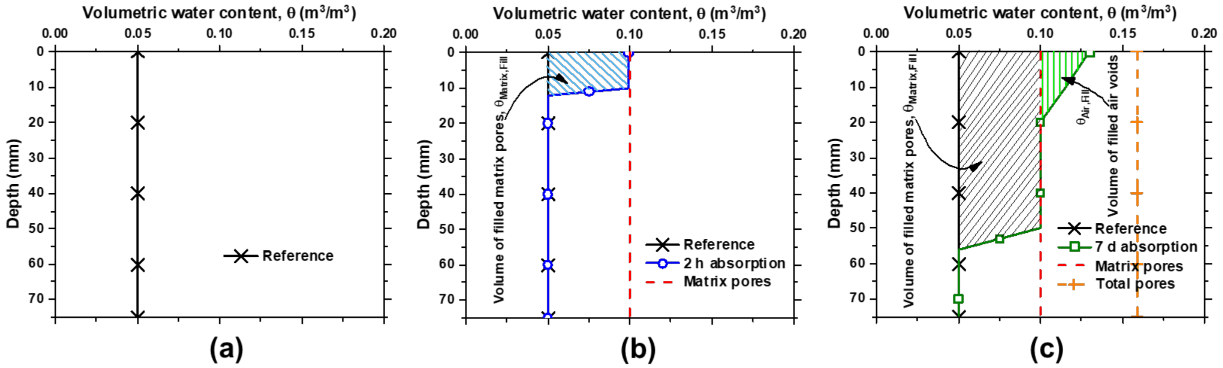

Fig. 2 – A procedure of determining volume of water filled pores: (a) An example of initially filled pores after conditioning at 50% RH obtained from reference radiograph, (b) an example of matrix pores filling during absorption at early ages, and (c) an example of concurrent matrix pores and air voids filling during the absorption experiment. (Note: Volume of total pores obtained from a vacuum-saturated radiograph).

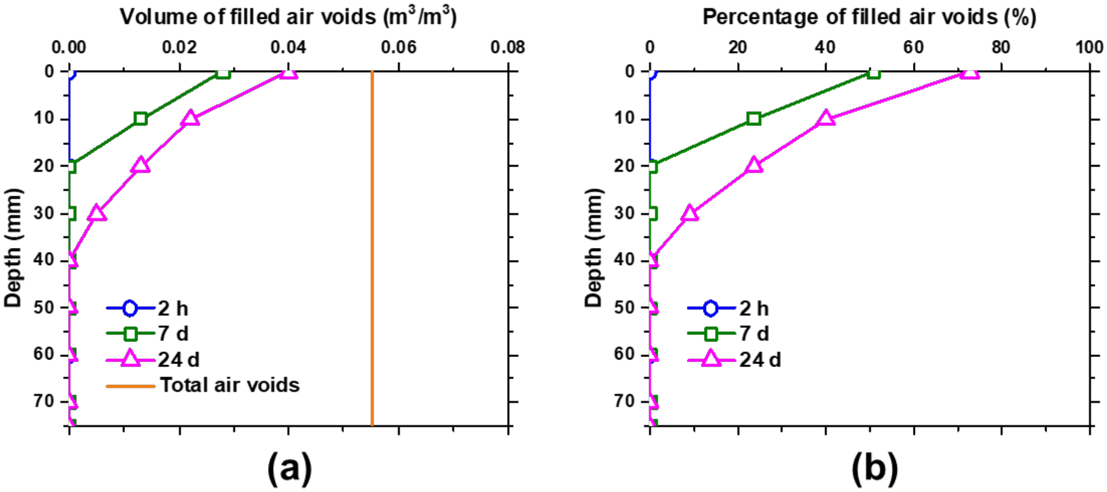

Fig. 3 – An example of smoothed: (a) Time-dependent profiles of volume of water filled air voids and (b) time-dependent percentage of water filled air voids (i.e., DoS of air voids).

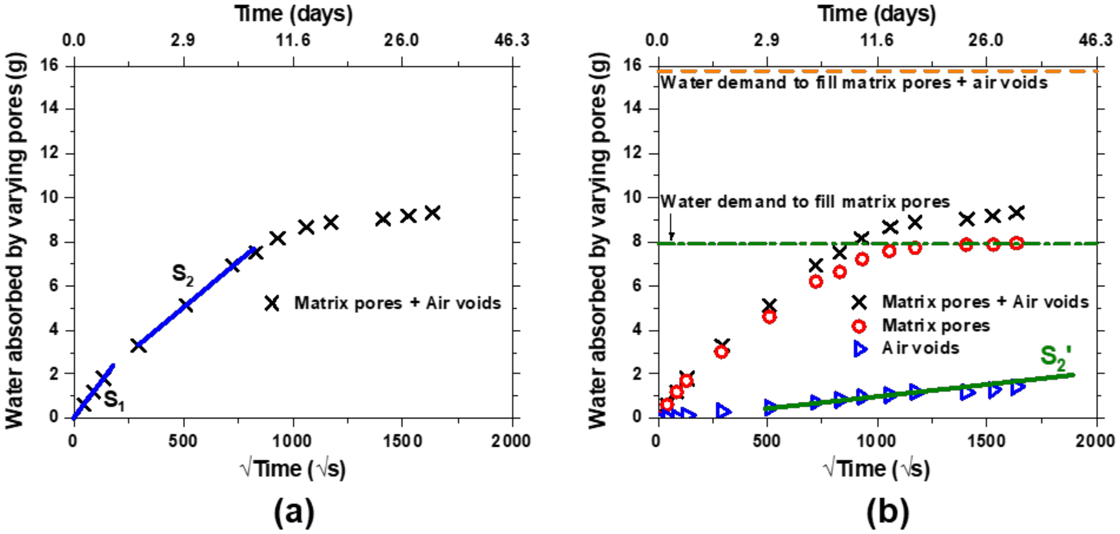

Fig. 4 *– An example of the time-dependent water mass absorbed by matrix pores and air voids from NR: (a) represents the initial and secondary absorption rates (S_1 and S_2) based on ASTM C 1585-14 definition and (b) represents the filling rate of air voids (S_2')' based on Eq. 10.*

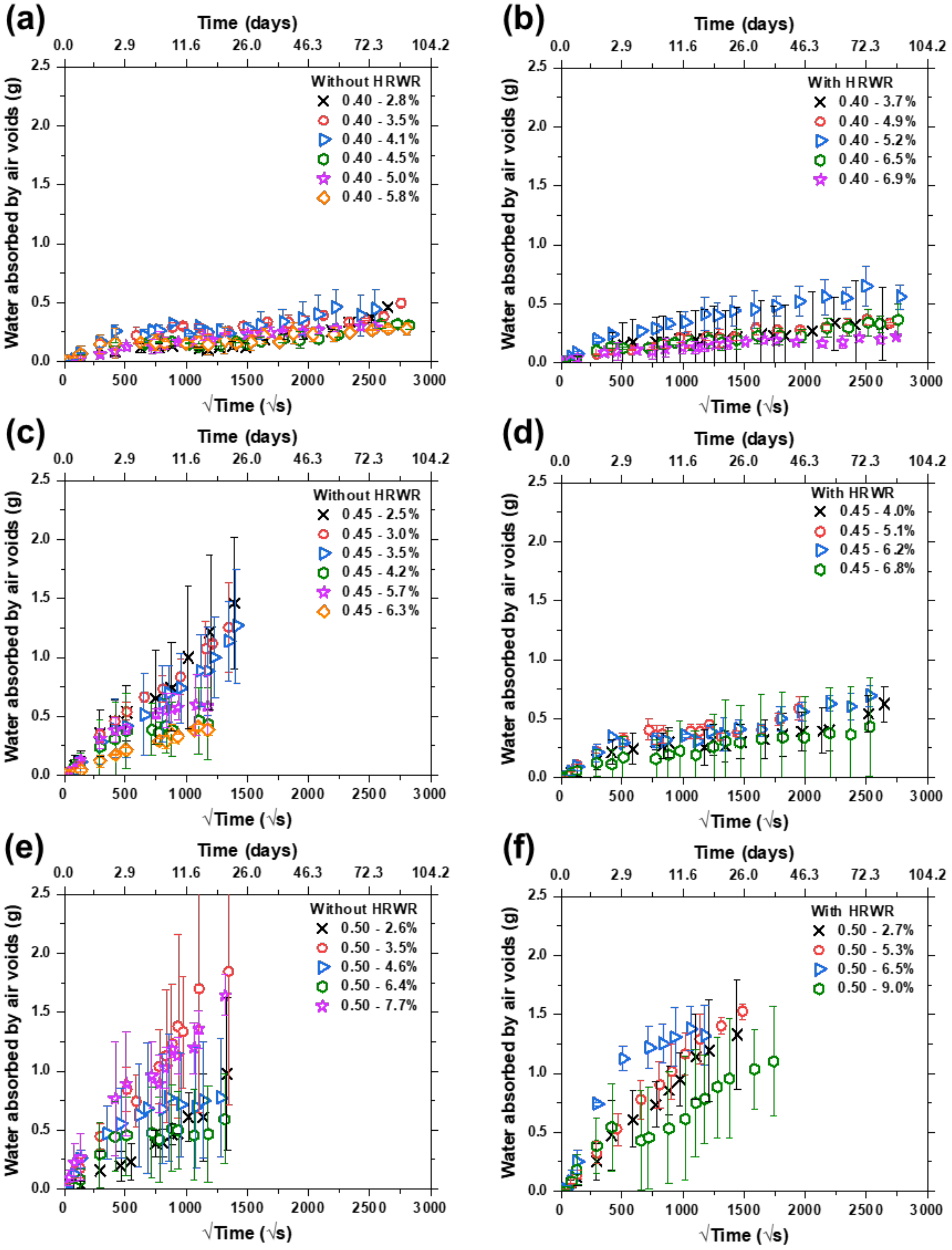

***Fig. 5** – Time-dependent amount of fluid absorbed by air voids in the samples with varying w/c and air contents with and without HRWR.*

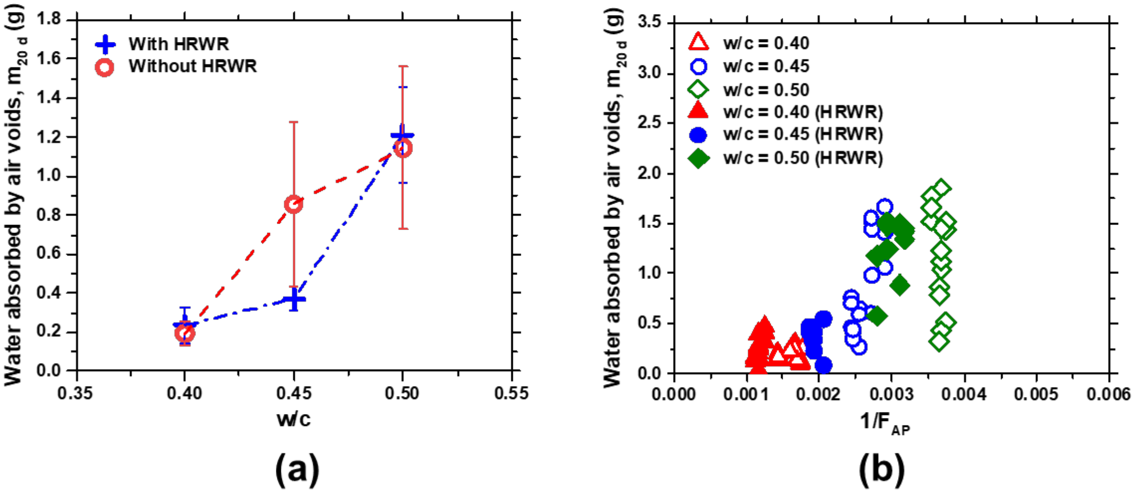

Fig. 6 *– Amount of water absorbed by air voids after 20 d versus (a) w/c and (b) the inverse of apparent formation factor for the samples with varying air content with and without HRWR.*

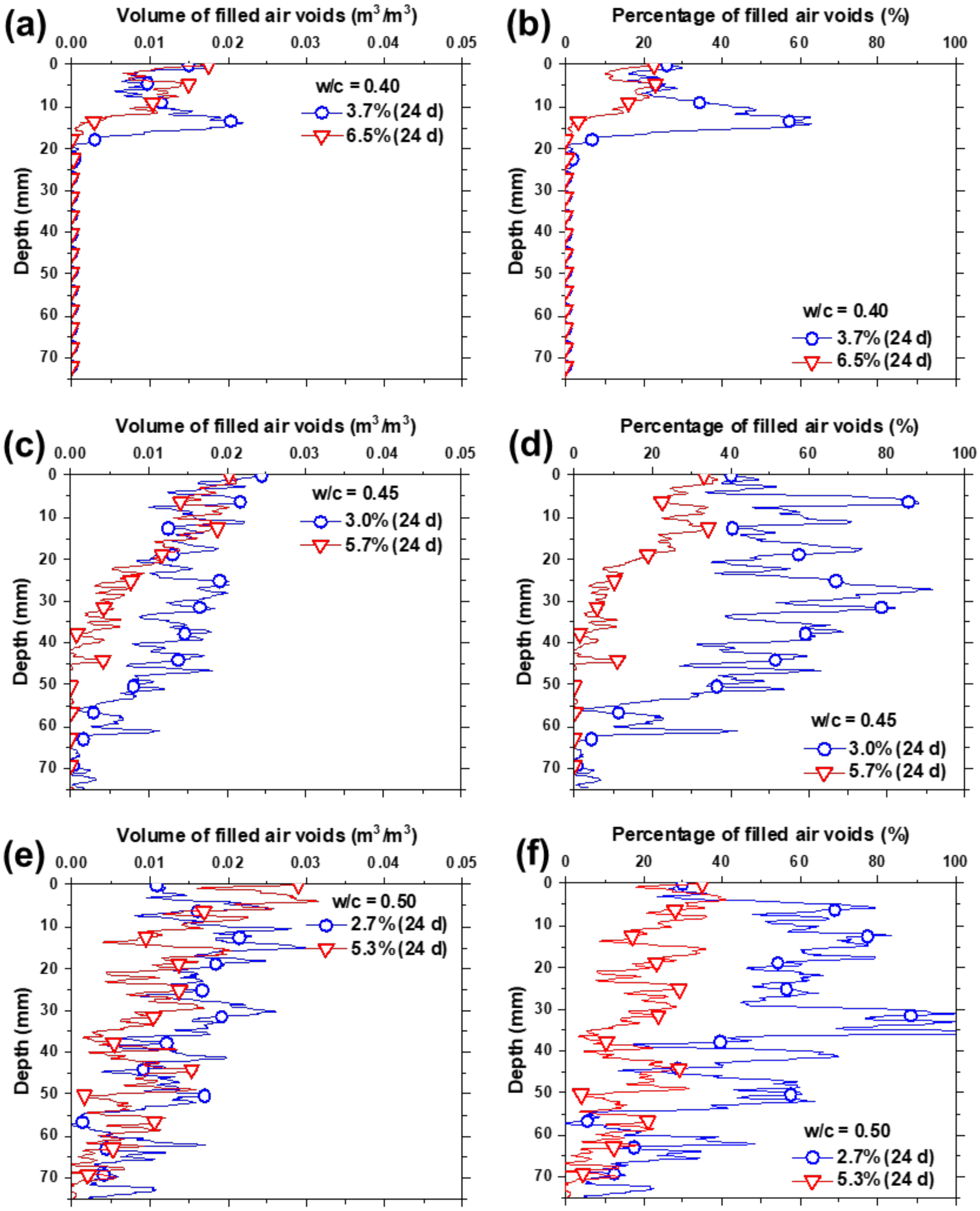

***Fig.** 7 – The profiles of the volume and percentage of water filled air voids for the samples with varying w/c and air contents: (a), (c), and (e) present the volume of filled air voids over depth for the samples with varying w/c and air contents at a comparable time, and (b), (d), and (f) compare the percentage of filled air voids (i.e., DoS of air voids) for the same set of samples.*

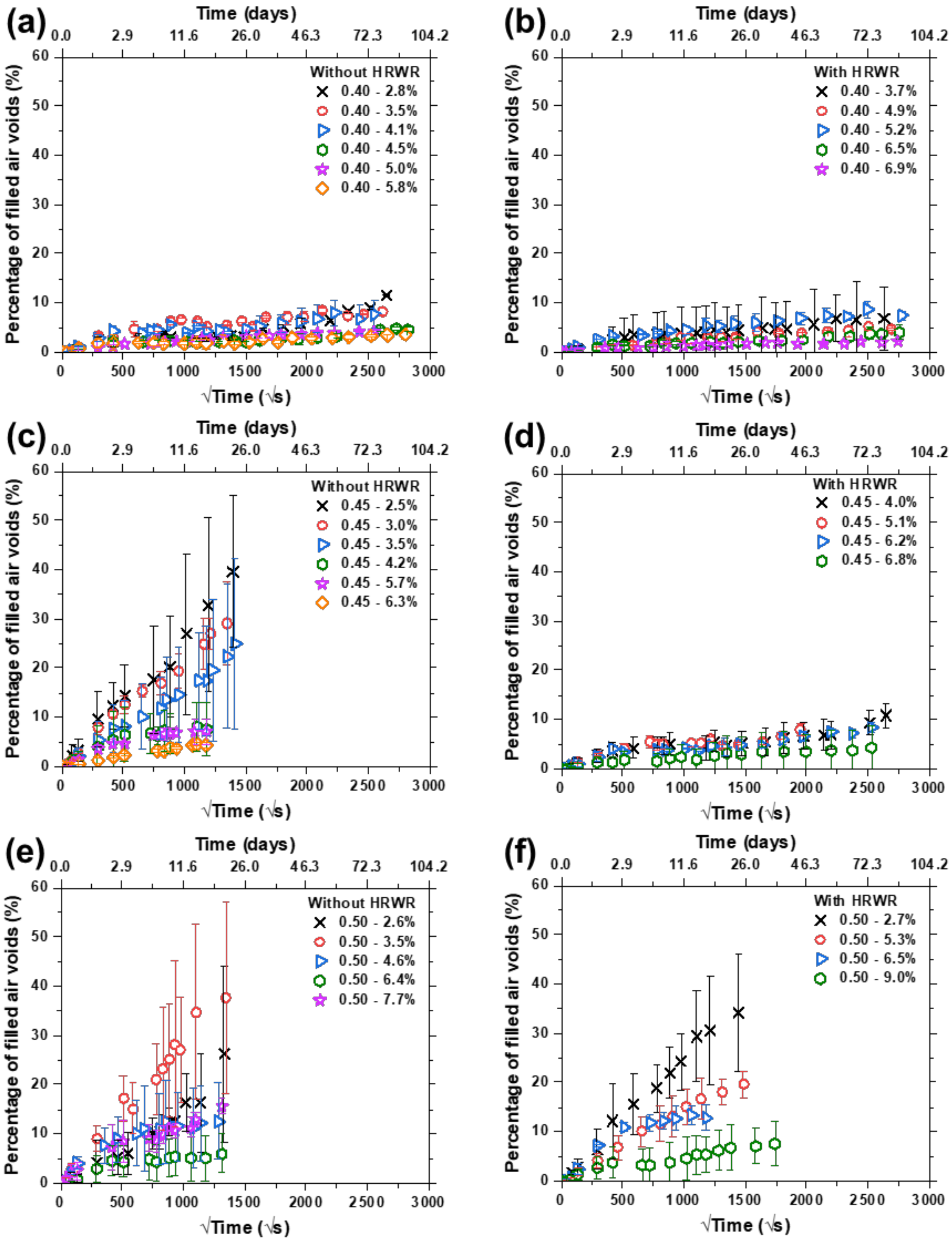

Fig. 8 *– The comparison of time-dependent percentage of water filled air voids for the samples with varying w/c and air contents with and without HRWR.*

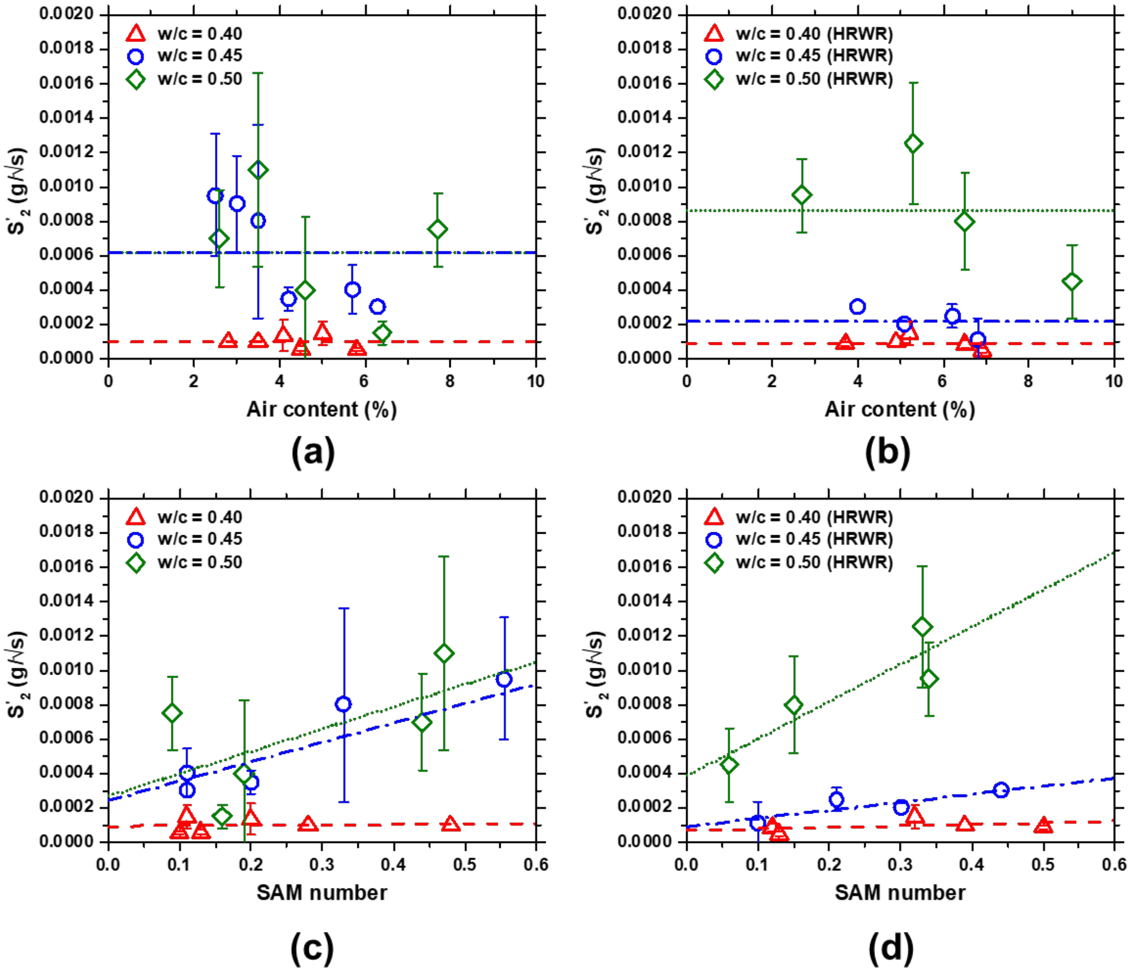

Fig. 9 *– The calculated water absorption rate by air voids (S_2') versus air content and SAM number for the samples with varying w/c with and without HRWR.*

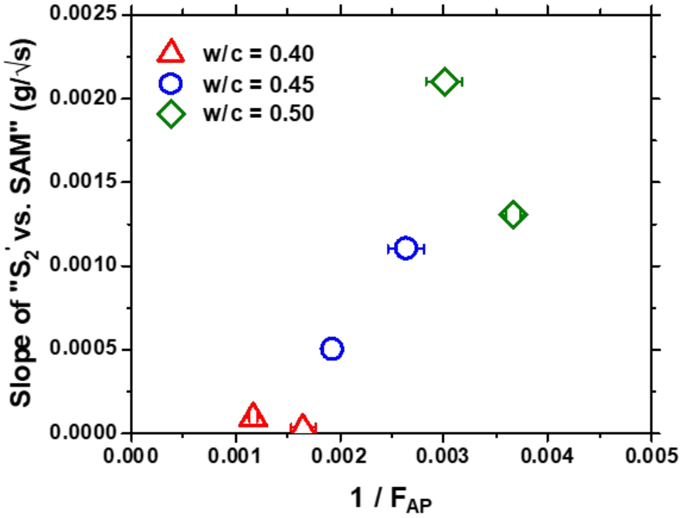

Fig. 10 *– The slope of "S$_2$' versus SAM number" (calculated from Figs. 9c and d) versus the inverse of apparent formation factor for the samples with varying w/c.*

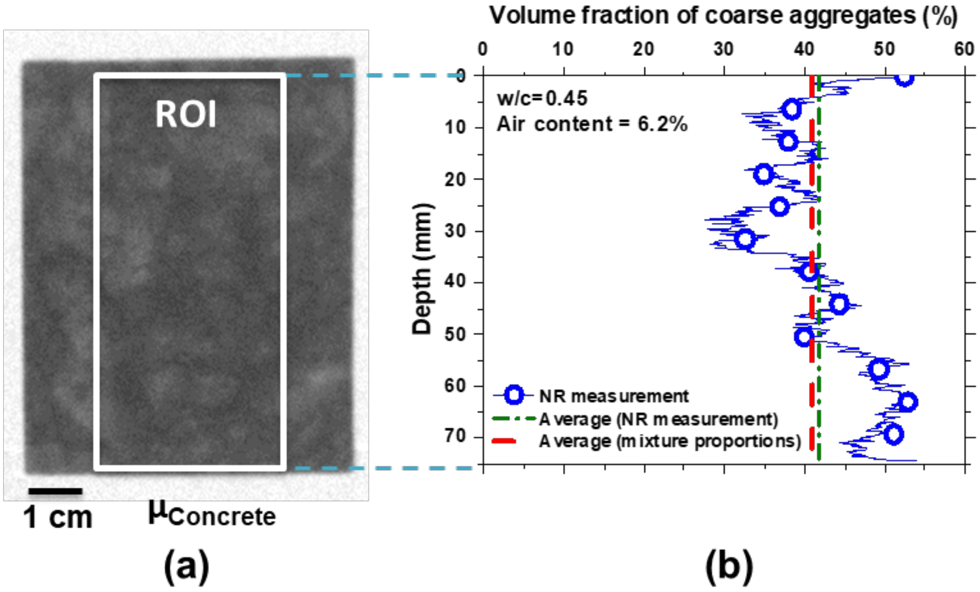

Fig. A.1 *– An example of: (a) Radiograph from concrete sample with selected ROI to determine the attenuation coefficient of concrete over depth and (b) calculated volume fraction of coarse aggregate over the sample depth.*

ESTABLISHING A FREEZE-THAW PREDICTION MODEL: DETERMINING THE FREEZING AND THAWING PERFORMANCE OF MORTAR SAMPLES USING LENGTH CHANGE MEASUREMENTS

Rita Maria Ghantous[1, 3], Mehdi Khanzadeh Moradllo[1], Hope Hall[2], M. Tyler Ley[2],

W. Jason Weiss[1]

[1] *School of Civil and Construction Engineering, Oregon State University, 1491 SW Campus Way,*
Corvallis, OR 97331, USA
Corresponding author e-mail: jason.weiss@oregonstate.edu

[2]*Department of Civil and Environmental Engineering, Oklahoma State University, Stillwater,*
OK 74078, USA

[3]Civil Engineering Department, French School of High Studies in Engineering, 13 Rue de Toul,
Lille, 59000, France

Abstract

Freezing and thawing (FT) damage in cementitious materials is dependent on its degree of saturation. It has been proposed that a critical value exists for the degree of saturation (DOS_{CR}) of cementitious materials. Cementitious materials with a $DOS>DOS_{CR}$ are susceptible to FT damage. Recently, a systematic methodology has been developed to determine DOS_{CR} of cement paste samples based on length change measurements. This article explores the extension of this methodology from cement paste samples to mortar samples. In addition, the influence of three parameters were investigated to determine their impact on the FT performance of the mortar samples. The first investigation focused on the preconditioning phase of the samples, especially the drying temperature. The second investigation examined the influence of the heating/cooling rate as well as the lowest temperature experienced by the sample. The third investigation examined the characteristics of the mortar samples like the volume and quality of the air voids in the system. The results obtained from this study further confirm that length change measurements can be used to determine DOS_{CR} of mortar samples. Drying the samples at 105°C during preconditioning can induce micro cracks in the samples that lead to an overestimation of DOS_{CR}. The tested heat/cool rates and lowest exposure temperatures do not show a significant impact on the FT performance of the mortar samples. Finally, a correlation exists between the air void quality and the FT performance. Samples with a high quality air void distribution (a sample with a Sequential Air Method (SAM) number ≤0.20) show better FT performance compared to those with a poor air void distribution.

Keywords: length change, Freeze thaw performance, mortar samples, critical degree of saturation

Introduction

Several previous studies have shown that freezing and thawing damage in concrete is dependent on its degree of saturation (DOS) [1-6]. The DOS is the ratio of the volume of the fluid-filled pores to the total volume of pores inside the cementitious sample. The critical degree of saturation (DOS_{CR}) is the threshold value for the DOS. A concrete with a DOS higher than DOS_{CR} develops freezing and thawing damage while no damage will be visible when the DOS of concrete is smaller than DOS_{CR} [6-10].

A sorption-based model was originally proposed by Fagerlund [11] and updated through several recent studies [7, 8, 12-19] to quantify the performance of concrete in a freeze-thaw environment. This model is discussed in the CEB model code as well as AASHTO PP-84. This model uses a two-stages sorption process. During the first stage of the sorption process, the gel and capillary pores get filled with water in a short period of time. During the second stage of sorption, the entrained and entrapped air voids begin to be filled with water. The second stage in this model takes substantial more time than the first because entrained air pores are bigger than the gel and capillary pores. They are therefore difficult to fill with water because the capillary suction is low in pores with a large diameter [20]. Further, it has been speculated that the diffusion of vapor out of the sample can also limit the rate of sorption. Consequently, the DOS in cementitious materials containing entrained air is generally lower than the DOS of non-air entrained concrete, which explains their higher resistance to FT cycles [7]. In addition, the voids induced by the entrained air provide a space for the relief of pressure (hydraulic, osmotic, electrical or other) when the ice forms [21, 22]. This reduces the stress on the cement surrounding the ice and consequently reduces the damage. Furthermore, the preliminary results of Todak [23] proposed that the DOS_{CR} is dependent on the quality of the air system.

Several techniques were used in previous studies to assess the freezing and thawing performance of concrete. The most common techniques used to assess freezing and thawing damage of concrete are based on either quantifying the reduction in the dynamic modulus of elasticity [23-25] or quantifying the reduction in the ultrasonic pulse velocity [12, 15, 23, 26]. Electrical resistivity measurements have also been used as an indicator oF FT damage [8]. Conventional FT tests like ASTM C666 require several samples and a long duration (6 to 9 weeks) for the FT damage assessment. A recent study [27] developed a systematic methodology based on length change measurements that allows reducing the time for the quantification of the DOS_{CR}. It consists in testing small specimens that can be conditioned rapidly, which allows specific scientific features to be studied more quickly and with a high accuracy. Length change measurements have been proven able to be used for determining accurately DOS_{CR} of cement paste samples. However, the determination of DOS_{CR} of mortar samples using length change measurements has not been established yet. Consequently, the first objective of this study is to extend the use of the length change measurements for determining DOS_{CR} of cement paste to mortar samples. In addition, this study will investigate the impact of the volume and quality of air voids on DOS_{CR}.

Experimental program

Materials and mixture proportions

Type I ordinary portland cement (OPC I) consistent with the specification of ASTM C150 was used in this study. The physical and chemical properties of this cement are described in Table 1. The specific gravity of this cement is 3.15 and its Blaine finesses is 386 m2/kg. Natural river sand was used as a fine aggregate. The natural sand had a specific gravity of 2.61 and an absorption of 0.44%. Two coarse aggregates were used in this study with specific gravity of 2.75 and 2.72, an absorption of 0.73% and a maximum size of 19.1 mm. A wood rosin air-entraining admixture (AEA) and a polycarboxylate (PC)-based high range water reducing admixture (HRWR) were added to the mixtures in order to induce air voids and alter their size and distribution.

Nine different mortar mixtures were prepared with varying air void content and air void quality. Fresh concrete was first mixed using the procedure described in [28]. The Sequential Air

Method (SAM) number was used to indicate the air void quality (air void content, size, and distribution) based on AASHTO TP 118-17 [28, 29]. The mixture characteristics are shown in Table 2.

After the air void content and SAM were measured on the fresh concrete. Mortar was obtained from the fresh concrete by sieving coarse aggregates out of it. The mortar was cast in plastic cylindrical molds of 102 mm (4 inches) in diameter and 203 mm in height (8 inches). The mortar was cured in the sealed molds for 90 days at 23 ± 2°C.

Table 7. Properties of the cement used in this study

Item	Percent by mass (%)
	Type I cement (OPC I)
Silicon Dioxide (SiO_2)	21.1
Aluminum Oxide (Al_2O_3)	4.7
Ferric Oxide (Fe_2O_3)	2.6
Calcium Oxide (CaO)	62.1
Magnesium Oxide (MgO)	2.4
Sulfur Trioxide (SO_3)	3.2
Sodium Oxide (Na_2O)	0.2
Potassium Oxide (K_2O)	0.3
Loss on Ignition	2.70
Tricalcium Silicate (C_3S)	56.7
Dicalcium Silicate (C_2S)	17.8
Tricalcium Aluminate (C_3A)	8.2
Tetracalcium Aluminoferrite (C_4AF)	7.8

Table 8. The mixture proportions and fresh properties of the mortar samples

Mixture	M1	M2	M3	M4	M5	M6	M7	M8	M9
Coarse aggregate 1 (kg/m^3)	1946.8	1946.8	1946.8	1946.8	1901.3	1901.3	1901.3	1901.3	1901.3
Coarse aggregate 2 (kg/m^3)	1297.9	1297.9	1297.9	1297.9	1267.5	1267.5	1267.5	1267.5	1267.5
Fine aggregate (kg/m^3)	2106.9	2106.9	2106.9	2106.9	2056.4	2056.4	2056.4	2056.4	2056.4
Cement (kg/m^3)	950.7	950.7	950.7	950.7	950.7	950.7	950.7	950.7	950.7
Water (kg/m^3)	427.8	427.8	427.8	427.8	475.3	475.3	475.3	475.3	475.3
w/c	0.45	0.45	0.45	0.45	0.45	0.45	0.45	0.45	0.45
AEA (g/m^3)	21.44	16.9	5.48	8.69	10.04	15.84	20.04	?	11.56
HRWR (g/m^3)	-	-	-	-	80.1	81.07	79.99	?	80.13
Air content (%)	4.9	4.1	2.6	3.2	4.2	5.9	8.3	9.5	4.5
SAM number	0.21	0.13	0.51	0.29	0.63	0.32	0.24	0.35	0.43

Samples geometry and preconditioning

Core samples of 10 mm diameter and 45 mm length were obtained from mortar samples using a diamond core bit. To obtain flat and parallel surfaces, both ends of each core were cut using a precision diamond saw that was water lubricated. The final mortar cores were 10 ± 0.2 mm diameter and 20.5 ± 0.4-mm length (Figure 1). More details about this procedure for cores preparation can be found in [27]. The number of cores obtained from every mixture is given in Table 3.

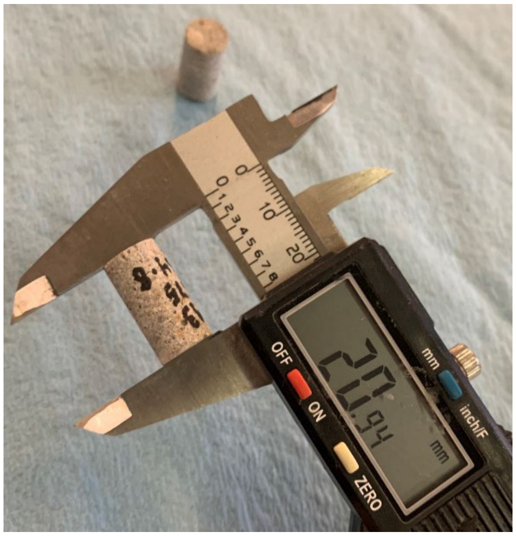

Figure 19. Example of the mortar core used for length change measurements

Table 9. Number of cores from every mixture

Mixture	M1	M2	M3	M4	M5	M6	M7	M8	M9
Number of cores	13	13	13	13	13	13	13	23	20

These mortar cores were first oven dried until reaching a constant mass (mass evolution over 24 hours less than 0.1%). This mass at the end of the drying period was recorded as an oven dried mass “m_{OD}”. The mortar cores of all the mixtures were dried in a 60°C oven. However, only 10 mortar cores from mixture 9 (M9) were dried at 105°C temperature instead of 60°C temperature in order to determine the impact of the drying temperature on the measured DOS_{CR}.

The samples were then fully saturated with lime-water solution at 6 Torr pressure in a vacuum saturator according to the procedure described in [30]. The mortar cores were kept immersed in the solution for an additional 72 ± 4 hours after being removed from the vacuum saturator.

In order to determine DOS_{CR}, the freezing and thawing damage in mortar cores with different degrees of saturation ranging from 70% to 100% needed to be quantified. For this reason, each mortar core was dried at 23 ± 1°C until the desired saturation level was reached. They were then sealed in separate bags for 7 days at 23 ± 1°C in order to allow the moisture content throughout the depth of the core to reach equilibrium. The DOS evaluated in this study are: 70, 73, 75, 78, 80, 82, 84, 85, 88, 90, 95, 97 and 100%.

Experimental method

A methodology has been developed in [27] to determine DOS_{CR} of cement paste based on length change measurements. The length change of the cementitious core samples was measured during FT cycle using a thermomechanical analyzer (Q400 TMA) equipped with a macroexpansion probe [27]. A cooling unit was connected to the TMA in order to reach temperatures below freezing.

This research study aimed on extending the methodology developed in [27] for cement paste to mortar samples with varying air content and air quality. In addition, the influence of the FT temperature range and FT heat/cool rate on the FT damage and DOS_{CR} were tested.

The following sections will give more details on the methodology for determining DOS_{CR} as well as the different FT parameters tested.

Determination of DOS_{CR} based on length change measurements

Each mortar core was taken out of the sealed bags after the preconditioning period of 7 days. Its mass was measured and the sample was immediately sealed with aluminum tape along their vertical surfaces in order to minimize moisture loss during the duration of the FT cycle (Figure 1(a)). The freezing and thawing cycle applied on the mortar cores in order to determine the impact of air voids quality on DOS_{CR} is shown in Figure 1 (b).

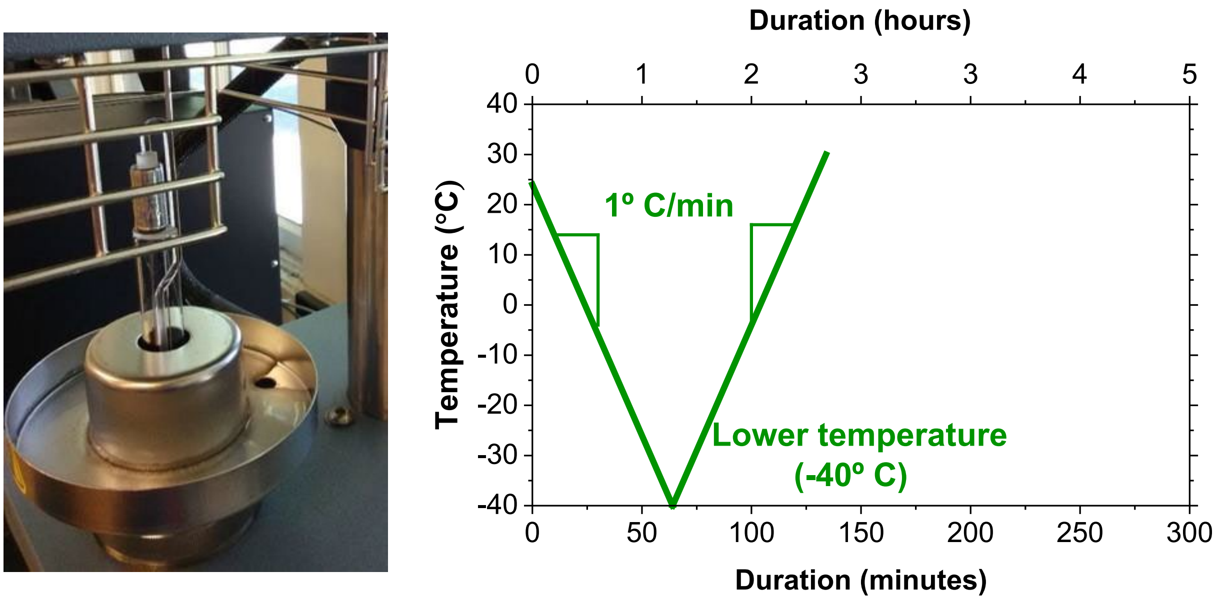

(a) (b)

Figure 20. Length change measurements: (a) Mortar sample inside the furnace of the TMA; (b) FT cycle

A typical strain-temperature plot of a mortar sample exposed to FT cycle in TMA in a saturated state ($DOS > DOS_{CR}$) is shown in Figure 2 (a). The strain measured in the sample decreases with the decrease in the temperature until the freezing point. When the ice develops in the pores of the mortar core, the volume of the sample increases and that is illustrated by the increase in the measured strain around -10°C (freezing point). When the sample is exposed to an increase in the temperature, the ice melts and is accompanied with a reduction in the volume, which is visualized, by a reduction in the measured strain around 0°C. The length of the sample at the end of the FT cycle is higher than its length before the FT cycle. This is illustrated by the positive residual strain identified in (Figure 2 (a)). Several studies [5, 10, 31] related the residual strain in cementitious materials to FT damage. The residual strain is determined based on Equation 1.

$$Residual\ strain = \frac{l_B - l_A}{l_A} \qquad 3$$

Where, l_B is the length of the sample at point B; l_A is the length of the sample at point A.

Figure 2 (b) shows the strain-temperature plot for a mortar sample with a DOS that is less than DOS_{CR}. Samples with a low DOS show a nearly linear response in length change throughout the FT cycle (Figure 2 (b)). In addition, the residual strain values measured on these samples is not positive, which indicated the absence of FT damage.

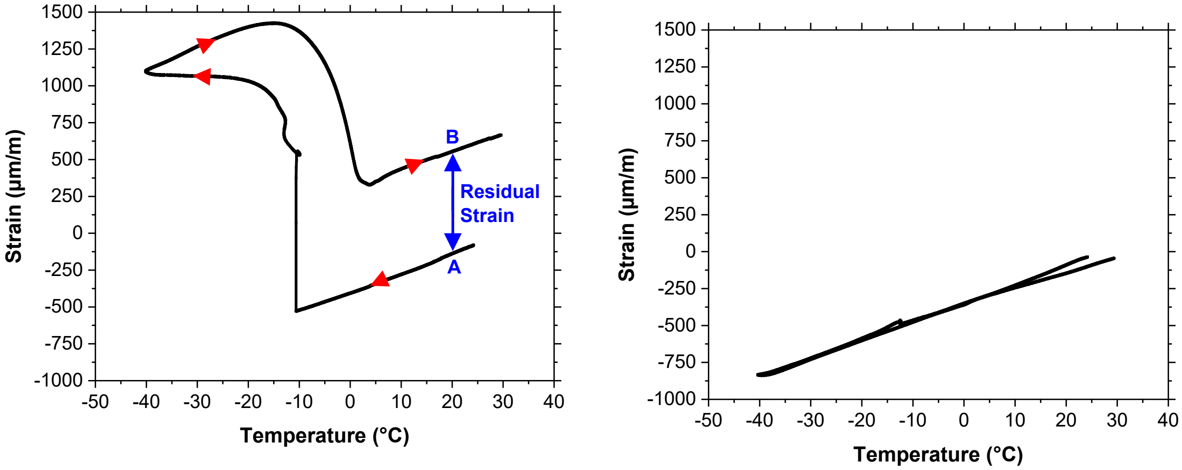

(a) DOS > DOS$_{CR}$ (b) DOS<DOS$_{CR}$

Figure 21. Strain evolution with respect to temperature: (a) DOS > DOS$_{CR}$; (b) DOS < DOS$_{CR}$

A sample with a DOS less than DOS$_{CR}$ (60% DOS <DOS$_{CR}$) was exposed to 12 FT cycles inside the TMA. At this DOS, the sample would not be expected to develop any FT damage. Consequently, the residual strains measured at the end of each cycle on this mortar core can be used to determine a threshold value for residual strain. Only samples that show a residual strain above this threshold value are considered damaged. The residual strains obtained at the end of every FT cycle are shown in Figure 3 (a). It can be seen that all the measured residual strains are negative (i.e. range between -28.82 µm/m and -55.80 µm/m). Consequently, samples with a residual strain below zero do not develop any FT damage, for this reason, 0µm/m was considered as a threshold value for the residual strain. Negative values for the residual strain were first explained by Powers [32]. He stated that when ice develops in a cavity, it draws unfrozen water from the surrounding pores. Consequently, the flow of water from the gel to the capillary pores induces shrinkage, which can result in negative residual strain values after FT cycle.

Figure 3 (b) shows the evolution of the residual strain versus the DOS of the mortar cores. The DOS$_{CR}$ can be obtained by fitting a line as shown in Figure 3(b) and identifying the DOS associated with residual strain that is equal to 0µm/m.

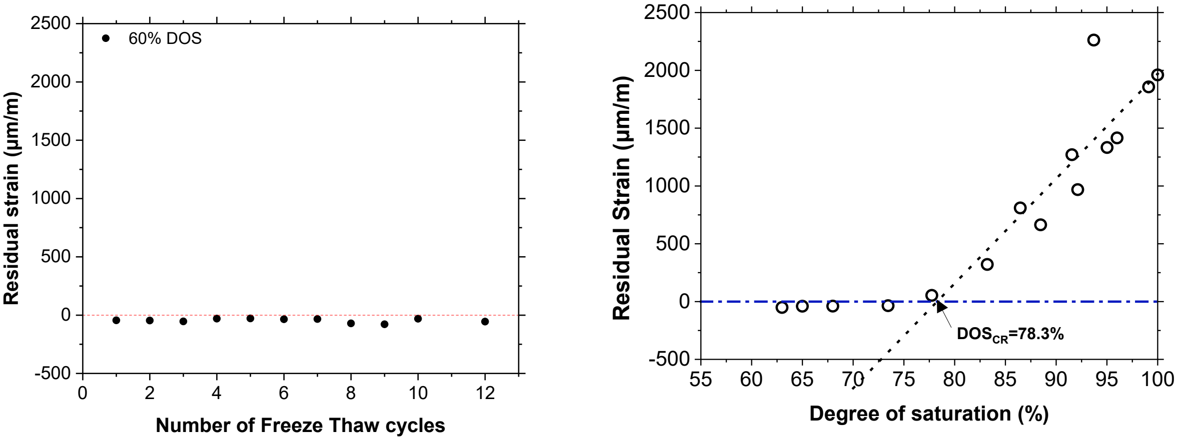

(a) (b)

Figure 22. Determination of DOS$_{CR}$ based on length change measurements

The procedure illustrated in Figure 4(b) was used to determine DOS$_{CR}$ on mortar samples with different volumes and quality of air voids. In addition, ultrasonic pulse velocity measurements were performed on the mortar cores before and after each FT cycle using 150 kHz transducers connected to Pundit PL-200 ultrasonic pulse velocity (UPV). The reduction in ultrasonic wave speed was used to quantify FT damage as shown in equation 2 [9]. The damage obtained from ultrasonic pulse velocity measurements was compared to the one obtained from residual strain values in order to prove the reliability of the use of the TMA procedure on mortar to quantify FT damage.

$$D = 1 - \frac{E}{E_0} = 1 - \left(\frac{V}{V_0}\right)^2 = 1 - \left(\frac{t_0}{t}\right)^2 \qquad 4$$

Parameters tested: FT temperature range

The influence of the temperature range on the FT damage was investigated in this study. Mortar cores from mixture 9 were exposed to different temperature cycles shown in Figure 4. For samples exposed to a minimum temperature of -12°C, the duration at which this lowest temperature was held was higher than the other cycles. This was chosen to be done in order to allow the time needed for ice formation. The FT damage was quantified on each mortar core exposed to these FT cycles using the residual strain values. The obtained data were compared between each other.

A Q20 Low Differential Scanning Calorimetry LT-DSC was used to measure the amount of ice that develops during each of the freezing and thawing cycles shown in Figure 4. For this experiment, a mortar specimen from mixture 9 was dried at 60°C until reaching a constant mass (difference between mass evolution within 24 hours is less than 0.1%). A slab-shaped sample of 35±2 mg was obtained from this dried mortar specimen and weighed. This mass was considered as oven dried mass (m_{OD}). The slab shaped samples were saturated under vacuum at 6 Torr pressure according to the procedure described in [30]. The mortar cores were kept immersed in the solution for an addition 48 ± 2 hours after being removed from the vacuum saturator. Each of them was then sealed in a stainless steel pan for 60 minutes at 24°C constant temperature before being exposed to the corresponding freezing and thawing cycle. The data collected during the cooling phase in LT-DSC were not reliable to use for quantifying the amount of ice that developed due to nucleation and super cooling effect. The energy associated with ice melting between -10°C and -1°C was measured using the LT-DSC (Figure 5). The amount of ice that developed in the measured mortar specimen was quantified by dividing the measured energy by the latent heat of ice melting (334 J/g). The amount of measured ice was correlated with the amount of FT damage that was measured using TMA.

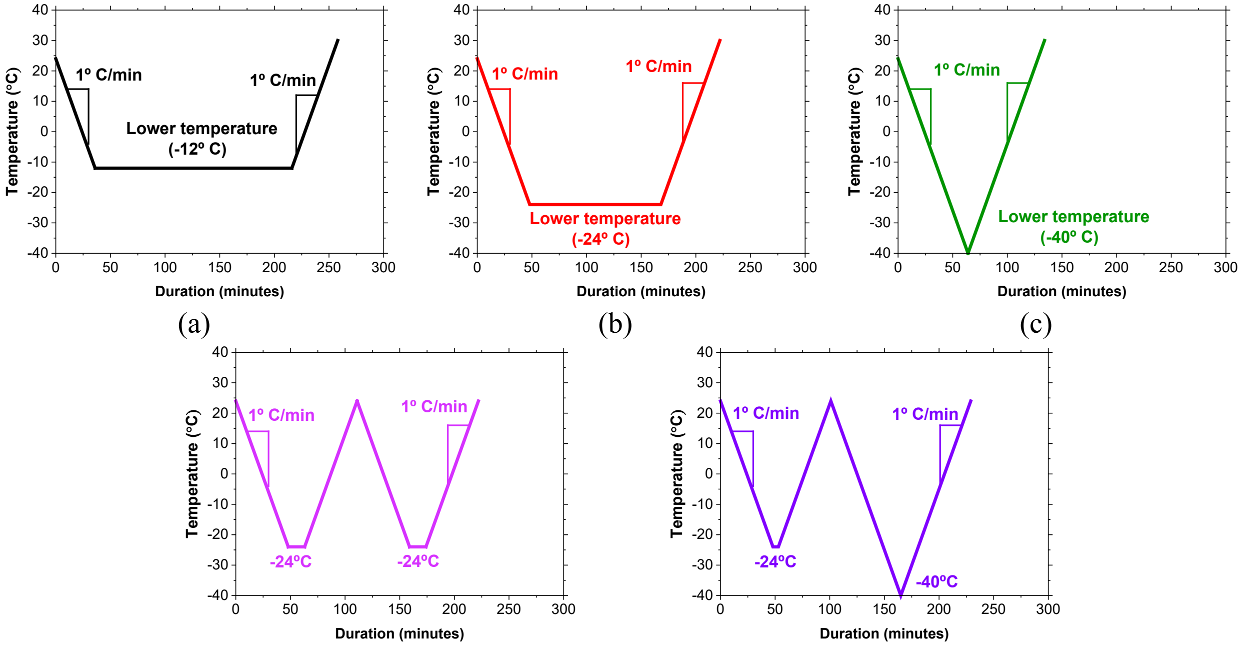

(a) (b) (c)

(d) (e)

Figure 23. FT cycles in the TMA: (a) one FT cycle with a minimum temperature of -12°C; (b) one FT cycle with a minimum temperature of -24°C; (c) one FT cycle with a minimum temperature of -40°C; (d) two FT cycles with a minimum temperature of

- 24°C both; (e) two FT cycles: -24°C minimum temperature for the first one and -40°C minimum temperature for the second cycle.

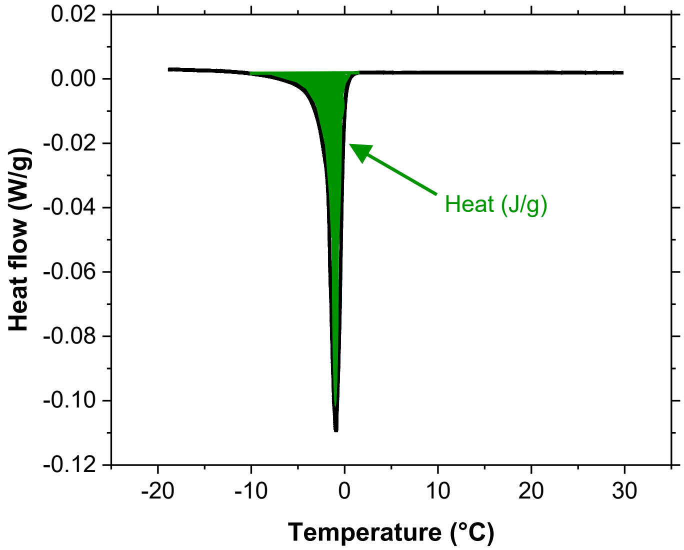

Figure 24. Heat flow signal due to ice melting

Parameters tested: FT heat/cool rate

FT damage was quantified using Acoustic Emission Longitudinally Guarded Comparative Calorimeter (AE-LGCC) with a lower heating and cooling rate than the one used in the TMA [23]. In order to compare the impact of heat/cool rate on the DOS_{CR}, a number of samples from mixture 9 were exposed to FT cycle inside the TMA at 0.08°C/min cool rate; 0.13°C/min heat rate (Figure 6). The DOS_{CR} was determined for these samples exposed to small heat/cool rate and compared with the one obtained on other samples from the same mix exposed to the faster FT cycle shown in Figure 1(b).

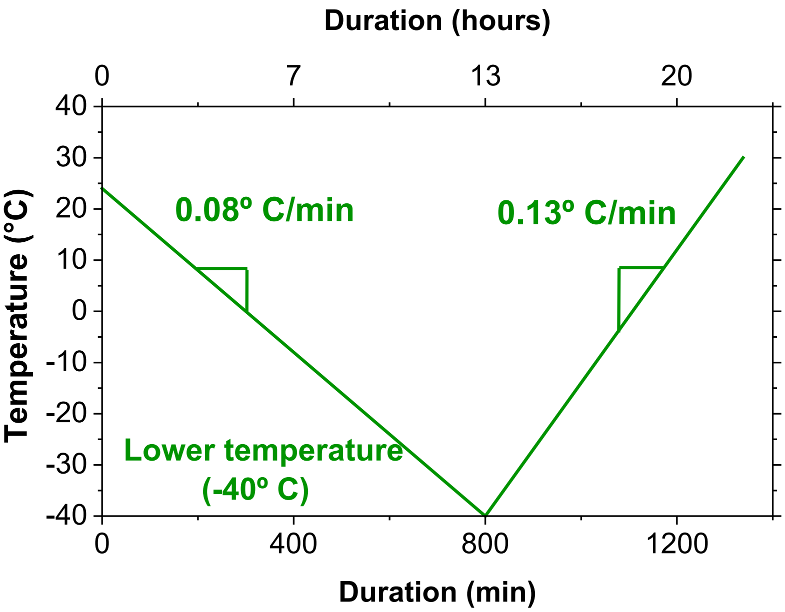

Figure 25. FT cycle in the TMA with a small heat/cool rate

Results and discussion

1. Impact of the drying temperature on the DOS_{CR}

During the preconditioning phase, samples from mixture 8(M8) were dried at 105°C while other samples from the same mix were dried at 60°C. They were then preconditioned at different DOS and exposed to FT cycles inside the TMA. DOS_{CR} was determined for the samples dried at 105°C and compared with the one obtained on samples dried at 60°C according to the procedure described in Figure 3(b). It is shown in Figure 7 that the DOS_{CR} measured on samples dried at 105°C is higher than the one measured on samples dried at 60°C. The hypothesis that explains this difference is that the drying of the mortar cores at 105°C temperature induces micro cracks inside the cores, which creates space for the ice to develop during the FT cycle. This induces a reduction in the pressure accompanied by ice formation and consequently a reduction in the FT damage.

In order to prove this hypothesis, some cores from all the mixtures were dried at 105°C while others were dried at 60°C until reaching a constant mass (mass evolution within 24 hours is less than 0.1%). After the drying period, they were all saturated in a vacuum saturator at 6Torr in order to determine the total Pore volume according to the procedure described in [30]. After the saturation was completed, their surface-dry mass and their immersed apparent mass was measured.

At 60°C, some of the pores do not dry similarly to 105°C. In order to be able to correlate the difference in the porosity to the presence of micro cracks only, the samples that were initially dried at 60°C were dried again in the 105°C and their dry mass at 105°C was used to calculate their porosity according to equation 3.

$$Porosity\ (\%) = \frac{B - A}{B - C} \times 100 \tag{5}$$

Where B is the mass of the surface-dry sample in air after vacuum saturation; C is the apparent mass of sample in the water after vacuum saturation and A is the oven-dried mass of the sample.

For samples that were initially dried at 105°C, A corresponds to the mass recorded at the end of the drying process. As mentioned previously, the samples that were initially dried at 60°C were dried again at 105°C after determining the values for B and C. The mass of the samples at the end of drying at 105°C temperature was used as a value for A parameter. The comparison between the measured porosity is given in Figure 8. It is visible that the porosity measured on samples dried at 105°C is on average 1% higher than the one measured on samples dried at 60°C.

In addition, UPV measurements were performed on the samples before and after the drying. It should be noted that all the cores were at 50% DOS before drying. The reduction in the time of the travel of the UPV signal was calculated according to equation 4.

$$\Delta t = \left(1 - \left(\frac{t_b}{t_a}\right)^2\right) \times 100 \tag{6}$$

Where, t_b is the time needed for the UPV signal to travel from one transducer to another before the drying period; t_a is the same measurements but after the drying period.

Δt for samples dried at 60°C was equal to 13±1% while the one measured on samples dried at 105°C was equal to 27±1.5%.

Consequently, the higher porosity measured on samples dried at 105°C as well as the higher Δt calculated on these samples compared to those dried at 60°C could be an indicator that drying the samples at 105°C induces microcracks inside the matrix. Therefore, DOS_{CR} measured on mortar samples dried at 105°C could potentially be overestimated.

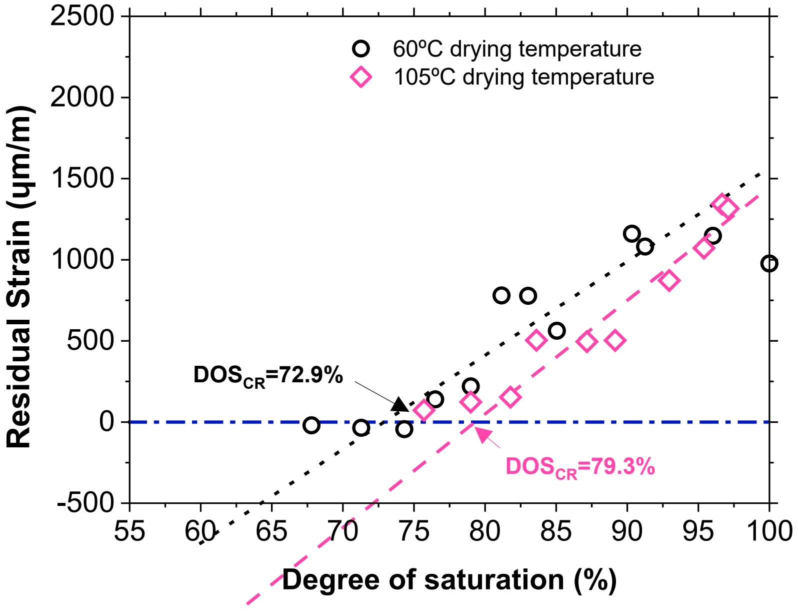

Figure 26. Impact of the drying temperature on the residual strain measured on mortar cores dried at 105°C in mortar samples with different DOS during FT cycle

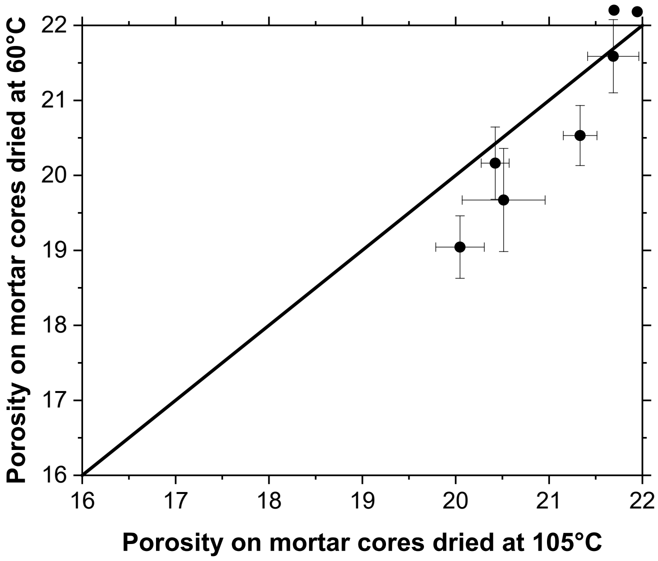

Figure 27. Comparison between the porosity of the mortar cores dried at 60°C with the one measured on the cores dried at 105°C

Impact of the temperature range on FT damage

Figure 9 (a) shows the residual strain measured at the end of the three different FT cycles presented in Figure 4 (a, b, c). The residual strain (indicator of FT damage) does not increase with the decrease in the lowest exposure temperature in the FT cycle.

Figure 9 (b and c) show the evolution of the strain as a function of temperature for the FT cycles described in Figure 4 (d,e). The two mortar samples were exposed to two consecutive FT cycles. The first FT cycle goes to a minimum temperature of -24°C for both samples. However, in the second FT cycle, one of the samples was exposed to a minimum temperature of -24°C while the second was exposed to a FT cycle with a minimum temperature of -40°C. The residual strains measured at the end of the first FT cycles was equal to 938 μm/m and 1160 μm/m for the two tested mortar samples. The sample exposed to a minimum temperature of -40°C during the second FT cycle shows a residual strain of 490 μm/m. On the other side, a residual strain of 561 μm/m was measured on the sample exposed to -24°C minimum temperature during the second cycle.

Consequently, the data shows that reducing the minimum temperature of a FT cycle from -12°C to -40°C does not measurably increase the FT damage. In order to understand the mechanism behind this observation, the percentage of freezable water for each FT cycle was quantified and the obtained results are shown in Figure 10. The percentage of freezable water measured on mortar samples exposed to a temperature as low as -40°C is 7% higher than the one measured on samples exposed to less aggressive FT cycles (-12°C and -24°C). However, this increase in the percentage of freezable water when the temperature drops from -12°C to -40°C is insignificant with respect to the total percentage of ice that developed around -12°C . Consequently, it could be hypothesized that when the temperature is below the freezing point of water, the 85% of ice develops and induces the main FT damage due to osmotic and hydraulic pressure as well as electrical charges. In addition, the increase in freezable water between -12°C and -40°C is not enough to induce addition FT damage.

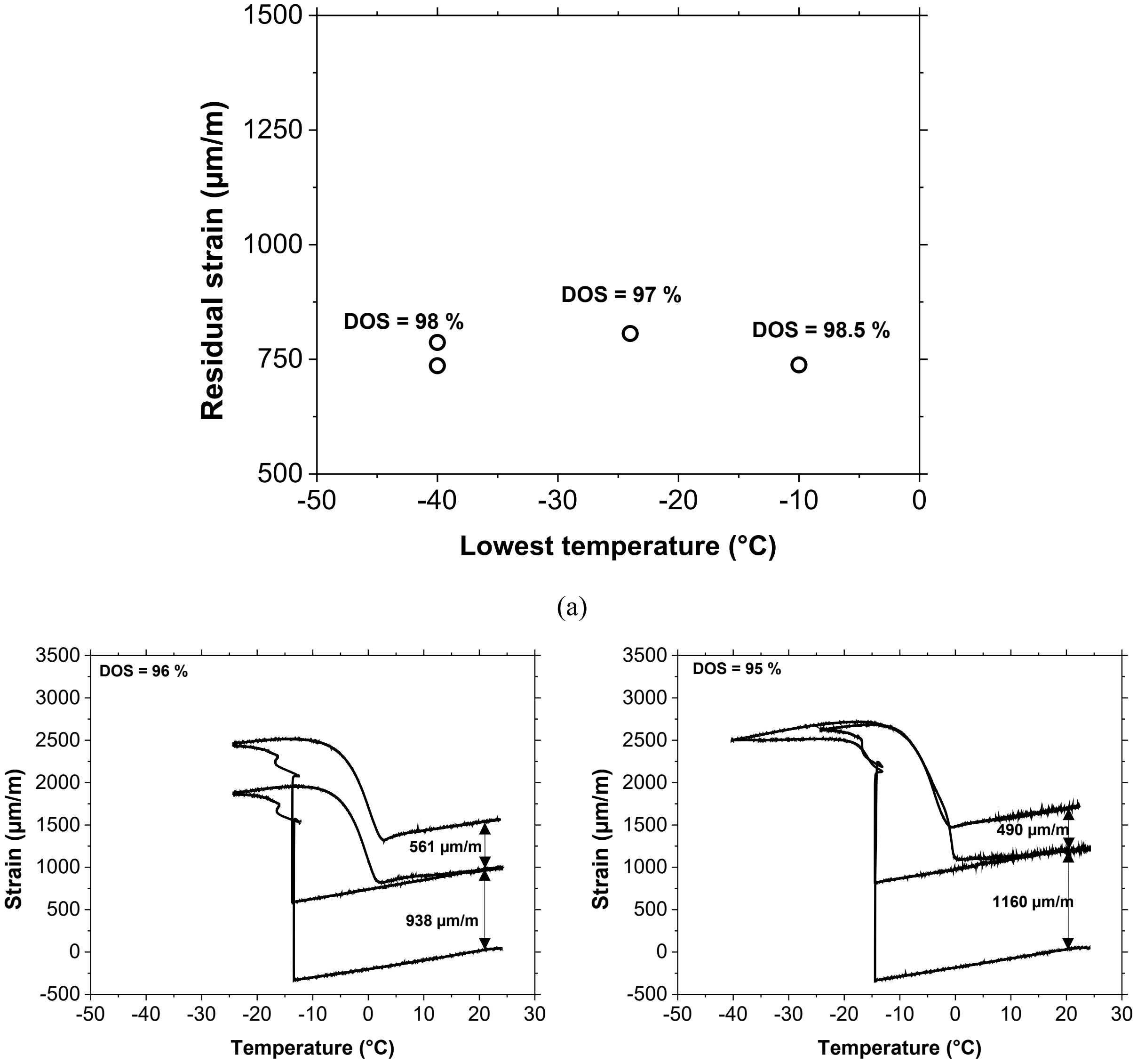

(a)

(b)

(c)

Figure 28. Impact of the lowest temperature in each FT cycle on the FT damage (a) residual strain measured in mortar samples exposed to different values of the lowest temperature; (b) Residual strain measured at the end of each of the two FT cycles with a minimum temperature of - 24°C both; (c) Residual strain measured at the end of each of the two FT cycles with a minimum temperature of - 24°C and -40°C respectively.

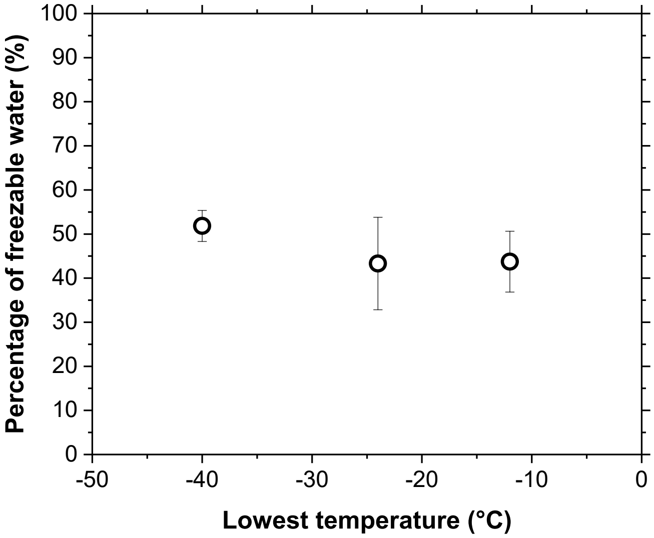

Figure 29. Percentage of freezable water as a function of the lowest temperature in the FT cycle

Impact of the heat/cool rate on FT damage

Figure 11 shows the evolution of the residual strain as a function of the DOS of mortar samples for FT cycles with two different heating and cooling rates. It is evident from this figure that the DOS_{CR} measured on mortar samples is similar for both of the two different heating and cooling rates tested in this study. This agrees with the finding of Fagerlund [33]. In summary, a 1°C/min heating and cooling rate can be used on small samples in order to determine DOS_{CR} values. However, this statement needs to be validated in further studies for larger sample sizes. In samples with bigger dimensions, a fast heating and cooling rate could lead to a temperature gradient inside the sample which could lead to additional damage.

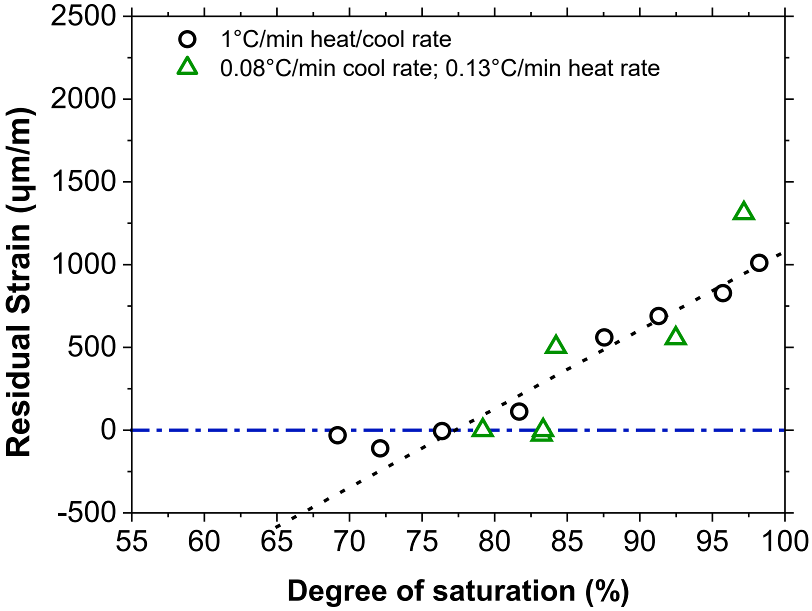

Figure 30. Impact of the Heat/cool rate of the FT cycle on the measured DOS_{CR} of mortar samples

Extending the quantification of FT damage using length change measurements from paste to mortar samples

Based on the previously discussed data, the results presented in this section were obtained on mortar samples that were exposed to drying in an oven at 60°C, and then exposed to FT cycles in the TMA according to the procedure presented in Figure 1(b).

Figure 12 (a) shows the residual strain values versus the damage index obtained from UPV measurements on the mortar samples. The threshold for the damage index was determined experimentally based on the variability in the ultrasonic wave speed and is found to be equal to 8%. It is visible in Figure 13(a) that samples with a damage index higher than 8% show positive values for residual strain. On the other side, Figure 12(b) shows that the DOS_{CR} obtained from UPV measurements align very well with the one obtained from length change measurements. Consequently, these data show that the length change measurements can be used on mortar samples with varying air content and quality to determine their DOS_{CR}.

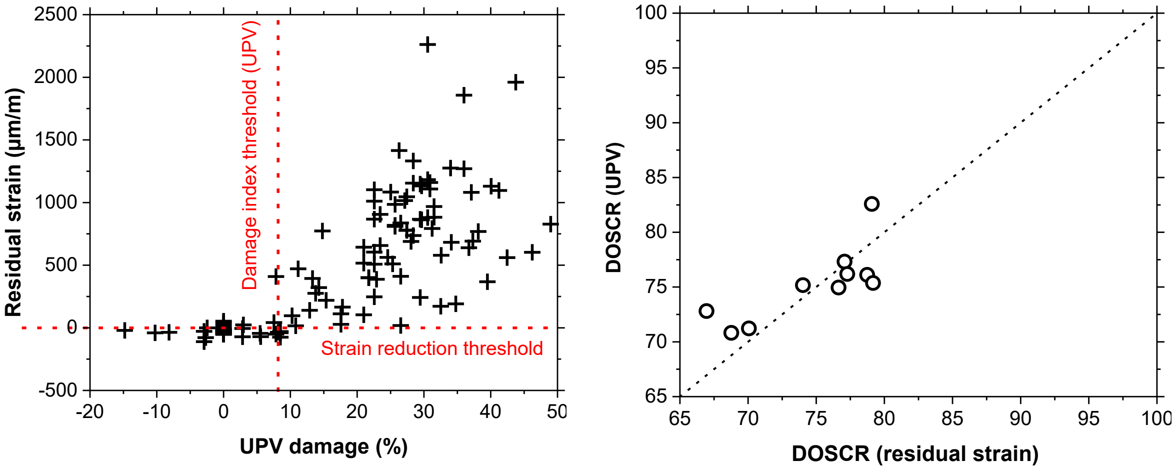

(a) (b)

Figure 31. Comparison of the FT damage obtained from length change damage with the one obtained using UPV on mortar samples with varying air volume and quality

Impact of air voids quality on FT performance

Figure 13 illustrates the probability of failure due to freeze-thaw cycles as a function of DOS in the mortar samples. A bin size of 5% was selected for the probability of failure calculations and the probability values are presented in the center of the bins. Any samples that show a residual strain higher 0µm/m indicates potential freeze-thaw damage. The probability of failure increases with increase of DOS in the sample (Figure 13). For example, all the samples with DOS higher than 88% fail after one FT cycle in the TMA. On the other side, the failure region starts at DOS of ≈77.5% for the samples with a SAM number ≤0.20 compared to the DOS of ≈72.5% for the samples with a SAM number between 0.20 and 0.6. In addition, when the DOS of the sample is around the critical level of saturation (72.5% <DOS<88%), the probability of failure tends to be higher for samples with high SAM number (SAM > 0.20) compared to samples with a low SAM number (≤0.20). Tanesi et al. [34] showed that 0.2 is a SAM number limit. Samples with a SAM number above 0.2 has a poor quality of air void distribution, which is identified by a high spacing factor. The poor quality of air void distribution explains the higher probability of failure in samples with a SAM number bigger than 0.20. This is in accordance with the data collected in Todak thesis [23], where it was concluded that higher quality air-void systems, quantified by lower SAM numbers, may resist freeze-thaw damage at higher levels of saturation than those with poorly distributed air void systems.

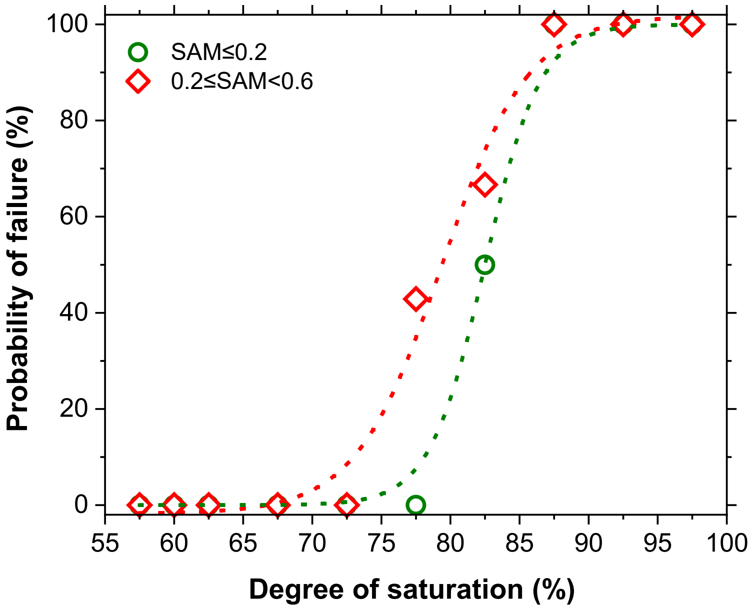

Figure 32. Probability of failure versus the degree of saturation

Conclusion

The DOS_{CR} of cementitious samples can be determined based on length change measurements performed using TMA. A systematic methodology for conducting tests on paste that is described in a previously published study [27]. The objective of this paper is to extend the use of this methodology from cement paste samples to mortar samples. For this reason, mortar samples with different volumes and quality of air voids were prepared. They were then exposed to freezing and thawing cycle inside the TMA where their length was continuously measured using a thermomechanical analyzer with a high precision linear variable displacement transducer (LVDT). Ultrasonic Pulse Velocity measurements, one of the conventional techniques for FT damage quantification, was performed on each mortar sample before and after exposure to FT cycle in the TMA. The freezing and thawing damage index was determined based on the UPV measurements. This damage index was compared with the FT damage obtained from length change measurements. Experimental results show a correlation between the UPV measurements and the length change measurements. Consequently, lit was concluded that length change measurements can be used to quantify DOS_{CR} of mortar samples.

The quality of the air void system (volume, size and distribution of these air voids) inside the mortar samples has a significant impact on the FT performance. Samples with a high quality of air void distribution (SAM<0.20) show a resistance to FT cycles compared to samples with a poor air voids quality.

In addition, the drying temperature, heating and cooling rate as well as the temperature range of a FT cycle were assessed to study their impact on FT performance of concrete.

During sample preparation, the mortar cores need to be first dried. This study investigated the impact of the drying temperature on the measured DOS_{CR}. Based on the data collected, it is concluded that 105°C drying temperature induces microcracks inside the mortar samples. These micro cracks apparently reduce the pressures accompanied by ice formation, which lead to less FT damage compared to samples dried at lower temperature (i.e. 60°C). Consequently, the DOS_{CR} obtained on samples dried at 105°C is overestimated and drying at 60°C is recommended.

The impact of two different heating and cooling rates on the DOS_{CR} was investigated in this study. The results show that the two different heating and cooling rates tested in this study do not show an influence on DOS_{CR} of mortar samples with 10 mm diameter and 20 mm height.

It was also concluded that the FT damage in mortar samples does not increase when the temperature is lowered from -12°C to -40°C. Based on the LT-DSC data, it was proved that 85% of the freezable water in the mortar pores freezes when the temperature drops below the freezing point. The ice that forms below the freezing point induces the majority of the FT damage. A 7% increase in the percentage of the freezable water occurs when the temperature is dropped to lower values (-40°C for example). However, this increase in the percentage of freezable water appears to be insignificant for most samples to induce additional noticeable FT damage.

Acknowledgement

The authors gratefully acknowledge support for this work from the pooled fund study (Project No. U1117C) managed by the Oklahoma Department of Transportation. This work was performed at Oregon State University. The authors are grateful to Bhauvesh Jaya, Joey Biever, and Audrey Collins, undergraduate research assistants at Oregon State University, who helped in conducting some of the experiments reported here. The contents of this paper reflect the views of the authors, who are responsible for the facts and the accuracy of the data presented herein. The contents do

not necessarily reflect the official views or policies of the sponsors. These contents do not constitute a standard, specification, or regulation.

Reference

1. Fagerlund, G., *The Signifcance of Critical Degrees of Saturation at Freezing of Porous and Brittle Materials.* ACI Special Publication, 1975. 47: p. 13-66.
2. Fagerlund, G., *A service life model for internal frost damage in concrete (Report TVBM; Vol. 3119)*. 2004: Division of Building Materials, LTH, Lund University.
3. Litvan, G.G., *Freeze-thaw durability of porous building materials*, in *Durability of building materials and components*. 1980, ASTM International. p. 455-463.
4. Hall, C., *Water sorptivity of mortars and concretes: a review.* Magazine of Concrete Research, 1989. 41(147): p. 51-61.
5. Fagerlund, G., *The international cooperative test of the critical degree of saturation method of assessing the freeze/thaw resistance of concrete.* Matériaux et Construction, 1977. 10(4): p. 231-253.
6. Li, W., et al., *Water absorption and critical degree of saturation relating to freeze-thaw damage in concrete pavement joints.* Journal of Materials in Civil Engineering, 2011. 24(3): p. 299-307.
7. Todak, H., C. Lucero, and J. Weiss, *Why is the air there? Thinking about freeze-thaw in terms of saturation.* Concrete inFocus, 2015: p. 3-7.
8. Farnam, Y., et al., *Electrical response of mortar with different degrees of saturation and deicing salt solutions during freezing and thawing.* Cement and Concrete Composites, 2015. 59: p. 49-59.
9. Todak, H., et al., *Freeze-Thaw resistance of concrete: The influence of air entrainment, water to cement ratio, and saturation*, in *Proc. Int. Symp., Brittle Matrix Composites 11*. 2015. p. 101-109.
10. Fagerlund, G., *The critical degree of saturation method of assessing the freeze/thaw resistance of concrete.* Matériaux et Construction, 1977. 10: p. 217-229.
11. Fagerlund, G., *The long-time water absorption in the air-pore structure of concrete*. 1993, Division of Building Materials, LTH, Lund University.
12. Farnam, Y., et al., *Acoustic emission and low-temperature calorimetry study of freeze and thaw behavior in cementitious materials exposed to sodium chloride salt.* Transportation Research Record: Journal of the Transportation Research Board, 2014(2441): p. 81-90.
13. Qian, Y., Y. Farnam, and J. Weiss. *Using acoustic emission to quantify freeze–thaw damage of mortar saturated with NaCl solutions*. in *4th International Conference on the Durability of Concrete Structures*. 2014. Purdue University, West Lafayette, IN, USA.
14. Lucero, C.L., et al., *Using Neutron Radiography to Quantify Water Transport and the Degree of Saturation in Entrained Air Cement Based Mortar.* Physics Procedia, 2015. 69(Supplement C): p. 542-550.
15. Todak, H., et al. *Freeze-Thaw resistance of concrete: the influence of air entrainment, water to cement ratio, and saturation*. in *Proc. Int. Symp., Brittle Matrix Composites 11*. 2015. Warsaw: Institute of Fundamental Technological Research.
16. Weiss, J., M. Tsui-Chang, and H. Todak, *Is the Concrete Profession Ready for Peformance Specifications that Provide an Alternative to Prescriptive w/c and Air Content Requirements?*, in *2016 INTERNATIONAL CONCRETE SUSTAINABILITY CONFERENCE*. 2016: Washington, DC.
17. Esmaeeli, H.S., et al., *Numerical simulation of the freeze–thaw behavior of mortar containing deicing salt solution.* Materials and structures, 2017. 50(1): p. 96.
18. Qiao, C., P. Suraneni, and J. Weiss, *Measuring volume change due to calcium oxychloride phase transformation in a $Ca(OH)_2$-$CaCl_2$-H_2O system.* Advances in Civil Engineering Materials, 2017. 6(1): p. 157-169.

19. Weiss, J., et al., *Toward Performance Specifications for Concrete Durability: Using the Formation Factor for Corrosion and Critical Saturation for Freeze-Thaw.* Transportation Research Board, 2016. submitted.
20. Hall, C. and W.D. Hoff, *Water transport in brick, stone and concrete*. 2004: CRC Press.
21. Powers, T.C. and R. Helmuth. *Theory of volume changes in hardened portland-cement paste during freezing*. in *Materials and construction*. 1953.
22. Powers, T.C. and T.F. Willis, *The air requirement of frost resistant concrete.* Proceeding of Highway Research Board, 1950. 29: p. 189-211.
23. Todak, H.N., *Durability assessments of concrete using electrical properties and acoustic emission testing*, in *School of Civil Engineering*. 2015, Purdue University: West Lafayette. p. 143.
24. Li, W., et al., *Water Absorption and Critical Degree of Saturation Relating to Freeze-Thaw Damage in Concrete Pavement Joints.* Journal of Materials in Civil Engineering, 2012. 24(3): p. 299-307.
25. Materials, A.S.o.T.a., *Standard Terminology for Nondestructive Examinations*, in *ASTM E1316*. 2014. p. 1-38.
26. Kawamoto, S.W.R.S., *Acoustic Emission and Acousto-Ultrasonic Techniques for Wood and Wood-Based Composites A Review*, in *General technical report FPL-GTR-134*. 2002, United States Department of Agriculture. p. 10.
27. Ghantous, R.M., et al., *Examining the Influence of the Degree of Saturation on Length Change and Freeze-Thaw Damage.* Advances in Civil Engineering Materials, 2019. 8(1).
28. Ley, M.T., et al., *Determining the air-void distribution in fresh concrete with the Sequential Air Method.* Construction and Building Materials, 2017. 150: p. 723-737.
29. Felice, R.V., J.M. Freeman, and M.T. Ley, *Durable Concrete with Modern Air-Entraining Admixtures.* Concrete International, 2014. 36(8): p. 37-45.
30. 1.6a, A.T., *Standard Method of Test for Determining the Total Pore Volume in Hardened Concrete Using Vacuum Saturation*. 2018.
31. Trofimov, B.Y., L.Y. Kramar, and K. Schuldyakov. *On Deterioration Mechanism of Concrete Exposed to Freeze-Thaw Cycles*. in *IOP Conference Series: Materials Science and Engineering*. 2017. IOP Publishing.
32. Powers, T.C. *Basic considerations pertaining to freezing-and-thawing tests*. in *ASTM Proceedings*. 1955.
33. Fagerlund, G., *Effect of the freezing rate on the frost resistance of concrete.* Nordic concrete Research, Publication number 11, 1992.
34. Tanesi, J., et al., *Super Air Meter for Assessing Air-Void System of Fresh Concrete.* Advances in Civil Engineering Materials, 2016. 5(2): p. 20150009.

TIME TO REACH CRITICAL SATURATION (TTRCS) MODEL

Mehdi Khanzadeh Moradllo[1], Chunyu Qiao[2], Rita Maria Ghantous[1], Myo Zaw[1], Hope Hall[3], M. Tyler Ley[3], and W. Jason Weiss[1]

1. School of Civil and Construction Engineering, Oregon State University, Corvallis, OR 97331, USA
2. DRP, A Twining Company, Boulder, CO 80301, USA
3. School of Civil & Environmental Engineering, Oklahoma State University, Stillwater, OK 74078, USA

ABSTRACT

Many State Highway Agencies have been working to develop performance-based specifications for concrete pavements and bridges in freeze-thaw environments. A time to reach critical saturation (TTRCS) model has been proposed to estimate the freeze-thaw performance of concrete. This study evaluates the TTRCS model for thirty different concrete mixtures with varying w/c, air contents, and quality of air void (size and spacing). Simple quality control test methods are used to determine the inputs parameters for the TTRCS model. The estimated time to reach critical saturation is compared with the measured durability factor using ASTM C 666-15. Results indicate that 90% of the mixtures with air content above 4.5% and a SAM Number below 0.20 have a normalized time to reach critical saturation of greater than 20 and durability factor higher than 90%. The mixtures with a high range water reducer require a higher volume fraction of entrained air to satisfy the recommended limit for durability factor. This appears to be due to an interaction between the high range water reducer and air entraining admixture resulting in greater air void spacing. However, the addition of high range water reducer was also found to increase the time to reach critical saturation in the mixtures with a low w/c due to an increase in the tortuosity of matrix pores. Reducing the w/c improves the freeze-thaw performance due to a reduction in the pore volume, tortuosity, and absorption rate of the concrete. A relationship is developed to estimate the time to reach critical saturation based on SAM Number and apparent formation factor. In addition, a relationship is proposed to estimate the critical degree of saturation based on air void content and quality.

Keywords: Air entrainment; Critical saturation; Capillary absorption; Formation factor; Freeze-thaw durability; Service-life model.

INTRODUCTION

The damage caused by freezing and thawing cycles is a prevalent and costly durability problem with concrete in cold environments [1-5]. Many State Highway Agencies (SHAs) have been developing performance-based specifications (e.g., AASHTO PP 84-18) for improving the construction of concrete pavements and bridges in freeze-thaw environment. Use of performance-based specifications can complement the conventional prescriptive guidelines such as ACI 318.R-14 and typical Department of Transportation (DOT) specifications. Current durability specifications (e.g., ACI 318.R-14) require a minimum target air content and a maximum water-to-cement ratio (w/c) in concrete mixtures based on environmental exposure condition. However, in performance specifications, a performance-based model is required to predict concrete service life in cold environments based on inputs from the materials properties and simple quality control test methods to also account for the impact from other mixture properties such as the distribution of the air voids (i.e., spacing factor) and fluid transport properties [6-8].

The degree of saturation (*DoS*) of concrete is a key parameter in assessing mixtures susceptibility to freeze-thaw damage [3, 8-10]. In 1977, Fagerlund [3, 9, 11] introduced a time to reach critical saturation (TTRCS) model. This model has been extended by Todak [7] and Weiss et al. [8]. This model relies on three main parameters: critical degree of saturation (DoS_{CR}), matrix degree of saturation (DoS_{Matrix}), and the air void filling rate (i.e., secondary rate of absorption (S'_2)) [3, 6-9]. The DoS_{CR} can be defined for each mixture and when the DoS in the concrete exceeds DoS_{CR}, damage will develop during freezing-thawing [3]. The air void quality (i.e., the air void spacing factor) has the most important influence on DoS_{CR} [8, 9]. The DoS_{Matrix} of concrete is defined as the DoS when the capillary, gel, and chemical shrinkage pores are filled with water, but the air voids (entrained and entrapped) only contain vapor [12]. The amount of air in concrete (i.e., volume of air) is the most influential factor on DoS_{Matrix} at a given w/c. The S'_2 is the absorption rate of fluids above matrix saturation point of concrete. Recent study by Khanzadeh Moradllo et al. [10, 13, 14] showed that the S'_2 is primarily dependent on permeability of the concrete matrix (i.e., formation factor of concrete).

Todak [7] and Weiss et al. [8] developed a conceptual framework for the specification of concrete durability in a freeze-thaw environment using TTRCS modelling concepts. In these studies [7, 8], a simple accelerated experimental procedure was introduced to determine the DoS_{CR} and DoS_{Matrix} using acoustic emission and an immersion test (i.e., bucket test), respectively. These studies illustrated the effect of various changes in concrete mixture proportions (i.e., w/c and air void properties) on predicted time to reach critical saturation (i.e., service life). Recent work [10, 13] has shown that the S'_2 in concrete can be predicted using the apparent formation factor (F_{APP}) determined from electrical resistivity measurements. In another study, Bharadwaj et al. [6] developed an approach to use thermodynamic modelling and a pore partitioning model to predict the resistance of concrete to freeze-thaw damage using TTRCS modelling concepts.

While the frameworks and models that have been developed have great potential to predict the time to reach critical saturation of concrete using the discussed mixture properties, they require further calibration and evaluation based on experimental results on varying materials and mixture proportions [8]. The aim of the current study is to systematically investigate the influence of entrained air voids (air void volume and distribution) on time to reach critical saturation in concrete mixtures with varying w/c. A high range water reducer (HRWR) was used to modify the air void size and air void distribution (i.e., air void quality). In addition, this study experimentally examines the relationship between air quality and the DoS_{CR} for the concrete mixtures with and without HRWR. This study also compares the estimated time to reach critical saturation to the measured durability factor using ASTM C 666-15 for thirty different concrete mixtures.

Time to Reach Critical Saturation Model

A common form of the TTRCS model is shown in Eq. 1 [6, 8]. Equation 1 is based on a two stage absorption process. The initial and secondary stages (absorption rates) represent the fluid filling of matrix pores (i.e., DoS_{Matrix}) and air voids, respectively. The air void filling process is slower than the filling of the matrix pores [13].

$$DoS = DoS_{Matrix} + \varphi S_2' \sqrt{t} \leq DoS_{CR} \tag{1}$$

where, φ is a parameter to account for the drying exposure conditions and t (year) is the time for the concrete to reach critical saturation. The φ can be taken as 1 when concrete is in continuous contact with water at a constant temperature.

Equation 1 can be rearranged to calculate the time to reach critical saturation, as shown in Eq. 2.

$$t = \left(\frac{DoS_{CR} - DoS_{Matrix}}{\varphi S_2'}\right)^2 \tag{2}$$

Recent work [10, 13] has shown that the S'_2 (*%DoS/√year*) in concrete is linearly related to the reciprocal of the square root of the apparent formation factor, F_{APP} (determined using electrical resistivity measurements), as shown in Eq. 3.

$$S_2' = c_1\sqrt{\frac{1}{F_{APP}}} \tag{3}$$

The values of the constant c_1 can be empirically determined from experimental results [10, 13]. It has been observed that S'_2 is relatively independent of the air content [10, 13].

This relationship (Eq. 3) can provide a powerful tool in quality control to obtain S'_2 based on F_{APP} using a simple electrical resistivity test. Further research is needed to evaluate Eq. 3 holds for mixtures with different materials such as supplementary cementitious materials (SCMs).

Equations 2 and 3 can be combined to estimate time to reach critical saturation as:

$$t = \left(\frac{DoS_{CR} - DoS_{Matrix}}{\varphi \cdot c_1\sqrt{\frac{1}{F_{APP}}}}\right)^2 \tag{4}$$

The time to reach critical saturation can be normalized (using c_1 and φ), as shown in Eq. 5 [6]. This normalized time to reach critical saturation is based on the DoS_{Matrix}, DoS_{CR}, and F_{APP}. A simple experimental procedure to measure these parameters is described in the following section.

$$t \cdot (\varphi \cdot c_1)^2 = F_{APP}(DoS_{CR} - DoS_{Matrix})^2 \tag{5a}$$

$$t \cdot (\varphi \cdot c_1)^2 = F_{APP}.\Delta^2 \tag{5b}$$

where, Δ (*%DoS*) is the difference between the DoS_{CR} and DoS_{Matrix}. The Δ is the percentage of air voids that are fluid filled and will cause a damage during freeze-thaw cycles.

EXPERIMENTAL PROGRAM

3.1. MATERIALS AND MIXTURE PROPORTIONS

Thirty concrete mixtures were tested with three different w/c (0.40, 0.45, and 0.50), a wide range of air contents (2.5 – 9.0%), and a wide range of air qualities (air size and distribution). The air quality was altered by using a polycarboxylate based high range water reducing admixture (HRWR). The air content and Sequential Air Method (SAM) Number of the freshly mixed concrete was measured according to AASHTO TP 118-17. Concrete specimens were sealed cured in plastic cylindrical molds with inside dimensions of 102 mm (diameter) × 203 mm (height) at 23 ± 1 °C for 180 days for the immersion and DoS_{CR} measurements. Prismatic samples with dimensions of 406.0 mm × 101.6 mm × 76.2 mm were made for hardened air-void analysis (ASTM C 457-16) and rapid freeze-thaw testing (ASTM C 666-15). The prismatic samples were cured according to the procedure described in ASTM C 666-15. The materials properties were reported in [10, 12, 15]. The mixture proportions are provided in Table 1.

***Table 1** – The mixture proportions (SSD) of concrete (in kg/m^3).*

w/c	Mixture	Coarse aggregate 1	Coarse aggregate 2	Fine aggregate	Cement	Water	AEA (g/m^3)	HRWR (g/m^3)
0.40	M1	677.3	451.5	762.7	372.8	149.1	6.46	-
	M2	672.4	448.3	757.2	370.1	148.1	14.41	-
	M3	668.2	445.5	752.5	367.8	147.1	32.95	-
	M4	665.4	443.6	749.4	366.3	146.5	33.18	-
	M5	661.9	441.3	745.5	364.4	145.8	33.94	-
	M6	656.4	437.6	739.2	361.3	144.5	52.41	-
0.45	M1	697.3	464.9	754.7	340.5	153.3	6.66	-
	M2	693.7	462.5	750.8	338.8	152.5	9.82	-
	M3	690.2	460.1	747.0	337.0	151.7	16.28	-
	M4	685.2	456.8	741.5	334.6	150.6	29.61	-
	M5	674.4	449.6	729.9	329.3	148.2	40.93	-
	M6	670.1	446.8	725.3	327.2	147.3	52.66	-
0.50	M1	680.2	453.5	735.7	340.1	170.1	5.56	-
	M2	674.0	449.3	728.9	337.0	168.5	10.49	-
	M3	666.3	444.1	720.6	333.1	166.6	18.19	-
	M4	653.7	435.8	707.0	326.9	163.4	28.97	-
	M5	644.6	429.7	697.2	322.3	161.2	32.95	-
0.40	M1	671.0	447.3	755.7	369.4	147.8	14.01	130.11
	M2	662.6	441.8	746.3	364.8	145.9	19.57	130.01
	M3	660.5	440.4	743.9	363.6	145.4	23.46	129.29
	M4	651.5	434.3	733.7	358.6	143.5	27.91	130.21
	M5	648.7	432.5	730.6	357.1	142.8	31.84	128.65
0.45	M1	686.6	457.7	743.1	335.3	150.9	5.39	112.69
	M2	678.7	452.5	734.6	331.4	149.2	13.83	112.39
	M3	670.8	447.2	726.1	327.6	147.4	17.68	102.19
	M4	666.6	444.4	721.4	325.5	146.5	21.46	102.15
0.50	M1	679.5	453.0	735.0	339.8	169.9	2.69	51.87
	M2	661.4	440.9	715.3	330.7	165.3	5.94	51.93
	M3	653.0	435.3	706.3	326.5	163.3	6.64	52.21
	M4	635.5	423.7	687.4	317.8	158.9	9.09	51.40

3.2. Experimental Methods

3.2.1 MATRIX SATURATION AND APPARENT FORMATION FACTOR FROM IMMERSION TEST

A simplified immersion test was performed on the concrete samples (102 ± 2 mm (diameter) × 203 ± 2 mm (height)) to determine the DoS_{Matrix} from mass measurement and apparent formation factor (F_{APP}) derived from electrical resistivity measurement. For each mixture, two samples were submerged in a 19 L bucket containing 13.5 L simulated pore solution. The mass change and electrical resistance were periodically recorded over 91 days of submersion, as shown in Fig. 1. The impedance of the samples was measured using a bulk resistivity meter with a frequency of 1 kHz at 23 ± 1 °C according to AASHTO TP 119-19. The detail on testing procedure and calculation of DoS_{Matrix} and F_{APP} can be found in [12].

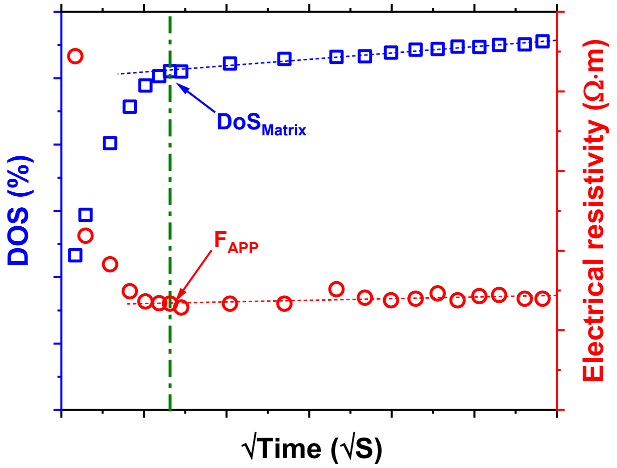

Fig. 1 – An example of time-dependent DoS and electrical resistivity values from the immersion test.

3.2.2 CRITICAL DEGREE OF SATURATION FROM ULTRASONIC PULSE VELOCITY

After curing, 38.0 mm (height) × 102.0 mm (diameter) slices were cut from 203.0 mm (height) × 102.0 mm (diameter) cylindrical samples to measure damage due to freeze-thaw using Ultrasonic Pulse Velocity (UPV). The height of the cylindrical slices (38 mm) is 100% larger than the maximum size of coarse aggregates (19 mm) in the concrete mixtures. Each mixture with and without HRWR was tested at six (100%, 96%, 92%, 90%, 85%, and 80% ± 2%) and seven (100%, 96%, 92%, 90%, 85%, 80%, and 75% ± 2%) different *DoS*, respectively. Two samples were tested for each *DoS*. These *DoS* values were selected based on preliminary experiment to provide a wide range of *DoS* in order to precisely predict the DoS_{CR} in the samples using the measured damage index from UPV measurements. The samples were oven dried at 105 ± 2 °C and vacuum saturated according to the procedure described in [16] to measure the dry mass and the full saturation mass (i.e., 100% *DoS*), respectively. Samples that needed to be tested at *DoS* different from 100% were dried at 23 ± 1 °C until the desired saturation level was reached. The samples were then stored in a sealed bag for two weeks at 23 ± 1 °C to allow the internal moisture content to equilibrate before testing. The samples with 100% *DoS* were tested immediately after the vacuum saturation process.

Following the samples conditioning, a cold plate was used to expose the samples to three freeze-thaw cycles between 23 ± 1 °C and -20 ± 1 °C. The cold plate was placed inside an insulated chamber to limit heat loss during the freeze-thaw cycles. The cooling and heating rates were -4.6 ^{o}C/h and +8.0 ^{o}C/h, respectively. The samples were kept inside a sealed bag to minimize the change in the *DoS* during testing. The mass of the samples was monitored during the cycles and a ≈1-2% decrease in *DoS* was observed throughout the three freeze-thaw cycles. Therefore, the average *DoS* during testing is reported. The pulse velocity through the samples was recorded at the start of testing (V_0 *(m/s)*) and after each heating cycle (V_t) at three different locations on the sample. The pulse velocity of the samples was measured using a UPV meter (Pundit PL-200) and a pair of exponential transducers with a frequency of 54 kHz at 23 ± 1 °C.

The damage index due to freeze-thaw cycles can be computed in terms of the reduction in pulse velocity, as shown in Eq. 6 [4, 7].

$$DI = 1 - \frac{E_t}{E_0} = 1 - \left(\frac{V_t}{V_0}\right)^2 \tag{6}$$

where, *DI* (*%*) is the damage index due to freeze-thaw cycles; E_0 (N/m^2) is the modulus of elasticity at the start of testing; and E_t is the modulus of elasticity after damage.

Figure 2 presents an example of calculated damage index after three freeze-thaw cycles at varying *DoS* based on Eq. 6. A linear trend was observed between damage index and *DoS* in the sample. A threshold value of 3.3% was defined for damage index based on precision of the UPV setup (transition of 0.1 μs) using the Eq. 6 for the range of the measured values of transition on concrete samples, as shown in Fig. 2. Any value above the threshold indicates potential freeze-thaw damage. The intersection between the threshold damage index (3.3%) and the linear regression (between DoS and damage index) was defined as DoS_{CR}, as shown in Fig. 2.

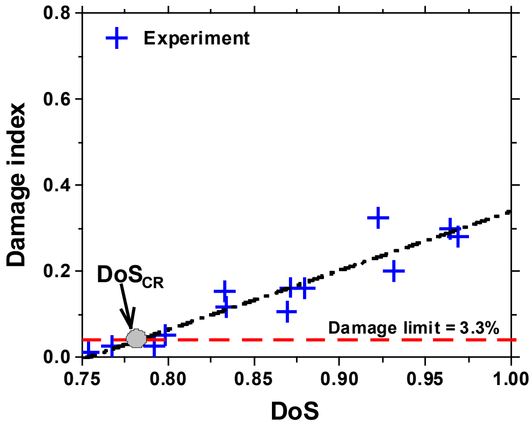

***Fig. 2** – An example of measured damage index at different DoS using UPV after three freeze-thaw cycles.*

3.2.3 AIR VOID SPACING FACTOR FROM HARDENED AIR VOID ANALYSIS

The prismatic samples were cut into 19 mm thick slabs. Surface of the samples was treated and polished using the procedure described in [15]. The prepared surface was inspected under a stereo microscope to obtain a satisfactory surface for microscopic analysis. The surface was then investigated with ASTM C 457-16 method C by using the Rapid Air 457 from Concrete Experts, Inc [15]. Sample preparation and data analysis details can be found in other publications [15].

3.2.4 DURABILITY FACTOR FROM RAPID FREEZE-THAW TEST

After curing, the prismatic samples were tested according to ASTM C 666-15 for 300 freeze-thaw cycles. As per ASTM C 666-15 dynamic modulus, expansion, and mass change in the samples were measured every 36 cycles or before. More details on testing procedure and data analysis can be found in other publications [17].

EXPERIMENTAL RESULTS AND DISCUSSION

4.1. RELATING SAM NUMBER TO THE AIR CONTENT AND SPACING FACTOR

Figure 3a shows the relationship between air content and SAM Number for the mixtures with and without HRWR. This relationship depends on the quality of the air void system in a given concrete. However, the following equation can be used to relate SAM Number to the volume fraction of air.

$$SAM = A\,.\,Air^{-B} \tag{7}$$

where, 'A' and 'B' are constants. Based on Fig. 3a, 'B' is equal to 1.70 for both systems with and without HRWR. However, 'A' depends on air void quality. A lower 'A' value refers to a higher quality air void system while a higher value is typical of a lower quality air void system with more coarse air voids.

According to Fig. 3a, the samples without HRWR have a better air void distribution when compared to the samples with HRWR at a given air content. As a result, to achieve a lower SAM Number, a higher volume fraction of air is required for the samples with HRWR.

Figure 3b shows a comparison between the SAM Number and spacing factor for different concrete mixtures with and without HRWR. Based on the results, there is a correlation between the spacing factor and SAM Number. Therefore, SAM Number can be an indicator of spacing factor in fresh concrete. However, a variation exists in the data.

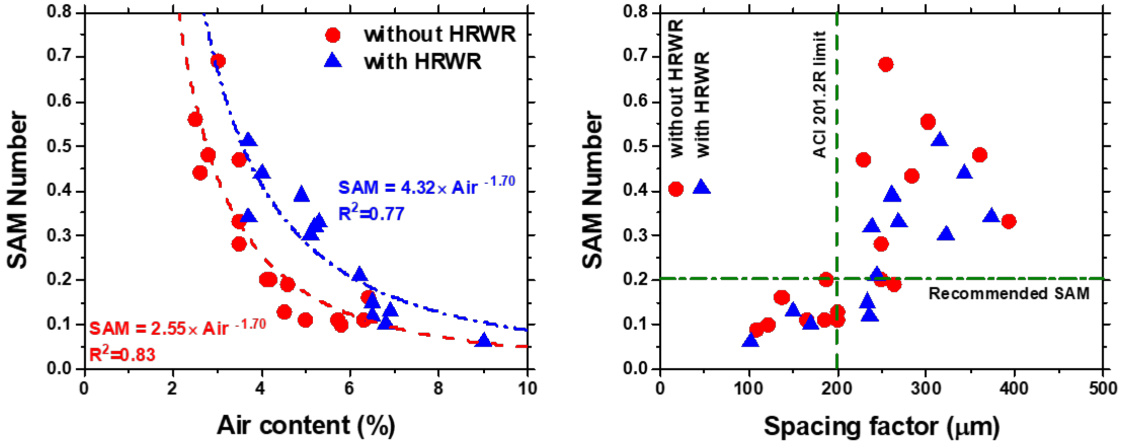

(a)

(b)

Fig. 3 *– (a) the relationship between air content and SAM Number and (b) SAM Number versus spacing factor for the mixtures with varying w/c and with and without HRWR.*

4.2. IMPACT OF AIR CONTENT AND AIR QUALITY ON '*Δ*'

As discussed, the *Δ* is the difference between the DoS_{CR} and DoS_{Matrix}. The *Δ* is the percentage of air voids that are fluid filled and will cause a damage during freeze-thaw cycles. The *Δ* is an indicator of freeze-thaw resistance of concrete and it primarily depends on air void system [3]. Concrete with a higher air content (i.e., lower DoS_{Matrix}) and a higher quality air void system (i.e., higher DoS_{CR}) will have a higher value of *Δ,* which is indicator of better freeze-thaw resistance. This section examines the impact of air content and air quality on *Δ* in concrete mixtures with and without HRWR.

Figure 4 shows the measured value of *Δ* as a function of the SAM Number (i.e., air void quality) and air content for the mixtures with varying w/c and with and without HRWR. Based on Fig. 4a, the *Δ* decreases following a power relationship with an increase of the SAM Number. The rate of decrease of *Δ* is lower in the samples with SAM Number above 0.30. The *Δ* increases with an increase of the air content, as shown in Fig. 4b. However, the samples with HRWR show lower

Δ (i.e., lower freeze-thaw resistance) when compared to the samples without HRWR at a given air content. This can be attributed to the fact that the addition of HRWR coarsens the air void distribution (Fig. 3a) which increases the critical flow distance (the maximum distance that water can flow from freezing site to the surrounding nearest air-filled space, D_{CR} [4, 9]) [15]. In addition, the lower Δ in the samples with HRWR can be explained by the lower filling rate of air voids (i.e., lower S'_2) in these samples due to higher tortuosity of the matrix [10, 13]. Figure 5 illustrates that the DoS_{CR} increases with an increase of S'_2, which indicates that at higher S'_2 water can travel faster from freezing site to the surrounding nearest air voids.

Based on Fig. 4a, the samples with and without HRWR present a similar trend for the Δ as a function of the SAM Number. Based on the two-way analysis of variance (ANOVA), there is a probability of less than 5% that the Δ values of the samples with and without HRWR as a function of the SAM Number is not the same. However, the value of Δ is statistically different as a function of air content for the samples with and without HRWR. This highlights that the SAM Number is better indicator of freeze-thaw resistance irrespective of the admixture combination. Therefore, the following equation (derived based on experimental data (Fig. 4a)) can be used to estimate the Δ based on SAM Number.

$$\Delta = C\,.SAM^{-D} \tag{8}$$

where, *'C'* and *'D'* are constants. Based on experimental data, the values of *'C'* and *'D'* are 6.03 and -0.645, respectively. It seems that these constants are independent of mixture proportions. However, further work is needed to examine Eq. 8 for the mixtures with different materials.

Equation 8 can be combined with Eq. 7 to estimate the Δ based on volume fraction of air, as shown in Eq. 9.

$$\Delta = C.(A.Air^{-B})^{-D} \tag{9}$$

As discussed, it seems that the values of '*B*', '*C*', and '*D*' are independent of mixture proportions. By replacing these constants based on experimental results, Eq. 9 can be simplified as following:

$$\Delta = 6.03\,.\,A^{-0.645}.\ Air^{1.10} \tag{10}$$

The predicted *Δ* as a function of air content based on Eq. 10 for varying values of '*A*' (i.e., air quality) is presented in Fig. 4b. The value of '*A*' is between 1.5 and 6.0 for the tested concrete mixtures.

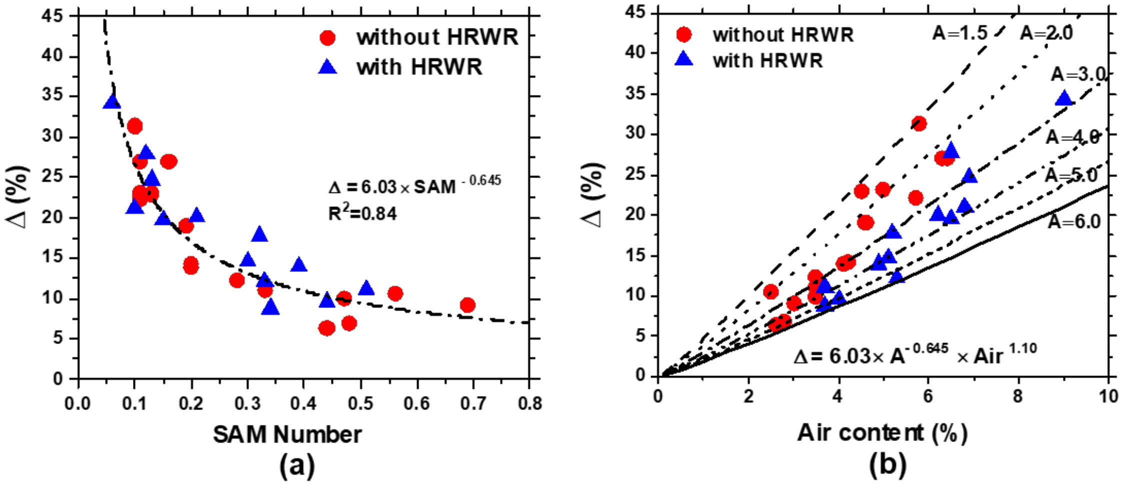

Fig. 4 *– The 'Δ' versus (a) SAM Number and (b) air content for the samples with and without HRWR.*

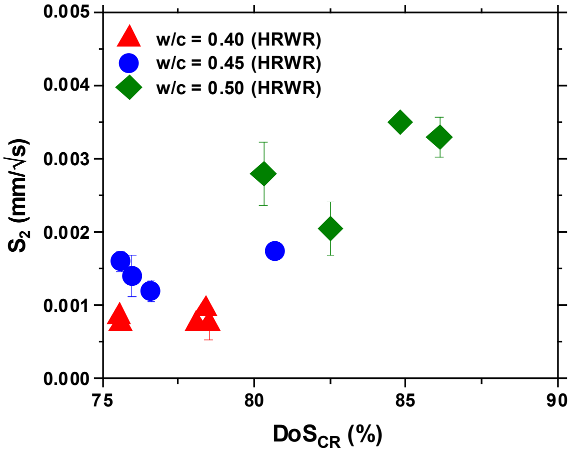

Fig. 5 – The measured DoS_{CR} versus secondary rate of absorption (S'_2) [10,13] for the mixtures with varying w/c without HRWR.

4.3. IMPACT OF W/C, AIR CONTENT, AND AIR QUALITY ON TIME TO REACH CRITICAL SATURATION

The normalized time to reach critical saturation (based on Eq. 5) as a function of the air content and SAM Number for the samples with varying w/c and with and without HRWR is illustrated in Figs 6 and 7 (experimental data points), respectively. In addition, Eq. 5 is combined with Eqs 9 and 10 to predict the normalized time to reach critical saturation using SAM Number and air content (dashed lines), respectively.

$$t \cdot (\varphi \cdot c_1)^2 = F_{APP} \,.\, (6.03 \,.\, SAM^{-0.645})^2 \tag{11}$$

$$t \cdot (\varphi \cdot c_1)^2 = F_{APP} \,.\, (6.03 \,.\, A^{-0.645} .\, Air^{1.10})^2 \tag{12}$$

The average F_{APP} for the mixtures with different w/c was used in Eqs 11 and 12 to estimate the time to reach critical saturation. Based on Fig. 3a, the '*A*' values of 2.55 and 4.32 were used in Eq. 12 for the mixtures with and without HRWR, respectively.

Based on Fig. 6, the samples with higher air content have a longer time to reach critical saturation. This is due to the increase in the Δ as shown in Fig. 4. Reducing the w/c improves the freeze-thaw performance. This improvement is in part due to a small change in DoS_{Matrix} [12] but due to a more substantial decrease in the tortuosity (i.e., F_{APP}) and absorption rate of the concrete [10, 13]. The addition of HRWR reduces the normalized time to reach critical saturation at a given air content and w/c due to an increase in the critical flow distance (Fig. 5).

The normalized time to reach critical saturation exponentially increases by a decrease in the SAM Number (i.e., better air quality). All samples with SAM Number below 0.20 exhibited a normalized time to reach critical saturation greater than 10. While the samples without HRWR showed a similar trend for the time to reach critical saturation as a function of the SAM Number irrespective of the w/c, different trends were observed for the samples with HRWR with respect to w/c, as illustrated in Fig. 7b. This is primarily attributed to a bigger impact from the addition of HRWR on tortuosity of the samples (i.e., F_{APP}) with a lower w/c (w/c=0.40) [10, 12, 13]. The predicted time to reach critical saturation based on Eq. 11 shows good agreement with the calculated values based on Eq. 5. The results indicate that the SAM Number can be used to improve the understanding the performance of concrete in freeze-thaw environment, especially in modern concrete with combination of chemical admixtures.

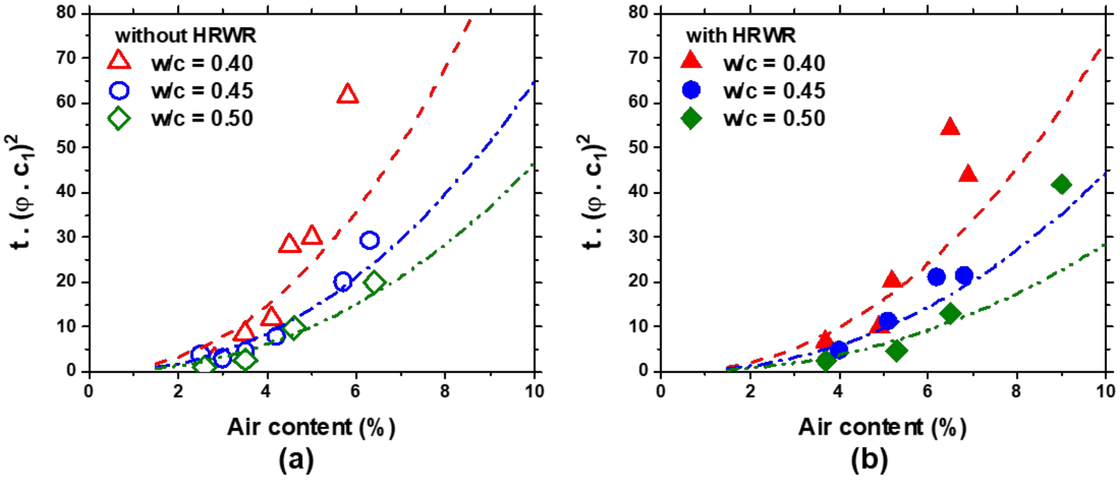

Fig. 6 *– The normalized time to reach critical saturation as a function of the air content for the mixtures with varying w/c and (a) with and (b) without HRWR. Note: The lines present the predicted values based on Eq. 12.*

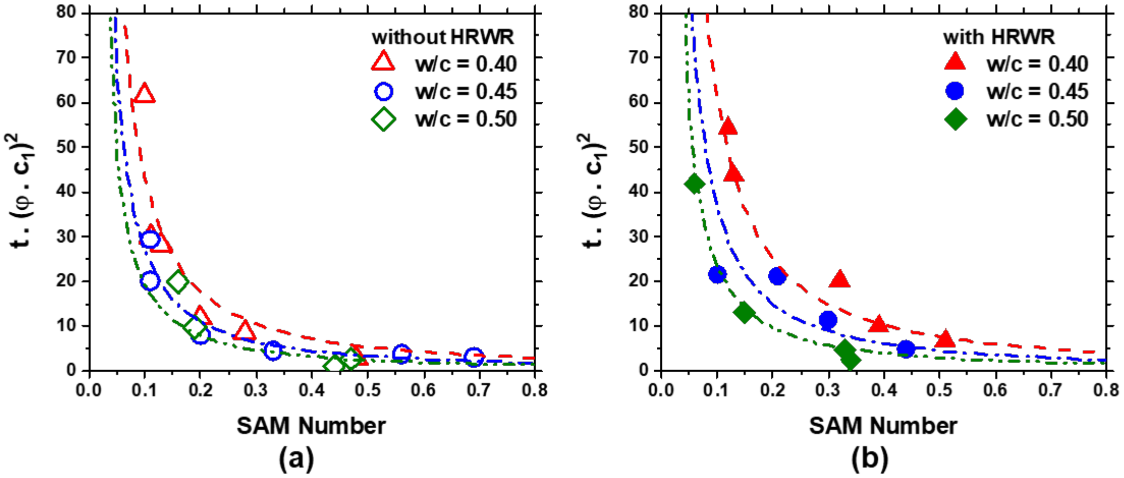

Fig. 7 *– The normalized time to reach critical saturation as a function of the SAM Number for the mixtures with varying w/c and (a) with and (b) without HRWR. Note: The lines present the predicted values based on Eq. 11.*

4.4. TIME TO REACH CRITICAL SATURATION VERSUS DURABILITY FACTOR FROM ASTM C 666

Figure 8 illustrates the durability factor measured according to ASTM C 666-15 as a function of air content and SAM Number for the concrete samples with varying w/c and air quality. Figure 8a shows that the mixtures with HRWR require a higher volume fraction of entrained air (≈5% air content) to satisfy the recommended limit for durability factor (75% according to ASTM C 666) when compared to the mixtures without HRWR (≈3% air content). This is consistent with the results of the time to reach critical saturation. The addition of HRWR coarsens the air void distribution and increases the critical flow distance, as discussed in Fig. 5. Based on Fig. 8b, the samples with and without HRWR exhibit a similar trend when the SAM Number is used to investigate the concrete performance under freeze-thaw cycles.

The normalized time to reach critical saturation as a function of the durability factor is presented in Fig. 9. According to ACI 318-14, a minimum target air content of 4.5% is required for the freeze-thaw resistant concrete mixtures in F2 and F3 environments. In addition, a SAM Number of 0.20 was recommended to satisfy the spacing factor limit of ACI 201.2R (200 μm) [15]. Based on results, the durability factor is higher than 80% and the normalized time to reach critical saturation is greater than 10 for all the mixtures with air content above 4.5% and a SAM Number below 0.20. While 90% of the mixtures with air content above 4.5% and a SAM Number below 0.20 have a normalized time to reach critical saturation of above 20, over 80% of the mixtures with air content below 4.5% and a SAM Number above 0.20 demonstrate a normalized time to reach critical saturation of below 10.

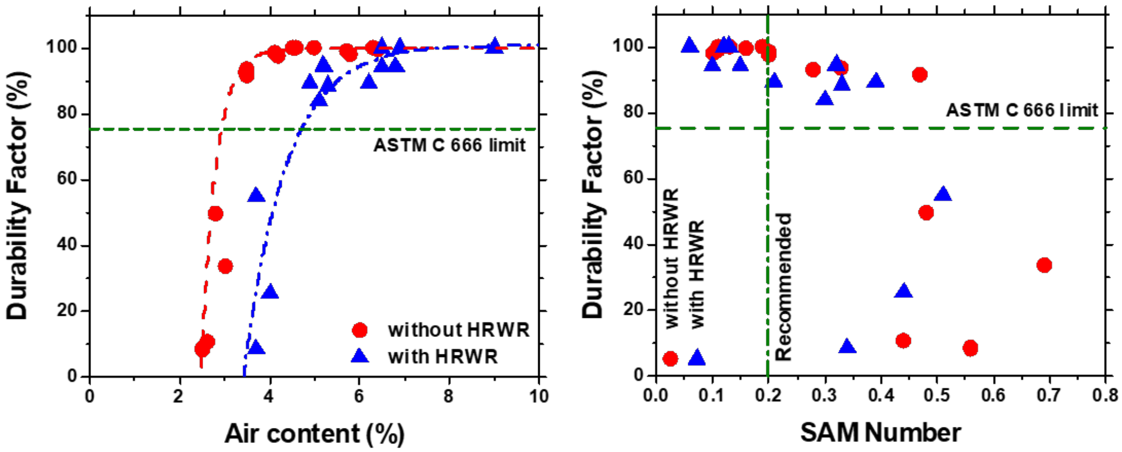

(a) (b)

Fig. 8 *– The measured durability factor (ASTM C 666-15) as a function of (a) air content and (b) SAM Number for the mixtures with varying w/c and with and without HRWR.*

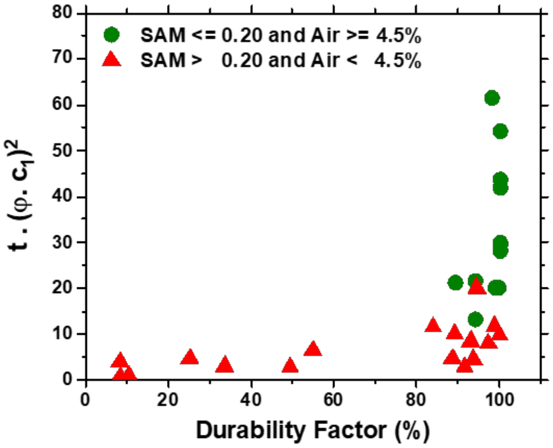

Fig. 9 *– The measured durability factor (ASTM C 666-15) versus the normalized time to reach critical saturation for the mixtures with varying w/c, air content, and air quality.*

4.5. ESTIMATING THE DOS_{CR} BASED ON SAM NUMBER AND AIR CONTENT

The air void quality has the most important impact on DoS_{CR} [8, 9]. Weiss et al. [8] and Todak [7] proposed that the DoS_{CR} can be related to the SAM Number based on Eq. 13 which was obtained as a fitted lower bound to experimental data.

$$DoS_{CR} = 87 - 10\,.\,SAM \tag{13}$$

Figure 10 illustrates the measured DoS_{CR} using UPV as a function of SAM Number for the mixtures with and without HRWR. It can be noticed that Eq. 13 shows good accordance with the experimental results of the mixtures without HRWR. However, the mixtures with HRWR have a lower DoS_{CR} compared to the mixtures without HRWR and the intercept value of Eq. 13 needs to be reduced to 82% in order to represent the lower bound of experimental data, as shown in Fig. 10b. The lower DoS_{CR} in the samples with HRWR can be explained by the lower filling rate of air voids (i.e., lower S'_2) in these samples due to higher tortuosity of the matrix, as shown in Fig. 5 [10, 13]. Figure 5 illustrates that the DoS_{CR} increase with an increase of S'_2, which indicates that at higher S'_2 water can travel faster from freezing site to the surrounding nearest air voids. It is worth noting that further research is needed to examine Eq. 13 for the mixtures with different materials such as SCMs.

The probability of failure due to freeze-thaw cycles as a function of *DoS* in the sample is illustrated in Fig. 11. A bin size of 2.5% was selected for the probability of failure calculations and the probability values are presented in the center of the bins. A threshold value of 3.3% was defined for damage index. Any value above the threshold indicates potential freeze-thaw damage. Based on Fig. 11, the failure region starts at *DoS* of ≈85% for the samples without HRWR compared to the *DoS* of ≈75% for the samples with HRWR. As expected, the probability of failure increases with increase of *DoS* in the sample. All the samples with *DoS* higher than 88% (samples with

HRWR) and 95% (samples without HRWR) fail under three applied freeze-thaw cycles. The DoS_{CR} of 75% and 85% can be used for the samples with and without HRWR respectively when the quality of the air is not known.

Equation 7 can be combined with Eq. 13 to estimate the DoS_{CR} based on volume fraction of air, as shown in Eq. 14.

$$DoS_{CR} = 87 - 10\cdot\ A\cdot Air^{-1.70}\ ,\ without\ HRWR \tag{14a}$$

$$DoS_{CR} = 82 - 10\cdot\ A\cdot Air^{-1.70}\ ,\ with\ HRWR \tag{14b}$$

Figure 12 compares the measured DoS_{CR} values as a function of the air content using UPV with the estimated trend based on Eq. 14. Based on Fig. 3a, the '*A*' values of 2.55 and 4.32 were used in Eq. 14 for the mixtures with and without HRWR, respectively. It can be noted that Eq. 14 illustrates a lower bound to experimental data.

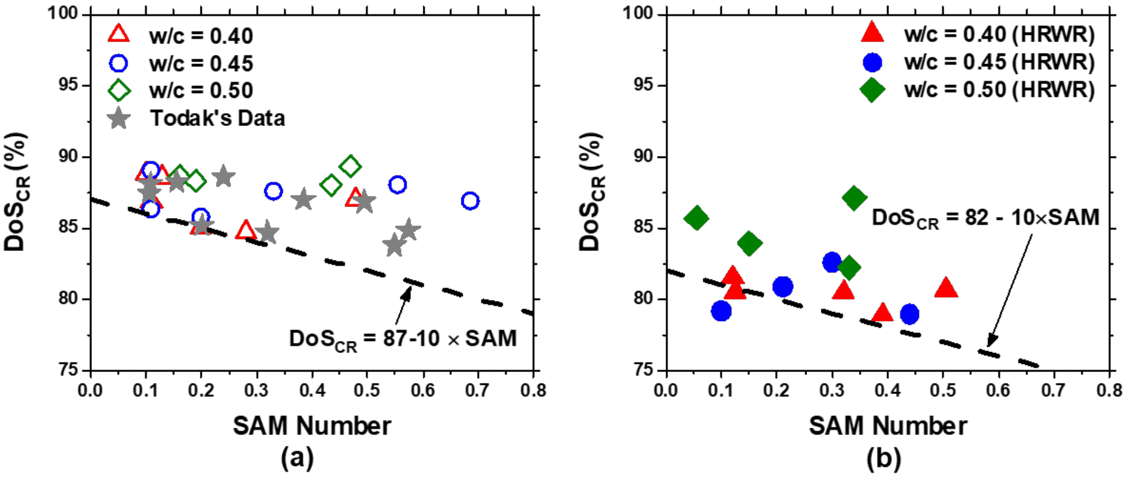

Fig. 10 *– The measured DoS_{CR} (based on UPV measurements) versus SAM Number for the mixtures with varying w/c: (a) with and (b) without HRWR. Note: A comparison with Todak's data [7] is presented in (a).*

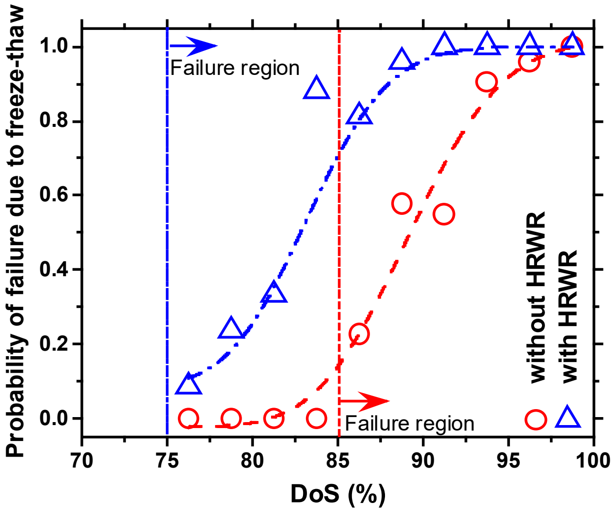

Fig. 11 – *The probability of failure due to freeze-thaw cycles versus DoS for the mixtures with varying w/c and with and without HRWR.*

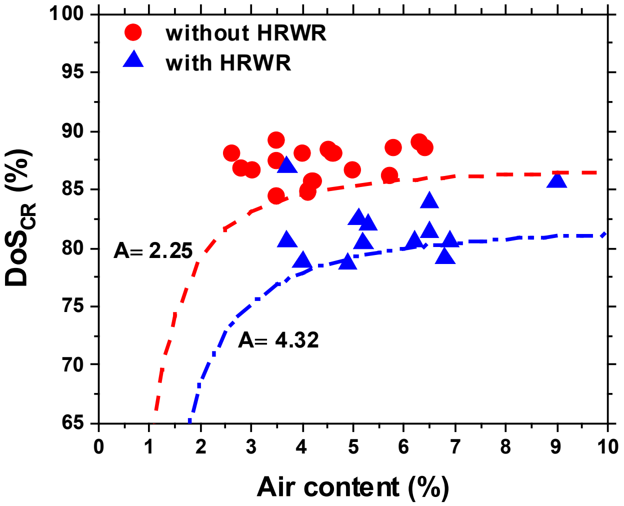

Fig. 12 – The relationship between DoS$_{CR}$ and air content for the mixtures with varying w/c and with and without HRWR based on Eq. 14.

CONCLUSIONS

This paper investigated the freeze-thaw durability of thirty different concrete mixtures with varying w/c (0.40, 0.45, and 0.50), air contents (2.5% – 9%) and air qualities (SAM Number = 0.06 – 0.70) using the time to reach critical saturation (TTRCS) modelling approach. The TTRCS model was compared to the measured durability factor using ASTM C 666-15. The following conclusions can be drawn:

- A relationship between air content and SAM Number was suggested for the mixtures with and without HRWR. This relationship depends on the quality of the air void system.
- The samples with and without HRWR showed a similar trend for the '$\Delta = DoS_{CR} - DoS_{Matrix}$' as a function of the SAM Number. Therefore, an exponential relationship was developed to estimate the Δ based on SAM Number. This relationship can be used in TTRCS model to predict the time to reach critical saturation just using SAM Number and apparent formation factor (Eq. 11). However, further work is needed to examine this equation for the mixtures with different materials.
- The time to reach critical saturation exponentially increases as the SAM Number decreases (i.e., better air quality). All samples with SAM Number below 0.20 exhibited a normalized time to reach critical saturation greater than 10. In addition, the samples with higher air content have a longer time to reach critical saturation.
- The addition of HRWR increased the normalized time to reach critical saturation in the mixtures with a low w/c at a given SAM Number (i.e., air quality). This is primarily attributed to the influence of the addition of HRWR on tortuosity of the samples (i.e., F_{APP}) with a lower w/c (w/c=0.40) which reduces the filling rate of air voids.
- Based on time to reach critical saturation results, reducing the w/c improves the freeze-thaw performance. This improvement is due to a reduction in the pore volume, tortuosity, and absorption rate of the concrete.

- The mixtures with a HRWR require a higher volume fraction of entrained air (≈5% air content) to satisfy the recommended limit for durability factor (≈70%) than the mixtures without HRWR (≈3% air content).
- According to ACI 318-14, a minimum target air content of 4.5% is required for the freeze-thaw resistant concrete mixtures in F2 and F3 environments. In addition, a SAM Number of 0.20 was recommended to satisfy the spacing factor limit of ACI 201.2R (200 μm). Based on TTRCS model and ASTM C 666 results, 90% of the mixtures with air content above 4.5% and a SAM Number below 0.20 have a normalized time to reach critical saturation of longer than 20 and durability factor that is higher than 90%.
- Experimental models were developed to estimate the DoS_{CR} based on SAM Number and air content. The mixtures with HRWR have a lower DoS_{CR} compared to the mixtures without HRWR. This lower DoS_{CR} can be explained by the lower filling rate of air voids in these samples, where water travel from freezing site to the surrounding nearest air voids is slow.
- The failure region due to freeze-thaw cycles starts at DoS of ≈85% for the samples without HRWR compared to the DoS of ≈75% for the samples with HRWR.

A summary of proposed equations to estimate the time to reach critical saturation and the critical degree of saturation based on SAM Number and air content is reported in Table 2. The derived constants in these equations based on experimental work are also reported in Table 2. However, more research is needed to examine these equations for other materials and mixture designs.

Table 2 – Summary of proposed equations to estimate time to reach critical saturation and DoS_{CR}.

Relationship	Equation	Constants
Time to reach critical saturation based on SAM Number	$t \cdot (\varphi \cdot c_1)^2 = F_{APP}.(C\ .\ SAM^{-D})^2$	A= 2.55 (no HRWR) A= 4.32 (with HRWR) B= 1.70 C= 6.03 D= 0.645
Time to reach critical saturation based on air content	$t \cdot (\varphi \cdot c_1)^2 = F_{APP} \times (C.A^{-D}.\ Air^{B\ \cdot\ D})^2$	
Critical degree of saturation based on SAM Number	$DoS_{CR} = 87 - 10\ .\ SAM\ , no\ HRWR$ $DoS_{CR} = 82 - 10\ .\ SAM\ , with\ HRWR$	
Critical degree of saturation based on air content	$DoS_{CR} = 87 - 10 \cdot A \cdot Air^{-B}\ , no\ HRWR$ $DoS_{CR} = 82 - 10 \cdot\ A \cdot Air^{-B}\ , with\ HRWR$	

ACKNOWLEDGEMENTS

The authors gratefully acknowledge support for this work through the pooled fund study (Project No. U1117C) managed by the Oklahoma Department of Transportation. This paper is the 4th in a series with [12], [10], and [13].

REFERENCES

[1] J.J. Beaudoin, C. MacInnis, The mechanism of frost damage in hardened cement paste, Cement and Concrete Research 4(2) (1974) 139-147.

[2] L. Du, K.J. Folliard, Mechanisms of air entrainment in concrete, Cement and Concrete Research 35(8) (2005) 1463-1471.

[3] G. Fagerlund, The critical degree of saturation method of assessing the freeze/thaw resistance of concrete, Matériaux et Construction 10(4) (1977) 217-229.

[4] W. Li, M. Pour-Ghaz, J. Castro, J. Weiss, Water absorption and critical degree of saturation relating to freeze-thaw damage in concrete pavement joints, Journal of Materials in Civil Engineering 24(3) (2011) 299-307.

[5] T.C. Powers, R. Helmuth, Theory of volume changes in hardened portland-cement paste during freezing, Highway research board proceedings, 1953.

[6] K. Bharadwaj, D. Glosser, M. Khanzadeh Moradllo, B. Isgor, J. Weiss, Toward the Prediction of Pore Volumes and Freeze-Thaw Performance of Concrete Using Thermodynamic Modelling, Cement and Concrete Research Under-review (2019).

[7] H.N. Todak, Durability assessments of concrete using electrical properties and acoustic emission testing, Purdue University, 2015.

[8] W.J. Weiss, T. Ley, O.B. Isgor, T. Van Dam, Toward performance specifications for concrete durability: using the formation factor for corrosion and critical saturation for freeze-thaw, Proceedings of the 96th Annual Transportation Research Board, Washington, DC, USA (2017) 8-12.

[9] G. Fagerlund, A service life model for internal frost damage in concrete, Lund University, Lund, Sweden, 2004, p. 139 pp.

[10] M.K. Moradllo, C. Qiao, M. Keys, H. Hall, M.T. Ley, S. Reese, W.J. Weiss, Quantifying Fluid Absorption in Air Entrained Concrete Using Neutron Radiography, ACI Materials Journal in press (2019).

[11] G. Fagerlund, The international cooperative test of the critical degree of saturation method of assessing the freeze/thaw resistance of concrete, Matériaux et Construction 10(4) (1977) 231-253.

[12] C. Qiao, M.K. Moradllo, H. Hall, T. Ley, J. Weiss, Electrical Resistivity and Formation Factor of Air Entrained Concrete, ACI Materials Journal 116(1) (2018) in press.

[13] M. Khanzadeh Moradllo, C. Qiao, H. Hall, M.T. Ley, S. Reese, J. Weiss, Quantifying Fluid Filling of the Air Voids in Air Entrained Concrete Using Neutron Radiography, Cement and Concrete Composites in press (2019).

[14] M.K. Moradllo, C. Qiao, B. Isgor, S. Reese, W.J. Weiss, Relating the Formation Factor of Concrete to Water Absorption, ACI Materials Journal 115(6) (2018) 887-898.

[15] M.T. Ley, D. Welchel, J. Peery, S. Khatibmasjedi, J. LeFlore, Determining the air-void distribution in fresh concrete with the Sequential Air Method, Construction and Building Materials 150 (2017) 723-737.

[16] Y. Bu, R. Spragg, W. Weiss, Comparison of the pore volume in concrete as determined using ASTM C642 and vacuum saturation, Advances in Civil Engineering Materials 3(1) (2014) 308-315.

[17] R.V. Felice, Frost resistance of modern air entrained concrete mixtures, Oklahoma State University, 2012.

USING X-RAY COMPUTED TOMOGRAPHY TO INVESTIGATE MORTAR SUBJECTED TO FREEZE-THAW CYCLES

Ghazal Sokhansefat [1], Masoud Moradian[1], Mark Finnell[1], Amir Behravan[1], M. Tyler Ley[1],*
Catherine Lucero[2], and Jason Weiss[3]

[1] Department of Civil and Environmental Engineering, Oklahoma State University,
Stillwater, OK, USA
[2] US Bureau of Reclamation, Denver, CO, USA
[3]Department of Civil and Construction Engineering, Oregan State University,
Corvallis, OR, USA

Abstract

This work uses X-ray computed micro tomography (XCT) to investigate the role of the critical degree of saturation (DOS) and air void system on the crack propagation of portland cement mortar subjected to freeze-thaw cycles. Three-dimensional imaging before and after freezing allow quantitative measurements on the location and volume of the formation of new cracks and the infilling of air voids. Cracks present before freeze-thaw cycles are observed to extend and new cracks initiate from the paste-aggregate interface. In addition, calcium-rich products were observed to fill > 20% of the volume of the air voids with a diameter < 50 μm. These observations provide insights into the freeze-thaw performance of mortar and are a step in understanding the damage in concrete.

---

*Corresponding author Tel.: +1-330-861-2361.
E-mail address: ghazal.sokhansefat@okstate.edu.

1-Introduction

It has been suggested that frost-induced cracking can occur when the concrete reaches a critical level of saturation and then experiences freeze-thaw cycles [1-7]. Samples with a saturation level greater than the critical degree of saturation (DOS) can result in microcracking even with a single freeze-thaw cycle [2, 7]. This critical DOS is reported to be between 78% and 91% in different conditions [7, 8]. It has been widely shown in previous laboratory and field experiments that the durability of concrete to freeze thaw damage can be improved by air entrainment [8-12].

Although a great deal of efforts has been spent over the past decades toward understanding the freeze-thaw damage mechanisms, there are still several unanswered questions [1, 3, 5, 7-10, 13, 14]. Some of these include how ice forms in pores [3], how the air entrainments and air void size distribution affect the freeze-thaw damage [9, 10], how different parameters such as DOS, water absorption, and freezing rate affect freeze-thaw damage [1, 7, 8], and how microcracks initiate and propagate into the cementitious materials [15]. Because of this, direct observation of the microstructure before and after freeze-thaw cycles can give insights to address some of these questions.

Several techniques have been developed to investigate the microstructure damage caused by freezing. Recent publications have characterized microcracks in a cut mortar or concrete slices with optical microscopy or scanning electron microscopic (SEM) [16-19]. The major limitation of these techniques is that they can only make observations on the exposed surface. These observations may not necessarily be representative of the performance in the rest of the system. In addition, they require preparation and testing condition that may disturb the sample and could affect the results.

X-ray computed tomography (XCT) is a powerful non-destructive tool that can be used to investigate the 3D microstructure of materials. It has been widely used in medical science to investigate biological organisms [20-22]. This method has also been used to study construction materials. Some examples include cement hydration [21, 23-27], aggregate spatial distribution [28-30], transport properties [5, 31], crack propagation [15, 32, 33], and air void distribution [26, 34-36]. In this method, a series of 2D X-ray radiographs are captured from different viewing angles and the collected data sets are used to build a 3D measurement of the internal structure called a tomograph. The tomograph can be then used for qualitative and quantitative analyses [37-41]. Because of the non-destructive nature of XCT, multiple scans can be acquired from the same sample under different conditions. This allows samples to be investigated both before and after an event like freezing.

Some recent publications have used XCT to investigate microstructural changes in concrete or mortar exposed to freeze-thaw damage [42-45]. Previous work investigated the internal structure of fly ash and portland cement mortars with different air contents exposed to frost action by using XCT [42]. The work found that anisotropic cracking occurred in the non-air-entrained samples. There are also publications that have measured the entrained air-void parameters of concrete using XCT [46-49]. It was found that the volume of microcracking decreased as the DOS was decreased. This trend continued until a critical DOS was reached and then there was no significant crack volume observed in the sample. However, this work did not investigate the change of air voids in resisting frost damage.

Although the previous work supplies important findings, these studies did not investigate the samples before and after freezing. This paper uses XCT to quantify the initiation and volume of cracking as well as the changes in air void volume caused by a single freezing cycle at very high levels of DOS. In addition, Micro X-ray Fluorescence (µXRF) and Scanning Electron Microscope (SEM) were used to evaluate the chemical composition of the materials formed.

2-Materials and methods

2.1. Materials, sample preparation, and testing condition

One non-air-entrained (nAE) and one air-entrained (AE) mortar mixtures were prepared in accordance with ASTM C192/C192M-13 using the mixture proportions as reported in Table 1. In this table, the air content of the samples was determined in accordance with ASTM C231. All mixtures were made with ASTM C618 Type I ordinary portland cement (hereafter termed OPC) and constant water to cement ratio (w/c) of 0.42. The chemical composition and physical properties of OPC are shown in Table 2.

Table 1. Mixture proportion used in freeze-thaw experiments.

Mixture ID	air content (% by volume of mortar)	Type I cement, kg/m^3 (lb/yd^3)	Water, kg/m^3 (lb/yd^3)	Sand, kg/m^3 (lb/yd^3)
nAE	5	573.3 (966.3)	240.8 (405.9)	1333.3 (2247.4)
AE	9	548.9 (925.2)	230.6 (388.7)	1276.5 (2151.6)

Table 2. Chemical and physical properties of OPC.

Material	Blaine fineness (cm^2/g)	Density (gr/cm^3)	Chemical Composition (mass %)						Phase concentration (%)			
			SiO_2	CaO	Al_2O_3	MgO	Fe_2O_3	SO_3	C_3S	C_2S	C_3A	C_4AF
Type I ordinary portland cement	3680	3.15	19.3	64.0	5.2	2.6	2.9	3.3	63.4	8.4	9	8.7

The mortar samples were cast in prism molds with nominal dimensions of 25 × 25 × 125 mm (0.98 × 0.98 × 4.92 in.). A small core 1 cm (0.39 in.) in diameter and 1 cm (0.39 in.) in height was then drilled from the specimens and used for experiments.

The samples were scanned and then conditioned to different DOS before freeze-thaw cycles. For this purpose, all samples were oven-dried in steps to 105°C for 2 days. The samples were placed in a desiccator and evacuated to a pressure of 30 mm Hg for 3 h. Following evacuation while still under vacuum, the samples were submerged in deionized water for 24 h. This condition was defined as 100% DOS. Some samples were also subjected to DOS between 85% and 95% by saturating the specimens and allowing them to dry in short periods of time at 23 °C +1 °C and 50% relative humidity (RH). When each sample was conditioned to the desired moisture content or mass, they were re-weighed and wrapped with aluminum tape to ensure no moisture loss. The tape was left in place for the remainder of the testing. The DOS and the air content for each specimen are listed in Table 3. In Table 3, the first number and the second number in the specimen ID shows if it was air-entrained (AE or nAE) and the DOS, respectively. As an example, nAE_100 is an air-entrained mortar sample with 100% DOS. There were two repeats for nAE_93 and these samples are distinguished by adding a number to the end of their name.

The samples were first scanned with XCT and then subjected to a single freeze-thaw cycle that lasted 43.5 h. The temperature was reduced and then raised from 23 °C to −35 °C with a cooling rate of 2 °C/h and a heating rate of 4 °C/h. This was done with a freezing plate on one side of the sample. The samples were then scanned after the freeze-thaw cycle.

Two samples (nAE_100, and AE_85) were then scanned by micro x-ray fluorescence (µXRF) and scanning electron microscope (SEM) to provide insight into the products formed inside air voids after a single freeze-thaw cycle.

Table 3. The list of investigated samples.

Specimen ID	Degree of saturation (%)	Air content of mortar (%)
nAE_100	100	5
nAE_93_1	93	5
nAE_93_2	93	5
AE_95	95	9
AE_85	85	9

2.2. X-ray computed tomography

Each sample was scanned before and after exposure to a freeze-thaw cycle by a ZEISS XRADIA 410 with a photon energy of 100 keV at a resolution of 4.85 μm/voxel. The captured volume of the interest was a cylinder 4.85 mm in diameter and 4.85 mm in height located near the surface of the sample as shown in Figure 1. The scan settings are summarized in Table 4.

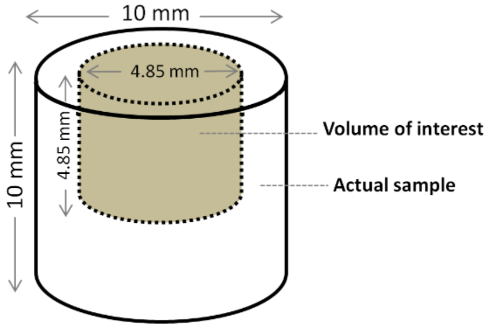

Fig. 1. Location and dimension of the investigated volume of interest (VOI).

Table 4. X-ray scan setting.

Resolution	4.85 μm/pixel
Source energy	100 keV
Optical magnification	4X
Total scan time	4 h
Number of projections	2800
Exposure time	3 s

The reconstruction was performed by XMReconstructor to create a stack of 2D slices. An example of the dataset is shown in Figure 2. Figure 2 shows the 3D representation of the sample, a typical cross-section, and a histogram of the gray value in the 3D data set. Each 8-bit 2D image consists of pixels with gray values ranging from 0 to 255 corresponding to X-ray absorption which is a function of density and composition of the material [50, 51]. The gray value contrast can be used to separate the sample into different constituent phases by image segmentation process [15, 34, 52].

The major mortar constituents are air voids, aggregates, and OPC paste. Since the air voids have the lowest density, their X-ray absorption is the lowest among other constituents and so they are highlighted as dark voxels in the reconstructed images. Conversely, aggregates absorb more x-ray because of their higher density and appear as the brightest voxels in the reconstructed image. The paste has a gray value between these two constituents (Figure 2).

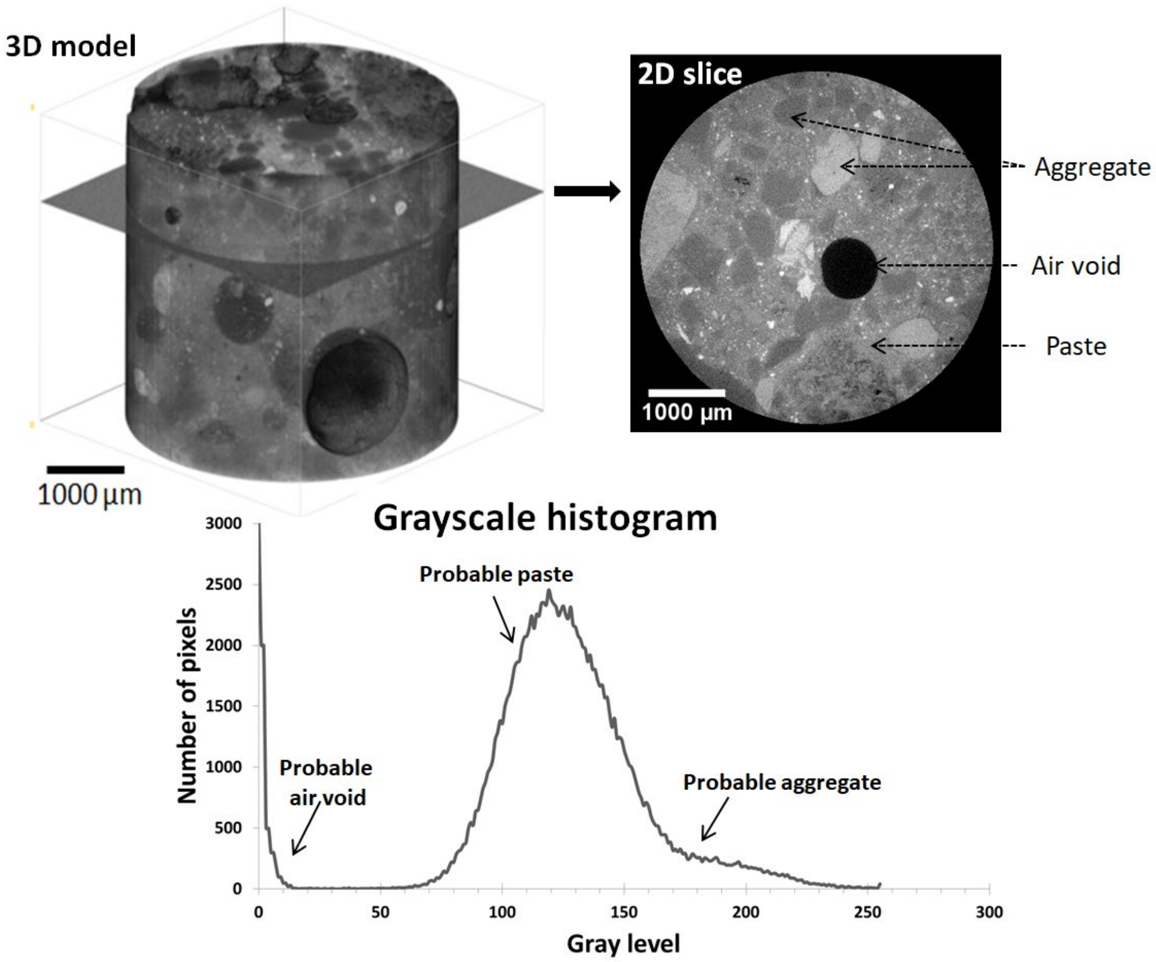

Fig. 2. A typical XCT dataset showing 3D tomography, 2D cross-section of the reconstructed image, and corresponding grayscale histogram.

2.3. Image Processing and Analysis

Different image processing techniques were used to provide quantitative and qualitative data from the XCT datasets. The data sets before and after the freeze-thaw cycles were aligned. Image subtraction and segmentation were then performed to investigate the freeze-thaw damage and identify the mortar constituents or cracks before and after a freeze-thaw cycle. For these purposes, all images were processed, analyzed, and visualized by MATLAB codes, ImageJ, and Amira 4.1.1 software.

2.3.1. Alignment of XCT datasets

To aid one-to-one comparison of the samples before and after the freeze-thaw cycle the data sets needed to be aligned. The data sets were transformed from 16-bit to 8 bit images to save computation time. Next, the histogram of the data after the freeze-thaw cycle was shifted to match the histogram of the first tomograph. Subsequently, a self-authored computer code was used to align the XCT datasets before and after the freeze-thaw cycles. The program uses the first dataset as a reference to find the matching plane in the second 3D tomography dataset. Details of the technique can be found in other publications [15, 53, 54].

2.3.2. Image subtraction

Image subtraction is a well-established image processing technique that has been previously used to study microcracks in a mortar [33, 40]. This technique uses gray value differences to detect changes between two images. The image subtraction can be mathematically defined as the difference between the digital numerical value of the reference and second image [15]:

$$r(X) = f(X) - [a \cdot g(\varphi(X)) + b] \qquad (1)$$

Where $r(X)$ is image subtraction, $g(\varphi(X))$ is gray level in the second image, a and b are coefficient of overall contrast and coefficient of brightness respectively. $f(X)$ is the gray level in the reference image which could be defined as either the image before or after the freeze-thaw cycle. A 3D median filter with a radius of 1 pixel was applied to remove noise from the subtracted image. In order to remove artifacts around the sample, image boundaries were established for both images. More details are given in the appendix.

2.3.3. Segmentation

Segmentation of XCT datasets is used to obtain quantitative data. In this study, two different methods of segmentation are used and then the results are combined. The cracks and air voids were first identified by using an Otsu analysis to identify them based on their gray value [55]. The spherical shape of the air voids was then used to separate them from the cracks. Next, the aggregate was identified by a local thresholding method. Twenty different aggregate regions were identified. The average mean and two standard deviations away from the mean of the identified regions were used to find the gray values that represent the aggregates. More details are given in the appendix. An overview of the segmentation process is shown in Figure 3 and the results of the segmentation are shown in Figure 4.

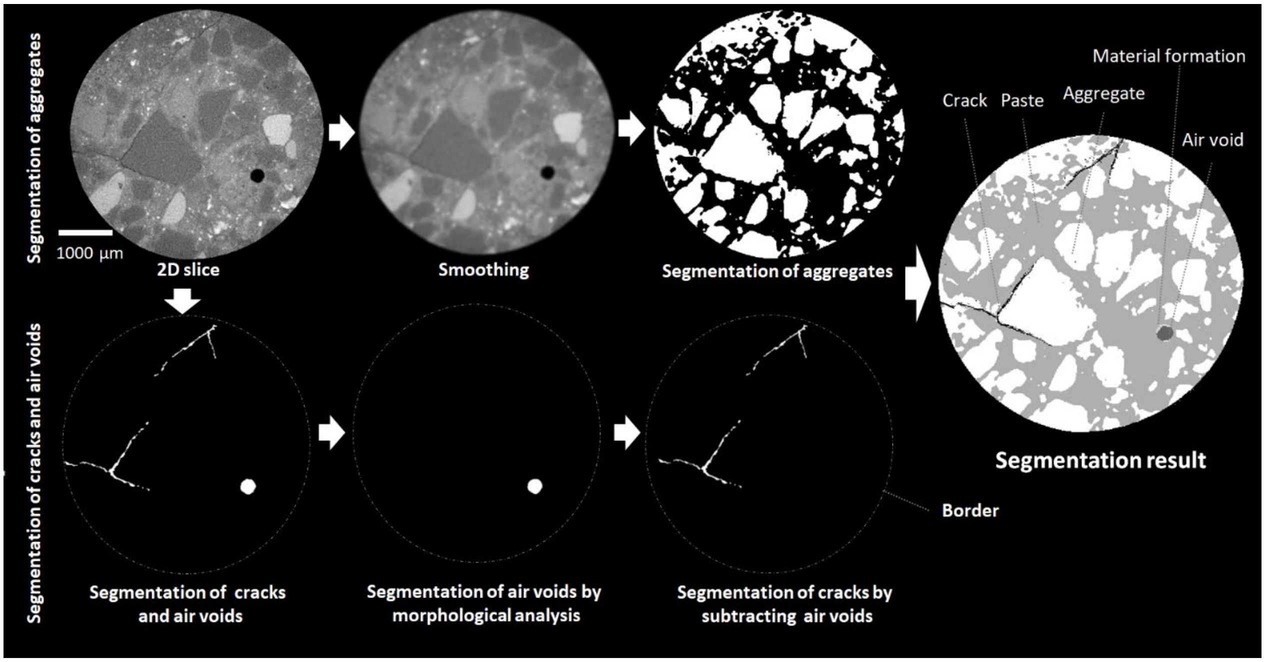

Fig.3. Segmentation process of mortar constituent including air voids, cracks, materials formed within air voids, aggregates, and paste.

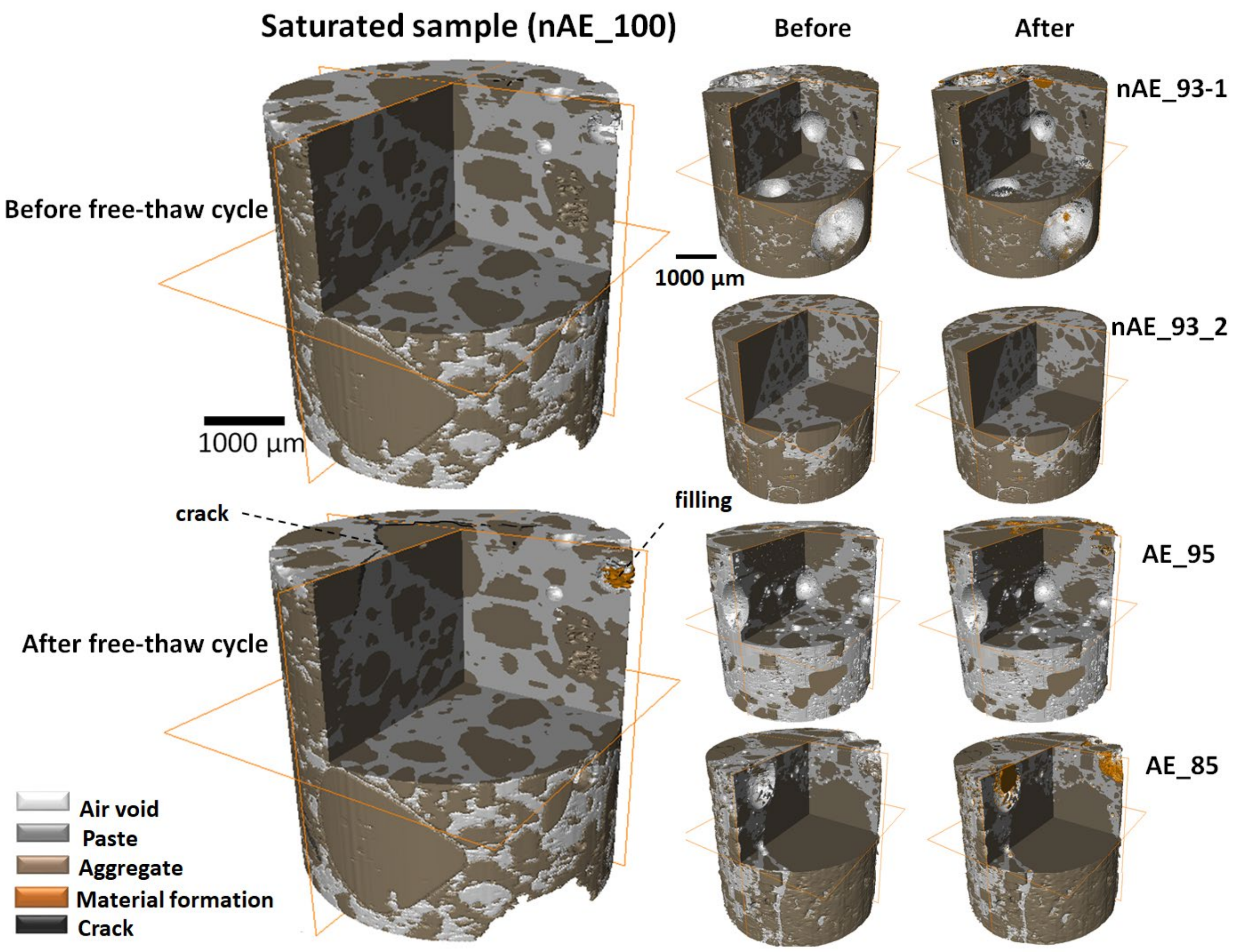

Fig.4. The result of the segmentation for all the samples.

To investigate the accuracy of these methods the aggregate volume estimated from segmentation is compared to the values from the mixture design in Table 5. The XCT data estimates a fine aggregate volume of 53.1% and the mixture design suggests 55% by volume. This is less than a 4% difference. Differences could be caused by the limited sampling region analyzed by XCT (4.85 mm diameter × 4.85 mm in height). In addition, it is possible that there are aggregates smaller than the resolution of XCT that cannot be detected. There are also decisions made in the image processing methods that may impact the results. It is also possible that the material varies within the sample. Despite these reasons, there was a small difference between the measured and expected values.

Table 5. The volume of aggregates calculated by XCT data and mixture design.

Sample No	**Volume of aggregate (%) XCT data**	**Volume of aggregate (%) mixture design**
nAE_100	56.8	55
nAE_93_1	52.0	
nAE_93_2	52.1	
AE_95	51.2	
AE_85	53.2	
Average	53.1	55

Figure 5 also compares the air void content measured by XCT data and mixture design in the lab. According to the figure, except sample nAE_93_2, the air content calculated by XCT datasets for all samples was similar to the measured air content. All of the results closely match except for sample nAE_93_2. This difference could be caused by the limited size of the volume of interest which is not necessarily represented in the entire sample. This difference will be discussed in more details later in the paper.

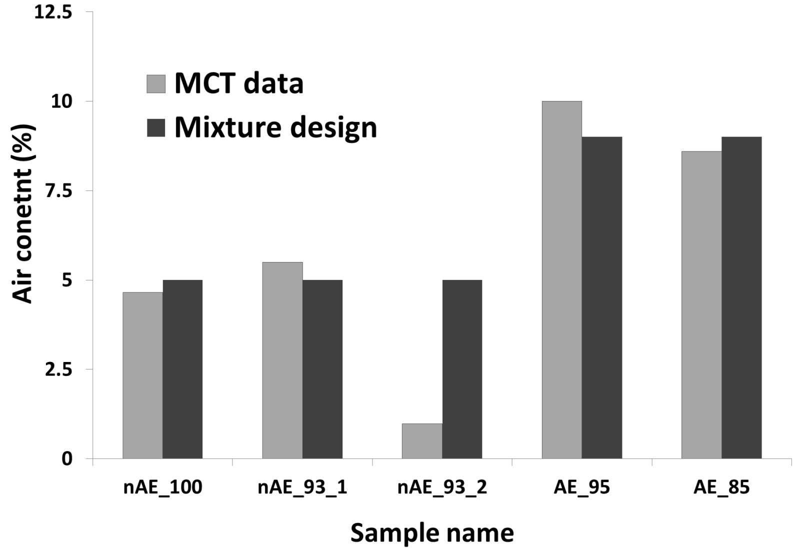

Fig.5. Comparison of air content measured by XCT data and mixture design for all samples.

The air voids were then compared before and after the freeze-thaw cycle to highlight the material that had filled the air voids. The material filling the void could be identified because regions within the voids had changed in gray value and this could be identified with image subtraction. After identifying the air voids the remaining material was assumed to be cracks. These regions are shown in Figure 3.

2.4. µXRF

A variety of spots were investigated within the cement paste and within air voids with the Orbis µXRF by EDAX. This instrument is equipped with an 80 mm² Silicon Drift Detector Energy Dispersive Spectrometer (SDD-EDS). The µXRF uses a polycapillary optic to focus X-rays to a spot size of approximately 50 µm in diameter. As the focused beam interacts with the sample, characteristic X-rays are emitted. The intensity of these X-rays is measured by SDD-EDS and stored in a database for later processing and analysis. Table 6 contains a summary of the µXRF settings used. These measurements are sensitive to trace (0.1% by weight or lower) elements, and they are useful for tracking small changes in chemistry. More details are included in the appendix.

The samples were polished to reach a cross-section where the filled air voids are observable. The samples were kept in a vacuum chamber for 12 hours to reduce the moisture content of the sample as this can be detrimental to the instrument. Next, 20 spots on the filled air voids and 20 spots on the paste were scanned.

Table 6. Settings used in µXRF imaging.

Pixel Size (µm)	30
Voltage (Kev)	40
Current (mA)	1000
Filter	25 µm Al
Live Collection Time (s)	20
Chamber Condition	vacuum
Dead Time	maximum of 20%

2.5. SEM/EDS

To make complementary observations of the structure of the material contained in the voids, the samples were examined by SEM/EDS after a single freeze-thaw cycle. In order to reach the voids containing the substance, each sample was cut and ground down and an optical microscope was used to find the voids. Next, a sample of the substance was carefully extracted from the void by placing epoxy on a graphite needle and extracting the material from a void. The needle was then placed in a vacuum chamber for 24 hours to remove any water retained in the substance and to let the epoxy cure. Three samples were taken from different voids to compare the results.

The chemical analysis of the substance was performed using the EDS on the Aspex Explorer. A needle with a sample of the substance was placed on a stage and was set in the SEM. Next, the filament drive was set to have an energy potential of 20 KeV and a current of 55 µA. Fifteen different points were investigated on the surface of the collected material. The recording period for each point was 30 seconds to obtain the proper counts from the SEM. Three samples from three voids were analyzed and their data was recorded.

3. Results and Discussion

3.1. 3D analysis of initiation and propagation of cracks

Figure 6 shows the 3D rendering of the cracks for sample nAE_100 both before and after a freeze-what cycle. The initial scans show that the sample had some initial cracks. The newly formed cracks are primarily observed near the top 20% surface of the sample (within ≈ 970 µm of the surface of the sample) after a single freeze-thaw cycle. The presence of cracks at the interface of the paste matrix and aggregate suggests that the cracks are formed in the ITZ as shown in Figure 4. No crack propagation was observed in the other samples. This could be caused by their lower DOS and the low number of freeze-thaw cycles. More information about the crack propagation of other samples can be found in the Appendix.

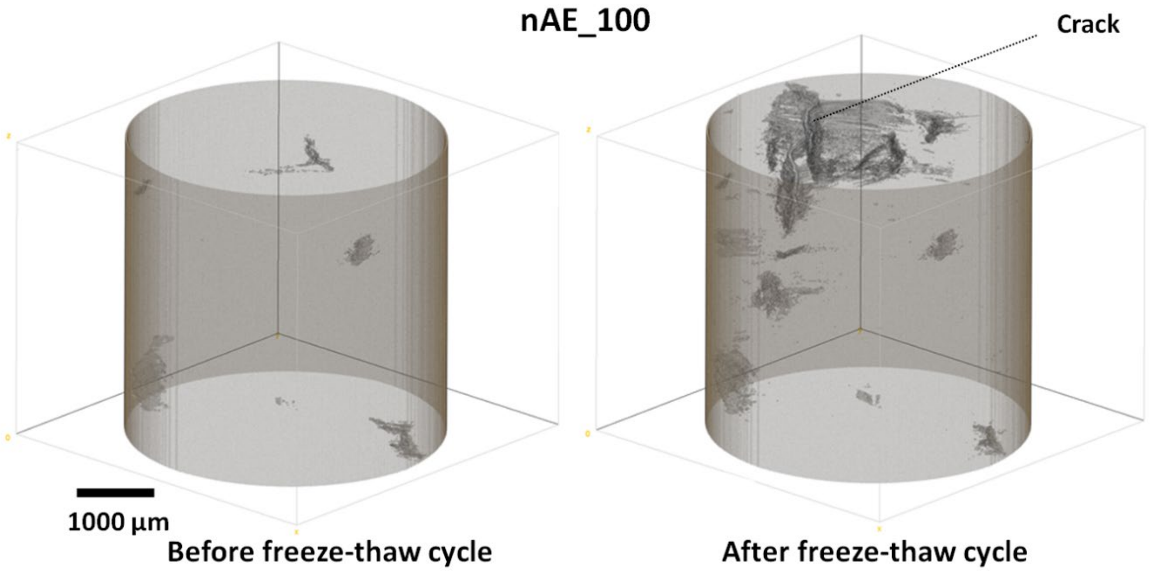

Fig.6. An example of the 3D rendering of cracks for saturated sample both before and after freeze-thaw damage for nAE_100.

Figure 7 shows th volume of cracks that occurred in either paste or aggregate both before and after the freeze-thaw cycle. This bar chart shows that the crack volume within the aggregate increased by 4.5x and the cracks found within the paste increased by ≈ 13x. After the freeze-thaw cycle, the volume of cracks within the aggregates is ≈ 1.85x higher than the volume of cracks in the paste.

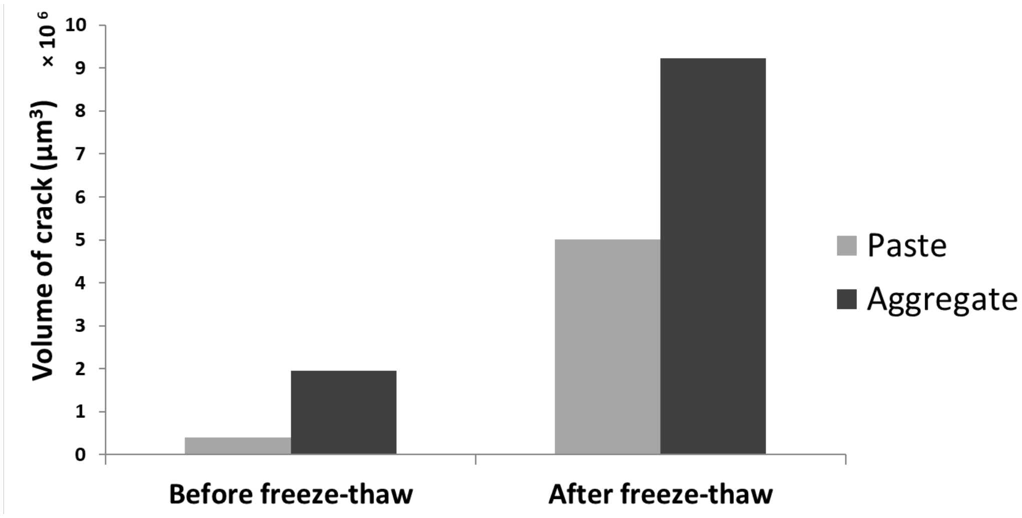

Fig.7. The volume of cracks in the paste and aggregate before and after the freeze-thaw cycle in nAE_100 sample.

Next, a detailed comparison is made. The 3D rendering of cracks, 2D reconstructed images with highlighted cracks acquired from the top 20% of the saturated sample before and after are shown in Figure 8. This region was used because of the high density of damage observed. The images in the middle and right side of Figure 8 show a large volume of cracks forming within an aggregate. It should be noted that crack propagation within aggregates in Sample nAE_100 was only observed for those aggregates that showed cracking or imperfection before being exposed to the freeze-thaw cycle. This means that aggregate that is cracked prior to the freeze-thaw cycle were more susceptible to additional cracking. Additional analysis is included in the appendix to examine the percentage of the volume of aggregate, paste, and air at different distances from the cracks. These findings support the observations of the 3D crack observations shown in Figure 8.

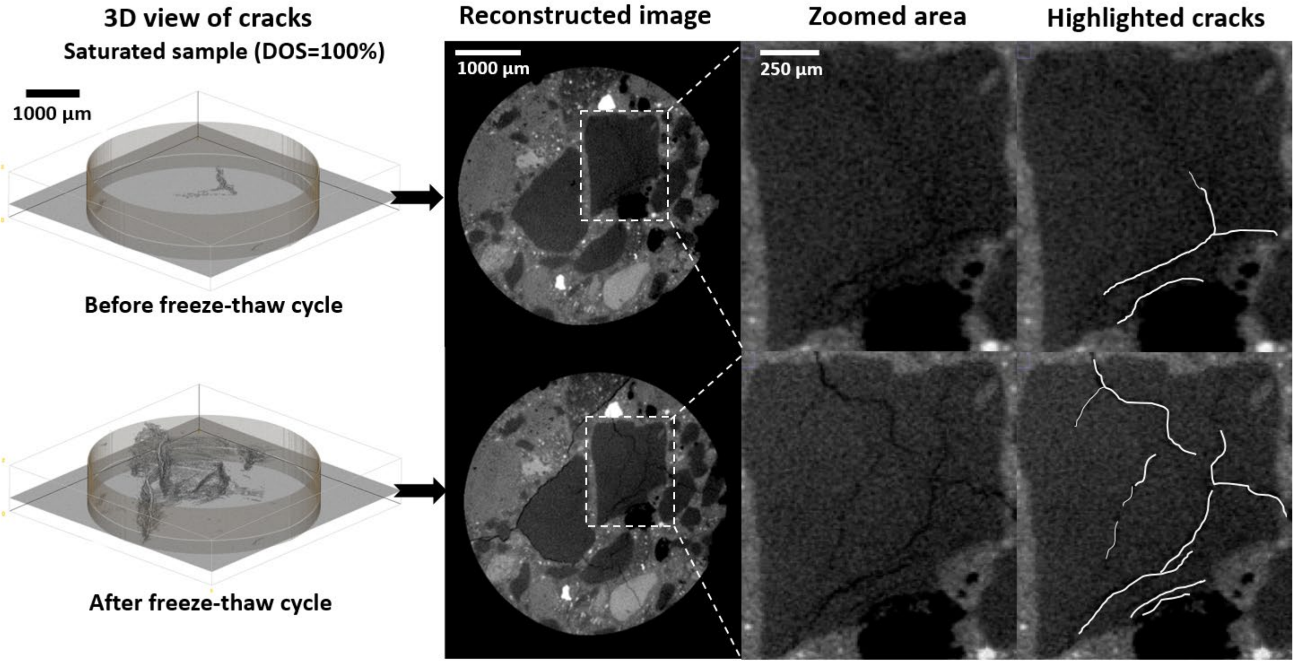

Fig.8. An overview of the initiation and propagation of cracks in the top 20% of the saturated sample (nAE_100) before and after the freeze-thaw cycle. Zoomed area is highlighted as white dash line in the reconstructed images.

3.2. 3D analysis of air voids after freeze-thaw damage

Figure 9 and Figure 10 show 3D renderings of the air voids, cracks, and infilled voids. The air voids are shown in white, cracks are highlighted in black, and infilled voids are shown in orange. Based on the 3D renderings, the infilled voids were observed in all samples. When a void is observed to fill, this suggests that pore solution entered the void during the freezing cycle and that the concentration within the void was high enough to cause solids to precipitate. These solids are important as they can reduce the overall volume of the void and reduce the space available for future freeze-thaw cycles.

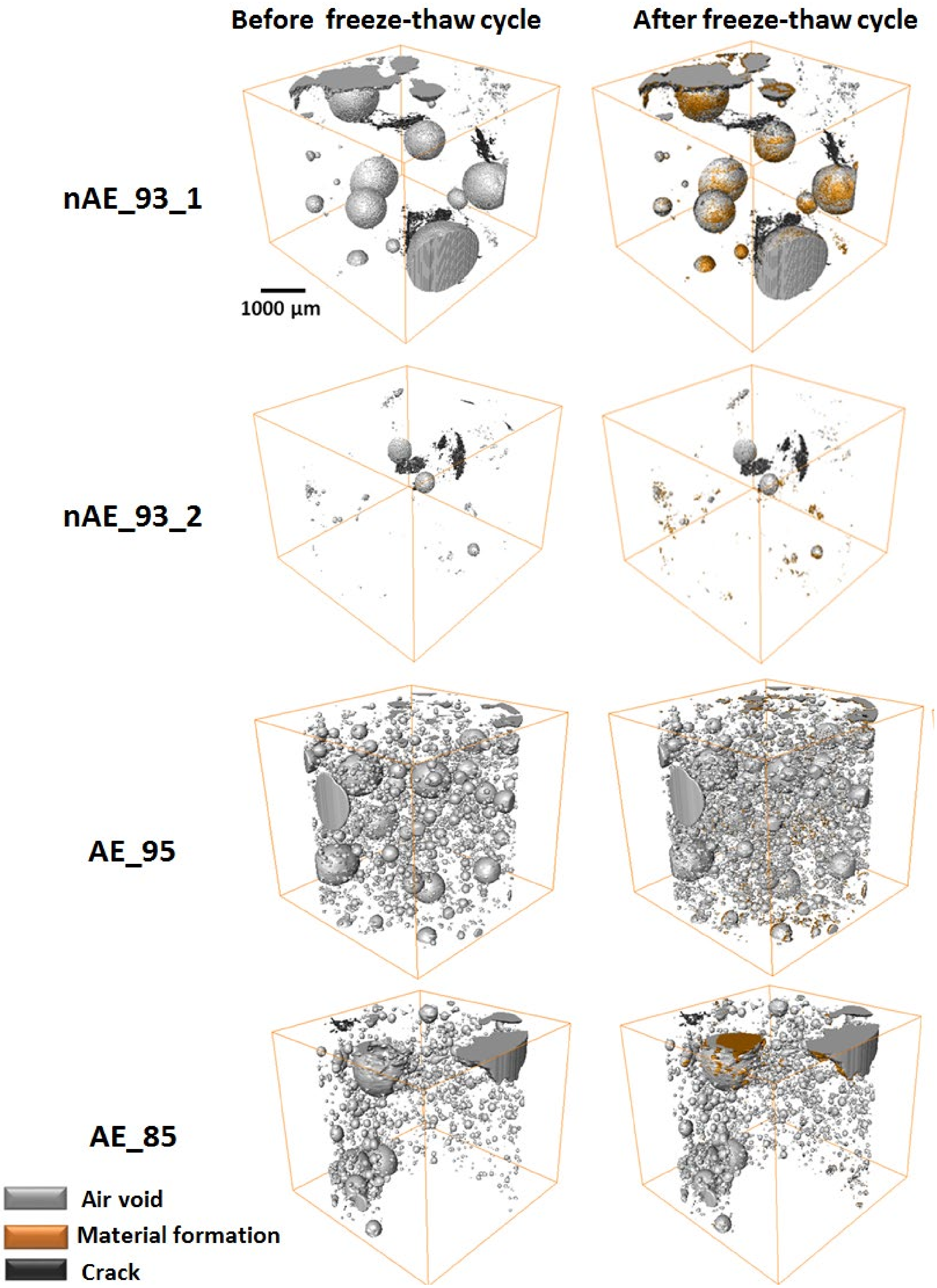

Fig.9. 3D rendering of the air voids, cracks, and infilled voids for samples with DOS lower than 100% before and after freeze-thaw testing.

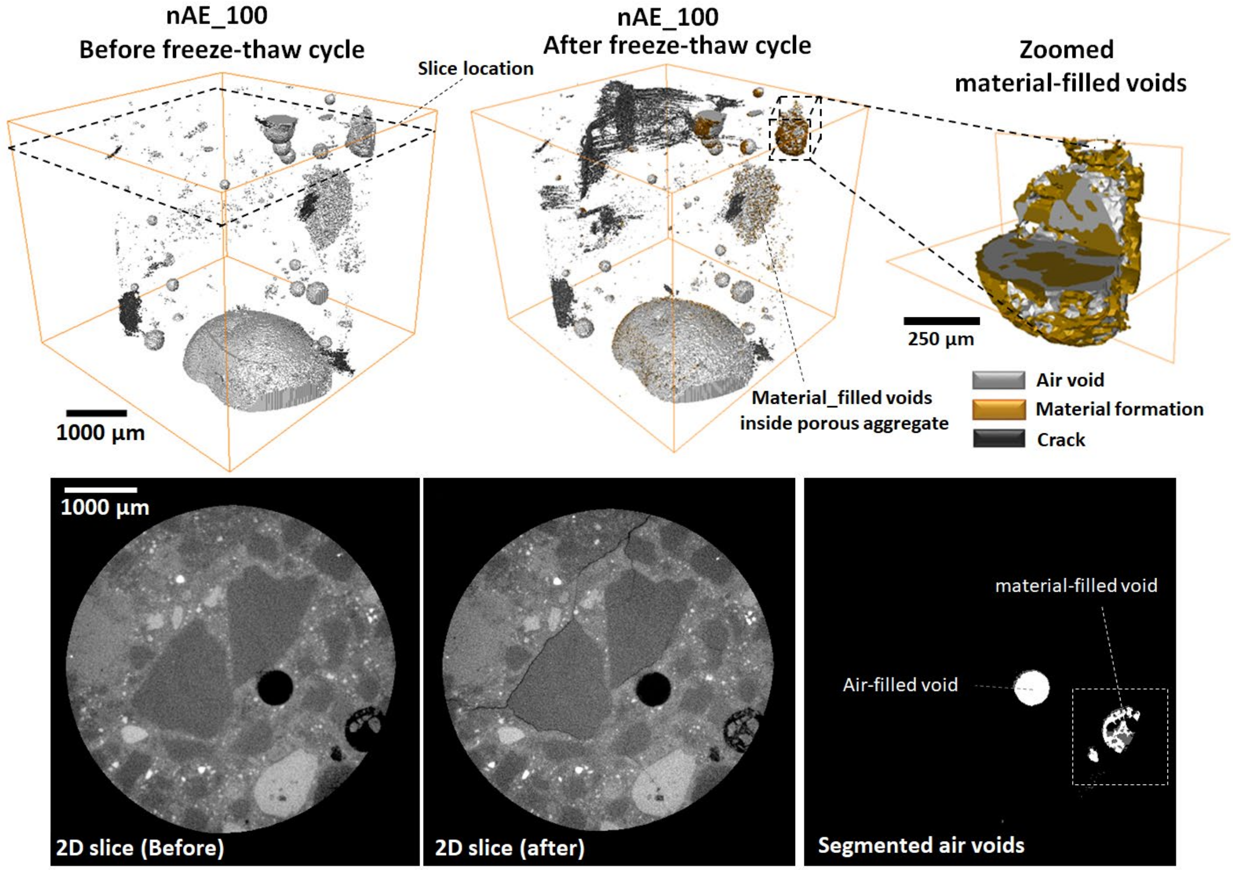

Fig.10. An example of a 3D rendering of the air voids, cracks, and infilled voids for the saturated sample (DOS=100%) before and after freeze-thaw testing.

3.3. Quantitative evaluation of air void filling

Figure 11 shows the percentage of voids that lost at least 20% of their volume after a single freeze-thaw cycle. This volume was chosen based on the image processing results as it was large enough that the volume change was measurable and not likely an artifact. The number of individual air voids used in these calculations is about 500 and 30,000 for each non-air-entrained and air-entrained sample, respectively.

The saturated sample (nAE_100) had the lowest percentage of voids that were filled compared to the other samples. As shown in Figure 10, this sample also had the most damage. The damage from the freezing cycle may have reduced the internal fluid pressure and not caused the voids to fill. This is an area of further study.

For all of the other samples with a DOS ≤ 95% it was common to observe air void filling. This air void filling was observed in > 50% of the voids ≤ 75 µm. All voids are assumed to be spherical and their diameter will be used to refer to their respective sizes. In > 75% of the voids with a diameter ≤ 50 µm at least 20% of the volume was lost to the infilling material. It should also be noted that this was observed in samples with and without air entrainment.

Both samples nAE_93_1 and nAE_93_2 are thought to be similar in air volume, mixture proportions, and degree of saturation; however, nAE_93_2 shows a higher percentage of infilling for the voids > 50 µm. While the voids > 50 µm show differences, the voids < 50 µm showed very similar behavior. It is not clear what causes these differences and this should be investigated further. Figure 12 shows the air void size distribution for samples nAE_93_1 and nAE_93_2 and both are similar. However, the graph shows that nAE_93_2 has a higher number of finer air voids and ≈ 1.5x higher number of detectable voids compared to nAE_93_1. This difference between the void sizes might explain the difference between the void volume of samples nAE_93_1 and nAE_93_2.

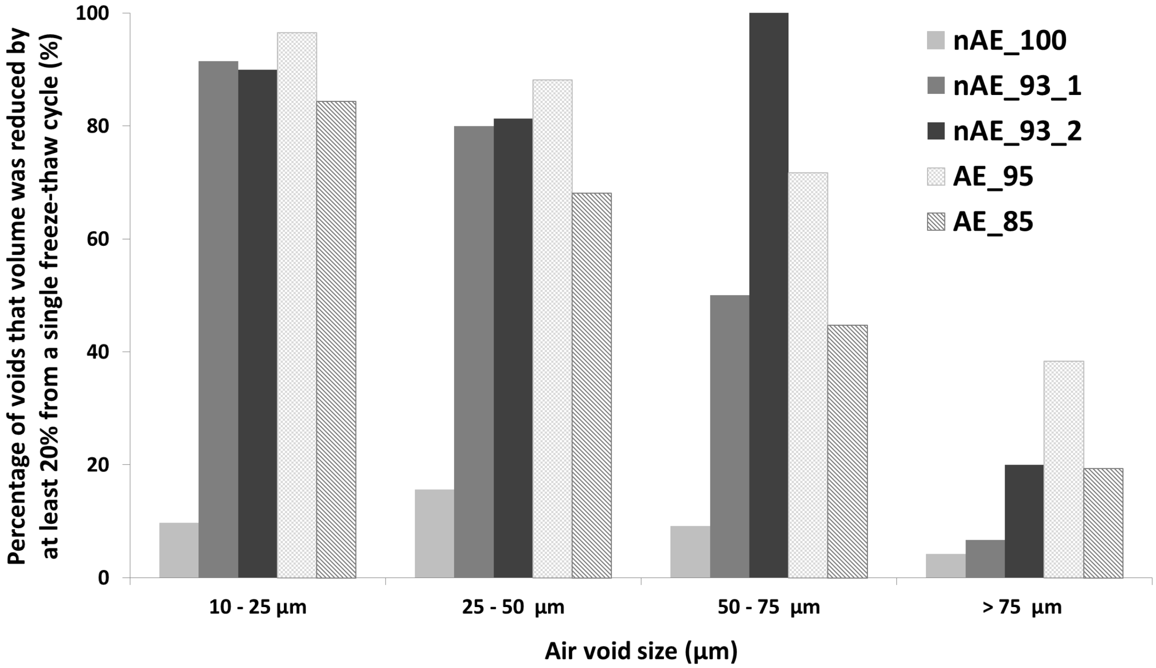

Fig.11. Percentage of voids that volume was reduced by at least 20% from a single freeze-thaw cycle

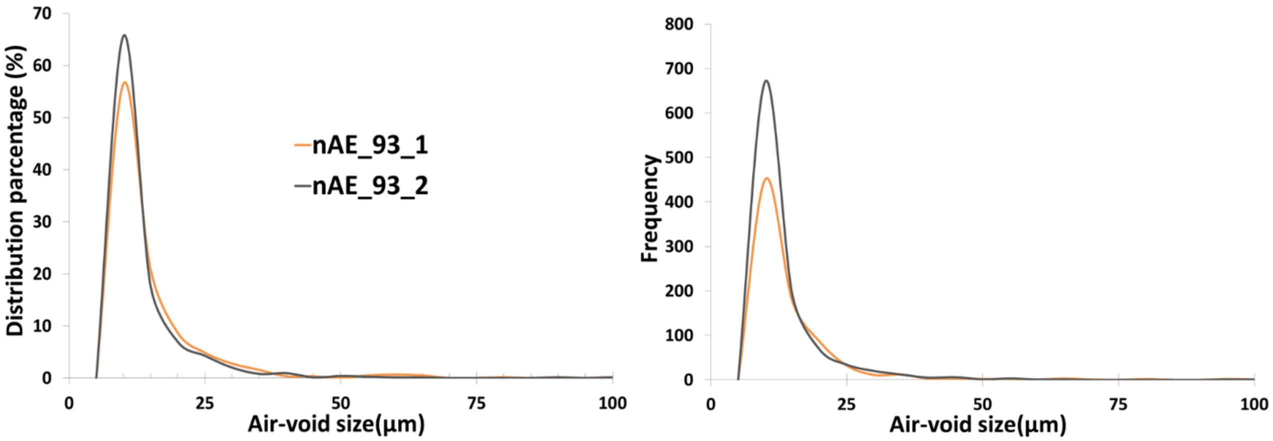

Fig.12. Air void size distribution for sample nAE_93_1 and nAE_93_2

The average infilled volume of partially filled voids for a single freeze-thaw cycle in these high DOS samples is shown in Figure 13. Some examples of the calculation of this value for four individual voids with different sizes are also shown at the bottom of the graph with corresponding 3D renderings. As expected, the smallest group of air voids with a size between 10 and 25 µm has the highest percentage of infilled volume compared to the larger voids. This higher value in the smaller voids can be attributed to the larger surface/volume of this group and that these voids probably contained more fluid during freezing than the larger voids. The sample nAE_100 again shows a lower amount of filled voids. This is probably due to the observed damage in this sample. More information about the average distance between air voids can be found in the Appendix.

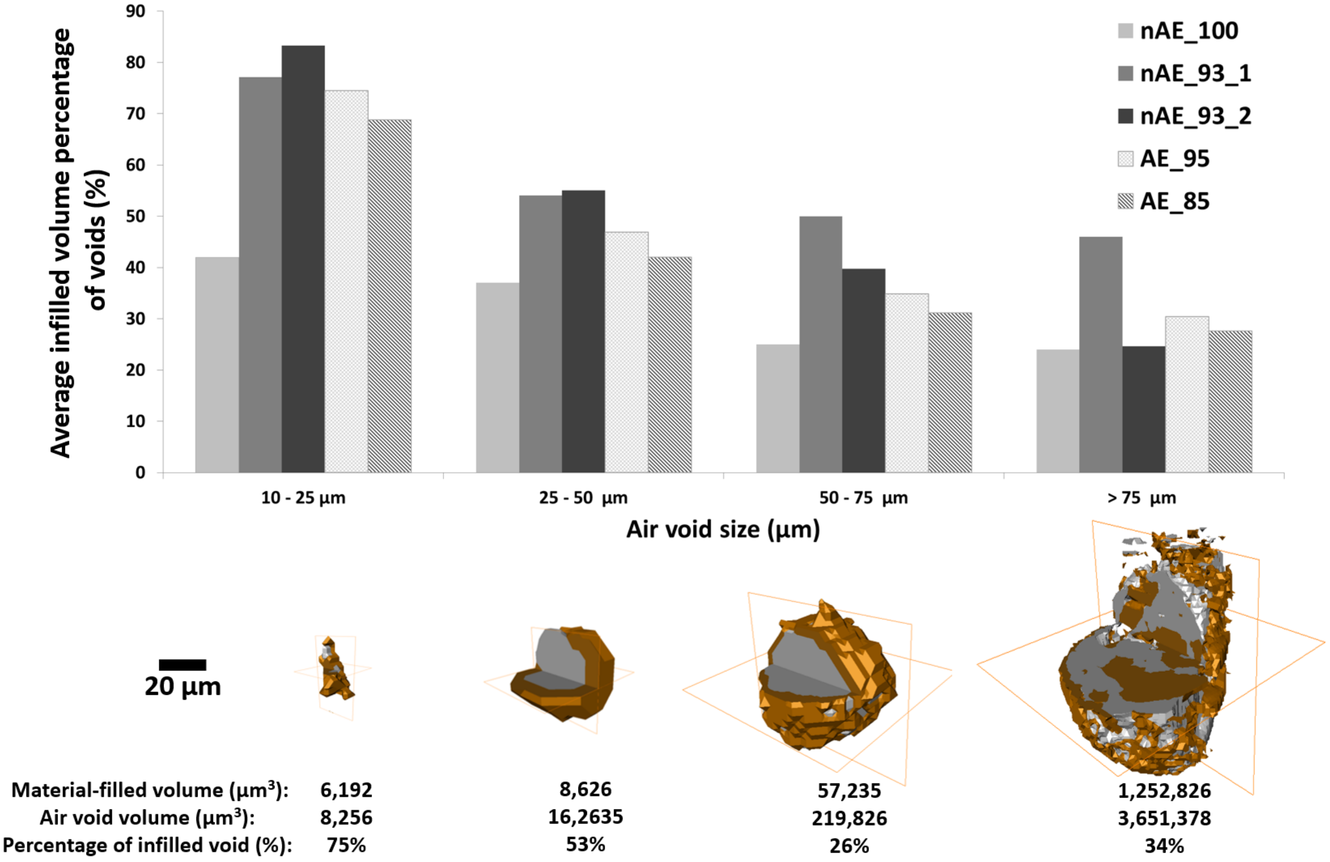

Material-filled volume (µm³):	6,192	8,626	57,235	1,252,826
Air void volume (µm³):	8,256	16,2635	219,826	3,651,378
Percentage of infilled void (%):	75%	53%	26%	34%

Fig.13. The average infilled volume percentage in voids with at least 20% partial infilling. An example of a 3D rendering of individual partially material-filled voids for each size range with corresponded air void and material-filled volume, and infilled void percentage are also shown in the bottom of the graph.

Figure 14 shows the 3D rendering of material formation and the volume of material-filled voids at different cross-sections. In all of the samples, except nAE_93_2, there is a higher volume of infilled material near the surface of the sample. For nAE_93_2 there was no significant change in the infilled air voids over the depth. This could be because of the low amount of air content (1%) detected by XCT in the investigated volume of interest compared to the expected mixture design air content (5%).

One of the reasons for the higher volume of infilled material near the surface of the samples could be the thermal gradient caused by the placement of the freezing plate. Since the freezing plate is at the bottom of the sample this would mean that the top of the sample would be the last portion to freeze. The solution in the last region to freeze would be expected to have a higher concentration of dissolved ions and therefore would form a larger volume of precipitated solids within the air voids.

From the XCT data, the material formed within the voids has a similar X-ray absorption as hydrated cement paste. Based on previous publications this means this material is not likely to be pure calcium hydroxide [56]; however, it could be a mixture of calcium hydroxide and other precipitated salts such as Friedel's salt, Kuzel's salt, or salts originated from the aggregates [57-59]. The chemical composition of the materials formed within the voids is examined by µXRF and SEM in the following section.

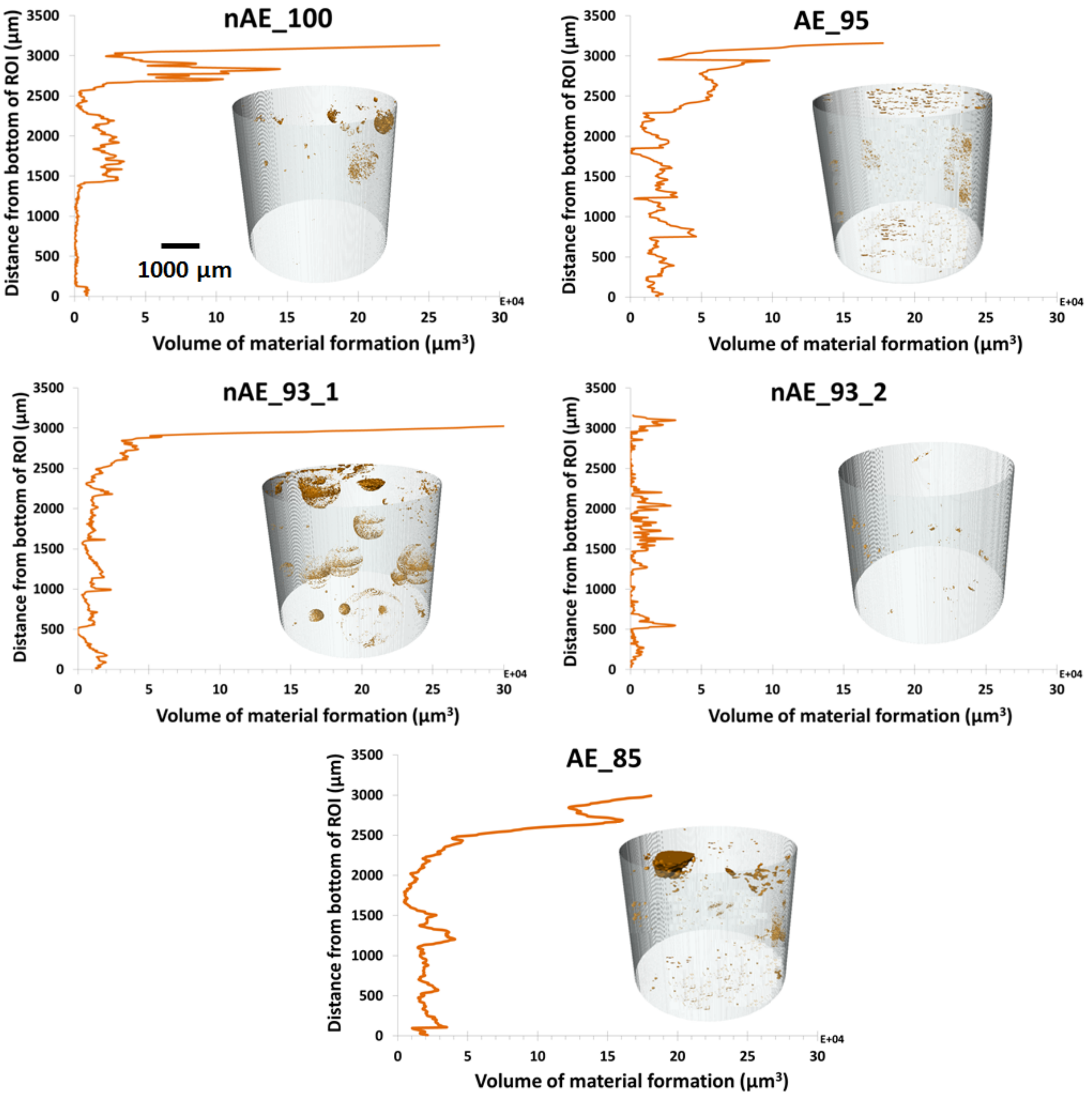

Fig.14. Material formation at different image cross-section and corresponding 3D rendering of material loss. The border of specimens in 3D rendering is shown as transparent gray.

3.3.1. Investigation of the chemical composition of the formed material

3.3.1.1 µXRF measurements

Table 7 shows the average intensity of the counts from the air voids and the mortar matrix for each sample from µXRF. The results showed that Ca is the major element found within the air voids, with a lower concentration of all other elements found within the paste. These differences are evaluated by the student's t-Test to investigate if the obtained results are statistically significantly different. For each element, a p-value of < 0.05 was obtained for average intensity within the air void and the paste which showing that the results are statistically significantly different with a 95% confidence interval.

Table 7. The Average intensity of some elements within the paste and within the filled air voids as measured by μXRF.

Element	Average intensity (cps)		Standard error		P value (T-test)
	Paste	filled voids	Paste	filled voids	
Mg	9	4	2.3	0.2	0.018
Al	74	41	11.0	6.1	0.005
Si	986	226	150.5	16.7	5.57E-06
S	119	72	16.3	4.5	0.004
Ca	43728	54636	3858.5	3684.8	0.022
Ti	208	69	28.2	12.2	1.8E-05
Mn	124	60	23.7	4.5	0.005
Fe	5193	1628	917.9	262.2	0.002

3.3.1.2. SEM/EDS measurements

Table 8 shows chemical compositions found within the three different voids. Also, Figure 15 shows the morphology of the materials found in the air voids. The result showed that Ca is the main element of the substance found within the examined air voids, with traces of other elements like Si, Al, Fe, S, K. This suggests that the material is primarily calcium hydroxide with some other salts. These findings confirm the results from the μXRF measurements.

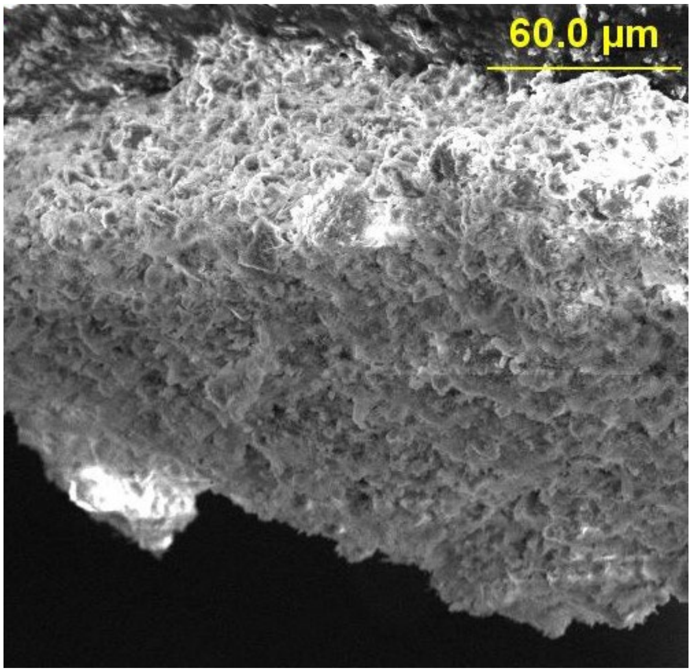

Fig.15. An example of the morphology of the materials formed in air voids by SEM.

Table 8. Chemical composition of substance within the examined air voids as measured by SEM.

Element	Element By Mass %			Standard error		
	S1	S2	S3	S1	S2	S3
Ca	90.9	75.3	75.9	1.9	5.7	4
Si	0.8	1.7	2.9	0.2	0.6	1.3
O	7.9	17.9	19.9	1.9	5.5	3.2
Al	0.4	3.9	0.5	0.2	1	0.3
Fe	0	0.7	0.2	0	0.6	0.2
S	0	0	1	0	0	0.9
Na	0	0	0	0	0	0
Mg	0	0	0.3	0	0	0.2
K	0	0.5	0.3	0	0.4	0.3

4. Practical Significance

This work gives important insights into the mechanisms of freeze-thaw damage as it shows that the air void filling can occur in the smaller voids after only a single freeze-thaw cycle at high levels of DOS. Another significant observation is that the samples with DOS ≤ 95% showed void filling after a single freeze-thaw cycle. The only sample that did not show void filling was the 100% DOS sample that was damaged. This difference in performance is attributed to this sample being damaged by the freezing events and so the fluid did not enter the voids. Figure 13 shows that the voids that were filled were primarily < 20 μm and these voids were the furthest from the freezing surface. Furthermore, up to 70% of the volume of voids < 20 μm are observed to fill after a single freeze-thaw cycle.

These small voids are arguably the most important for the freeze-thaw durability of the concrete as they provide a significant amount of protection for a given volume against freeze-thaw damage [2, 60]. As the DOS increases, the ratio of the fluid to space increases. This makes it more likely that the fluid will fill the voids on freezing. If these voids are infilling with the material then it means that they are not able to accommodate additional solution on freezing. Therefore, the air voids cannot provide appropriate protection and this could cause premature failure on freezing. While it is common for air void filling to be observed in freeze-thaw damaged concrete in the field, this work shows that samples with a DOS between 85% and 95% that this filling happens with a single cycle. This infilling of air voids could explain why rapid damage is observed in concretes if their DOS is high.

It should also be noted that samples with DOS near 100% showed damage after a single freeze-thaw cycle. Furthermore, it was found that the majority of the cracks formed either in or near aggregates. However, Figure 4 shows that no visible damage was observed for the air entrained and non-air entrained samples, even with DOS as high as 95%. It is expected that a higher number of freeze-thaw cycles are needed for observable damage in these samples.

5. Conclusion

In this study mortar samples made with different air volume and DOS were examined with XCT to investigate the microstructural changes caused by a single freeze-thaw cycle. This work was able to observe a change in the crack distribution and volume as well as the significant air void filling that occurred. Although all of the samples had a DOS > 85%, the non-air entrained saturated sample with DOS ≈ 100% was the only sample where damage was observed. However, it is possible that cracks formed that are below the resolution of the methods used and so they would not be detected. The findings for cracking and void filling are reported below.

Key findings for cracking:

- Crack initiation and propagation were primarily observed away from the freezing surface of the sample and within 970 µm of the surface.
- A single freeze-thaw cycle caused an increase in the volume of cracks within aggregate by 4.5x and an increase in the volume of cracks within the paste by 13x compared to the volume of cracks before the freeze-thaw cycle.
- Cracks within aggregates before the freeze-thaw cycle were observed to extend.

Findings for air void filling:

- The air void filling was observed away from the freezing surface and within 700 µm of the surface.

- The µXRF, as well as SEM data, show that the material formed within the voids are > 75% Ca and have trace amounts of Si and Al.
- Greater than 70% of the volume of air voids < 20 µm filled after a single freeze-thaw cycle.
- The air voids were not filled in the sample with significant damage after one freeze-thaw cycle.

Research is needed to investigate how multiple freeze-thaw cycles will impact the findings from this work. Additional work to study the filling materials with more detailed chemical composition would also be useful. While limited cracking was observed in the samples, these results show that this procedure shows great promise to be used to investigate samples under higher numbers of freeze-thaw cycles.

6. References

1. Fagerlund, G., *Critical degrees of saturation at freezing of porous and brittle materials*. 1972, Lund Institute of Technology: Division of Building technology.
2. Litvan, G.G., *Frost action in cement paste.* Materials and structures, 1973. **6**(4): p. 293-298.
3. Scherer, G.W., *Crystallization in pores.* Cement and Concrete Research, 1999. **29**(8): p. 1347-1358.
4. Scherer, G.W. and J.J. Valenza, *Mechanisms of frost damage.* Materials science of concrete, 2005. **7**(60): p. 209-46.
5. Bentz, D.P., et al., *Microstructure and transport properties of porous building materials. II: Three-dimensional X-ray tomographic studies.* Materials and Structures, 2000. **33**(227): p. 147-153.
6. Li, W.T., et al., *Water Absorption and Critical Degree of Saturation Relating to Freeze-Thaw Damage in Concrete Pavement Joints.* Journal of Materials in Civil Engineering, 2012. **24**(3): p. 299-307.
7. Fagerlund, G., *The critical degree of saturation method of assessing the freeze/thaw resistance of concrete.* Materials and Structures, 1977. **10**(4): p. 217-229.
8. Li, W., et al., *Water absorption and critical degree of saturation relating to freeze-thaw damage in concrete pavement joints.* Journal of Materials in Civil Engineering, 2011. **24**(3): p. 299-307.
9. Powers, T.C. and T.F. Willis, *The air requirement of frost resistant concrete*, in *Highway Research Board Proceedings*. 1950.
10. Shang, H.S., Y.P. Song, and J.P. Ou, *Behavior of Air-Entrained Concrete after Freeze-Thaw Cycles.* Acta Mechanica Solida Sinica, 2009. **22**(3): p. 261-266.

11. Sun, Z.H. and G.W. Scherer, *Effect of air voids on salt scaling and internal freezing.* Cement and Concrete Research, 2010. **40**(2): p. 260-270.
12. Yang, Z., W.J. Weiss, and J. Olek, *Water transport in concrete damaged by tensile loading and freeze–thaw cycling.* Journal of materials in civil engineering, 2006. **18**(3): p. 424-434.
13. Scherer, G.W. and J. Valenza, *Mechanisms of frost damage.* Materials science of concrete, 2005. **7**(60): p. 209-46.
14. Powers, T.C. and R.A. Helmuth. *Theory of volume changes in hardened portland-cement paste during freezing*. in *In Highway research board proceedings*. 1953.
15. Nguyen, T.T., *Modeling of complex microcracking in cement based materials by combining numerical simulations based on a phase-field method and experimental 3D imaging*. 2015, Université Paris-Est.
16. Ammouche, A., et al., *Image analysis for the automated study of microcracks in concrete.* Cement & Concrete Composites, 2001. **23**(2-3): p. 267-278.
17. Elzafraney, M. and P. Soroushian, *Assessment of microcrack development in concrete materials of different strengths.* Materials and Structures, 2004. **37**(274): p. 724-731.
18. Jacobsen, S., J. Marchand, and H. Hornain, *Sem Observations of the Microstructure of Frost Deteriorated and Self-Healed Concretes.* Cement and Concrete Research, 1995. **25**(8): p. 1781-1790.
19. Litorowicz, A., *Identification and quantification of cracks in concrete by optical fluorescent microscopy.* Cement and Concrete Research, 2006. **36**(8): p. 1508-1515.
20. Christiansen, B.A., *Effect of micro-computed tomography voxel size and segmentation method on trabecular bone microstructure measures in mice.* Bone Rep, 2016. **5**: p. 136-40.
21. Hu, Q., et al., *Direct three-dimensional observation of the microstructure and chemistry of C3S hydration.* Cement and Concrete Research, 2016. **88**: p. 157-169.
22. Romao, M.M.A., et al., *Micro-computed tomography and histomorphometric analysis of human alveolar bone repair induced by laser phototherapy: a pilot study.* International Journal of Oral and Maxillofacial Surgery, 2015. **44**(12): p. 1521-1528.
23. Moradian, M., *Direct Observations on Microstructure Evolution of Cement Systems at Early Ages*. 2017, Oklahoma State University.
24. Moradian, M., et al., *Direct observation of void evolution during cement hydration.* Materials & Design, 2017. **136**: p. 137-149.
25. Moradian, M., M.T. Ley, and Z.C. Grasley, *Stress induced dissolution and time-dependent deformation of portland cement paste.* Materials & Design, 2018. **157**: p. 314-325.
26. Moradian, M., et al., *Direct in-situ observation of early age void evolution in sustainable cement paste containing fly ash or limestone.* Composites Part B: Engineering, 2019: p. 107099.
27. Ley, M., et al. *Combining Nano X-ray Tomography and Nano X-ray Fluorescence to Create Time-dependent Three Dimensional Constitutive Maps*. in *2nd International Conference on Tomography of Materials and StructuresQuebec City, Canada*. 2015.
28. Erdogan, S.T., E.J. Garboczi, and D.W. Fowler, *Shape and size of microfine aggregates: X-ray microcomputed tomography vs. laser diffraction.* Powder Technology, 2007. **177**(2): p. 53-63.
29. Garboczi, E.J., *Three-dimensional mathematical analysis of particle shape using X-ray tomography and spherical harmonics: Application to aggregates used in concrete.* Cement and Concrete Research, 2002. **32**(10): p. 1621-1638.

30. Sokhansefat, G., et al., *Investigation of concrete workability through characterization of aggregate gradation in hardened concrete using X-ray computed tomography.* Cement and Concrete Composites, 2019. **98**: p. 150-161.
31. Bentz, D.P., et al., *The Visible Cement Data Set.* Journal of Research of the National Institute of Standards and Technology, 2002. **107**(2): p. 137-148.
32. Kim, K.Y., T.S. Yun, and K.P. Park, *Evaluation of pore structures and cracking in cement paste exposed to elevated temperatures by X-ray computed tomography.* Cement and Concrete Research, 2013. **50**: p. 34-40.
33. Sinha, S.K. and P.W. Fieguth, *Automated detection of cracks in buried concrete pipe images.* Automation in Construction, 2006. **15**(1): p. 58-72.
34. Hu, Q., et al., *Combined three-dimensional structure and chemistry imaging with nanoscale resolution.* Acta Materialia, 2014. **77**: p. 173-182.
35. Hu, Q.N., et al., *3D chemical segmentation of fly ash particles with X-ray computed tomography and electron probe microanalysis.* Fuel, 2014. **116**: p. 229-236.
36. Ley, M.T., et al., *Combining Nano X-ray Tomography and Nano X-ray Fluorescence to Create Time-dependent Three Dimensional Constitutive Maps*, in *2nd International Conference on Tomography of Materials and Structures*. 2015: Quebec City, Canada.
37. Gallucci, E., et al., *3D experimental investigation of the microstructure of cement pastes using synchrotron X-ray microtomography (mu CT).* Cement and Concrete Research, 2007. **37**(3): p. 360-368.
38. Hu, Q., et al., *Direct measurements of 3d structure, chemistry and mass density during the induction period of C3s hydration.* cement and Concrete Research, 2016. **89**: p. 14-26.
39. Trtik, P., et al., *Density mapping of hardened cement paste using ptychographic X-ray computed tomography.* Cement & Concrete Composites, 2013. **36**: p. 71-77.
40. Fukuda, D., et al., *Investigation of self-sealing in high-strength and ultra-low-permeability concrete in water using micro-focus X-ray CT.* Cement and Concrete Research, 2012. **42**(11): p. 1494-1500.
41. Zolghadr, A., et al., *Biomass microspheres–A new method for characterization of biomass pyrolysis and shrinkage.* Bioresource technology, 2019. **273**: p. 16-24.
42. Promentilla, M.A.B. and T. Sugiyama, *X-Ray Microtomography of Mortars Exposed to Freezing-Thawing Action.* Journal of Advanced Concrete Technology, 2010. **8**(2): p. 97-111.
43. Sugiyama, T., et al., *Application of synchrotron microtomography for pore structure characterization of deteriorated cementitious materials due to leaching.* Cement and Concrete Research, 2010. **40**(8): p. 1265-1270.
44. Tekin, I., R. Birgul, and H.Y. Aruntas, *Determination of the effect of volcanic pumice replacement on macro void development for blended cement mortars by computerized tomography.* Construction and Building Materials, 2012. **35**: p. 15-22.
45. Farnam, Y., et al., *Measuring freeze and thaw damage in mortars containing deicing salt using a low-temperature longitudinal guarded comparative calorimeter and acoustic emission.* Advances in Civil Engineering Materials, 2014. **3**(1): p. 316-337.
46. Lu, H., K. Peterson, and O. Chernoloz, *Measurement of entrained air-void parameters in Portland cement concrete using micro X-ray computed tomography.* International Journal of Pavement Engineering, 2016: p. 1-13.

47. Lu, S., E.N. Landis, and D.T. Keane, *X-ray microtomographic studies of pore structure and permeability in Portland cement concrete.* Materials and Structures, 2006. **39**(6): p. 611-620.
48. Suzuki, T., et al., *Use of acoustic emission and X-ray computed tomography for damage evaluation of freeze-thawed concrete.* Construction and Building Materials, 2010. **24**(12): p. 2347-2352.
49. Kim, K.Y., et al., *Determination of air-void parameters of hardened cement-based materials using X-ray computed tomography.* Construction and Building Materials, 2012. **37**: p. 93-101.
50. Otsu, N., *A threshold selection method from gray-level histograms.* Automatica, 1975. **11**: p. 23-27.
51. Markoe, A., *Analytic tomography*. Encyclopedia of mathematics and its applications. 2006, Cambridge ; New York: Cambridge University Press. viii, 400 p.
52. Wong, R.C.K. and K.T. Chau, *Estimation of air void and aggregate spatial distributions in concrete under uniaxial compression using computer tomography scanning.* Cement and Concrete Research, 2005. **35**(8): p. 1566-1576.
53. De Borst, R., et al., *Fundamental issues in finite element analyses of localization of deformation.* Engineering computations, 1993. **10**(2): p. 99-121.
54. Lenoir, N., et al., *Volumetric digital image correlation applied to X-ray microtomography images from triaxial compression tests on argillaceous rock.* Strain, 2007. **43**(3): p. 193-205.
55. Otsu, N., *A threshold selection method from gray-level histograms.* IEEE transactions on systems, man, and cybernetics, 1979. **9**(1): p. 62-66.
56. Moradian, M., et al., *Multi-scale In-Situ Observations of Structure and Chemistry Changes of Portland Cement Systems During Hydration.* Construction and Building Materials. **212**: p. 486-499.
57. Suryavanshi, A., J. Scantlebury, and S. Lyon, *Mechanism of Friedel's salt formation in cements rich in tri-calcium aluminate.* Cement and concrete research, 1996. **26**(5): p. 717-727.
58. Farnam, Y., et al., *Acoustic emission and low-temperature calorimetry study of freeze and thaw behavior in cementitious materials exposed to sodium chloride salt.* Transportation Research Record: Journal of the Transportation Research Board, 2014(2441): p. 81-90.
59. Jensen, T.R., A.N. Christensen, and J.C. Hanson, *Hydrothermal transformation of the calcium aluminum oxide hydrates CaAl2O4· 10H2O and Ca2Al2O5· 8H2O to Ca3Al2 (OH) 12 investigated by in situ synchrotron X-ray powder diffraction.* Cement and concrete research, 2005. **35**(12): p. 2300-2309.
60. Powers, T.C. and T. Willis. *The air requirement of frost resistant concrete*. in *Highway Research Board Proceedings*. 1950.